論文 / 著書情報
Article / Book Information

題目(和文)	
Title(English)	Selective catalytic reduction of nitrogen oxide by hydrocarbon over Cu/zeolite catalysts
著者(和文)	LeeKyungseok
Author(English)	Kyungseok Lee
出典(和文)	学位:博士(工学), 学位授与機関:東京工業大学, 報告番号:甲第11227号, 授与年月日:2019年6月30日, 学位の種別:課程博士, 審査員:佐藤 進,花村 克悟,小酒 英範,店橋 護,野﨑 智洋
Citation(English)	Degree:Doctor (Engineering), Conferring organization: Tokyo Institute of Technology, Report number:甲第11227号, Conferred date:2019/6/30, Degree Type:Course doctor, Examiner:,,,,
学位種別(和文)	博士論文
Type(English)	Doctoral Thesis

Doctoral Thesis

Selective catalytic reduction of nitrogen oxide by hydrocarbon over Cu/zeolite catalysts

A dissertation submitted to
Tokyo Institute of Technology

for the degree of
Doctor of Engineering

by
Kyungseok LEE

Supervised by
Associate Professor Susumu SATO
Professor Hidenori KOSAKA

Department of Mechanical and Aerospace Engineering
Graduate School of Science and Engineering
Tokyo Institute of Technology

Table of Contents

List of Nomenclatures

Symbols	Definitions	Units
a_m	Cross sectional area of nitrogen molecule	nm^2
A_{BET}	BET specific surface area	m^3/g
AC_{NOx}	Adsorption capacity of NOx	mmol/L
$B.E$	Binding energy	eV
C_{BET}	BET constant	–
C_{Cu}	Copper concentration	ppm
$C^{in}_{C_3H_6}$	C_3H_6 concentration at catalyst inlet	ppm
$C^{in}_{C_4H_{10}}$	C_4H_{10} concentration at catalyst inlet	ppm
C^{in}_{CO}	CO concentration at catalyst inlet	ppm
C^{in}_{NO}	NO concentration at catalyst inlet	ppm
$C^{out}_{C_3H_6}$	C_3H_6 concentration at catalyst outlet	ppm
$C^{out}_{C_4H_{10}}$	C_4H_{10} concentration at catalyst outlet	ppm
C^{out}_{CO}	CO concentration at catalyst outlet	ppm
C^{out}_{HCN}	HCN concentration at catalyst outlet	ppm
C^{out}_{HNCO}	HNCO concentration at catalyst outlet	ppm
$C^{out}_{NH_3}$	NH_3 concentration at catalyst outlet	ppm
C^{out}_{NO}	NO concentration at catalyst outlet	ppm
$C^{out}_{N_2O}$	N_2O concentration at catalyst outlet	ppm
$C^{out}_{NO_2}$	NO_2 concentration at catalyst outlet	ppm
D_{Cu}	Particle diameter of Cu	nm
D_P	Average pore diameter	nm
d_h	Hydraulic diameter of monolithic cordierite	mm
d_k	Channel width of monolithic cordierite	mm
d_P	Pore diameter of powder catalyst	nm
F_{gas}	Flow rate of supplied synthetic gas	L/min
GSA	Geometry surface area of monolithic cordierite	cm^2/cm^3

I_{ref}	Relative intensity	a.u.
L	Cell spacing of monolithic cordierite	mm
K/M	UV-vis absorbance using Kubelka–Munk function	a.u.
m_{cat}	Mass of powder catalyst	g
N	Cell density of monolithic cordierite	cell/in^2
N_A	Avogadro's number	mol^{-1}
OFA	Open frontal area of monolith cordierite	%
P	Adsorption pressure of liquid N_2 at 77 K	kPa
P_0	Saturation vapor pressure of liquid N_2 at 77 K	kPa
$R_{CO/COx}$	CO over CO + CO_2 (COx) ratio	%
S_{BET}	Slop of BET-plot	cm^3/g
S_{N2}	N_2 yield	%
S_{NH3}	NH_3 selectivity	%
$GHSV$	Gas hourly space velocity	h^{-1}
T	Reaction temperature	℃
t_{sat}	Exposure time up to saturation level	min
V_{Ads}	Adsorbed volume of liquid N_2 at 77 K	cm^3/g
$V_{idela\ gas}$	Molar volume of ideal gas at 150℃	L/mol
V_{Micro}	Micropore volume	cm^3/g
$V_{Monolith}$	Volume of monolithic honeycomb	cm^3
V_P	Total pore volume	cm^3/g
W_{Cu}	Copper loading amount	wt%
Y_i	Y-intercept of BET-plot	cm^3/g
δ_{27Al}	Chemical shift of ^{27}Al MAS–NMR	ppm
ΔH^0_{298}	Standard enthalpy of formation	kJ/mol
η_{C3H6}	C_3H_6 conversion	%
η_{C4H10}	C_4H_{10} conversion	%
η_{CO}	CO conversion	%

η_{NOx}	NOx conversion	%
θ	Diffraction angle of XRD	°
λ	Wavelength of UV–vis DRS spectroscopy	nm
v_m	Monolayer adsorption capacity	cm^3/g

List of Abbreviations

Abbreviations	Definitions
A/F	Air to fuel ratio
Ag	Silver
Al_2O_3	Aluminium oxide
BaO	Barium oxide
BEA	Beta zeolite
BET	Brunauer–Emmett–Teller
BJH	Barrett–Joyner–Halenda
C_3H_6	Propene
C_4H_{10}	Butane
CHA	Chabazite zeolite
CeO_2	Cerium(IV) oxide
CO	Carbon monoxide
Cu	Copper
CO_2	Carbon dioxide
cpsi	Cells per square inch
DOC	Diesel oxidation catalyst
DPF	Diesel particulate filter
DRS	Diffuse reflectance spectroscopy
EGR	Exhaust gas recirculation
ECE	Economic commission for Europe
EEA	European environment agency
EUDC	Extra urban driving cycle
Fe	Iron
FE–SEM	Field emission–scanning electron microscope
FTIR	Fourier transform infrared spectroscopy
GHG	Greenhouse gas emission

GHSV	Gas hourly space velocity
H_2	Hydrogen
H_2O	Water
HC	Hydrocarbon
HCN	Hydrogen cyanide
HNCO	Isocyanic acid
HSDI	High speed direct injection
ICP–AES	Inductively coupled plasma–atomic emission spectrometry
IUPAC	International union of Pure and applied chemistry
LEV	Low-emission vehicle
LOT_{50}	Light-off temperature
LNT	Lean NOx trap
MAS–NMR	Magic angle spinning–nuclear magnetic resonance
NAC	NOx adsorber catalyst
N_2	Nitrogen
N_2O	Nitrous oxide
NEDC	New European driving cycle
NH_3	Ammonia
NO_2^-	Nitrite
NO_3^-	Nitrate
NOx	Nitrogen oxide
NSR	NOx storage-reduction
O_2	Oxygen
OSC	Oxygen storage capacity
PGM	Precious group metal
PM	Particulate matter
PPM	Parts per million
PSD	Pore size distribution

Pt	Platinum
Rh	Rhodium
SCR	Selective catalytic reduction
SDA	Structure directing agent
SiO_2	Silicon dioxide
SRS	Steam reforming reaction
STEM	Scanning transmission electron microscope
SULEV	Super ultra-low-emission vehicle
TiO_2	Titanium(IV) oxide
TMAdaOH	*N*,*N*,*N*-trimethyl-1-adamantammonium hydroxide ($C_{13}H_{24}N{\cdot}OH$)
TPD	Temperature programmed desorption
TPO	Temperature programmed oxidation
TWC	Three-way catalyst
UHD	Unburned hydrocarbon
ULEV	Ultra-low-emission vehicle
UV–vis DRS	Ultraviolet–visible diffuse reflectance spectroscopy
V_2O_5	Vanadium(V) oxide
WGSR	Water-gas shift reaction
WLTC	Worldwide harmonized light-duty driving test cycle
WO_3	Tungsten(VI) oxide
XPS	X-ray photoelectron spectroscopy
XRD	X-ray diffraction
ZrO_2	Zirconium(IV) dioxide
ZSM-5	Zeolite Socony Mobil-5 (MFI zeolite)

List of Figures

Chapter 1

Chapter 2

Chapter 4

Chapter 5

Appendices

List of Tables

Abstract

Cu-impregnated zeolite-based catalysts have been presented and discussed in this research thesis for the practical application of passive type HC-SCR system. The Cu/zeolite catalysts were prepared by an incipient wetness impregnation method by varying the Cu loading in a range of 1–10 wt%. The zeolite supports have different their frameworks, including SSZ-13 (CHA framework), ZSM-5 (MFI framework), and BETA (BEA framework). Several techniques, including HC/NOx ratio, hydrocarbon reductant, Cu content, zeolite framework, coexistent gas, and reaction environment (catalytic reactor system), were systematically explored and their effects on the NOx removal efficiency of Cu/zeolite catalysts were assessed.

The loading levels of Cu metal species were close to the theoretical loading amount, suggesting successfully introduction of Cu species. The XRD patterns demonstrated that the impregnation of Cu did not affect any modification of the respective zeolite structures. When increasing the Cu loading, chemical shift of ^{27}Al shifted to lower region, indicating the variation of average Al–O–Si angles in the zeolite framework. The valence states of Cu species were mainly presented as isolated Cu^{2+}, d-d transition of Cu^{2+}, and CuO clusters. The Cu/zeolites were more in favorable for the formation of CuO clusters with an increase in the Cu loading. The intra-crystalline diffuse diameter of respective zeolites affected the particle diameter of Cu, which was severely agglomerated over the SSZ-13 zeolite.

Cu/zeolite catalysts were evaluated for the main purpose of reducing NOx emissions by the C_3H_6-SCR process in the presence of O_2, CO, CO_2, and H_2O. To reach a high NOx conversion, a high HC/NOx ratio was needed. Increasing the HC/NOx ratio was favorable for the catalytic activity more reducing agnent could be available during the C_3H_6-SCR process. Among the prepared Cu/zeolite catalysts, 2Cu/ZSM-5 demonstrated the highest NOx

conversion to N_2 (68.5% at T = 360℃) at the highest HC/NOx ratio, followed by 1Cu/SSZ-13 (58.2% at T = 420℃) and 10Cu/BETA (56.1% at T = 375℃). Thus, the ZSM-5 zeolite, with a medium pore framework, was better suited for the C_3H_6-SCR process than SSZ-13, with a small pore framework, and BETA, with a large pore framework. The presence of isolated Cu^{2+} ions provided active sites for NOx reduction.

The effects of the zeolite framework and Cu loading on the catalytic activity for the C_4H_{10}-SCR were evaluated. The Cu loading improved the NOx conversion and shifted the temperature window of the maximum NOx conversion to lower regions compared to those for the parent zeolites. 2Cu/ZSM-5 exhibited the best de-NOx performance with nearly 74% at 465℃, followed by 10Cu/BETA (58% at T = 465℃) and 1Cu/SSZ-13 (38% at T = 585℃). These results were related to the effect of geometry-limited diffusion of C_4H_{10} in the respective zeolite channel system, in which the reductant had easy access to the active sites in the channels of ZSM-5 and BETA zeolite, but the diffusion of C_4H_{10} was highly restricted in the SSZ-13 channels.

Increasing the O_2 concentration in the feed gas had a positive effect on the de-NOx performance because the partial oxidation of hydrocarbons was enhanced at relatively low temperatures, indicating that O_2 is essential gas in HC-SCR process. However, a negative effect was observed when CO_2 was introduced in the feed gas because NOx adsorption and partial oxidation of hydrocarbos were highly inhibited by coexistent CO_2. When O_2 was not introduced, the NOx conversion increased with the reaction temperature, reaching 98% NOx conversion, but this condition induced an undesired side-reaction, producing a large amount of NH_3. The drop in NOx conversion after hydrothermal aging was attributed to the inhibitory effect of partial oxidation of hydrocarbons. The deactivation of the catalytic activity also induced the collapse of micropores, Cu sintering, and a drop in the zeolite crystallinity.

Chapter 1. Introduction

1.1 Background

Thanks to Rudolf Diesel (1858–1913), who firstly invented an internal-combustion diesel engine in 1898 [1], diesel engine has been utilized as a primary power source in the field of industry and transportation. The diesel engines for the passenger and commercial transportation particularly hold a significant market share in Europe, and their market share has captured more than 50% for the market [2]. They offer numerious advantages over the counterpart spark-ignited gasoline engines. The engine generally operates at a high compression ratio ranging from 16 to 22, thereyby improving the thermal-energy efficiency. Furthermore, the fuel combustion is also auto-ignition and takes place at very high air-to-fuel (A/F) ratios, leading to improvement of fuel economy as well as decrease in the amount of carbon dioxide (CO_2). However, current diesel engine is one of the major contributors to air pollution largely due to the harmful emissions; a diesel engine produces nitrogen oxides (NOx), carbon monoxide (CO), unburnt hydrocarbons (UHCs), and particulate matter (PM).

Over the last few decades, atmospheric pollutions emitted from both stationary and vehicle sources have been one of the major threats to all mankind, which has already received much attention how to deal with these pollutants. The large anthropogenic emissions of pollutants have been substantially increased, leading to a negative contribution to climate changes including global warming and ecological system as well as severe health risks [3]. Fortunately, to minimize these harmful emissions from a vehicle tail pipe, many feasible measures are focused largely on the engine management, alternative fuels, control of combustion including fuel injection, exhaust gas recirculation (EGR), catalytic reduction using after-treatment system, and diesel particulate filter (DPF).

1.2 Worldwide trends on automotive emission regulations

Figure 1.1 summarizes an overview of automotive emission regulations for passenger vehicle in Japan, Europe and United States, in which these countries have established by far the tightest regulations around the world. Each country has independent regulations, and a variety of stringent regulations are being taken to restore the atmospheric quality. Vehicles have commonly been evaluated on a certificated chassis dynamometer for testing the emission regulations and fuel consumption simultaneously with authorized vehicle test cycles; those are known as driving test cycles [4, 5], as illustrated in Figure 1.2. The driving cycles, for example, that had been introduced in the European Union for the passenger and light-duty vehicles were the urban driving cycle (ECE-15) and the ECE + EUDC beginning with Euro I regulation in 1992; the combination cycle of ECE and EUDC are known as a New European Driving Cycle (NEDC) from 2000 [4, 6, 7]. In the case of Japan, the regulation was first introduced by the Air Pollution Control Law in 1966, and it was established for spark-ignited light-duty vehicles in 1966 [8]. The J10-15 mode consists of three replications of J10 mode followed by one J15 mode (Figure 1.2(a)); the total distance and maximum speed is approximately 4.16 km and 70 km/h, respectively. Japanese authorities also introduced the JC08 test cycles as of 2009, in an attempt to reflect real driving conditions [9].

There are numerous types of vehicles depending on the countries with different displacement, specifications, and for this reason a new test procedure has been considered to make universal driving cycle as much as possible on a global scale; concretely, the major conference that is the World Forum for Harmonization of Vehicle Regulations (WP.29) was held under the United Nations Economic Commission for Europe (UNECE) [10, 11]. Subsequently, the worldwide harmonized light-duty driving test cycle (WLTC, Figure 1.2(d)) was developed with the aim to harmonize emission test procedures for light-duty vehicles; in

the case of WLTC class 3b, the total distance is 23.266 km/h, and the maximum speed is 131.3 km/h [4, 12]. Currently European NEDC procedure will be replaced by this WLTC occurring over 2017–2019 in European Union, as illustrated in Figure 1.1.

As mentioned above, the environmental awareness of exhaust emissions from vehicles has been elevated all over the world. Among various vehicle emissions, NOx, CO, HCs and PM are under control by strict emissions regulations [5, 13]. This is the fact that the majority of harmful emissions is related to road transportation equipped with internal combustion engines using fuels derived from fossil fuels [14]. The order of magnitude of the relative road transport in the total exhaust emissions of carbon monoxide, ammonia, non-methane volatile organic compounds (VOC), nitrogen oxide, particulate matter (PM_{10} or $PM_{2.5}$), and sulfur oxide is shown in Figure 1.3 [15]. From these data, it turns out that road transport is one of the major sources of carbon monoxide and nitrogen oxide.

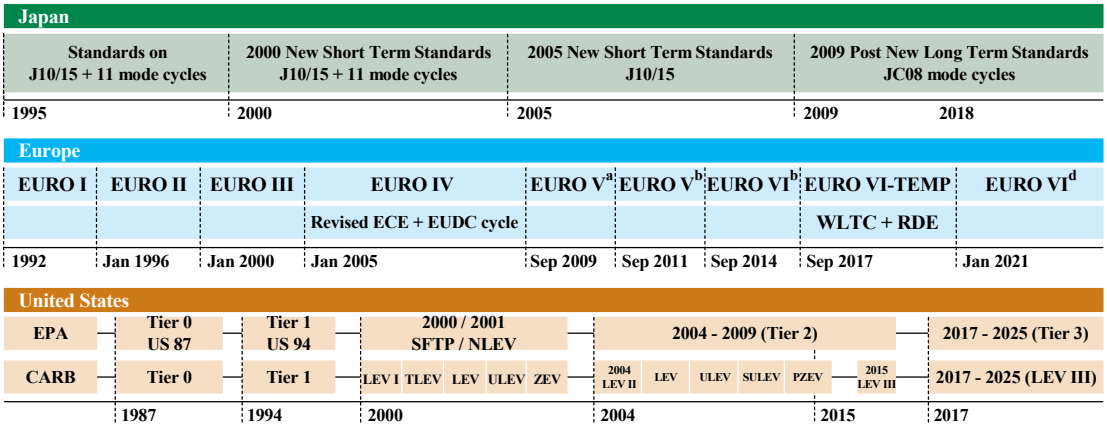

Figure 1.1 Historical overview of automotive emission regulations for diesel passenger vehicle.

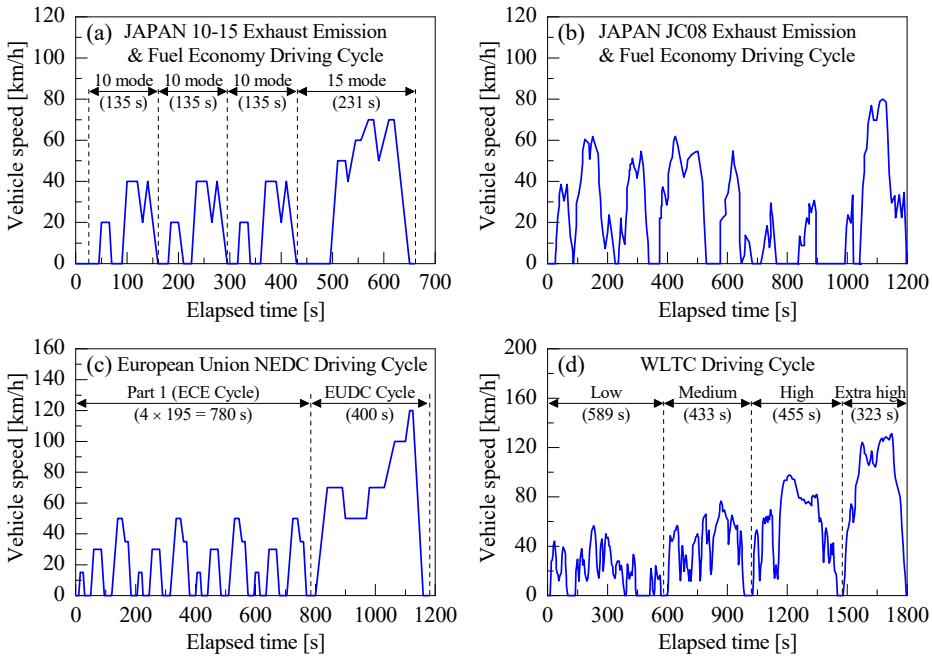

Figure 1.2 Speed profiles of authorized driving cycles for the determination of emissions and fuel consumption from light-duty vehicles: (a) Japan 10-15 mode, (b) Japan JC08 mode, (c) NEDC mode, and (d) WLTC (class 3b) mode.

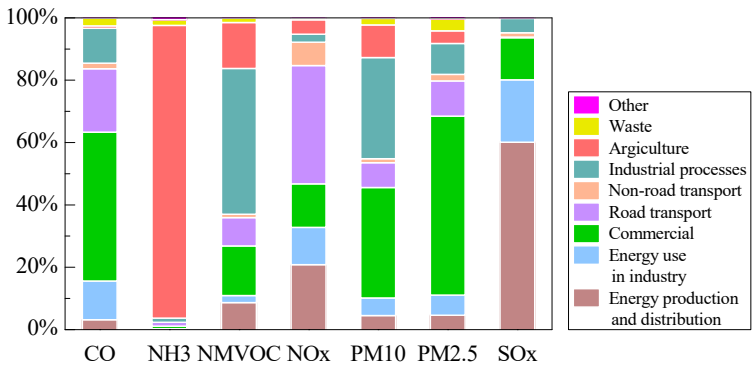

Figure 1.3 Share of EEA-33 emission of main air pollutants by sector group (European Environment Agency, emissions of the main air pollutants in Europe, reprinted from ref. [15]).

Over the last few decades, the number of countries enacting the legislative emissions regulations in force for these kinds of emissions (NOx, CO, HC, and PM) grew at a highly rate. The regulated emission trends have been lowered continuously, as illustrated in Figure 1.4. For example, in European Union the quantity of NOx emission (Figure 1.4(b)) was regulated at 0.5 g/km in Euro III stage, and this value was substantially reduced to 0.05 g/km in Euro VI stage. Although there is a wide variation in the level of regulation, the common characteristic on emission trends employed is expected that emission limits will continue to be tightened from now onwards [16–18]. The transition of emissions regulations has driven technological changes in the control of vehicle emissions from the diesel vehicle to comply with the strict emission limit, mostly by advanced automotive after-treatment technique [2].

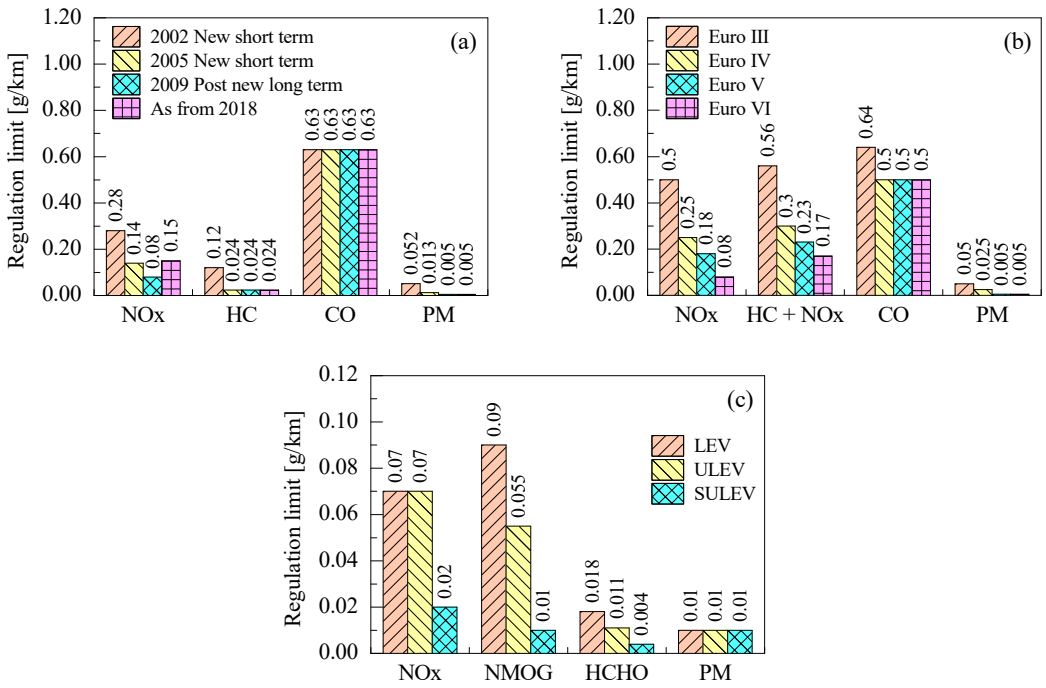

Figure 1.4 Worldwide trend on emissions regulations for passenger vehicle in (a) Japan, (b) European Union, and (c) United States.

1.3 Automotive emission control techniques

The initiative of automotive emissions regulations in the United States, European Union and Japan has been followed by the worldwide emission regulations in many countries, and these emissions regulations of varying stringency now exist in over 30 nations [19]. To meet the vehicle emissions regulations, there are two representative techniques available now which are so-called pretreatment and after-treatment, respectively.

The pretreatment is completely dependent upon the engine management or alternative fuels, which offers a possibility to abate the formation of harmful emissions during the combustion period. This technique is also related to the modicifications of fuel-injection process; modern fuel-injection system for diesel vehicles is required to fulfill the control of injection pressure, injection rate, and flexible timing [20–23]. On the other hand, the after-treatment techniques can help abatement of toxic emissions before being emitted into atmosphere. These techniques utilize typically the catalytic converters and diesel particulate filter (DPF) that is an open or close monolithic structure allowing exhaust gases to pass through the catalytic converter with some active phases coating applied to the channel walls of the monolithic converter [24–29]. In automotive applications, the monolith substrate is commonly made from ceramic cordierite ($2MgO{\cdot}2Al_2O_3{\cdot}5SiO_2$: 14% MgO, 35% Al_2O_3, and 51% SiO_2), having high melting temperature of 1,500℃ and low expansion coefficients. To understand the past and present automotive emission control techniques in more detail, the pretreatment and after-treatment systems will be reviewed in the following sections.

1.3.1 Recent techniques on pretreatment

The pretreatment technique is associated with the engine management or modification, which plays an important role to reduce automotive emissions as well as to improve both the

engine performance and fuel efficiency. The exhaust gas recirculation (EGR) has been utilized as one of the most popular solutions for an in-cylinder NOx control; EGR offers a way to abate NOx emissions by returning a certain ratio of exhaust into the intake manifold, thereby decrease in combustion temperatures and oxygen concentration, as illustrated in Figure 1.5. Theoretically, increasing heat capacity of in-cylinder combustion products, vapor and carbon dioxide, affects the local temperature in a combustion chamber [30]. Since NOx is formed by the Zeldovich mechanism, also called the thermal NOx mechanism, reducing the combustion temperature can help a theoretically effective suppression of NOx emissions. Therefore, the EGR is an established technique to reduce NOx emissions, however it is apprehended that the reduction of NOx with EGR can lead to complex and sometimes opposite phenomena [31–33]. Maiboom *et al*. [32] have reported some effects of EGR (intake temperature, the rate of heat release, and stoichiometric air-fuel ratio) on combustion and emissions with a typical high-speed direct injection (HSDI) engine. They have concluded from the experiment that NOx and PM emissions could be suppressed using high EGR rates at constant boost pressure. However, high EGR rates induce a negative effect on brake-specific fuel consumption, CO, and HC emissions.

The fuel-injection strategy also plays a significant role in improving engine performance and abatement of harmful emissions at the same time. High injection pressure generally leads to small droplet size of atomized fuels, resulting in improving combustion characteristics and decrease in PM emissions. This can be described why recent diesel vehicles have adopted high pressure common rail injection systems. In addition, multiple fuel injections along with common rail system have been extensively researched because it makes more homogeneous mixtures due to decrease in spray penetration and promoting the amount of fuel evaporation in the cylinder [23, 34].

The national program of greenhouse gas emissions (GHG) demands that carbon dioxide (CO_2) emissions should be further reduced, as illustrated in Figure 1.6. The abatement of CO_2 emissions can be achieved either via increase in thermal efficiency of engine or using alternative fuels such as biofuels. There are two feasible alternative fuels, in general bioalcohol/bioethanol and biodiesel [35]. To accomplish the GHG target, several improvements in thermal management, friction reduction and combustion efficiency have can help to reduce the fuel consumption [36]. Furthermore, an optimization of fuel injector and advanced design of combustion chamber can help drop in the fuel consumption.

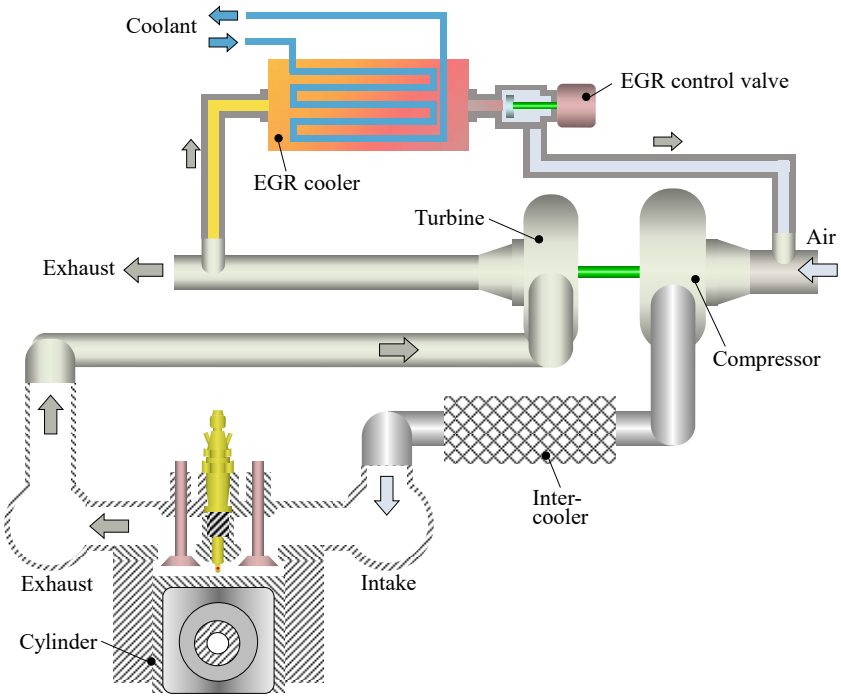

Figure 1.5 Schematic configuration of exhaust gas recirculation (EGR) (Reprinted by permission from Springer Nature of ref. [23]).

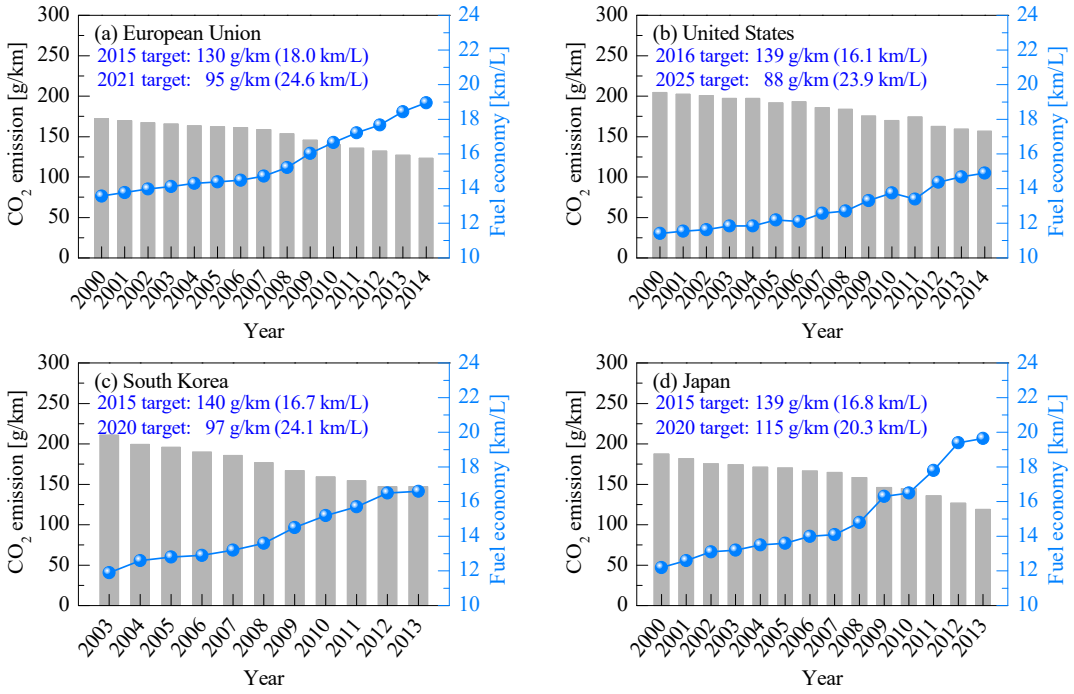

Figure 1.6 Historical trends of CO_2 emission, fuel economy, and future targets of passenger vehicles in (a) European Union, (b) United States, (c) South Korea, and (d) Japan.

1.3.2 Three–way catalyst (TWC)

Automotive catalysts for the abatement of vehicle emissions have been developed since 1974 when three-way catalysts were introduced in the United States and Japan, because of further reduction of emissions required by new emission regulations [37]; the catalysts were required to simultaneously convert the CO, NOx and HCs into CO_2, H_2O and N_2. The three–way catalyst (TWC) was developed as an effective solution to simultaneously reduce CO, NOx and HCs for gasoline vehicle. Because all three major emissions could be purified by this catalyst, the concept was christened the three-way catalyst [5]. The related reaction in the TWC can be described by the following reactions [39–41]:

i) Oxidation reactions

$$CO + \frac{1}{2}O_2 \rightarrow CO_2 \quad (1.1)$$

$$C_mH_n + \left(m + \frac{n}{4}\right)O_2 \rightarrow mCO_2 + \frac{n}{2}H_2O \quad (1.2)$$

ii) NO reduction reactions

$$2CO + 2NO \rightarrow N_2 + 2CO_2 \quad (1.3)$$

$$C_mH_n + \left(2m + \frac{n}{2}\right)NO \rightarrow \left(m + \frac{n}{4}\right)N_2 + mCO_2 + \frac{n}{2}H_2O \quad (1.4)$$

$$2H_2 + 2NO \rightarrow N_2 + 2H_2O \quad (1.5)$$

iii) Hydrogen production reactions (water-gas shift and steam reforming reaction)

$$CO + H_2O \rightarrow CO_2 + H_2 \quad (1.6)$$

$$C_mH_n + H_2O \rightarrow CO_2 + H_2O \quad (1.7)$$

Figure 1.7 represents a catalytic performance of TWC as a function of the air to fuel (A/F) ratios. The TWC can reach high rate of conversion of CO, NOx and HCs at a very narrow A/F ratio, in which three major emissions can be only reduced close to a stoichiometric range (A/F ratio = 14.5). When the engine runs in fuel rich atmosphere, the O_2 concentration is insufficient for the oxidation reaction of CO and HCs. On the contrary, the engine effectively improves the fuel efficiency under fuel lean atmosphere, however NOx reduction is extremely difficult due to oxidation of available reductants with high levels of coexistent oxygen. As a result, the engine should be operated in a very narrow range of A/F, and the traditional TWC is only effective as the catalytic convertor for gasoline engine to reduce NOx at the stoiometric point.

Rhodium (Rh) as an active material plays an important role in the TWC for the effective abatement of CO, NOx and HCs [42]. However, Rh supported on the alumina (Rh/γ-Al_2O_3) has been known for having many drawbacks under an oxidizing atmosphere. Beck *et al*. [43]

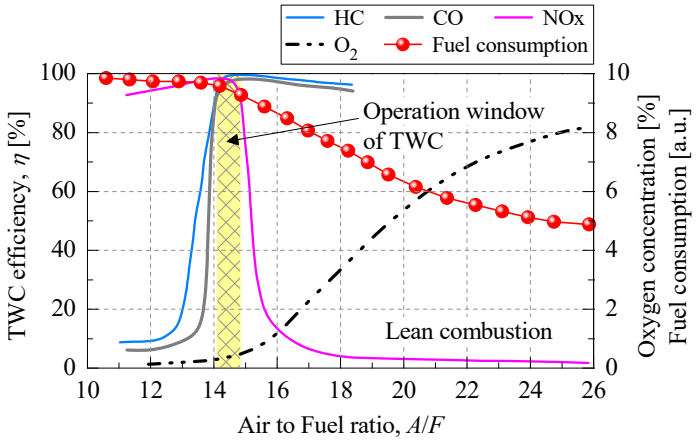

Figure 1.7 Catalytic performance of three–way catalyst and fuel consumption as a function of air to fuel (A/F) ratios over a spark-ignited engine (Reprinted by permission from Elsevier of ref. [38]).

have reported that Rh easily reacts with the γ-Al_2O_3 support to form different phases at high temperatures, resulting in losing its catalytic activities. An addition of cerium(IV) oxide (ceria, CeO_2) has been proved to be effective to enhance the thermal tolerance of Rh/γ-Al_2O_3 catalysts; in fact, CeO_2 was found to be a significant oxygen storage capacity (OSC), while γ-Al_2O_3 could not store or release O_2 under the vehicle exhaust conditions [44]. Recently, Han *et al*. [45] and Wang *et al*. [46] investigated the enhancement of the water-gas shift reactions (WGSR) and steaming reforming reactions (SRS) for the TWC, which favors the further removal of CO and HCs. The incorporation of zirconium(IV) dioxide (zirconia, ZrO_2) into the CeO_2 also improved the catalytic performance of oxygen storage capacity (OSC) as well as stabilized CeO_2 particles against the hydrothermal sintering.

1.3.3 NOx storage–reduction (NSR) catalyst

Gasoline engines operate close to stoichiometric point with an A/F ratio of 14.5. Diesel

engines and lean-burn gasoline engines operate under fuel lean atmosphere with a higher A/F ratio than the stoichiometric conditions. Although the lean-burn combustion has many benefits due to its higher fuel efficiency and lower CO_2 emission, NOx emission cannot be efficiently reduced over the conventional TWC, especially in the presence of excess O_2 [47–50]. Thus, NOx storage-reduction (NSR) catalyst emerged as an alternative after-treatment technology for passenger diesel vehicles to control NOx emissions in the fuel-lean operating conditions.

The NSR technique was first invented by Toyota Motor Corporation in 1990s [47, 51–53], and this catalyst, also referred to as a lean NOx trap (LNT) or NOx adsorber catalyst (NAC), was commercially released on the market [54]. Figure 1.8 schematically shows the related mechanism of NOx storage-reduction and a profile of NOx during repetitive lean or rich operation; the NSR catalyst works under repetitive conditions in the oxygen-rich and fuel-rich environments. The NSR catalyst consists of the precious group metal (PGM), NOx storage component and support that the general composition is $Pt/BaO/Al_2O_3$ [55–62]. When an engine operates in the lean-burn environment, NO is converted on the PGM surface into NO_2, and then there is a relative slow increase in the NOx concentration in the catalyst outlet. This phenomenon indicates that both NO and NO_2 are stored on the storage component in the form of nitrite or nitrate species. Before NOx storage capacity reaches the saturation level, the A/F ratio is changed to a fuel-rich mixture which leads to successfully reduce the stored NOx to N_2 due to the coexistent reductants. Based on these findings, periodic NOx storage and reduction cycle is the novel concept, namely the NSR catalysts [54]. The related reactions of the NOx storage and reduction for this catalyst are described in the following steps [48, 62, 63]:

i) Storage of NO at BaO or $Ba(OH)_2$ sites close to Pt sites

$$O_2 \leftrightarrow 2O^* \tag{1.8}$$

$$Ba + 2NO + O^* \rightarrow Ba(NO_2)_2 \tag{1.9}$$

$$Ba + 2NO + 3O^* \rightarrow Ba(NO_3)_2 \tag{1.10}$$

$$Ba(OH)_2 + 2NO + O^* \rightarrow Ba(NO_2)_2 + H_2O \tag{1.11}$$

$$Ba(NO_2)_2 + 2O^* \rightarrow Ba(NO_3)_2 \tag{1.12}$$

ii) $Ba(NO_3)_2$ formation via oxidation of NO to NO_2

$$NO + \frac{1}{2}O_2 \rightarrow NO_2 \tag{1.13}$$

$$2BaO + 4NO_2 \rightarrow Ba(NO_2)_2 + Ba(NO_3)_2 \tag{1.14}$$

$$BaO + 2NO_2 + O^* \rightarrow Ba(NO_3)_2 \tag{1.15}$$

$$Ba(OH_2) + 2NO_2 + O^* \rightarrow Ba(NO_3)_2 + H_2O \tag{1.16}$$

iii) Reduction reaction of stored NOx

$$Ba(NO_2)_2 + 3H_2 \rightarrow BaO + N_2 + 3H_2O \tag{1.17}$$

$$Ba(NO_3)_2 + 5H_2 \rightarrow BaO + N_2 + 5H_2O \tag{1.18}$$

iv) Overall reaction of NSR catalyst

$$NO \xrightarrow{O_2} NO_2 \xrightarrow{O_2} Ba(NO_2)_2 + Ba(NO_3)_2 \tag{1.19}$$

$$Ba(NO_3)_2 \xrightarrow{HC,\ H_2,\ CO} BaO + NO_2 \xrightarrow{HC,\ H_2,\ CO} N_2 + CO_2 + H_2O \tag{1.20}$$

Although many studies have demonstrated the catalytic phenomena of NSR catalysts, the reaction mechanism of NOx storage and reduction has not been clearly clarified. The NSR system operates under cyclic conditions by alternating long-lean phases (60–90 s) during which NOx is captured on the NSR surface, with short-rich phases (3–5 s) during which the stored NOx is reduced into N_2. As mentioned above, a typical NSR catalyst

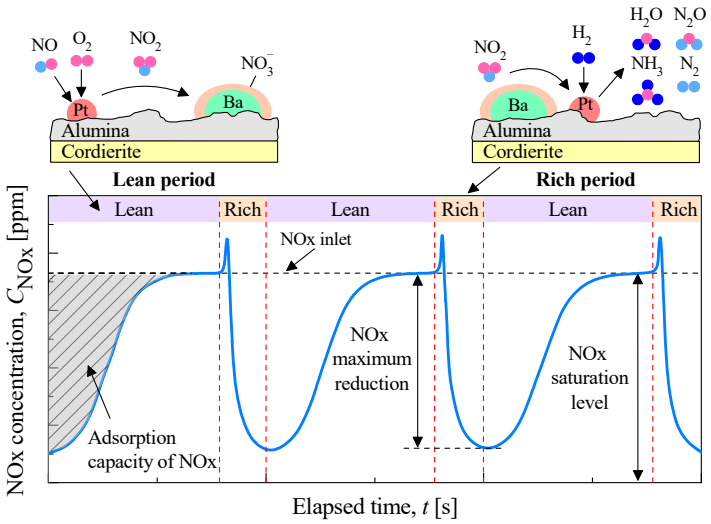

Figure 1.8 NOx profiles during the lean-rich cycles for adsorption and reduction of NOx over the NOx storage-reduction catalyst.

contains alkaline earth or alkaline metals such as barium (Ba) and potassium (K) to effectively store NOx, PGM such as platinum (Pt) with rhodium (Rh) or palladium (Pd) to oxidized NO, HCs and CO as well as to reduce the stored NOx, and support with a high BET surface area such as alumina (Al_2O_3), in which the active metals are dispersed evenly [62]. The catalytic material adopted is alumina (Al_2O_3), barium (Ba) and platinum (Pt), which is the major components of NSR catalyst [54].

The PGM of NSR catalyst plays several key roles in the respective NOx storage and reduction step. Especially the oxidation of NO into NO_2 is an initial reaction in the NSR mechanism, because the BaO or $Ba(OH)_2$ can effectively store NO_2 compared to NO. The major species stored on the catalyst surface was identified as nitrate (NO_3^-) by infrared (IR) spectroscopy [47]. Forzatti *et al.* [64] have reported that the presence of Pt–Ba couples (Pt–Ba interaction) is relevant for the nitrite or nitrate route, as illustrated in Figure 1.9. Furthermore, the effect of Pt dispersion on the performance of NSR catalyst has been widely investigated [65−67] because the particle sizes of respective Pt affected both the NO

oxidation and NOx reduction.

A typical layout of after-treatment system with combined EGR, NSR and DPF is illustrated in Figure 1.10. In this configuration, the diesel oxidation catalyst (DOC) is placed in front of the NSR catalyst, which can facilitate oxidation reactions of CO and HCs into CO_2 and H_2O, and NO oxidation into NO_2. Thus, ratio of NO_2/NOx in the exhaust increased, and the increased NO_2 can be easily stored on the behind NSR catalyst.

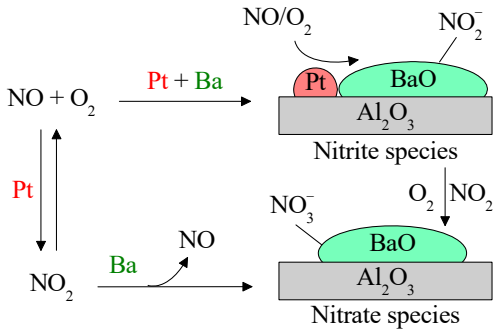

Figure 1.9 Reaction pathways for NOx oxidation and NOx adsorption over the Pt-Ba/Al_2O_3 catalysts (Reprinted by permission from Elsevier of ref. [64]).

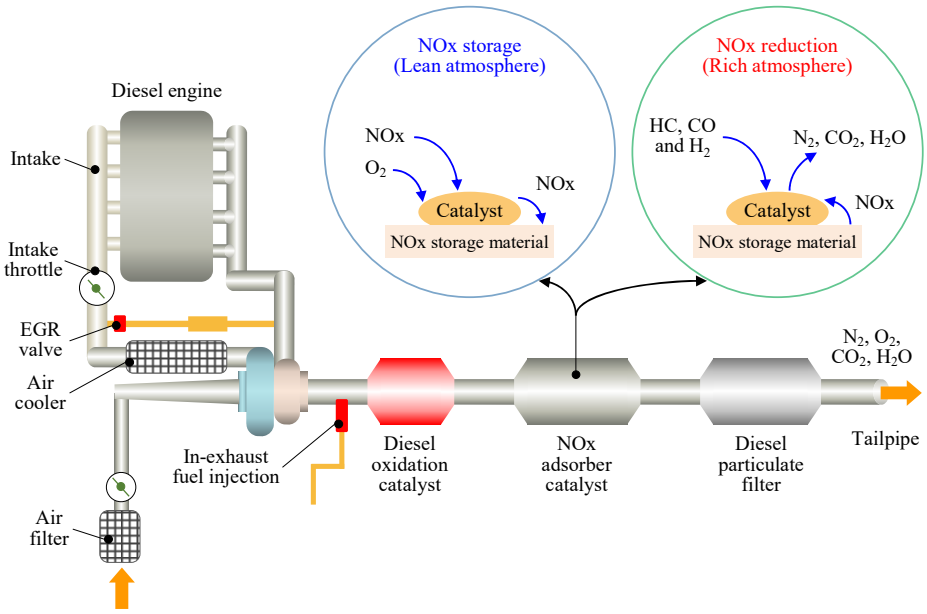

Figure 1.10 Layout of automotive after-treatment system equipped with EGR, NSR and DPF system (Reprinted by permission from Springer Nature of ref. [23]).

1.3.4 Selective catalytic reduction by urea (urea-SCR)

Since the selective catalytic reduction using urea as a reductant (urea-SCR) was introduced in the stationary plant in 1978 [68], this system has been intensively investigated to apply it to automobile after-treatment system, especially for suppression of NOx emission in the heavy-duty diesel vehicle. Urea-SCR was also introduced as European automotive technique to comply with the Euro IV regulation, and it was applied to light-duty and passenger vehicles in the United States and Europe. The urea-SCR technique is the fact that ammonia (NH_3) is the primary reductant that is derived from an aqueous urea solution because it is difficult to deal with the pure NH_3 regarding storage, toxicity, stability and so on. European automotive makers made a common consensus on the utilization of 32.5% aqueous urea solution for commercial vehicles [19]. Nowadays, this system becomes the most representative after-treatment technique for abatement of NOx emission.

Basically, the urea-SCR reactions proceed via three steps, including standard, fast and slow reaction; molar ratio of respective NO, NO_2 and NH_3 determines above reactions:

i) Standard SCR reaction

$$4NO + 4NH_3 + O_2 \rightarrow 4N_2 + 6H_2O \quad (1.21)$$

ii) Fast SCR reaction

$$NO + NO_2 + 2NH_3 \rightarrow 2N_2 + 3H_2O \quad (1.22)$$

iii) NO_2–SCR reaction (slow SCR reaction)

$$3NO_2 + 4NH_3 \rightarrow 3.5N_2 + 6H_2O \quad (1.23)$$

Reaction (1.21) is the standard SCR reaction, which is the main reaction because the NOx emitted from the diesel vehicle is comprised of more than 90% NO. The standard SCR

reaction represents an equimolar ratio of NO and NH_3 with a consumption of one mole of oxygen. This reaction without oxygen is very slow, and it is not applicable for exhaust after-treatment system [69]. The reaction (1.22) with equimolar amounts of NO and NO_2 is the fastest and highly desired reaction. On the other hand, if the NO_2 ratio increases, reaction (1.23) can be predominant in the SCR reaction that is the lowest reaction rate.

The NO_2/NOx ratio in the raw exhaust is very low less than 10%, as illustrated in Figure 1.11(a). An addition of DOC upstream the urea-SCR (Figure 1.11(b)) can significantly help enhance the fast SCR reaction, in which a part of engine-out NO could be oxidized into NO_2. In this DOC + SCR layout, the oxidation rate of NO into NO_2 should be controlled at nearly NO_2/NOx ratio = 0.5 because the NO_2–SCR reaction occurs, when the NO_2/NOx ratio exceeds this value (NO_2/NOx ≥ 0.5).

An example of typical on-board urea-SCR system for automobile is illustrated in Figure 1.12. The urea aqueous solution is injected and atomized via the exhaust gas stream, and then the pure urea undergoes multiple reactions by the following steps to yield available NH_3:

i) Evaporation of urea aqueous solution

$$NH_2—CO—NH_2\ (\text{aqueous}) \rightarrow NH_2—CO—NH_2\ (\text{molten}) + xH_2O\ (\text{gas}) \quad (1.24)$$

ii) Thermal decomposition of urea

$$NH_2—CO—NH_2\ (\text{molten}) \rightarrow NH_3\ (\text{gas}) + HNCO\ (\text{gas}) \quad (1.25)$$

iii) Hydrolysis of isocyanic acid (HNCO)

$$HNCO\ (\text{gas}) + H_2O\ (\text{gas}) \rightarrow NH_3\ (\text{gas}) + CO_2\ (\text{gas}) \quad (1.26)$$

iv) Overall reaction

$$NH_2—CO—NH_2\ (\text{aqueous}) + H_2O\ (\text{gas}) \rightarrow 2NH_3\ (\text{gas}) + CO_2\ (\text{gas}) \quad (1.27)$$

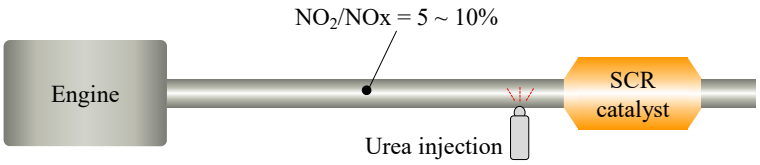

(a) Urea-SCR system without upstream diesel oxidation catalyst

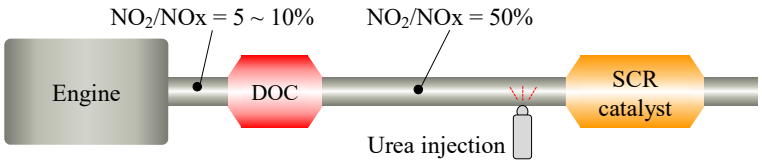

(b) Urea-SCR system with upstream diesel oxidation catalyst

Figure 1.11 Layout of urea-SCR system to reduce the NOx emissions for enhancing the fast SCR reaction with a DOC.

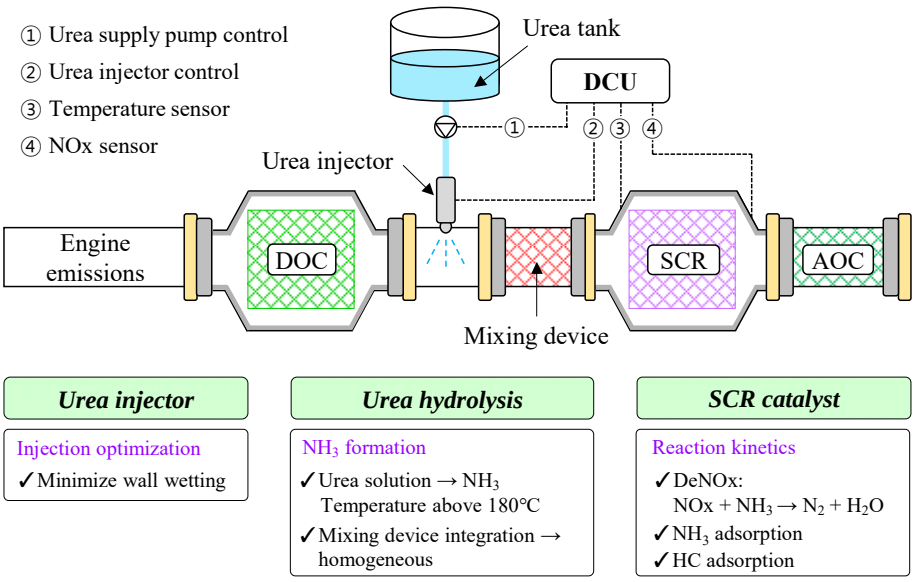

Figure 1.12 On-board urea-SCR system incorporating DOC, urea doing control unit and NOx sensor.

Reaction (1.24) is the evaporation of atomized urea solution from the urea water solution to molten urea, and then this atomized urea is thermally decomposed via reaction (1.25), yielding one mole of NH_3 and isocyanic acid (HNCO), respectively. Subsequently, HNCO yields another NH_3 via the hydrolysis of HNCO with H_2O [70]. When the urea is supplied in the exhaust line below 200°C, the hydrolysis reaction of HNCO and thermal decomposition is limited. Unfortunately, the use of urea aqueous solution usually induces some unexpected disadvantages including undesirable formation of solid deposits, especially at low temperature.

As illustrated in Figure 1.13, biuret (NH_2–CO–NH–CO–NH_2) is formed by the reaction of HNCO with urea above the melting point of urea (≥133°C) [71]. Some byproducts, biuret and cyanuric acid, are also observed at the temperatures up to 300°C; it is known that biuret is formed at 150–190°C and the formation of cyanuric acid ($C_3N_3(OH)_3$) is predominant at tempratures of 200–300°C [72, 73]. Because these byproducts are unfavorable for the subsequent urea-SCR, some feasible measures have been implemented, including a high spray quality and use of catalysts for promoting the hydrolysis reaction of HNCO [74, 75].

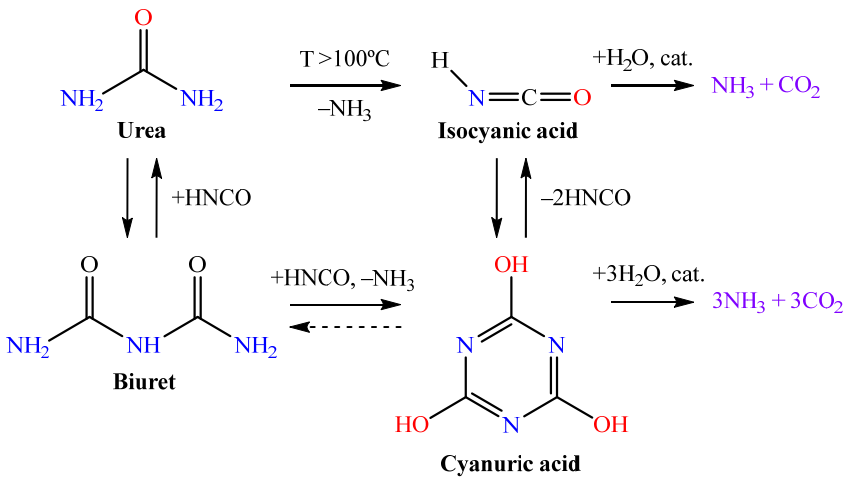

Figure 1.13 Reaction scheme for decomposition of urea aqueous solutions with the biuret and cyanuric acid (Reprinted by permission from Elsevier of ref. [71]).

Up to date, urea-SCR technique has been extensively investigated to elucidate the complex reaction schemes and active-catalytic materials. From a practical point of view, some promising candidates applied to urea-SCR or NH_3-SCR have been studied: for example, the catalysts contain metal oxides supported on titanium(IV) oxide (TiO_2), silica (SiO_2), vanadium(V) oxide (V_2O_5), tungsten(VI) oxide (WO_3), and zeolites. Among the various compositions of the urea-SCR catalyst, the ion-exchanged metals such as iron (Fe) or copper (Cu) on zeolites have been focused from academia and industrial area due to their high activities and cost effectiveness compared to other materials. The primary differences between iron and copper ion-exchanged zeolites are the active-operating temperature for NOx abatement. For the last few decades, Cu/ZSM-5 and Fe/ZSM-5 that are the most promising catalysts have been considered as the suitable SCR catalyst. Cu/ZSM-5 is suitable for which the reaction temperature is below 450℃. Whereas, Fe/ZSM-5 catalyst is preferred at temperatures from 450 to 600℃ [76, 77]. To widen the operating ranges, a combination of copper and iron has been also attempted, and the combined system demonstrated that the operating temperature could be expanded to some extent.

Figure 1.14 shows the catalytic performance of commercial Fe/ZSM-5, Cu/ZSM-5 and V_2O_5/WO_3-TiO_2 catalyst coated on the monolithic cordierite substrate. Cu/ZSM-5 is even higher NOx conversion than that of Fe/ZSM-5 and V_2O_5/WO_3-TiO_2 catalyst at $T \leq 300$℃, and Cu/ZSM-5 is more active than V_2O_5/WO_3-TiO_2 at high temperatures, $T \geq 500$℃ [78]. Fe/ZSM-5 exhibits the lowest NOx conversion below 500℃, whereas it is more active than Cu/ZSM-5 and V_2O_5/WO_3-TiO_2 at higher temperatures above 500℃. From the results of Figure 1.14, Cu/ZSM-5 catalyst is the best choice for the low and medium temperature ranges. V_2O_5/WO_3-TiO_2 catalyst seems to be suitable for a broad intermediate temperature range, whereas Fe/ZSM-5 catalyst appears to be a best option for high temperature applications [78].

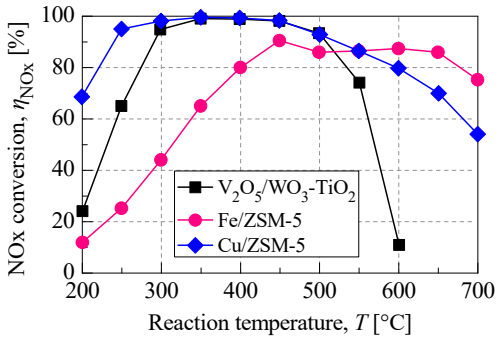

Figure 1.14 NOx conversion efficiency as a function of reaction temperature over Fe/ZSM-5, Cu/ZSM-5 and V_2O_5/WO_3-TiO_2 catalyst.
Feed gas: 1000 ppm NO, 10% O_2, 5% H_2O, 1000 ppm NH_3 at GHSV = 52,000 h^{-1} (Reprinted by permission from Elsevier of ref. [78]).

1.3.5 LNT+SCR combined system

The NSR catalyst has strong potential for abatement of NOx by both the storage of NOx and regeneration of the catalyst surface. When stored NOx reacts with a reductant such as H_2, NH_3 is reported to be produced as a byproduct. The related reaction of H_2 consumption and NH_3 formation is due to the reduction reaction of adsorbed nitrate species or nitrite species according to the following reactions [79]:

$$Ba(NO_2)_2 + 6H_2 \rightarrow 2NH_3 + BaO + 3H_2O \quad (1.28)$$

$$Ba(NO_3)_2 + 8H_2 \rightarrow 2NH_3 + BaO + 5H_2O \quad (1.29)$$

$$Ba(NO_3)_2 + 8H_2 \rightarrow 2NH_3 + Ba(OH)_2 + 4H_2O \quad (1.30)$$

The yield of NH_3 in the fuel-rich phase over the LNT catalyst is proscribed, and these undesirable reactions should be limited. However, in the combination of LNT and SCR system, NH_3 formed is reused over the downstream SCR catalyst as a reductant, thereby

further improving the de-NOx performance via the selective catalytic reaction as well as reducing unreacted NH_3 slip. The formed NH_3 on the LNT catalyst is captured on the downstream SCR catalyst, in which it subsequently can react with NOx during the fuel-lean period [80–83].

The first commercial LNT+SCR system was released to the United States market in the form of the 2007 E320 BlueTEC emission control system for light-duty vehicle [84]. The schematic layout of the catalyst system for the combination of LNT+SCR system is illustrated in Figure 1.15, in which the BlueTEC system uses a DOC and DPF to reduce CO, HC and PM emissions. This combined LNT+SCR can improve the NOx conversion over a stand-alone LNT without increase in fuel consumption, and it can also supress the NH_3 slip [85].

When H_2 is used as a reductant, the typical Pt–Ba/Al_2O_3 is highly selective for the formation of N_2 or NH_3, depending on the supplied H_2, amount of stored NOx, and catalytic reaction temperatures. Therefore, optimum management of the operating environments for the NOx adsorption and NOx reduction can help the selectivity to N_2 or NH_3 [85, 86].

The LNT+SCR combined system has been extensively studied regarding durability of hydrothermal aging [81], the effect of catalyst layout [87], operating conditions such as space velocity [88] and the effect of volume in the combined system [89]. In the downstream SCR catalyst, non-noble metals such as Fe and Cu ion-exchanged over the Beta or ZSM-5 zeolites

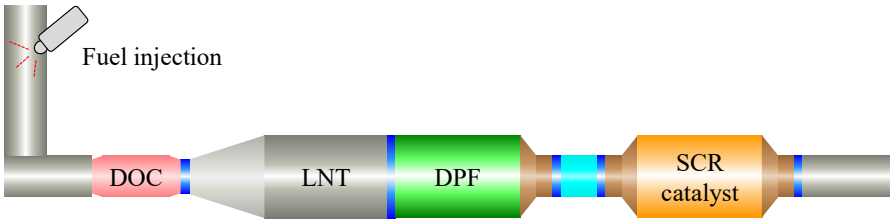

Figure 1.15 Schematic diagram of automotive after-treatment system configuration for the combination of LNT+DPF+SCR.

are among the most active catalysts. Torre *et al*. [90] have demonstrated the catalytic performance by combining the LNT catalyst with the SCR catalyst without providing the NH_3 reductant. Figure 1.16 represents a comparison of stand-alone LNT and LNT+SCR combined configuration regarding the NOx conversion, NH_3 production and N_2 production. It can be clearly observed that the LNT+SCR significantly improves the NOx conversion, particularly at the temperature window between 200 and 250℃. Moreover, this LNT+SCR configuration decreases the NH_3 slip at the reactor outlet as well as this configuration is favor of higher N_2 yields in the whole temperature range in comparison with a stand-alone LNT catalyst.

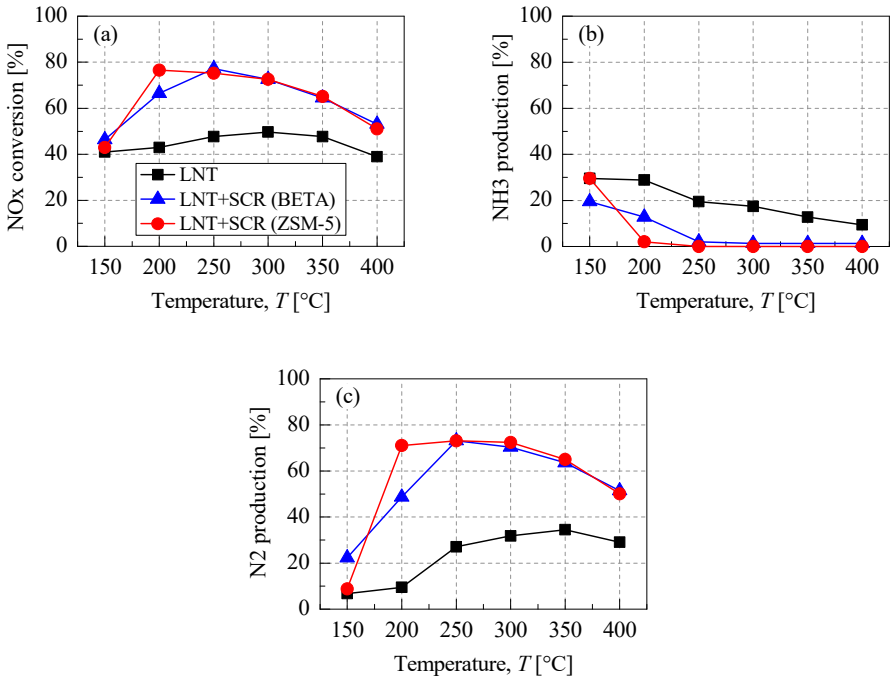

Figure 1.16 The catalytic performance of NOx conversion (a), NH_3 production (b), and N_2 production (c) for stand-alone LNT and LNT+SCR as a function of temperatures. (Reprinted by permission from Elsevier of ref. [90]).

1.4 Literature investigation on hydrocarbon–SCR

The direct decomposition of NO into N_2 and O_2 is one of the most exemplary methods because the direct decomposition of NO molecule is thermodynamically favorable at temperatures below 900°C, and it does not need any reductants [13]. However, the activation energy required for the direct NO decomposition is too high without the use of a catalyst as illustrated in the following reaction [91]:

$$\mathrm{NO} \rightarrow \frac{1}{2}\mathrm{N_2} + \frac{1}{2}\mathrm{O_2}, \quad \Delta H_{298}^{0} = -86.6 \text{ kJ/mol} \tag{1.31}$$

Although NO molecules are thermodynamically unstable and can be decomposed into N_2 and O_2, the direct NO decomposition is very slow reaction due to its high energy barrier [92, 93]. Therefore, the use of catalyst is required to help lower the activation energy, thereby promoting the NO decomposition.

Various catalysts have been reviewed to promote the direct NO decomposition, and the related catalysts can be divided into three categories, i.e., precious metals, metal oxides and zeolites. Among these catalysts, copper ion-exchanged zeolites have been considered as the most suitable catalyst for the direct decomposition of NO. Iwamoto and co-workers [94] demonstrated that "repeated ion-exchanged of Cu^{2+} species on the ZSM-5 zeolite resulted in excess exchange of these cations of more than 100%, and the catalytic performance of Cu/ZSM-5 showed high activity of NO decomposition", as illustrated in Figure 1.17. In the temperature dependence of NO decomposition experiment (Figure 1.17(a)), the decrease in the amount of NO is greater than those of N_2 and O_2 produced because of the formation of N_2O. The relation between NO decomposition and Cu cation-exchange level shows that the reaction rate of NO decomposition gradually improves at the lower exchange level and increases greatly from the Cu ion-exchange level of 40% (Figure 1.17(b)). The over-

exchanged Cu ions over the ZSM-5 are also effective way for the direct decomposition of NO molecules [94].

The major drawback of urea-SCR technique is that this system requires additional space for storage, deposition of urea aqueous solutions and complicated injection system of the reductant. Therefore, hydrocarbons instead of urea or NH_3 have been considered as an alternative reductant for the process of selective catalytic reduction. Since the discovery of hydrocarbon-SCR reaction by Iwamoto [95, 96] and Held [97] that Cu/ZSM-5 demonstrated the high catalytic activity for the reduction of NOx even in the presence of excess oxygen. From the above findings, the selective catalytic reduction using hydrocarbons as reducing agents (HC-SCR) has been considered as another candidate for NOx reduction.

Since the HC-SCR technique was proposed for abatement of NOx emissions from an automotive engine, various catalysts have been studied for effective HC-SCR, as summarized in Table 1.1. Three groups of catalysts can be classified in the following categories for the

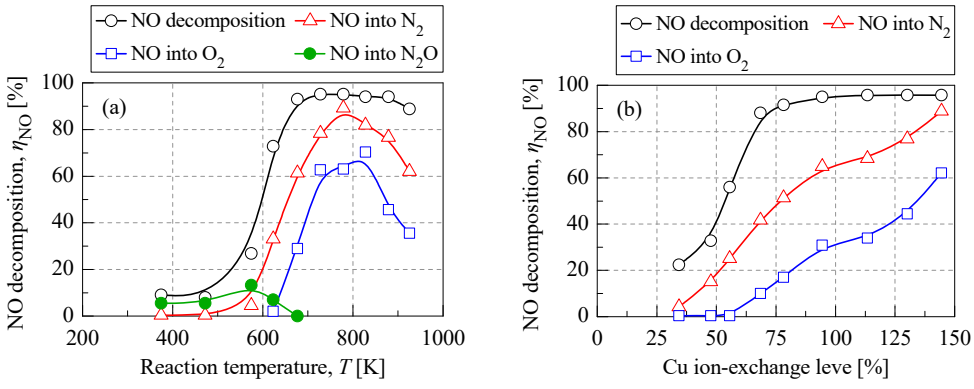

Figure 1.17 Direct NO decomposition of Cu/ZSM-5 catalyst as a function of temperature (a) and copper ion-exchange level (b).
Feed gas: 1.0% NO with balance He, 1.0 g of catalyst weight, W/F = 2.0 g s/cm^3 (Reprinted by permission from American Chemical Society of ref. [94]).

Table 1.1 HC-SCR catalysts with various active metals and supports.

Support	Active phase (metal)
Metal ion-exchanged zeolites	
BEA (Beta)	Co [98], Cu [99], and Pt [100]
MFI (ZSM-5)	Mn [101], Co [102], Fe [103], Cu [104], and Pt [105]
MOR (Mordenite)	Ag [106] and In [107]
FER (Ferrierite)	Co [108] and Fe [109]
Precious group metals supported on metal oxides	
γ-Al_2O_3	Ru [110], Rh [110], Pd [110], Pt [110, 111], and Ir [110]
TiO_2	Au [112]
$CeZrO_2$	Pd [113]

HC-SCR reaction: metal ion-exchanged zeolites, precious group metals supported on metal oxides, and transition metals supported on metal oxides. In recent studies, a metal oxide catalyst that is silver impregnated on γ-Al_2O_3 support (Ag/Al_2O_3) has attracted attention due to its high catalytic activities and hydrothermal tolerance for NOx reduction by hydrocarbons [114], considering this catalyst to be a feasible option for the practical application in the HC-SCR of NOx.

Many researchers have attempted to improve catalytic activities of Ag/Al_2O_3 catalyst by modifying preparation methods and adding some promoters [115]. However, the narrow operating window and the low-temperature activity should be addressed to achieve practical applications. The Ag/Al_2O_3 catalyst was first reported by Satokawa *et al*. [116] that "the catalytic activity of Ag/Al_2O_3 was greatly increased with addition of H_2 gas in the presence of excess oxygen and water". Figure 1.18 shows the NOx conversion over Ag/Al_2O_3 with various H_2 concentrations. Based on the Satokawa and coworker's experimental results, the NOx conversion of over 30% was attained in the specific operating window of 760 to 850 K.

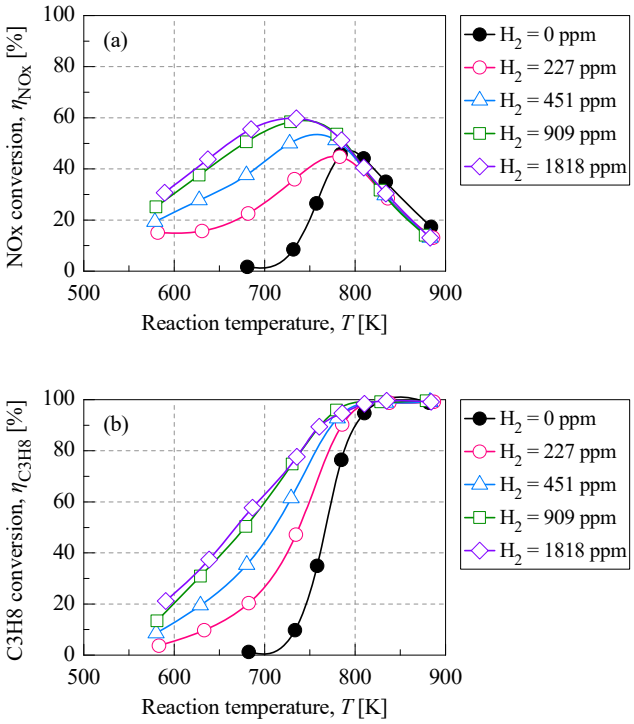

Figure 1.18 NOx and C_3H_8 conversion over Ag/Al_2O_3 catalyst according to H_2 concentrations. Feed gas: 91 ppm NO, 91 ppm C_3H_8, 9.1% O_2, 9.1% H_2O and 0–1818 ppm H_2, GHSV = 44,000 h^{-1} (Reprinted from ref. [116]).

A maximum de-NOx performance of 45.6% was observed at 780 K. However, the NOx conversion at relatively low temperatures was significantly improved in the presence of H_2. The reductant, C_3H_8, light-off temperature was also lowered in the presence of H_2, whereas the temperature of the complete C_3H_8 conversion was not changed [116].

Besides the metal oxide catalysts, metal ion-exchanged zeolites also have high activities of NOx abatement and a wide temperature window. Among the numerous zeolite-based catalysts, Cu or Fe ion-exchanged zeolite catalyst has been mainly studied, especially Cu/ZSM-5 or Fe/ZSM-5 [117, 118]. The Cu/ZSM-5 is the most investigated catalyst because this catalyst shows high NOx conversion with various HC reductants. Erkfeldt *et al.* [119] demonstrated the NOx conversion of Cu/ZSM-5 catalyst with various hydrocarbons,

including *n*-octane (*n*-C_8H_{18}), 1-heptanol ($C_7H_{15}(OH)$), *n*-pentane (*n*-C_5H_{12}), 1-butanol ($C_4H_9(OH)$), dibutyl ether ($C_8H_{18}O$), butyl methyl ether ($C_5H_{12}O$), ethanol ($C_2H_5(OH)$), and methanol ($CH_3(OH)$), and the results are summarized in Figure 1.19. Notably, the chemical nature of the hydrocarbon is very important aspect over the Cu/ZSM-5 catalyst. When comparing different hydrocarbons (alkane species, oxygenated hydrocarbon species and ether species), methanol could not reduce the NOx, whereas pentane showed the highest NOx conversion among the tested hydrocarbons. Erkfeldt and co-workers [119] have concluded that "a length of carbon chain had a significant effect on the NOx conversion in the HC-SCR process". Considering differences in chemical structure of the hydrocarbon reductants, they also suggested that a carbon–carbon bond played an important role in the reaction mechanism of NOx abatement over the Cu/ZSM-5 catalyst [119]. Therefore, the absence of carbon–carbon bond in methanol and methane would explain the low de-NOx performance over the Cu/ZSM-5 catalyst.

The typical HC-SCR system using hydrocarbons as a reducing agent can utilize many hydrocarbon species, and various kinds of hydrocarbons species are included in the diesel exhaust gas. Hydrocarbons can be provided upstream the HC-SCR catalyst by two different methods: they can be provided from the exhaust gas or fuel [120, 121]. The former is passive system in which the distribution of carbon-number peaks at the lower carbon-number, whereas the latter is active system by the post-injection of diesel fuel that contains higher carbon-number of hydrocarbons, as illustrated in Figure 1.20.

One of the important parameters is the amounts of hydrocarbons to achieve high NOx abatement. Although optimal HC/NOx ratios are dependent on the chemical propertis of hydrocarbons and the active phases of the catalyst, a two to fourfold surplus of hydrocarbons relative to the NOx concentration are preferred to obtain the NOx conversion of more than

80% [122–125].

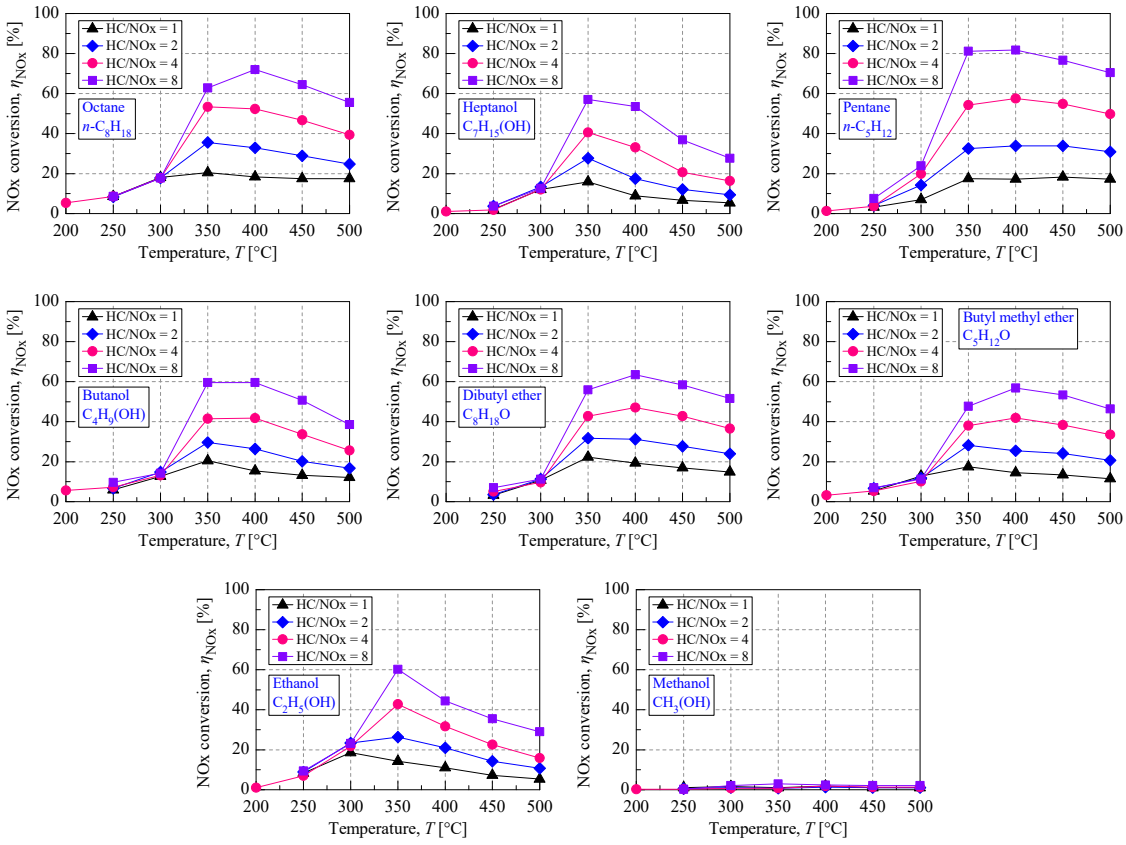

Figure 1.19 NOx conversion with various hydrocarbons over Cu/ZSM-5 at temperatures between 200–500°C.

Feed gas: 800 ppm NO, 10% O_2, 5% H_2O and HC reductant (800, 1600, 3,200, and 6,400 ppm C_1) at GHSV = 33,300 h^{-1} (Reprinted by permission from Elsevier of ref. [119]).

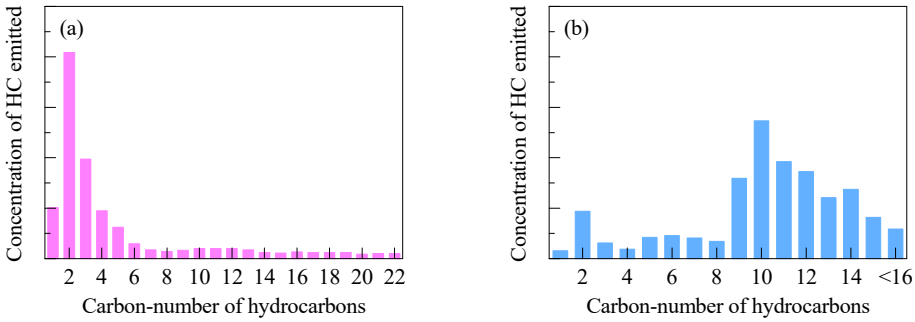

Figure 1.20 Distribution of carbon-number of hydrocarbons included in the diesel exhaust gas: (a) passive condition (exhaust gas) and (b) active condition (post-injection of fuel by common-rail system) (Reprinted by permission from Spinger Nature of ref. [120]).

The catalytic performance of HC-SCR highly affected by the chemical properties of the hydrocarbon species such as carbon-number, chain-length, chemical properties, and so on. A considerable number of reductants have been attempted to investigate the related reaction mechanisms and to further increase the catalytic activity of the HC-SCR catalysts, particularly over the Cu/ZSM-5 and Fe/ZSM-5 catalysts, as summarized in Table 1.2.

The preparation procedure of the catalyst also affects the catalytic performance of NOx abatement. Furthermore, the preparation method closely relates to the physical and chemical properties of the catalysts, including the mechanical strength, attrition resistance, pore volume, thermal stability, surface-activating sites of active phases, and accessibility of the active sites for reactants [137]. For example, Chajar *et al*. [138] have investigated the catalytic

Table 1.2 Various reducing agents of hydrocarbon over Cu or Fe/ZSM-5 catalysts for HC-SCR process.

Catalysts		Reducing agents	References
Catalyst type	SiO_2/Al_2O_3		
Cu/ZSM-5 (Cu 2.5 wt%)	73	Methane (CH_4)	[119]
Cu/ZSM-5 (Cu 2.4 wt%)	52	Ethylene (C_2H_4)	[126]
Cu/ZSM-5 (Cu 1.0 wt%)	56	Propylene (C_3H_6)	[127]
Cu/ZSM-5 (Cu 1.1 wt%)	78	Propane (C_3H_8)	[128]
Cu/ZSM-5 (Cu 3.8 wt%)	45	iso-butane (i-C_4H_{10})	[129]
Cu/ZSM-5 (Cu 2.5 wt%)	73	Pentane (C_5H_{12})	[119]
Cu/ZSM-5 (Cu 2.3 wt%)	45.2	n-octane (n-C_8H_{18})	[130]
Cu/ZSM-5 (Cu 4.6 wt%)	26.4	Decane ($C_{10}H_{22}$)	[131]
Fe/ZSM-5 (Fe 1.7 wt%)	14.2	Methane (CH_4)	[132]
Fe/ZSM-5 (Fe 4.0 wt%)	30	Propylene (C_3H_6)	[133]
Fe/ZSM-5 (Fe 5.4 wt%)	22.8	Propane (C_3H_8)	[134]
Fe/ZSM-5 (Fe 2.4 wt%)	90	iso-butane (i-C_4H_{10})	[135]
Fe/ZSM-5 (Fe 0.5 wt%)	30	Decane ($C_{10}H_{22}$)	[136]

activity of three different prepared catalysts for the purification of NOx by C_3H_8 under varying O_2 conditions, as illustrated in Figure 1.21. They prepared the three Cu/ZSM-5 catalysts by using the precipitation, impregnation, and ion-exchange procedures. The prepared catalysts showed the catalytic activity in the following order: Cu/ZSM-5 (ion-exchange) > Cu/ZSM-5 (impregnation) > Cu/ZSM-5 (precipitation). The reason can be described that the active phase of Cu was present as the isolated Cu^+ ions over the three Cu/ZSM-5 catalysts, and the Cu^+ species exhibited the highest dispersion over the catalyst prepared by ion-exchange procedure. They concluded that "the catalytic activity was closely related to a high dispersion of isolated Cu^+ ions on the ZSM-5 zeolite"; thus, the ion-exchange was the best procedure to prepare the metal-based zeolites for the HC-SCR process.

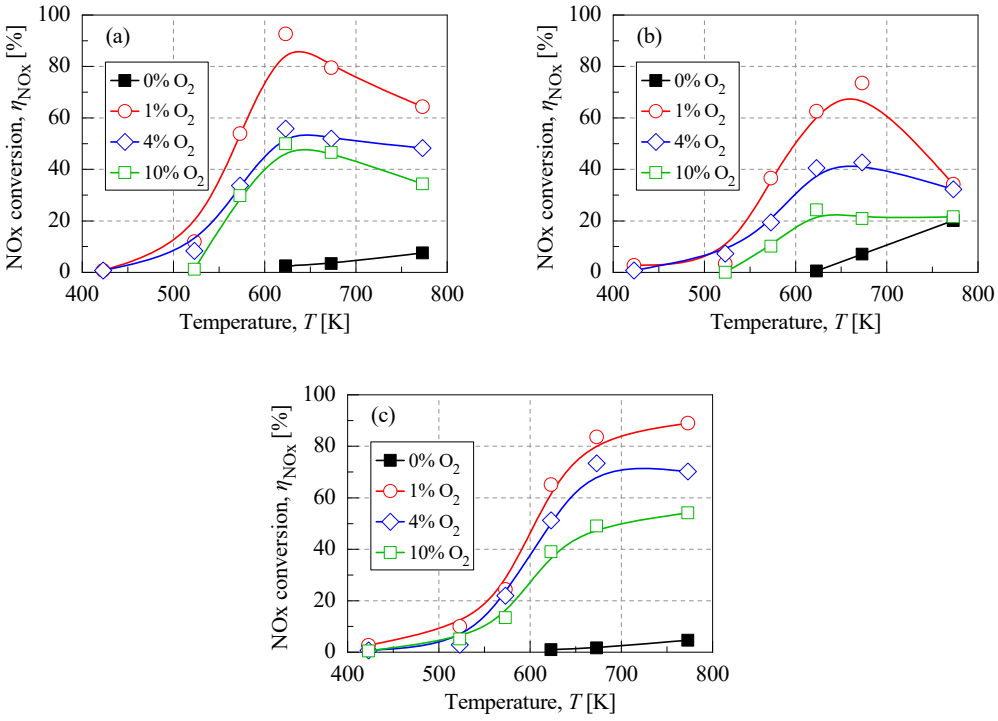

Figure 1.21 Effects of preparation procedures on NOx conversion over Cu/ZSM-5 catalyst: (a) precipitation, (b) impregnation, and (c) ion-exchange.
Feed gas: 2000 ppm C_3H_8, 2000 ppm NO, and 0–10 vol.% O_2 concentrations (Reprinted by permission from Elsevier of ref. [138]).

The reaction mechanism on the selective catalytic reduction of NOx by hydrocarbons has been debatable despite the various reviews for the past decades. Although some possible reaction mechanisms or reaction routes have been elucidated for the HC-SCR process, general reaction mechanisms are not available due to the different types of catalysts, reaction conditions, and numerous hydrocarbon species. The primary features of reaction mechanism for the HC-SCR process can be divided into the following three categories:

i) Oxidation of NO into NO_2 and selective reaction with hydrocarbons [139–143]

$$NO + \frac{1}{2}O_2 \rightarrow NO_2 \quad (1.32)$$

$$NO_2 + HC \rightarrow N_2 + CO_2 + H_2O \quad (1.33)$$

ii) Activated hydrocarbons react with NOx [144–148]

$$HC + O_2 \rightarrow HC^* + CO_2 + H_2O \quad (1.34)$$

$$HC^* + NOx \rightarrow N_2 + CO_2 + H_2O \quad (1.35)$$

iii) NO decomposition and regeneration by hydrocarbons [149–152]

$$2NO \rightarrow N_2 + 2O\,(\text{adsorption}) \quad (1.36)$$

$$2O\,(\text{adsorption}) + HC \rightarrow CO_2 + H_2O \quad (1.37)$$

The initial reaction is the oxidation of NO to NO_2 as an indispensable reaction, followed by the reduction of NO_2 with HC into N_2. The NO can be oxidized by oxygen in the presence of reaction gas or by the metal supported catalyst. The second mechanism is related to intermediates of the partially oxidized HCs (HC*) with O_2, followed by reduction of with NOx. The third mechanism is the catalytic decomposition of NO to N_2, and the adsorbed O_2 on the catalyst reacts with hydrocarbon to CO_2 and H_2O.

The reaction mechanism on the effect of hydrocarbon and carbon monoxide in the feed stream has been also investigated. Li *et al*. [153] demonstrated the de-NOx activity and de-NOx process over the copper ion-exchanged ZSM-5 catalyst coated on the honeycomb monolith, as illustrated in Figure 1.22. The relevant reaction mechanism of HC-SCR process is described in the following reactions [153]:

$$NO + CO + O_2 \rightarrow N_2 + CO_2 \quad (1.38)$$

$$NO + HC + O_2 \rightarrow N_2 + CO + H_2O \quad (1.39)$$

$$HC + NOx \rightarrow N_2 + CO_2 + H_2O \quad (1.40)$$

As illustrated in Figure 1.22(a), the reactions (1.38) and (1.39) are the primary reactions at temperatures between 400 and 500 K. However, reaction (1.38) becomes slow, and the rate of the reaction (1.39) increases at above 500 K, because the CO conversion sharply decreases from 500 K. This result indicates that the reaction mechanism of HC-SCR is dependent upon the reaction temperatures. When the reaction temperature increases above 650 K, the catalytic reaction of NOx abatement shifts from the reaction (1.39) to reaction (1.40), since CO conversion starts to increase that is related to the consumption of CO as a reductant. From the experimental results, Li *et al*. [153] proposed the de-NOx process in the following manner. "The NOx species and hydrocarbon species (CxHyOz) are simultaneously formed on the surface-activating sites; these species are the two significant reaction intermediates". The NOx and CxHyOz react with each other on the catalyst surface, giving out N_2, H_2O, and COx (CO at lower temperature and CO_2 at higher temperature, as illustrated in Figure 1.22(b)).

In the case of the transition metal oxides over the alumina support, some nitrogen-containing species such as –NCO, R–NH_2, and NH_3 are formed via the organo-nitrogen species [154]. The reaction of O_2 with NO or hydrocarbons to form the ad-NOx species and

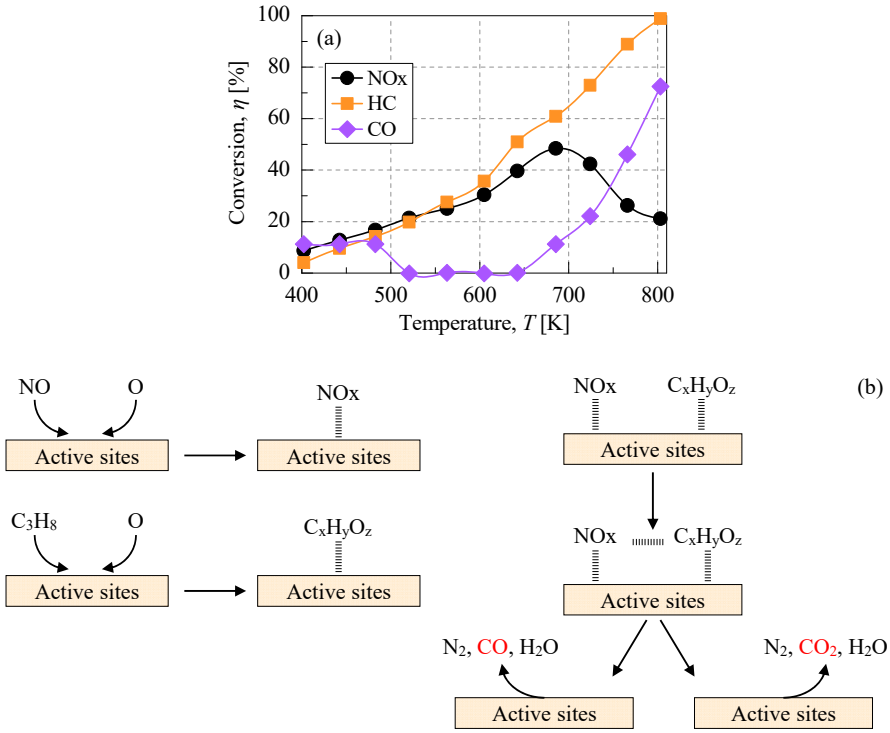

Figure 1.22 Catalytic reduction of NOx and proposed reaction mechanism regarding the effects of hydrocarbon and carbon monoxide over Cu/ZSM-5 cordierite catalyst: (a) catalytic performance of three components in exhaust gas (550 ppm NOx, 134 ppm HC, 0.11% CO, A/F = 21 at GHSV = 25,000 h^{-1}) and (b) proposed mechanisms over Cu/ZSM-5 cordierite catalyst on real lean burn (Reprinted by permission from American Chemical Society of ref. [153]).

partially oxidized hydrocarbons (CxHyOz) are considered as the crucial reactions [155]. Several researchers have therefore proposed that the reduced species of nitrogen (e.g., –NCO, R–NH_2 and NH_3) would react with the oxidized species of nitrogen (e.g., organo-nitrito or NO_2) to form N_2 [156, 157]. Figure 1.23 shows the schematic routes of global scheme for the C_3H_6-SCR over the transition metal promoted alumina catalysts. This reaction scheme emphasizes that the overall reaction route is very complicated because NO reacts via a series of consecutive routes forming the numerous reaction intermediates.

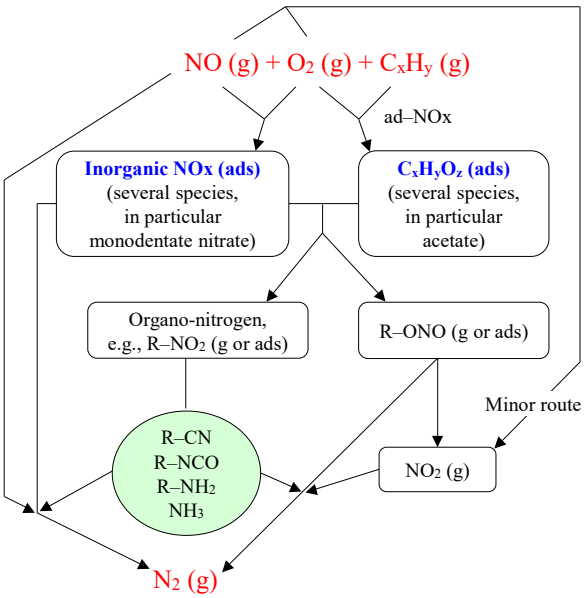

Figure 1.23 Reaction scheme of the C_3H_6-SCR of NO over transition metal oxide catalysts giving the nature of the different species likely to be involved. It is proposed that the reduction to N_2 occurs through the reaction of oxidized and reduced nitrogen compounds (Reprinted by permission from Elsevier of ref. [155]).

Although some researches have been carried out through the kinetic and spectroscopic studies to understand the HC-SCR over the Cu/ZSM-5 catalysts, many questions are still unclear. Park *et. al* [104] proposed the possible reaction mechanism of HC-SCR process over the ion-exchanged Cu/ZSM-5 catalyst; allyl (CH_2=CH–CH_2–), allyl oxime (R_2–C=N–OH), ethenyl isocyanate (CH_2=CH–NCO), and ethenyl amine (CH_2=CH–NH_2) reaction intermediates were observed by IR, as illustrated in Figure 1.24. They suggested "the formation of Cu(I)-allyl as the initial step by chemisorption of hydrocarbons over Cu(I) in ZSM-5, and then, Cu(I)-ethenyl amine reacts with NO_2 to form N_2 and Cu(I)-ethenyl in the final reaction step".

Numerous fundamental issues regarding the behavior of Cu/ZSM-5 in the absence or presence of NOx need to be solved. Especially, the partitioning of copper into Cu(I)

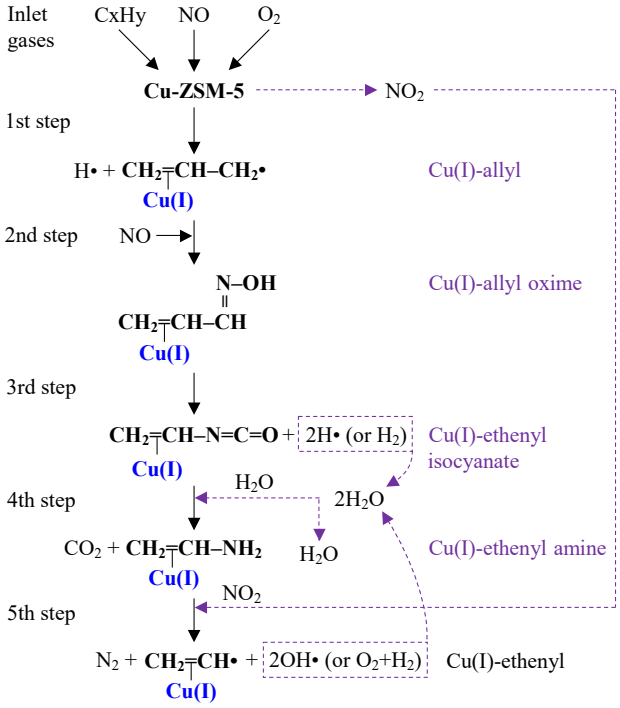

Figure 1.24 Reaction scheme of CxHy-SCR over Cu/ZSM-5 catalysts at 450℃ (Reprinted by permission from Royal Society of Chemistry of ref. [104]).

and Cu(II) or other possible copper species is still not yet clear. Both the Cu(I) and Cu(II) take part in the catalytic reaction as the active sites, and it has not been rationally determined whether active sites are essential in the HC-SCR process for NOx abatement [158].

Park *et. al* [158] have proposed the possible active sites of Cu(I) and Cu(II) on the redox cycles for NO decomposition over the dehydrated Cu(II)-exchanged ZSM-5, as illustrated in Figure 1.25. After NO adsorption on the Cu/ZSM-5, NO interactions with Cu(I), Cu(II)–O^-, and Cu(II) were investigated by electron spin resonance (ESR) and IR spectroscopy. They proposed that "Cu(II)–O^- reacts with NO to form Cu(I)–NO_2 and consequent interaction of NO involves the formation of Cu(II)–$(NO_2)(NO)$, and then Cu(I) reacts with NO to form Cu(I)–NO and Cu(I)–(NO_2) of which the latter further transforms to Cu(II)–$(N_2O)O^-$". Therefore, Cu(I), Cu(II)–O^-, and paramagnetic Cu(II) are highly active for NO adsorption,

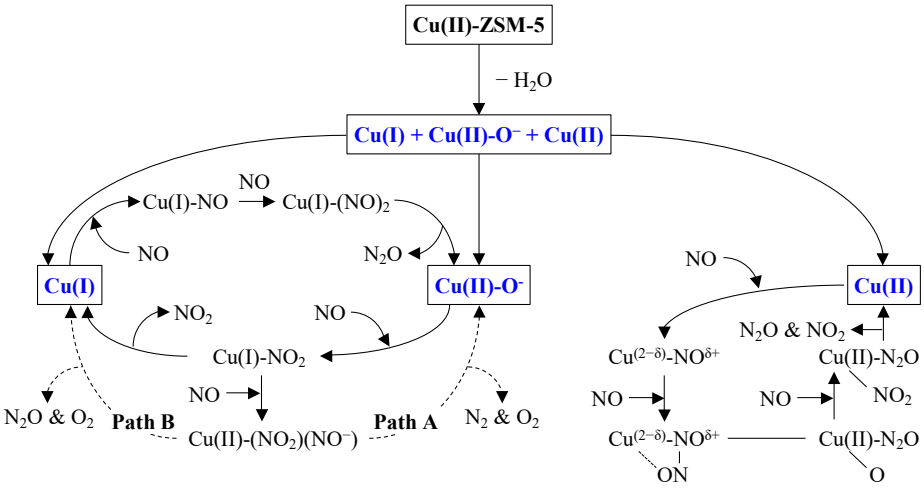

Figure 1.25 Possible reaction scheme of redox cycles for NO decomposition over Cu/ZSM-5 catalyst (Reprinted by permission from Elsevier of ref. [158]).

and they produce many Cu–NO complexes, which is related to the redox reactions [158].

To understand the complex reaction intermediates of HC-SCR, a recent study has reviewed the state of art of HC-SCR for NOx abatement under lean-burn operations of non-zeolite and precious group metal catalysts [159]. The hydrocarbon species are crucial for removing the adsorbed oxygen species, left from nitrogen oxide dissociation, and restoring the initial catalytic surface [149]. However, the HC-SCR mechanisms are largely relying on the catalytic materials and the characteristic of catalysts. Figure 1.26 represents the reaction mechanisms regarding interaction of NOx and HC, which is classified into two primary pathways. The first pathway (R–NOx route) is associated with the involvement of R–NOx species (CxHyNtOz) as the reaction intermediates, resulting from the interaction between NOx and hydrocarbon [161–164]. These reaction intermediates would directly involve the molecular N_2 or decompose into other intermediate species such as isocyanates (–NCO), ammonia (NH_3), oxime (RC=NOH), nitrile (–C≡N), azoxy compound ($RN{=}N^+(O^-)R$), and amino groups such as amide ($R–CONH_2$) and amine ($R–NH_2$). The second reaction pathway

is related to the formation of the oxygenated hydrocarbons (CxHyOz) as the reaction intermediates [165–171]. In this reaction scheme, the oxygenated hydrocarbons could be formed either by O_2 or NOx, which is considered as the potential oxidant in the reaction gas mixtures. The nitrogen-containing species such as nitrosonium ($[N{\equiv}O]^+$) and isocyanate (–NCO) may be possible candidates for reaction intermediates in the NO reduction scheme [172]. Other subsequent intermediates, comparable to those proposed R-NOx scheme as the initial intermediate, have been also suggested before the final formation of N_2. The proposed mechanism of HC-SCR is that the nitrates formed by the oxidation of NO could be reduced to N_2 by the partially oxidized hydrocarbons (CxHyOz), such as acetate species (CH_3COO^-) through the metal–NCO and –CN species.

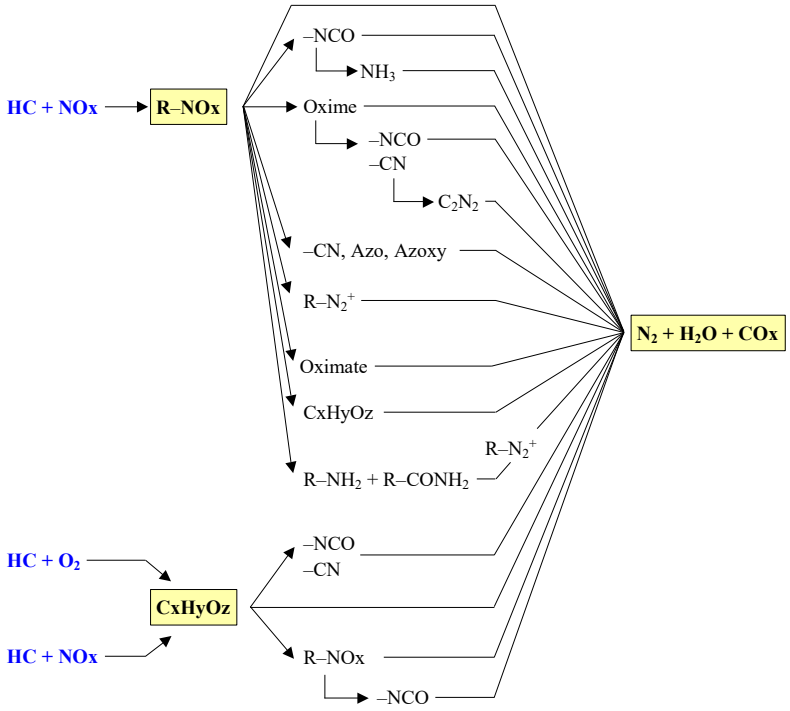

Figure 1.26 Reaction pathways involving organic species proposed in lean de-NOx catalysis reported in the previous literature over various type of catalysts (zeolite, metal oxide or platinum group metal) and HC: hydrocarbons, R–NOx: R–NO, R–ONO, R–NO_2, or R–ONO_2, and CxHyOz being an oxygenate compound of undefined composition (Reprinted by permission from Elsevier of ref. [160]).

On a basis of the reaction mechanisms, a comprehensive review of the chemistry for NOx abatement by HC-SCR process have been attempted to improve the de-NOx performance and to fulfill future requirements in terms of emissions regulations. There is an insufficient-general consensus to explain the reaction mechanisms because of various catalysts with different types of active materials, supports, and catalytic reaction conditions. Nevertheless, the development of more active and durable materials will exemplify a main issue in the future technique for the HC-SCR of NOx reduction.

1.5 Research objectives and scopes

The objective of the present research work is to investigate the effectiveness of hydrocarbon-selective catalytic reduction (HC-SCR) catalysts for the purpose of application possibility of passive type HC-SCR system. Cu-containing zeolite catalysts with different Cu loadings and zeolite frameworks (SSZ-13, ZSM-5, and BETA) were evaluated using laboratory-scale normal-pressure fixed-bed synthetic gas reactor system to identify optimal Cu/zeolite catalysts for the passive type HC-SCR. The reducing agents are propene (C_3H_6) and *n*-butane (*n*-C_4H_{10}); particularly, *n*-C_4H_{10} has rarely been studied in the field of HC-SCR. Therefore, the evaluation of catalytic performance of HC-SCR is of great importance for furthering the commercial de-NOx application. The research objectives and scopes of respective chapters are summarized below.

Chapter 1: Introduction

Relevant catalytic applications for the reduction of diesel exhaust emissions, including nitrogen oxides (NOx) by the three–way catalyst, NOx storage–reduction catalyst, selective catalytic reduction using urea and hydrocarbons, are presented and discussed. Recent literature on hydrocarbon-SCR system is also reviewed.

Chapter 2: Textual Characterization of Prepared Catalysts

The copper-loaded catalysts supported on SSZ-13 (CHA framework), ZSM-5 (MFI framework), and BETA (BEA framework) zeolites, having different zeolite frameworks, are prepared with varying copper-loadings from 1 to 10 wt% using an incipient wetness impregnation method. The physical and chemical properties of the prepared catalysts are analyzed using various analytical techniques. The detailed textual characterization of

respective Cu/zeolite catalysts is investigated and discussed.

Chapter 3: Catalytic Performance of C_3H_6-SCR

A series of Cu/zeolite catalysts are evaluated for the main purpose of reducing NOx emissions by the C_3H_6-SCR process in the presence of O_2, CO, CO_2, and H_2O. The effects of the C_3H_6/NOx ratios on the de-NOx performance, CO oxidation, partial oxidation of C_3H_6, and N_2 yield are investigated over the Cu/zeolite catalysts. The zeolite frameworks are also discussed to identify the optimal Cu/zeolite catalysts in the C_3H_6-SCR process.

Chapter 4: Catalytic Performance of C_4H_{10}-SCR

To compare the effect of hydrocarbon on HC-SCR performance, Cu/zeolite catalysts are evaluated in the C_4H_{10}-SCR process. The effects of zeolite framework, Cu loading, and C_4H_{10}/NOx ratio on the catalytic activity for C_4H_{10}-SCR are also investigated in the presence of O_2, CO, CO_2, and H_2O. The de-NOx performance, CO oxidation, partial oxidation of C_4H_{10}, temperature programmed oxidation of C_4H_{10}, temperature programmed oxidation of NOx, and N_2 selectivity are discussed in this chapter.

Chapter 5: Effects of Coexistent Gases and Hydrothermal Aging

Oxygen (O_2) and carbon dioxide (CO_2) are unavoidable in diesel exhaust emissions, and they are main products in the ideal reaction of NOx by hydrocarbons. The influence of O_2 and CO_2 concentrations in the feed gas on the catalytic activity over the 2Cu/ZSM-5 is evaluated in both the C_3H_6- and C_4H_{10}-SCR process for the purpose of trying to enhance the de-NOx performance. Moreover, the effect of hydrothermal aging on the catalytic performance over the Cu/zeolite catalysts is also investigated and the textual characterization

of aged catalysts is discussed for describing the effect of hydrothermal aging on the physical and chemical properties of catalyst.

Chapter 6: Conclusions

From the experimental results of all the present research, key findings of respective chapter are summarized. And, research recommendations and relevant developments of HC-SCR system are also suggested.

Chapter 2. Textual Characterization of Prepared Catalysts

2.1 HC–SCR catalyst preparation

2.1.1 Catalyst preparation

The parent zeolites used in the present study corresponds to H-ZSM-5 (JRC-Z5-90H, SiO_2/Al_2O_3 = 90) and H-BEA (JRC-Z-HB25, SiO_2/Al_2O_3 = 25) procured from the Catalysis society of Japan; these two zeolite samples are specified as Japan reference catalyst. SSZ-13 zeolite with the CHA topology was synthesized using a method similar to that reported by Zones and Imai [173, 174]. Figure 2.1 shows the preparation procedure of SSZ-13 zeolite. The SSZ-13 seed was prepared from synthetic gel with a following composition of 1 SiO_2: 0.05 $Al(OH)_3$: 0.2 TMAdaOH (SDA): 0.2 NaOH: 44 H_2O. The Na-type Al-containing SSZ-13 gel was transferred into an autoclave through a Teflon-lined inner tube, and then kept statically heated at 150℃ in an oven under stirring at 40 rpm for 5 days. The obtained product was recovered by filtration, followed by washing with deionized water and drying at 100℃. Thereafter, the as-made SSZ-13 was calcined at 600℃ for 6 h in air to remove the SDA. For preparing the CHA-type zeolite, the synthesized *N*,*N*,*N*-trimethyl-1-adamantammonium hydroxide (TMAdaOH) was used as a structure directing agent (SDA). Figure 2.2 shows the synthesis procedures of TMAdaOH.

A wide range of copper-containing zeolite catalysts was prepared by an incipient wetness impregnation method. After adding a predetermined amount of copper(II) nitrate trihydrate ($Cu(NO_3)_2 \cdot 3H_2O$, purity 99.9%, Kojundo Chemical Laboratory) to the mixtures of zeolite powder and deionized water at room temperature, the mixtures were dried at 100℃ in air overnight. The dried solid powders were then calcined at 500℃ in air for 5 h to eliminate the nitrate species and any impurities. The as-made catalysts powders are listed in Table 2.1. The respective samples with Cu loading of x wt% in the zeolites are hereafter referred to as

xCu/zeolite. When preparing 10 g of the 5Cu/ZSM-5 powder, mass of the calculated precursors and procedure of the incipient wetness impregnation are summarized in Figure 2.3.

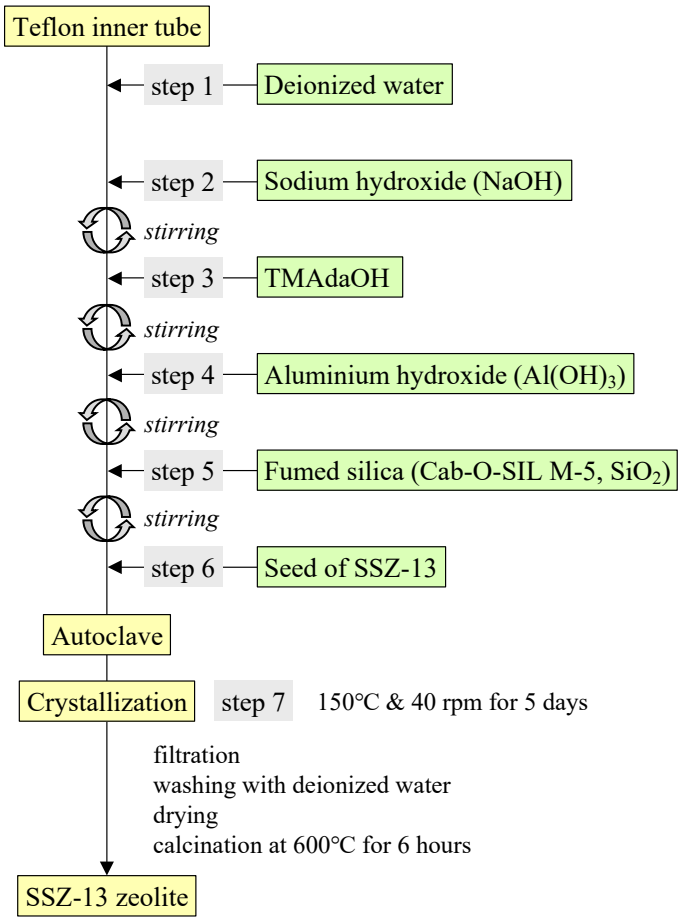

Figure 2.1 Synthetic procedures of SSZ-13 zeolite by using TMAdaOH as organic structure directing agent (OSDA).

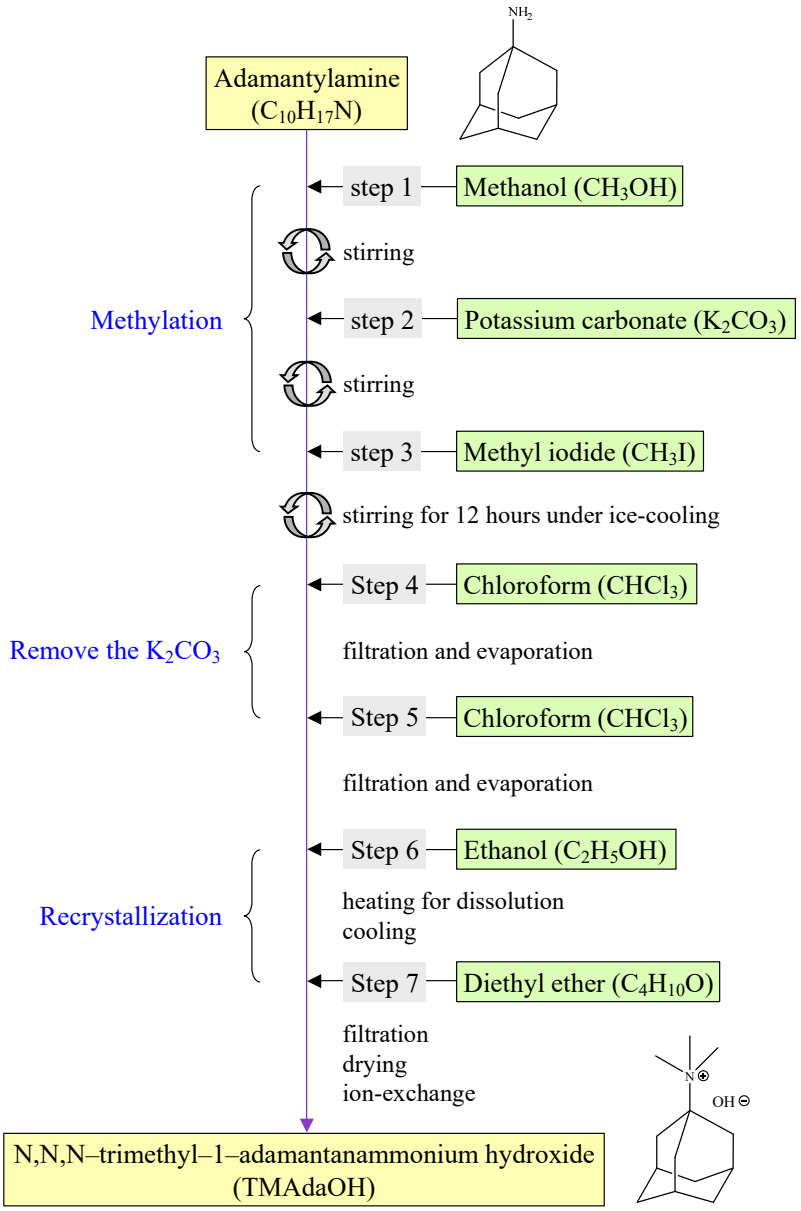

Figure 2.2 Synthetic procedures of *N*,*N*,*N*-trimethyl-1-adamantammonium hydroxide (TMAdaOH).

Table 2.1 Theoretical composition of Cu/zeolite catalysts prepared by incipient wetness impregnation procedure.

Catalysts	Zeolite topology (SiO_2/Al_2O_3)	Component proportion (wt%)	
		Copper	Zeolite
SSZ-13 zeolite	SSZ-13 (30)	0	100
1Cu/SSZ-13	SSZ-13 (30)	1	99
5Cu/SSZ-13	SSZ-13 (30)	5	95
ZSM-5 zeolite	H-ZSM-5 (90)	0	100
1Cu/ZSM-5	H-ZSM-5 (90)	1	99
2Cu/ZSM-5	H-ZSM-5 (90)	2	98
5Cu/ZSM-5	H-ZSM-5 (90)	5	95
10Cu/ZSM-5	H-ZSM-5 (90)	10	90
BETA zeolite	H-Beta (25)	0	100
1Cu/BETA	H-Beta (25)	1	99
2Cu/BETA	H-Beta (25)	2	98
5Cu/BETA	H-Beta (25)	5	95
10Cu/BETA	H-Beta (25)	10	90

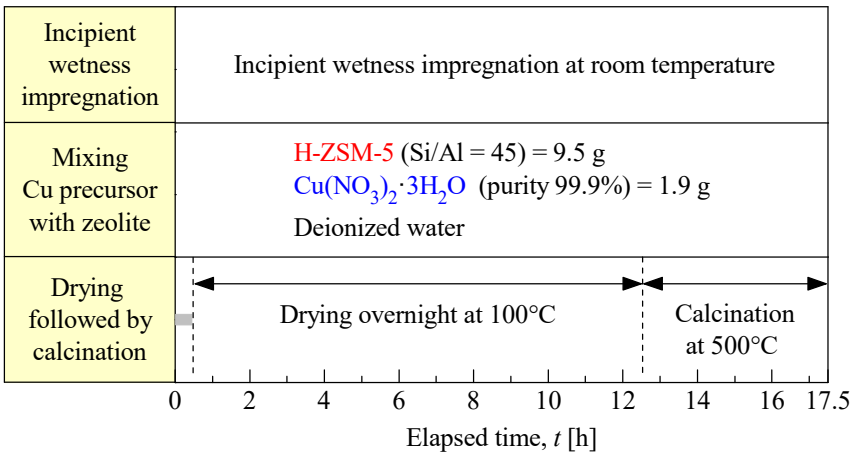

Figure 2.3 Preparation procedure of 5Cu/ZSM-5 zeolite by incipient wetness impregnation method (prepared weight of powder sample = 10 g).

2.1.2 Washcoating onto monolith substrate

The catalytic system widely used in the practical application is a monolithic convertor. The monolith substrate offers numerous advantages compared to the powder or pellet catalysts, the most important one being the low pressure drop through the catalytic convertor [27, 29]. The gaseous reactants enter the channels, reacting with the catalyst on the walls, and the products flow down to the outlet channels. The monolith is commonly manufactured as ceramic cordierite ($2MgO{\cdot}5SiO_2{\cdot}2Al_2O_3$) because this material can stand the thermal shocks with low thermal expansion, resulting in the high resistance to fracture [175, 176].

The as-made powder catalysts were coated on an open structured cordierite monolith (diameter 19.5 mm and length 26.8 mm) with a cell density of 300 cells/in^2 and wall thickness of 5 mil by using the dip-coating technique. Table 2.2 represents the physical properties of the monolithic cordierite adopted in the present study. The coating amount of powder catalyst was determined to be approximately 120 g per unit volume of substrate, as illustrated in Figure 2.4. The washcoated monolith was calcined at 400℃ in air for 3 h to decompose impurities and to insure good adherence of bonding between the catalyst and monolith wall.

2.2 Physical properties of monolithic cordierite substrate for 300 cpsi and 5 mil.

Cordierite monolith ($2MgO{\cdot}5SiO_2{\cdot}2Al_2O_3$)	
Wall thickness, t_w	5 mil
Cell density, N	300 cells/in^2 (cpsi)
Porosity, P_c	25%
Channel width, d_k	1.34 mm
Hydraulic diameter, d_h	1.34 mm
Cell spacing, L	1.47 mm
Open frontal area, OFA	83.4%
Geometry surface area, GSA	24.9 cm^2/cm^3

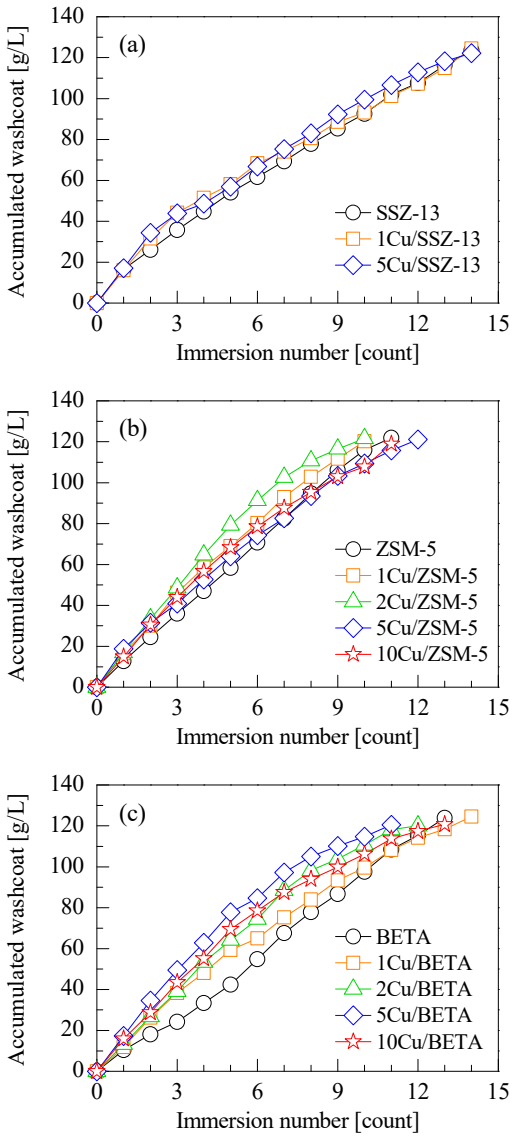

Figure 2.4 Washcoated catalyst onto the cordierite monolith as a function of immersion number of (a) Cu/SSZ-13, (b) Cu/ZSM-5, and (c) Cu/BETA: washcoat coating = 120 g/L.

2.2 Characterization of catalysts

2.2.1 Apparent copper loading

The Cu/zeolite catalysts were prepared by an incipient wetness impregnation method, in which the Cu precursor was impregnated into the parent zeolites. Because the impregnation procedure does not need any washing of the catalyst during the preparation, it is believed that the apparent content of metal loading over the as-made catalyst samples is in good accord with the pre-calculated amount of Cu loading.

Table 2.3 shows the results of apparent Cu loading amounts and Si/Al atomic ratios analyzed by the ICP–AES technique. The Si/Al ratios of all Cu impregnated catalysts over the Cu/zeolite were in good agreement with the parent zeolite's Si/Al ratios. As can be seen from the comparison of theoretical and ICP–AES results (Figure 2.5(a)), the loading levels of Cu metal for all powder catalysts prepared via impregnation procedure were close to the theoretical loading amount, suggesting that the Cu species has been successfully introduced into the zeolite. However, ICP induced some limitations of measurement for low concentrations below 1 ppm of Cu, which resulted in greater errors for 1Cu/zeolite catalysts, as shown in Figure 2.5(b).

2.2.2 N_2–isotherms

Figure 2.6 shows the nitrogen adsorption–desorption isotherms over the parent zeolite and Cu-impregnated zeolite catalysts. According to the IUPAC classification of physisorption isotherms [177, 178], the N_2 isotherm curves of the parent SSZ-13 and Cu-impregnated catalysts can be considered as the type I, and represent a minor hysteresis loop at a relativepressure (P/P_0) from 0.5 to 0.95, indicating the presence of pure micropores with

Table 2.3 Apparent Cu loading amounts of prepared Cu/zeolite powder catalysts.

Catalysts	Framework	Powder (mg)[a]	Si/Al ratio	Cu (ppm)	Cu (wt%)[b]
SSZ-13	CHA (Si/Al = 15)	2.5	16	N/A	N/A
1Cu/SSZ-13		2.4	16	0.69	1.44
5Cu/SSZ-13		5.4	17	4.60	4.26
ZSM-5	MFI (Si/Al = 45)	2.0	45	N/A	N/A
1Cu/ZSM-5		1.9	46	0.658	1.73
2Cu/ZSM-5		3.7	45	1.31	1.77
5Cu/ZSM-5		2.4	46	2.64	5.50
10Cu/ZSM-5		2.4	45	4.06	8.46
BETA	BEA (Si/Al = 12.5)	2.5	13	N/A	N/A
1Cu/BETA		3	15	0.726	1.21
2Cu/BETA		4.8	15	2.02	2.10
5Cu/BETA		2.7	14	2.81	5.20
10Cu/BETA		5.3	15	11.0	10.38

a. Powder is the powder weight of catalysts.

b. Cu (wt%) = [Cu (ppm) × (50/1000)/powder weight] × 100.

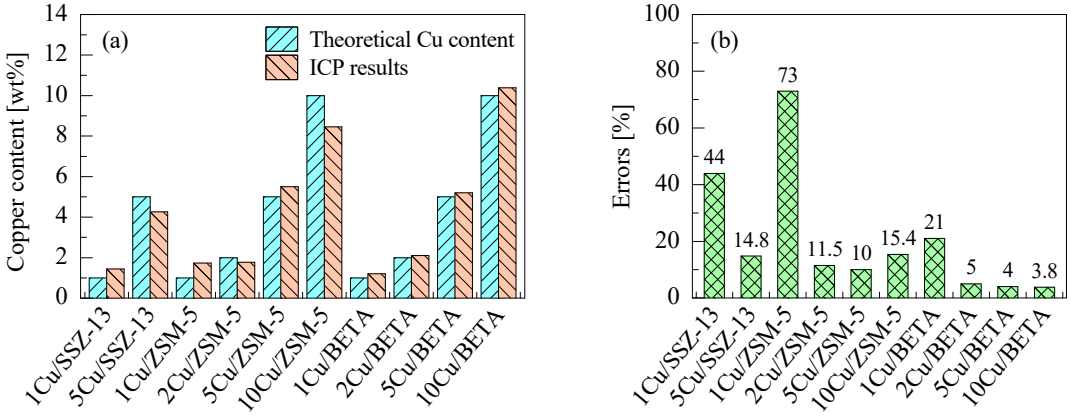

Figure 2.5 Comparison of (a) theoretical Cu content and ICP–AES results and (b) errors for Cu/zeolite powder.

uniformly cylindrical-shaped pores. The adsorption and desorption curves were similar to those before addition of Cu species to the SSZ-13, implying that the impregnation of Cu species does not modify the characteristics of zeolite pores.

The N_2–isotherm curves of the parent ZSM-5 and Cu-impregnated catalysts can be considered as a combination of type I and type IV isotherm. The adsorption hysteresis loop was in a range of relative pressure from 0.5 to 0.98, which is attributed to the presence of mesopores in the ZSM-5 zeolite. In contrast to SSZ-13, the adsorption curves of ZSM-5 were substantially increased above $P/P_0 = 0.8$, indicating the occurrence of capillary condensation in mesopores near the saturation pressure of the bulk N_2 liquid.

The profiles of isotherm curve for the parent BETA and Cu-impregnated catalysts were almost identical to the results of ZSM-5 zeolites, indicating a combination of type I and type IV isotherm. The adsorption hysteresis loop occurred in a range of relative pressure from 0.45 to 0.99, implying the presence of mesopores in the BETA zeolite. The adsorption isotherms of Cu-impregnated catalysts (Cu/ZSM and Cu/BETA) exhibited the same adsorption profiles before impregnation of Cu species into the respective zeolite, clearly implying that Cu species have a no effect on the pore shapes and characteristics of Cu/zeolites even higher Cu loading.

2.2.3 Specific surface area, pore size and pore volume

The BET specific surface area (A_{BET}) along with total pore volume (V_P) is summarized in Table 2.4. Among the parent zeolites, SSZ-13 zeolite with the chabazite topology had the largest BET specific surface area compared to that of the ZSM-5 (MFI) and BETA (BEA) zeolite. The order of BET specific surface area was SSZ-13 > BETA > ZSM-5, in which the BET specific surface area of SSZ-13 was 837.1 m^2/g and that of ZSM-5 was 434.3 m^2/g,

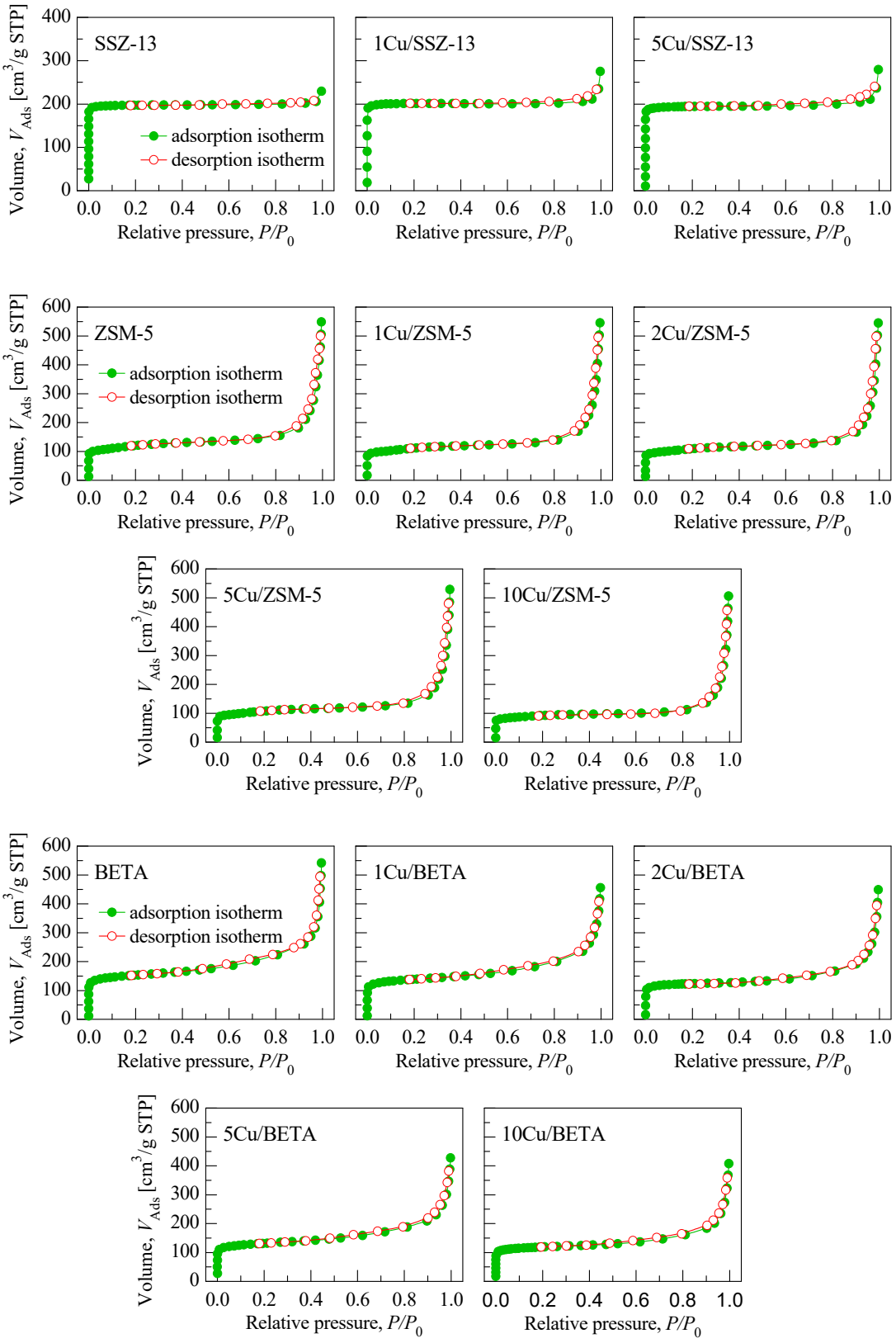

Figure 2.6 Nitrogen adsorption–desorption isotherms of pure zeolites and copper-containing zeolite catalysts (Cu/SSZ-13, Cu/ZSM-5, and Cu/BETA).

respectively. The micropore volume of parent SSZ-13 was 0.306 cm^3/g, which was almost twice as much as that of the parent ZSM-5 and BETA zeolites. The impregnation of Cu into the parent zeolite led to a decrease in BET specific surface area and pore volume. This can be explained that Cu species cover or permeate into both the internal and external surfaces of zeolite, leading to blocking accessible zeolite pores. One of the distinct features is that the mean pore diameter of SSZ-13 catalysts was in the micropore range of less than 2 nm; however, the mean pore diameter of ZSM-5 and BETA zeolites was in the mesopore range of more than 2 nm.

Figure 2.7 illustrates Barrett–Joyner–Halenda (BJH) pore size distributions (PSD) of the parent zeolites, indicating the presence of mesopores and macropores along with micropores in the parent zeolites. All zeolites exhibit a good hierarchical micro-meso-macroporosity.

Table 2.4 Physical properties of pure zeolites and copper-containing Cu/zeolites.

Catalysts	A_{BET} (m^2/g)	V_P (cm^3/g)	V_{Micro} (cm^3/g)	D_P (nm)
SSZ-13	837.1	0.3618	0.3063	1.7288
1Cu/SSZ-13	823.6	0.3440	0.3023	1.6707
5Cu/SSZ-13	805.2	0.3725	0.2934	1.8505
ZSM-5	434.3	0.6933	0.1559	6.3854
1Cu/ZSM-5	403.8	0.7075	0.1475	7.0084
2Cu/ZSM-5	398.7	0.7197	0.1456	7.2205
5Cu/ZSM-5	390.4	0.6574	0.1445	6.7357
10Cu/ZSM-5	345.1	0.5794	0.1274	6.7157
BETA	579.1	0.6793	0.1626	4.6921
1Cu/BETA	523.2	0.5736	0.1504	4.3853
2Cu/BETA	503.5	0.5471	0.1598	4.3464
5Cu/BETA	495.2	0.5373	0.1453	4.3401
10Cu/BETA	456.2	0.5092	0.1409	4.4647

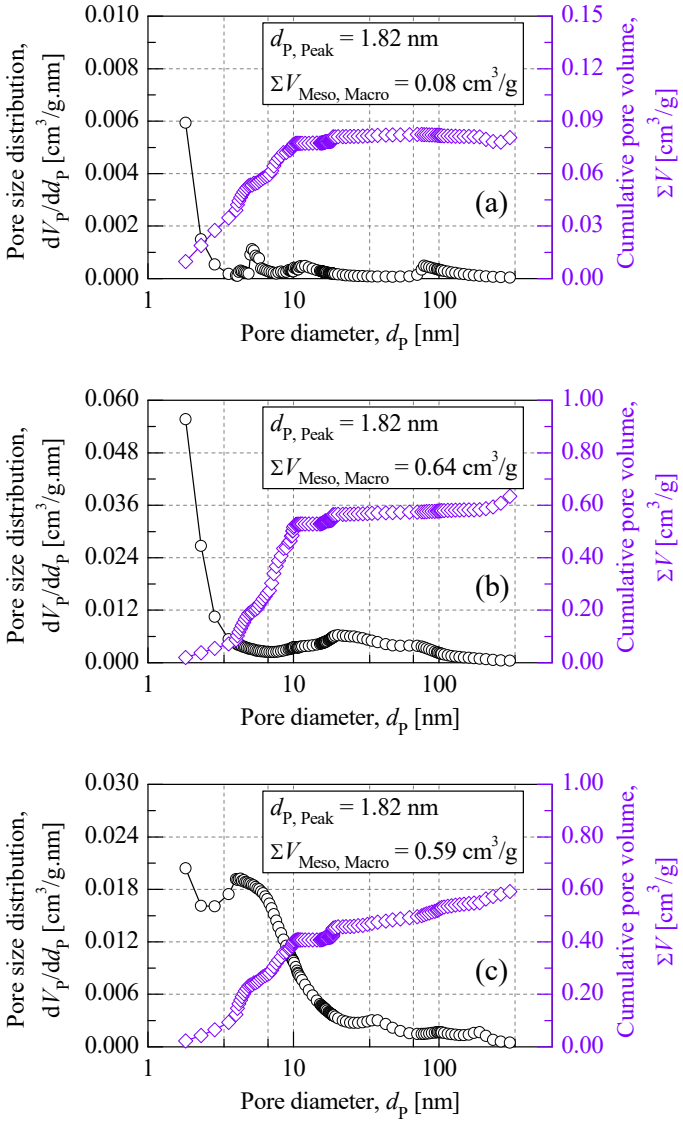

Figure 2.7 BJH pore size distributions (PSD) and cumulative pore volume of (a) parent SSZ-13, (b) parent ZSM-5, and (c) parent BETA.

2.2.4 Identification of zeolite frameworks

The powder XRD patterns of the parent zeolites and Cu-impregnated zeolites with different Cu loadings are depicted in Figure 2.8. As illustrated in Figure 2.8(a), the intrinsic chabazite structure was observed at 2θ = 9.64°, 13.07°, 14.19°, 16.27°, 18.01°, 20.90°, 25.29°, 26.31°, 31.06°, and 31.49°, indicative of the inherent chabazite framework [173, 179]. The XRD peaks of Cu/ZSM-5 (Figure 2.8(b)) were observed at 2θ = 7.95°, 8.81°, 13.23°, 13.96°, 14.79°, 23.08°, 23.94°, 24.41°, and 29.93°, which represents the connatural MFI zeolite framework [180, 181]. Similarly, the XRD peaks of Cu/BETA (Figure 2.8(c)) were also identified at 2θ = 7.61°, 13.49°, 14.61°, 21.55°, 22.60°, 25.45°, 27.14°, and 29.69°, indicating the inherent BEA framework of BEAT zeolite [182]. The identified diffraction angles (2θ) of Cu-impregnated catalysts were nearly identical to those of the parent zeolites, irrespective of the zeolites. The powder XRD patterns of all prepared catalysts could be clearly observed, implying the high crystalline degree of these Cu/zeolite catalysts. Notably, the impregnation of Cu to respective zeolite did not affect the modification of zeolite structures; thus, Cu/zeolite catalysts preserved the well-ordered hierarchical structures.

The major peak intensities of Cu/SSZ-13 decrease to a certain extend with an increase in Cu loading, in which the XRD intensity of 5Cu/SSZ-13 at 2θ = 9.64° was dropped by 15% compared to that of the parent SSZ-13. A similar phenomenon can be also observed over the Cu/ZSM-5 and Cu/BETA catalysts with an increase in Cu loading. The decrease in the relative crystallinity could be attributed to the unexpected collapse of some frameworks or the high x-ray absorption coefficient of the increasing number of CuO crystallites [183, 184]. The peaks ascribed to crystalline cupric oxide (CuO) were clearly observed at 2θ = 35.54°, 38.71°, and 48.85° in the case of a high Cu loading, i.e., 10 wt% Cu. Thus, when Cu loadings exceed 5 wt%, some Cu species were presented as crystalline CuO over the zeolite structure.

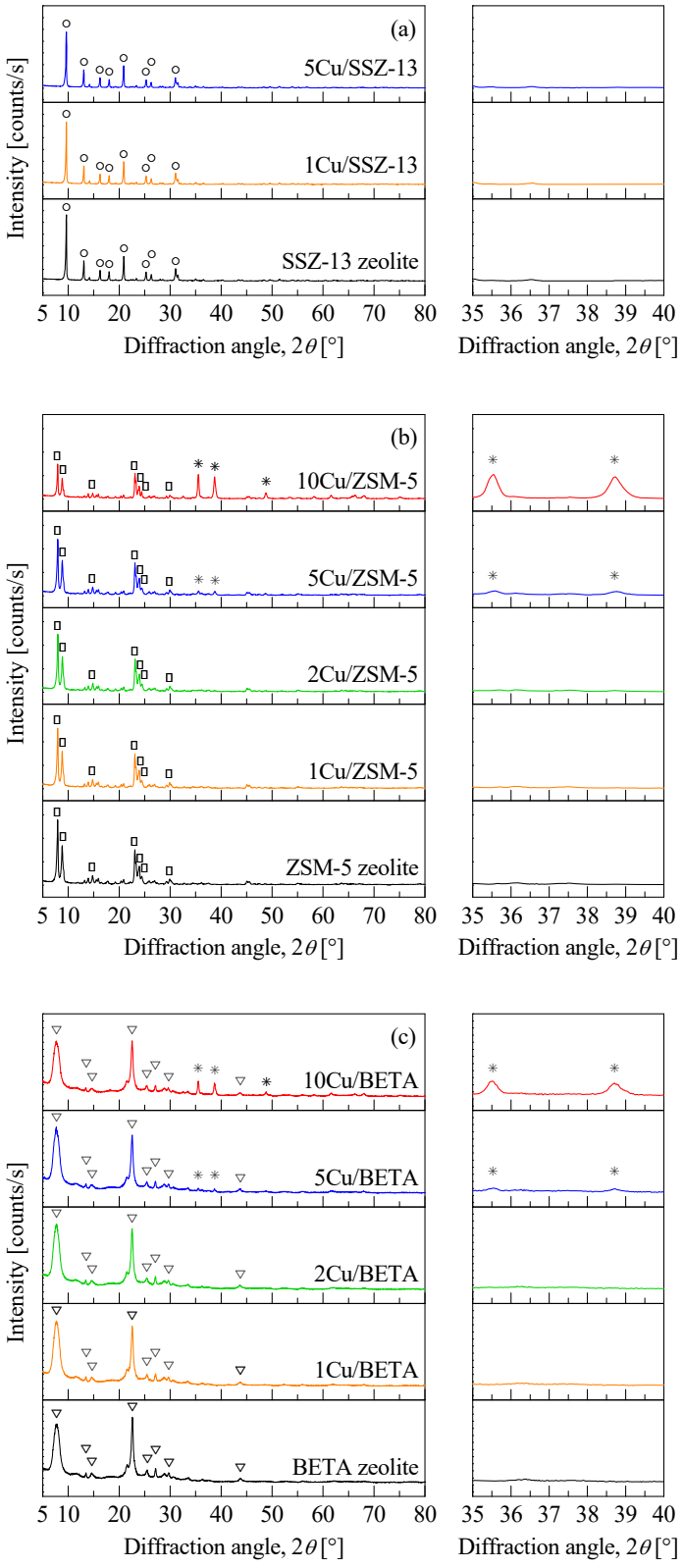

Figure 2.8 Powder XRD patterns of parent zeolites and Cu/zeolite catalysts: (a) Cu/SSZ-13, (b) Cu/ZSM-5, and (c) Cu/BETA.

2.2.5 Solid-state ^{27}Al MAS–NMR

Zeolites are microporous crystalline aluminosilicates, composed of TO_4 tetrahedra (T = Si or Al) with oxygen atoms by corner-sharing neighboring SiO_4 and AlO_4 tetrahedra to form the three-dimensional channel structures [185]. The amount of Al within the zeolite framework can vary in a wide range of SiO_2/Al_2O_3 ratio = 1 to ∞. The crystallographic positions of Al atoms and the local Al distributions govern the location of the active sites and catalytic properties [186]. The ^{27}Al NMR spectra provide the useful information concerning the framework connectivity of the aluminosilicate network like zeolite materials.

The local structure of Al species over the zeolite-based catalysts was analyzed to demonstrate the effect of Cu loading on the stability of framework Al over the Cu/zeolite catalysts, and the ^{27}Al MAS–NMR spectra are shown in Figure 2.9. For the parent SSZ-13, two peaks were observed at around δ_{27Al} = 0.1 ppm and 59.4 ppm, respectively, where a broad signal was associated with the tetrahedral framework of Al (Al^{IV}) at 59.4 ppm, whereas there was weak intensity of octahedral extra-framework of Al (Al^{VI}) at 0.1 ppm [187, 188]. After loading of Cu to the SSZ-13 zeolite, a notable feature was that the position of major peak shifted slightly toward low chemical shift region (δ_{27Al} of 1Cu/SSZ-13 and 5Cu/SSZ-13 = 58.7 ppm and 58.4 ppm). The shifting position of the ^{27}Al chemical shift was attributed to the varying average Al–O–Si angles.

As shown in Figures 2.9(b) and (c), a single peak was observed at δ_{27Al} = 54.9 ppm (parent ZSM-5) and δ_{27Al} = 54.2 ppm (parent BETA), respectively. The peak intensity of parent ZSM-5 at 54.9 ppm was related to tetrahedral framework of Al (Al^{IV}) [187, 189], and no octahedral Al species were identified. The peak intensity of parent BETA recorded at 54.2 ppm was also attributed to Al^{IV} framework in the BETA zeolite, and there was a minor signal of extra-framework of Al^{VI} at around −0.1 ppm [190, 191]. Similar to the Cu/SSZ-13 catalysts,

after Cu loading the chemical shift of Al^{IV} shifted slightly to low resonance region, indicative of the varying average Al–O–Si angles. From the ^{27}Al MAS–NMR spectra, it is suggested that Al species are well incorporated with the neighboring O atoms in the zeolite framework; thus, the loading of Cu species did not modify the zeolite networks over the Cu/zeolites.

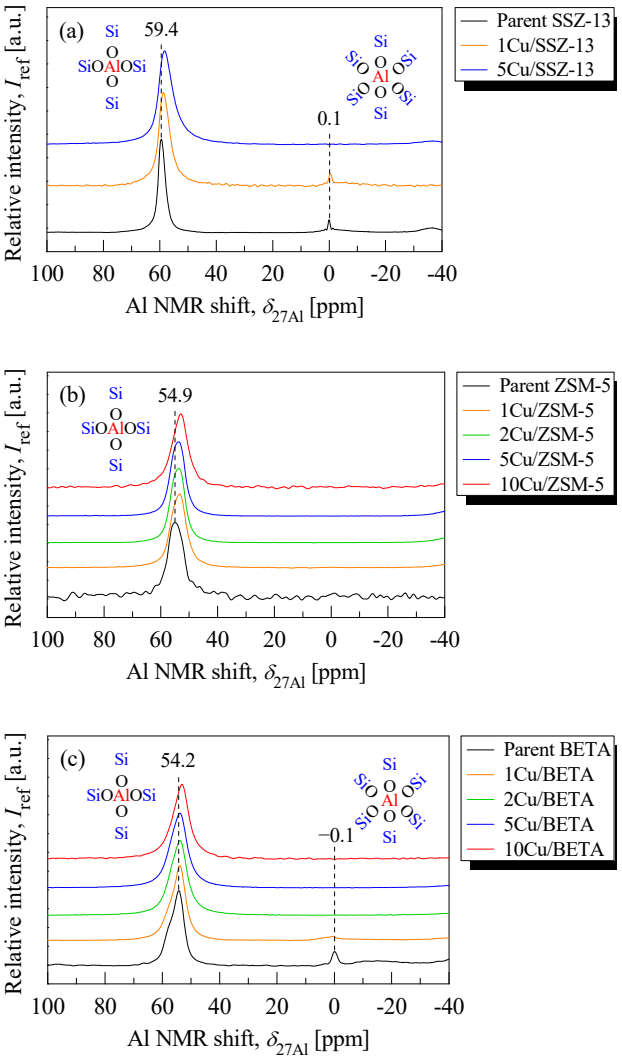

Figure 2.9 Solid-state ^{27}Al MAS–NMR spectra of parent zeolites and Cu/zeolite catalysts: (a) Cu/SSZ-13, (b) Cu/ZSM-5, and (c) Cu/BETA.

2.2.6 Valence state of Cu species

UV–vis diffuse reflectance spectroscopy (UV–vis DRS) was applied to understand the coordination and chemical nature of Cu species over the Cu/zeolite catalysts, providing the electron transitions of Cu species to distinguish the different Cu species. In the UV–vis spectra of Cu/zeolite catalysts (Figure 2.10), all the Cu/zeolite catalysts except for parent zeolites exhibited a wide range of UV–vis adsorption spectra. The adsorption spectra showed two different remarkable bands, where a narrow band with the peak center at about 210 nm and a broad band between 300 nm and 600 nm. The adsorption peak centered at nearly 210 nm is indicative of charge transfer band of the oxygen-to-metal related to the Cu^{2+} ions from lattice oxygen to isolated Cu ions stabilized in the zeolite framework [181, 192–194], which is characteristic of highly dispersed copper species (Cu^{2+}–O^{2-}). The flexure band at nearly 275–430 nm is also attributed to $O_{bridge} \rightarrow Cu$ charge-transfer in [Cu^{2+}–O^{2-}–Cu^{2+}] [195], implying the presence of Cu in the form of oligomeric species. The shoulder adsorption band at about 250 nm, assigned to Cu^{+}, was more pronounced with an increase in Cu loading [196, 197]. The shoulder band between 300 nm and 430 nm corresponds to the transitions of Cu^{2+} in tetragonal oxygen configuration [198]. The adsorption band at about 430–600 nm is related to the d-d transitions of Cu^{2+} in octahedral oxygen configuration or tetragonally distorted CuOx species [193, 199]. Obviously, the Cu/zeolites with Cu loading of more than 5 wt% exhibited a much strong adsorption peak at a high wavelength compared to Cu loading of less than 5 wt%, implying that Cu species are favorable for the formation of copper oxides on the zeolite surface. Furthermore, Cu/zeolite catalysts showed significant enhancements of intensities near 210 nm with an increase in Cu loadings, meaning that there was an increase in the amount of isolated Cu^{2+} ions. The results of UV–vis matched well with the XRD because CuO clusters were detected over the Cu/zeolites with Cu loading of more than 5 wt%.

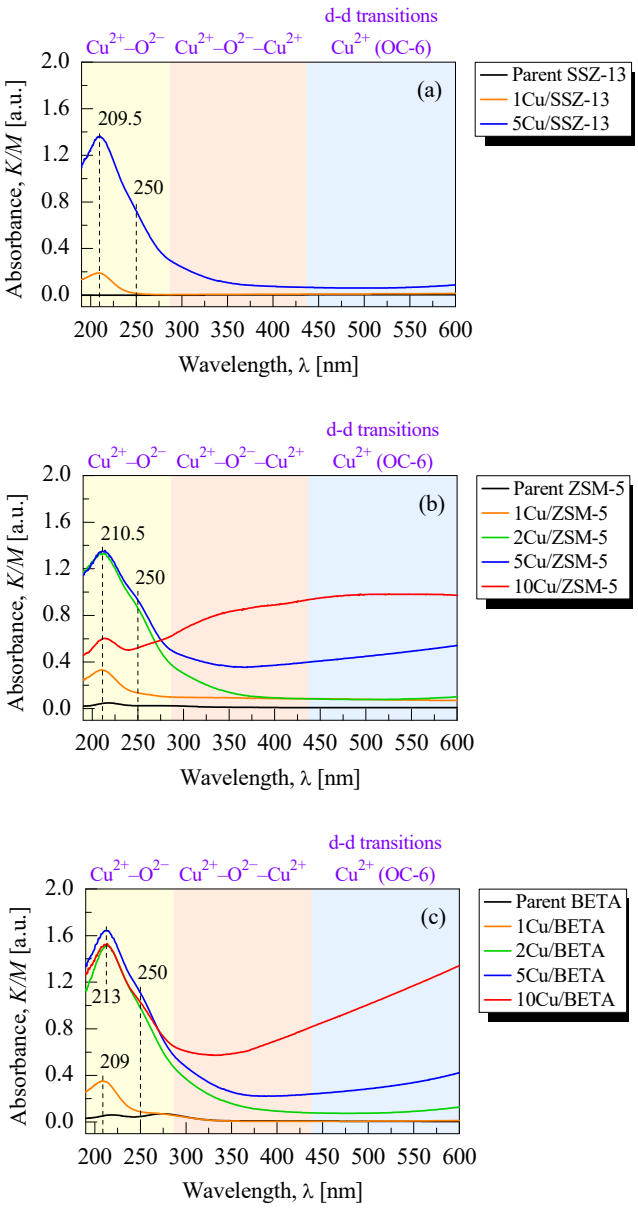

Figure 2.10 UV–vis diffuse reflectance spectroscopy (DRS) of parent zeolites and Cu/zeolite catalysts according to Cu loadings: (a) Cu/SSZ-13, (b) Cu/ZSM-5, and (c) Cu/BETA.

XPS characterization was carried out to further investigate the oxidation states of Cu oxides and various elements of 5Cu/zeolites. The XPS survey scan of 5Cu/zeolites showed the presence of Al 2p, Si 2p, Si 2s, C 1s, O 1s and Cu 2p peak, as shown in Figure 2.11(a). All the catalyst samples were mounted on a carbon tape, which was responsible for the C 1s spectra at 285.1 ± 1.0 eV in the survey scan. As shown in the high resolution XPS spectra of Cu 2p (Figure 2.11(b)), the copper oxide was present in two oxidation states, cupric oxide (CuO) and cuprous oxide (Cu_2O), on the surface of 5Cu/zeolites. In addition, three satellite peaks located at 941.6 ± 0.5 eV, 944.8 ± 0.4 eV, and 963.6 ± 0.4 eV were also observed, indicating the existence of divalent copper (Cu^{2+}) species [200, 201]. The two spectra of Cu $2p_{3/2}$ and Cu $2p_{1/2}$ located at 933.6 ± 0.1 eV and 953.3 ± 0.2 eV were attributed to the spin-orbit splitting of the bivalent Cu^{2+} [202]. The spectra of Cu $2p_{3/2}$ were deconvoluted into two peaks centered at 933.5 ± 0.2 eV and 935.8 ± 0.3 eV, corresponding to Cu^{+} in pure Cu_2O and Cu^{2+} in pure CuO, respectively [203, 204]. The deconvoluted spectra of Cu $2p_{1/2}$ were centered at 953.3 ± 0.2 eV and 956.2 ± 0.2 eV, where the former was assigned to the presence of Cu^{+} in Cu_2O and the latter to the presence of Cu^{2+} in CuO, respectively [203, 205].

The results of Cu 2p XPS spectra matched well with the XRD patterns because CuO species was present in the 5Cu/zeolites. Moreover, XPS measurement provided more precise valent states of Cu compared to XRD because Cu_2O was not observed in the XRD patterns. The Si 2p peaks for all the 5Cu/zeolite catalysts were observed at 103.8 ± 0.1 eV (Figure 2.11(c)), indicating the presence of O–Si–O bonds in the zeolite structure [206]. The XPS spectra of Al 2p were also observed at 75.2 ± 0.1 eV (Figure 2.11(d)), revealing the existence of trivalent aluminum ion (Al^{3+} in Al_2O_3) in the zeolite structure [207].

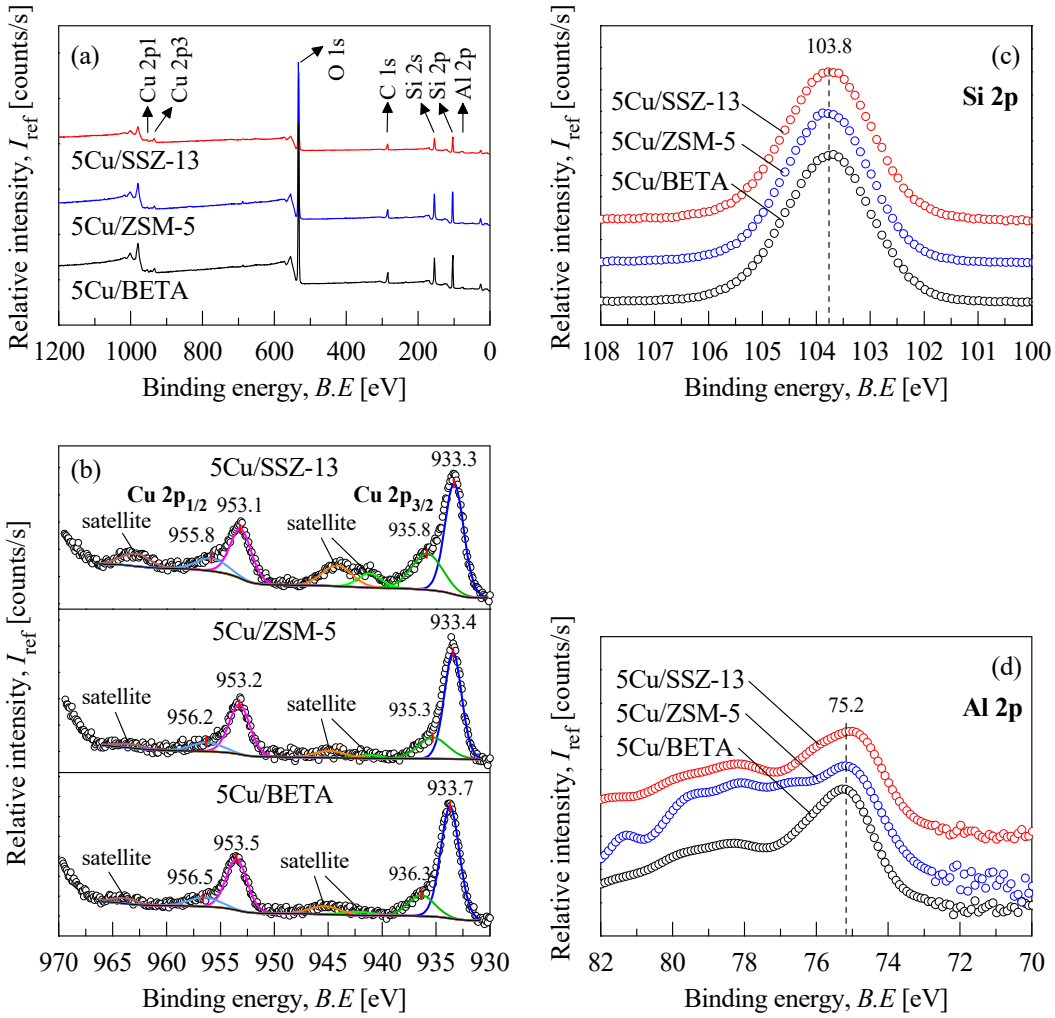

Figure 2.11 XPS spectra of 5Cu/zeolites: (a) full survey scan, (b) Cu 2p, (c) Si 2p, and (d) Al 2p.

2.2.7 Identification of zeolite morphology

Figure 2.12 shows the respective FE–SEM micrographs of the parent SSZ-13 zeolite and as-made Cu/SSZ-13 catalysts. The parent SSZ-13 exhibited a distinct morphology derived from the intrinsic chabazite framework, having three-dimensional cubic-shaped crystals. A clear shape edge of orthogonal morphology was observed for the parent SSZ-13, agglomerating small crystals with a size smaller than about 200 nm. The clear edge of morphology has resulted in the sharp intensities of XRD peak, as shown in Figure 2.8(a). The notable effect of Cu loading on the surface of Cu/SSZ-13 was that the edge of orthogonal morphology was relatively smooth compared to that of the parent SSZ-13, whereas no deformation and defect of the inherent SSZ-13 morphology was observed for the 1Cu/SSZ-13 and 5Cu/SSZ-13 catalysts.

As illustrated in Figure 2.13, the parent ZSM-5 zeolite exhibited a regular three-dimensional cubic-shaped morphology and agglomerated into spherical shape with a uniform size of nearly 15 nm. The impregnation of Cu species into the parent ZSM-5 caused little deformation of the inherent morphology, and the crystals were distributed uniformly. Furthermore, there were many inter-connected pores in the parent ZSM-5 and Cu/ZSM-5, indicating the presence of higher intercrystalline mesoporosity.

The SEM micrographs of the parent BETA and Cu/BETA are characterized as shown in Figure 2.14. The parent BETA zeolite had a three-dimensional sphere-shaped morphology, in which the boundaries of the primary nano-crystals could be distinctly observed, and moreover, the small crystals were irregularly distributed. After adding the Cu species, the primary particles were also observed, and there were no deformations or defects like those observed for Cu/SSZ-13 and Cu/ZSM-5. An average size of the primary crystals for the 5Cu/BETA, for example, were nearly 40 nm, and the amount of Cu loading into the parent BETA zeolite

did not affect the basic morphology of the BETA zeolite. This finding suggests that the Cu/BETA catalysts are phase-pure and have the high crystallinity like those of Cu/SSZ-13 and Cu/ZSM-5. The ZSM-5 and BETA zeolites had a lot of inter-connected mesopores in their frameworks, being consistent with the results of N_2–isotherms (Figure 2.6) and physical properties (Table 2.4) that both zeolites possessed more total pore volume compared to that of the SSZ-13 zeolite.

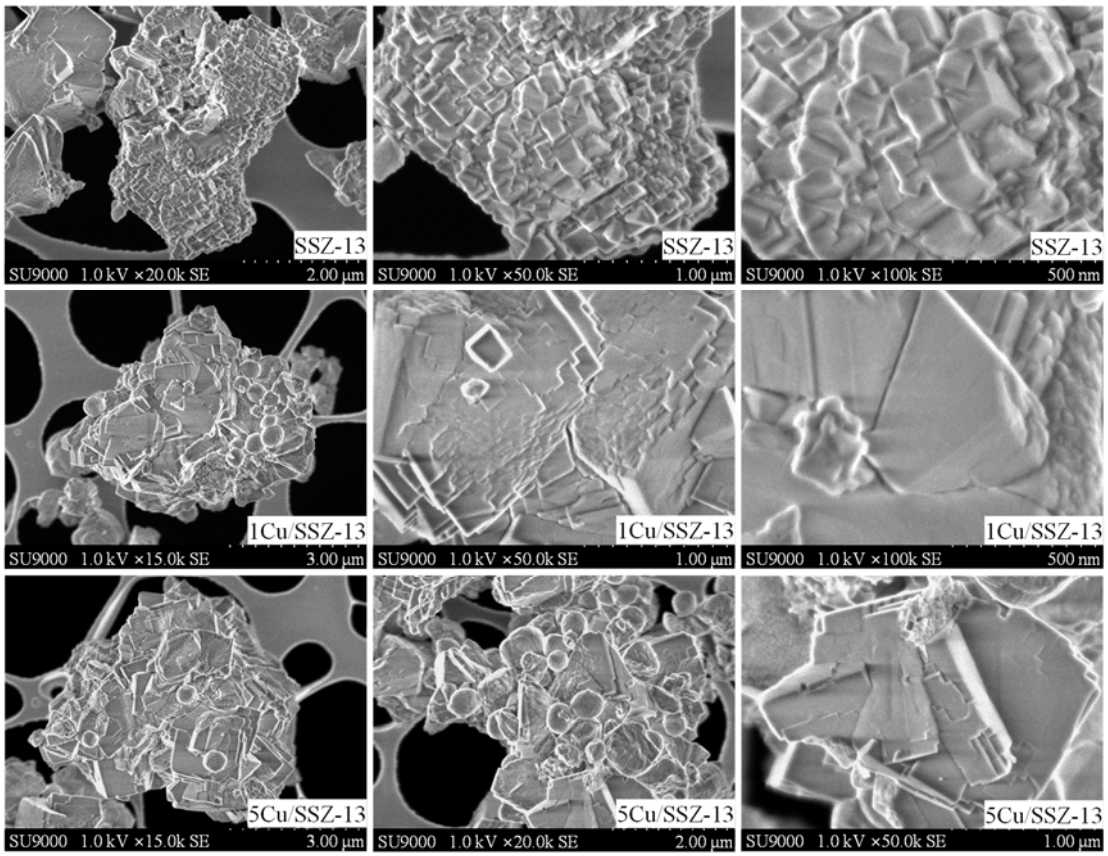

Figure 2.12 High-resolution FE–SEM micrographs of both parent SSZ-13 and as-made Cu/SSZ-13 with magnification from 15,000 to 100,000.

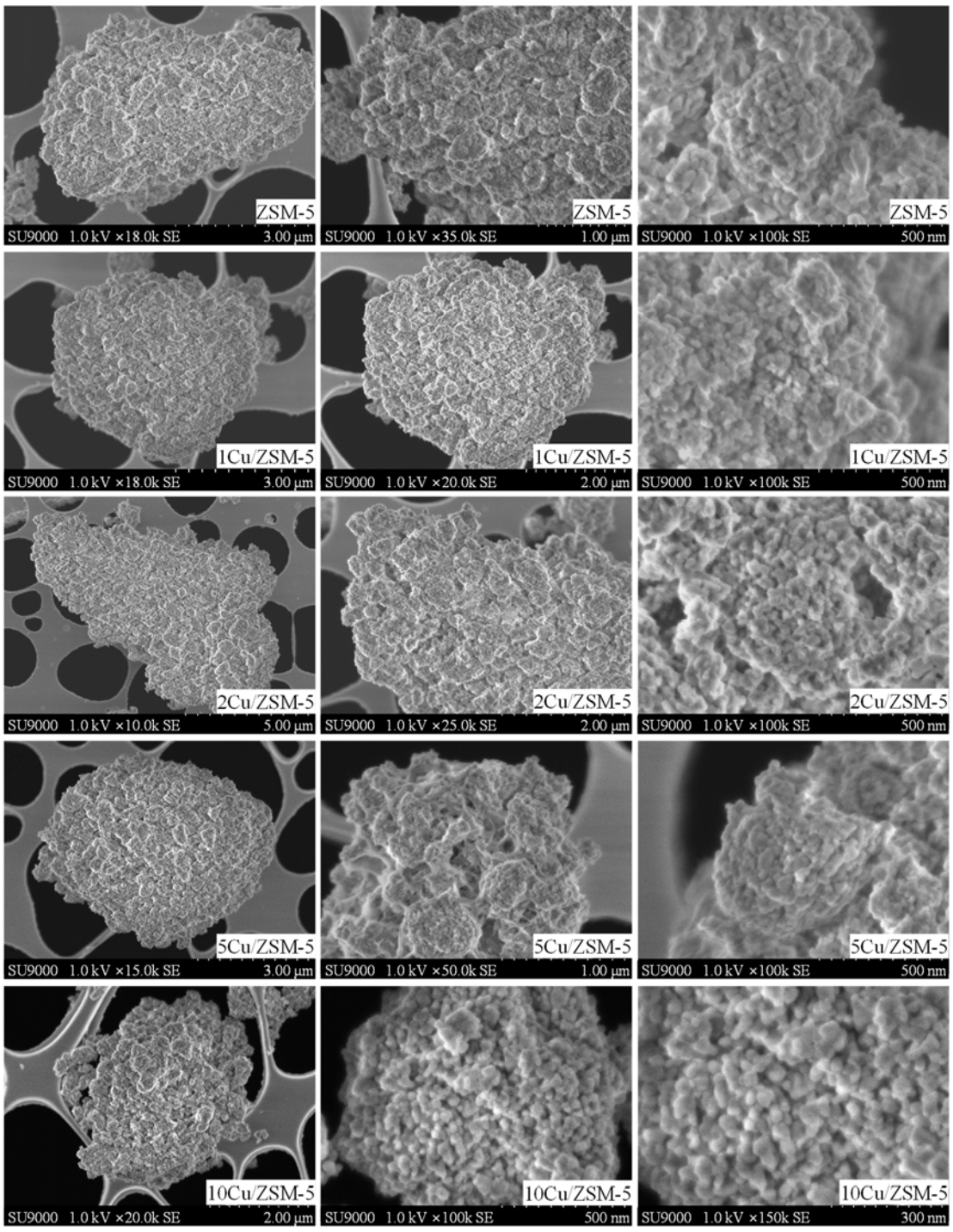

Figure 2.13 High-resolution FE–SEM micrographs of both parent ZSM-5 and as-made Cu/ZSM-5 with magnification of 15,000 to 150,000.

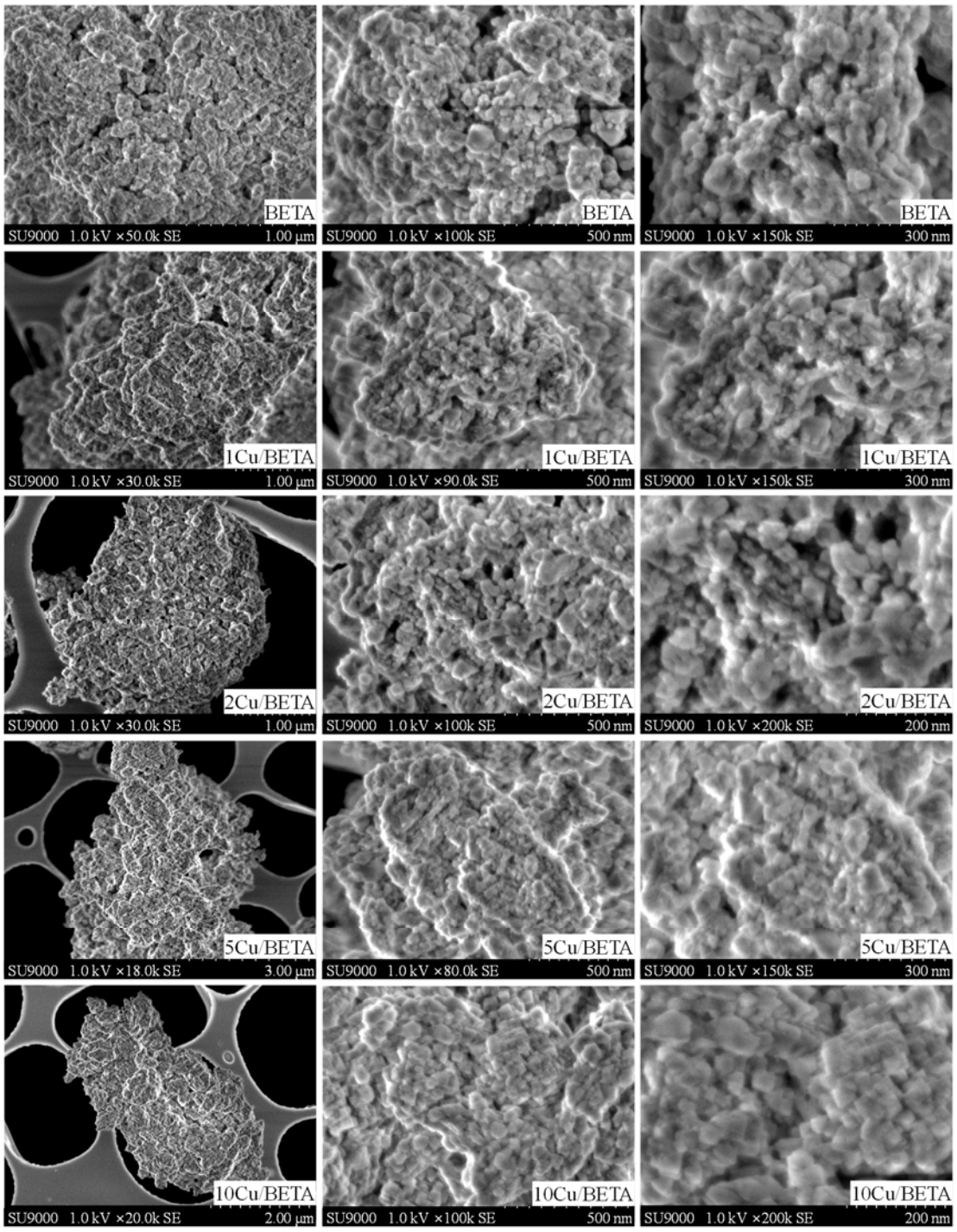

Figure 2.14 High-resolution FE–SEM micrographs of both parent BETA and as-made Cu/BETA with magnification of 18,000 to 200,000.

2.2.8 Identification of Cu particle size

To identify the impregnated Cu metal particles, the FE–TEM micrographs of as-made Cu/zeolite catalysts are analyzed, as illustrated in Figure 2.15. The small dark sphere-shaped spots are attributed to the nano-scaled copper oxide, and the faint background represents the zeolite support. The Cu particles were well homogeneously dispersed on the surface of respective parent zeolite, whereas the size of Cu particle grow with an increase in the Cu loading. For example, one large particle could be observed over the 5Cu/SSZ-13 and 10Cu/BETA, in which small Cu oxides may agglomerate together to form larger Cu clusters.

For in-depth understanding of the relation between the Cu loading and particle size of Cu oxide, the particle size of Cu and its distribution were analyzed using an ImageJ software. As illustrated in Figure 2.15, all the Cu/zeolite catalysts had relatively narrow particle size distributions of the Cu metal, whereas only 5Cu/SSZ-13 showed in a broad range of 5–20 nm. the amounts of Cu loading slightly affected the Cu particle size, growing the Cu diameter with an increase in the Cu loading. Almost 100 Cu particles was identified from the FE–TEM micrographs, and they were analyzed according to their diameter, as shown in Figure 2.16 and Figure 2.17. For the Cu/ZSM-5 and Cu/BETA catalysts, the particle diameter of Cu was distributed in a range of 1–5 nm. Furthermore, all the Cu particles were well dispersed even though the loading amount of Cu was more than 5 wt%, where the particle diameter of Cu was less than 5 nm for 10Cu/ZSM-5 and 10Cu/BETA. Whereas, the Cu/SSZ-13 catalysts showed a different trend, in which 5Cu/SSZ-13 showed a broad range of Cu diameter more than 6 nm. These findings indicate that the impregnated Cu species may be agglomerated together in the zeolite framework, when excess Cu was introduced to the SSZ-13 zeolite. For example, an average diameter of Cu particle was the order of 5Cu/BETA (D_{Cu} = 2.3 nm) < 5Cu/ZSM-5 (D_{Cu} = 2.5 nm) < 5Cu/SSZ-13 (D_{Cu} = 10.4 nm), whose findings were very

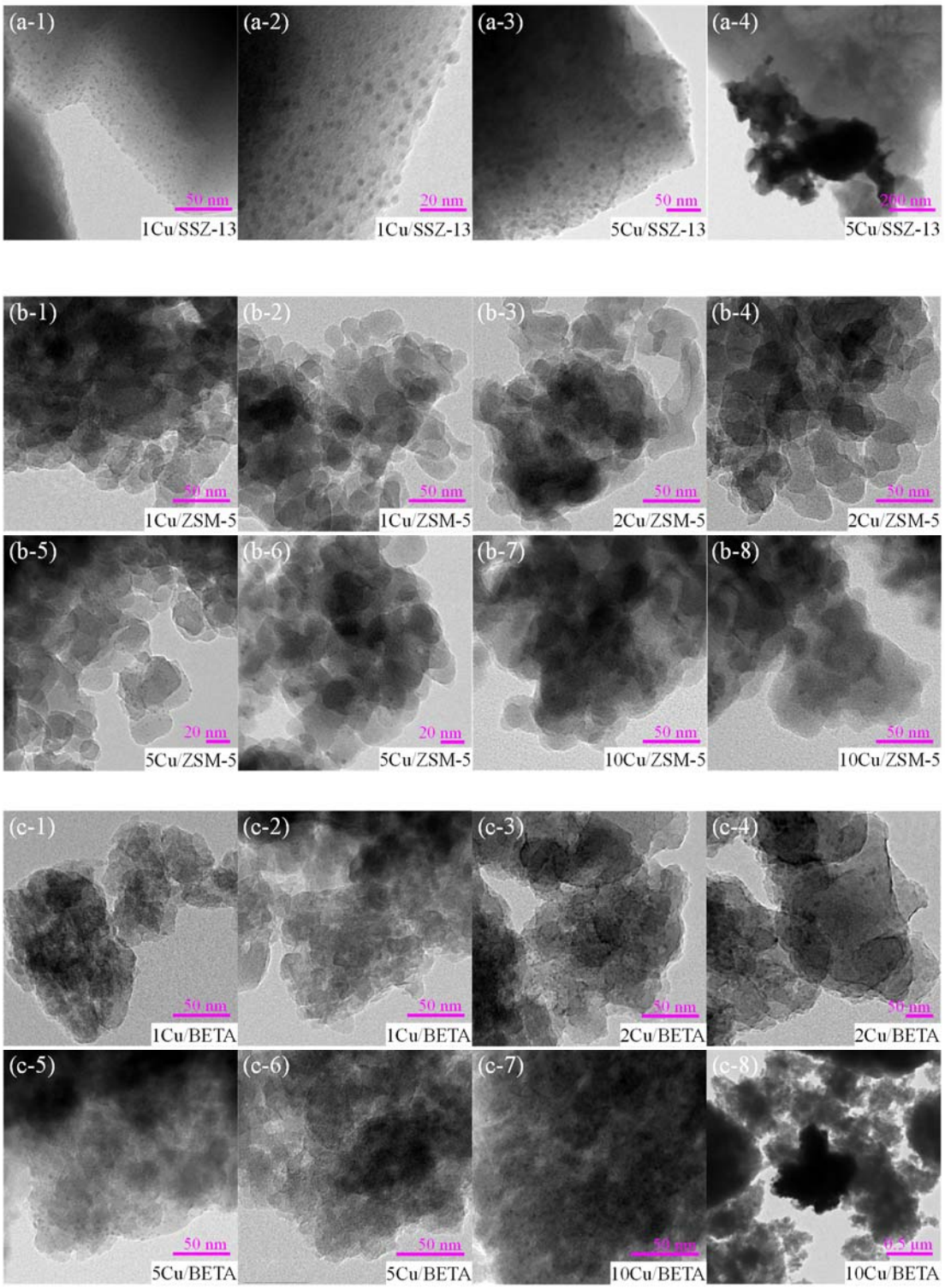

Figure 2.15 FE–TEM micrographs of Cu/zeolite catalysts according to Cu loading amounts: (a) Cu/SSZ-13, (b) Cu/ZSM-5, and (c) Cu/BETA.

interesting because the zeolite topology was expected to play an important role in dispersion of the Cu species. Similarly, to compare with the effect of Cu loading amounts, 1Cu/zeolite catalysts were also investigated; an average diameter of Cu was 3.1 nm (1Cu/SSZ-13), 2.0 nm (1Cu/ZSM-5), and 1.5 nm (1Cu/BETA), respectively. These results suggest that the zeolite topology would affect the particle diameter of Cu; thus, the smaller the pore-opening size of SSZ-13 with the CHA framework, the larger the size of the dispersed Cu particles.

These findings are in good agreement with a previous study reported by Pereda-Ayo *et al*. [208], where the Cu particle size distribution of Cu/ZSM-5 and Cu/BETA with 1.2–5.8 wt% Cu loading was compared. Only small particles (diameter < 1.5 nm) were dispersed on the Cu/BETA catalysts, whereas both small and large particles were dispersed on ZSM-5.

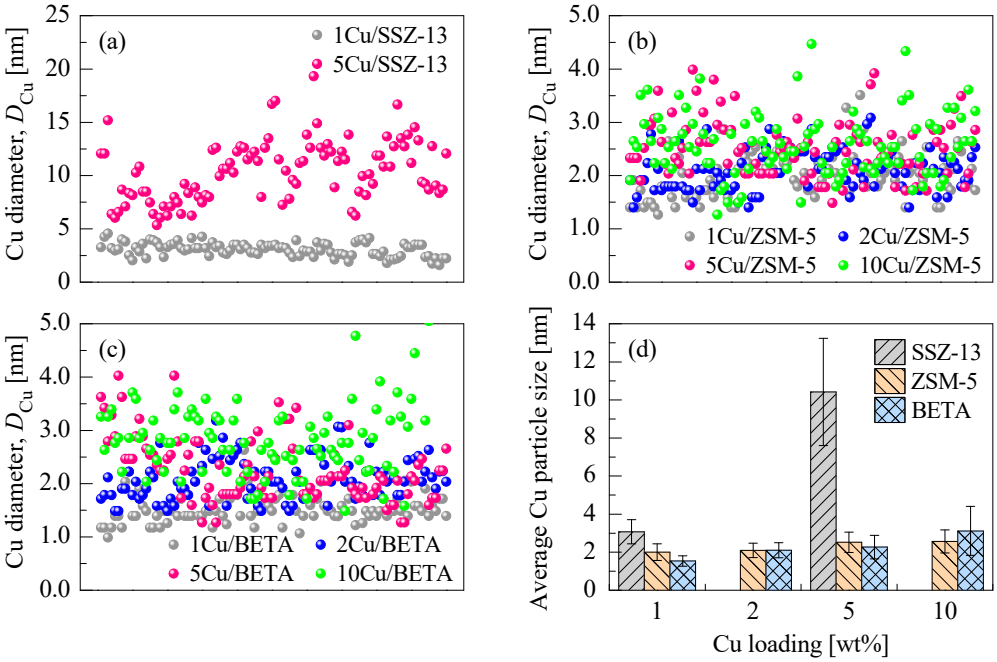

Figure 2.16 Cu particle distributions (a) Cu/SSZ-13, (b) Cu/ZSM-5, (c) Cu/BETA, and (d) average particle diameter of Cu for Cu/zeolites as a function of Cu loading: nearly 100 Cu particles were analyzed from FE–TEM micrographs.

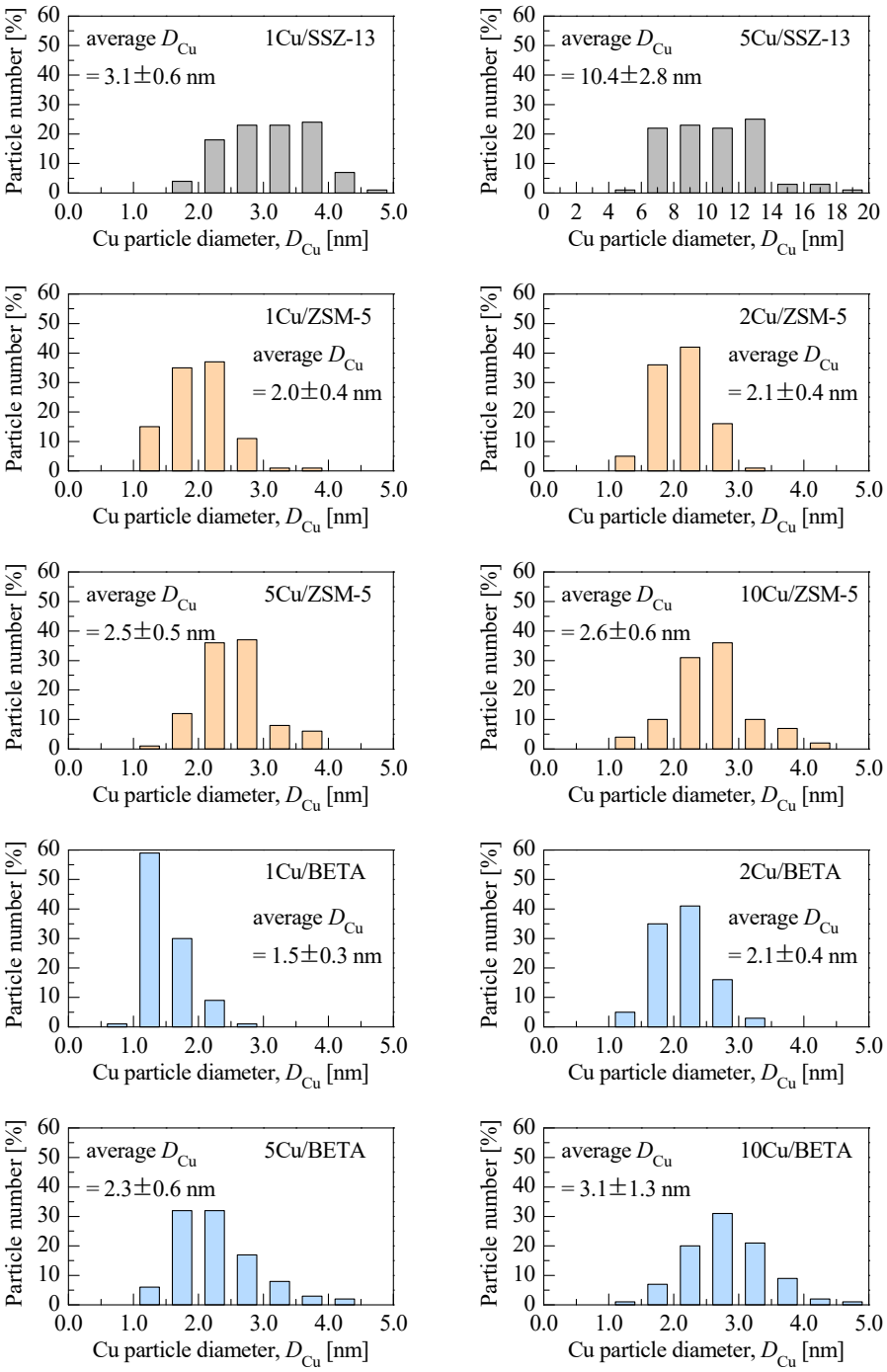

Figure 2.17 Particle size distributions and average particle diameter of Cu species for the as-made Cu/zeolite catalysts as a function of Cu loading.

The zeolites affected the nature of the Cu species formed, where the zeolite structures also seemed to be involved. They postulated that that the major reason for the size difference was related to the accessible volumes of each zeolite, where the accessible volumes of ZSM-5 and BETA were 10 and 23%, respectively [208–211]. The maximum diameter of a sphere that can be included in these zeolite structures was 6.36 Å for MFI and 6.68 Å for BEA. In the present study, the accessible volume and the maximum diameter of a sphere that can be accommodated in the SSZ-13 zeolite with the CHA framework are ca. 17.3% and 7.37 Å, respectively [211]. According to our findings, the Cu particle size was closely related to the diffusion diameter of the zeolite structure rather than the accessible volume and maximum diameter of the sphere. The intra-crystalline diffusion diameter of the respective zeolites followed the order: 3.73 Å (SSZ-13) < 4.70 Å (ZSM-5) < 5.95 Å (BETA) [209–211]. The copper precursor, copper(II) nitrate trihydrate solution, used for the impregnation process is expected to diffuse more easily into the ZSM-5 and BETA pores than into those of SSZ-13; therefore, relatively small particles could be dispersed on the ZSM-5 and BETA zeolites.

Furthermore, the effect of Cu loading on its distribution to the zeolite support may be related to the distinct framework types of zeolite. As illustrated in the Figure 2.18, the zeolites, CHA, MFI, and BEA, had a variety of channels and regular pore-opening sizes derived from the three-dimensional framework structures. The pore-opening of MFI with the medium pore (10-ring) and BEA with the large pores (12-ring) is ca. 5.1–5.6 Å [212, 213] and 5.6–6.7 Å [213, 214] in size, respectively. The pore-opening of CHA with the super small pores is ca. 2.9-3.8 Å [213]. The ionic radius of Cu^{+} and Cu^{2+} is nearly 0.77 Å and 0.73 Å, respectively. When the Cu precursor ($Cu(NO_3)_2 \cdot 3H_2O$) is introduced into the zeolite frameworks, it could be comparatively free to access to the internal channels of ZSM-5 and BETA zeolite, whereas Cu species was restricted by the geometry-limit in the SSZ-13 zeolite.

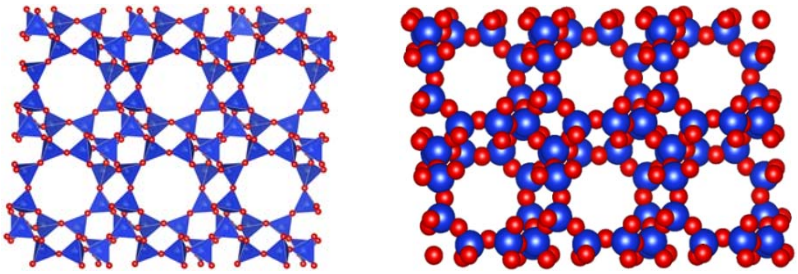

(a) CHA framework (⊥ [001] 8-ring, pore-opening = 3.8 × 3.8 Å)

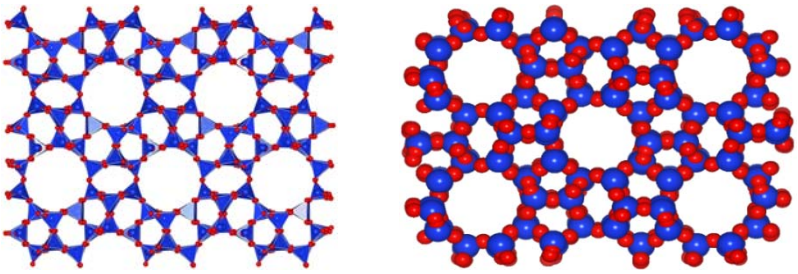

(b) MFI framework (⊥ [100] 10-ring, pore-opening = 5.1 × 5.6 Å)

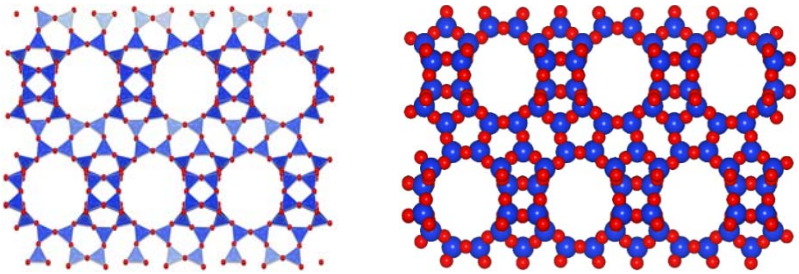

(c) BEA framework (⊥ [100] 12-ring, pore-opening = 5.6 × 6.7 Å)

Figure 2.18 Zeolite frameworks and pore-opening sizes: (a) CHA (chabazite), (b) MFI (ZSM-5), and (c) BEA (BETA) zeolite.

2.3 Summary

The Cu/zeolite catalysts were prepared by an incipient wetness impregnation method, in which the Cu precursor ($Cu(NO_3)_2 \cdot 3H_2O$) was impregnated to the three different parent zeolites, having distinct frameworks with CHA, MFI, and BEA, respectively. The loading of Cu for as-made Cu/zeolite has been determined in a range of 1–10 wt%. To investigate the physical and chemical properties, the powder Cu/zeolite catalysts have been analyzed by a variety of techniques, including the ICP–AES, N_2–isotherms, powder XRD, solid-state ^{27}Al MAS–NMR, UV–vis DRS, XPS, high-resolution FE–SEM, and FE–TEM.

From the ICP–AES analysis, the Si/Al ratios of all the Cu impregnated catalysts over the respective zeolite were in good agreement with those of the parent zeolite. The loading levels of Cu metal species for all the powder catalysts were close to the theoretical loading amount, suggesting that the Cu species has been successfully introduced to the respective zeolite framework.

The nitrogen adsorption-desorption isotherms at 77 K were carried out to characterize the surface area, pore size, and pore volume. Among the three parent zeolites, SSZ-13 with the chabazite topology showed by far the largest BET specific surface area; the order of BET specific surface area was SSZ-13 (837.1 m^2/g) > BETA (579.1 m^2/g) > ZSM-5 (434.3 m^2/g). The loading of Cu to the zeolite support led to a drop of BET specific surface area, which could be explained that metal Cu species covered both the internal and external surface of zeolite, resulting in blocking the accessible zeolite pores.

The powder XRD patterns of all the as-made Cu/zeolite catalysts have clearly indicated that the impregnation of Cu species did not affect any modification of the zeolite structure; thus, the Cu/zeolite catalysts could maintain their highly well-ordered hierarchical structures. The decrease in major peak intensities has been attributed to a higher adsorption coefficient

of metal Cu species, which was highly dispersed on the zeolite support.

The local coordination of Al species in the zeolite was identified to demonstrate the effect of Cu loading on the stability of zeolite framework over the as-made Cu/zeolite catalysts. ^{27}Al NMR chemical shift (δ_{27Al}) of the parent zeolites has been observed at around δ_{27Al} = 59.4 ppm (SSZ-13), 54.9 ppm (ZSM-5), and 54.2 ppm (BETA), implying that one aluminum atom was shared with the neighboring 4 oxygen atoms. Thus, Al species of all the parent zeolites were in tetrahedral coordination (Al^{IV}). When increasing the amounts of Cu loading into the parent zeolites, δ_{27Al} values have showed a tendency to shift toward lower chemical shift region with less than 2 ppm, which indicated that the average Al–O–Si angles were influenced by the impregnated Cu species.

To identity the structural coordination and chemical nature of Cu species, the Cu/zeolite catalysts were analyzed by UV–vis DRS spectroscopy. The adsorption spectra showed two different bands, where a narrow band with the peak center at nearly 210 nm and a broad band between 300 nm and 600 nm. The adsorption peak centered at nearly 210 nm was indicative of the charge transfer band of the oxygen -to-metal related to the Cu^{2+} ions from lattice oxygen to isolated Cu ions stabilized in the zeolite framework. The band between 300 nm and 450 nm was related to the transitions of Cu^{2+} in tetragonal oxygen configurations, and the band at about 600 nm corresponded to the d-d transitions of Cu^{2+} in octahedral oxygen configurations. The Cu/zeolite catalysts exhibited that Cu species was more in favorable for the formation of CuOx clusters in the zeolite structures with an increase in the Cu loading.

The crystal morphology of the Cu/zeolite catalysts was analyzed by high-resolution FE–SEM. The parent SSZ-13 and Cu/SSZ-13 exhibited a three-dimensional cubic-shaped morphology. The loading of Cu to the SSZ-13 zeolite made the edge of orthogonal morphology relatively smooth, resulting in a decrease in the crystallinity, whereas no

deformations and defects of the inherent SSZ-13 morphology could be observed. Cu/SSZ-13 and Cu/BETA exhibited a cubic and sphere-shaped morphology, respectively. After addition of the Cu species to the respective zeolite, the three-dimensional morphology maintained uniformly, and there was no deformation like in the case of Cu/SSZ-13. The ZSM-5 and BETA zeolite had a lot of inter-connected mesopores in their frameworks, resulting in having more total pore volume compared to that of the SSZ-13 zeolite.

The high-resolution STEM was analyzed to identify the distribution of impregnated Cu species over the Cu/zeolite catalysts. The nano-scaled Cu particles were well dispersed on the zeolite supports, growing the Cu diameter with an increase in the Cu loading. For the Cu/ZSM-5 and Cu/BETA, the particle diameter of Cu was in a range of 1–5 nm. The excess loading of Cu more than 5 wt% has resulted in slightly larger Cu particle less than 5 nm compared to 1Cu/zeolite. However, Cu/SSZ-13 showed an interesting feature, in which 5Cu/SSZ-13 had a broad range of Cu diameter more than 5 nm. These findings indicated that the Cu species might be agglomerated together in the zeolite framework, when excess Cu was introduced to the SSZ-13 zeolite. The effect of Cu loading on its particle distribution over the respective Cu/zeolite catalyst may be related to the inherent framework types of zeolite. The different three kinds of zeolites, which are CHA, MFI, and BEA, have various channels and determined pore-opening size derived from the hierarchical three-dimensional topology. The pore-opening size followed the order of CHA (8-ring, 2.9–3.8 Å) < MFI (10-ring, 5.1–5.6 Å) < BEA (12-ring, 5.6–6.7 Å); thus, Cu species was restricted by the geometry-limit diffusion in the SSZ-13 zeolite.

Chapter 3. Catalytic Performance of C_3H_6-SCR

3.1 Experimental conditions for evaluation of C_3H_6-SCR

In this chapter, the selective catalytic reduction of NOx using propene (C_3H_6) as a reducing agent is evaluated over the copper-containing zeolites with different types of frameworks to identify the optimal copper/zeolite catalysts. A detailed comparison of the zeolite frameworks for copper-loaded catalysts supported on a small pore 8-ring chabazite (Cu/SSZ-13), a medium pore 10-ring MFI (Cu/ZSM-5), and a large pore 12-ring BEA (Cu/BETA) under various copper loading conditions are performed.

To investigate the effect of reactor system on catalytic performance, the characteristics of NOx reduction for HC-SCR were evaluated by a laboratory-scale normal-pressure fixed-bed synthetic gas catalytic reactor. The washcoated monolithic catalyst was placed in the quartz reactor with a diameter of 19.5 mm and length of 350 mm. The reaction temperature of the quartz reactor was controlled by a ceramic electric furnace (ARF-40KC, Asahi Rika manufacturing) with kanthal (FeCrAl alloy) wire. A K-type thermocouple (1.0 mm of diameter) was located at 5 mm in front of the monolithic catalyst to monitor the catalytic reaction temperature. The catalytic activity of the SCR catalysts was investigated in transient mode within the 150–600℃ range at a ramp-up rate of 5 ℃/min. All the reaction temperatures of the catalyst reported herein refer to the inlet temperature. After the catalytic reaction in the quartz reactor, the concentrations of the product gas, NO, NO_2, N_2O, NH_3, HNCO, CO, and C_3H_6 were continuously measured by a Fourier transform infrared instrument (FTIR, Midac I-2004). The experimental apparatus of catalytic reactor equipped with the quartz reactor is illustrated in the Figure 3.1. Table 3.1 summarizes the gas compositions and reaction conditions for evaluating the C_3H_6-SCR catalyst.

The catalytic performance of NOx reduction for the HC-SCR process was evaluated in

transient-state conditions in a temperature range of 150–600°C with a heating rate of 5 °C/min. Prior to evaluating the catalytic reaction, the monolithic honeycomb catalyst was first exposed to 8 vol.% O_2 and N_2 balance 500°C for 30 min with at a flow rate of 1.5 L/min to clean the catalyst surfaces. Subsequently, pretreated catalyst was flushed with only pure N_2 gas at a flow rate of 1.5 L/min for 30 min, followed by cooling to 150°C by flushing with N_2. After the desired gases for evaluating the HC-SCR performance were introduced up to the saturation levels of NOx, CO, and reducing agent at 150°C, the reaction temperature was gradually increased from 150 to 600°C. The NOx conversion (η_{NOx}), C_3H_6 conversion (η_{C3H6}), C_4H_{10} conversion (η_{C4H10}), and CO conversion (η_{CO}) were respectively calculated by applying the following equations:

$$\eta_{NOx} = \left(\frac{C_{NO}^{in} - C_{NO}^{out} - C_{NO_2}^{out}}{C_{NO}^{in}} \right) \times 100\,[\%] \tag{3.1}$$

$$\eta_{C3H6} = \left(\frac{C_{C_3H_6}^{in} - C_{C_3H_6}^{out}}{C_{C_3H_6}^{in}} \right) \times 100\,[\%] \tag{3.2}$$

$$\eta_{C4H10} = \left(\frac{C_{C_4H_{10}}^{in} - C_{C_4H_{10}}^{out}}{C_{C_4H_{10}}^{in}} \right) \times 100\,[\%] \tag{3.3}$$

$$\eta_{CO} = \left(\frac{C_{CO}^{in} - C_{CO}^{out}}{C_{CO}^{in}} \right) \times 100\,[\%] \tag{3.4}$$

where, the superscripts “in” and “out” denote the gas concentrations monitored at the inlet and outlet of the reactor. The N_2 yield (S_{N2}) and NH_3 selectivity (S_{NH3}) were also calculated by applying the following equations to investigate the undesired side- reactions of HC-SCR.

$$S_{N2} = \left(\frac{C_{NO}^{in} - C_{NO}^{out} - C_{NO_2}^{out} - 2C_{N_2O}^{out} - C_{NH_3}^{out} - C_{HNCO}^{out}}{C_{NO}^{in}} \right) \times 100\,[\%] \tag{3.5}$$

$$S_{NH3} = \frac{C_{NH_3}^{out}}{C_{NO}^{in}} \times 100\ [\%] \tag{3.6}$$

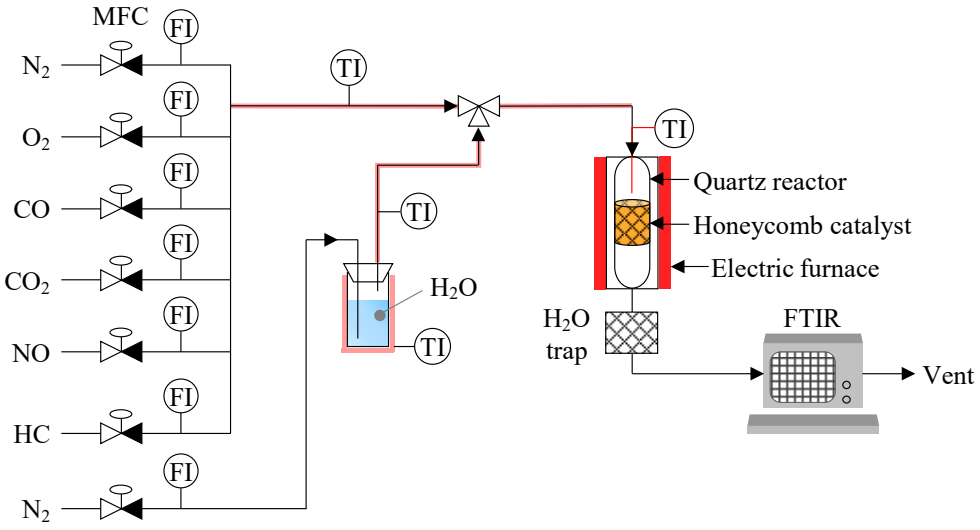

Figure 3.1 Experimental apparatus of laboratory-scale quartz reactor for evaluating catalytic reaction of HC-SCR process.

Table 3.1 Experimental conditions for evaluation of C_3H_6-SCR.

Parameters	C_3H_6–SCR reaction
Reductant	Propene (C_3H_6)
Nitrogen monoxide (NO)	500 ppm
Oxygen (O_2)	8 vol.%
Carbon monoxide (CO)	500 ppm
Carbon dioxide (CO_2)	10 vol.%
Water vapor (H_2O)	5 vol.%
Balance gas	N_2
Propene (C_3H_6)	500, 1000, 2000, and 4000 ppm C_1
HC/NOx ratio	1, 2, 4, and 8
Total flow rate	1.67 L/min
Temperature	150 – 600°C (5 °C/min ramp-up)
Gas hourly space velocity (GHSV)	12,500 h^{-1}

3.2 De-NOx performance of Cu/zeolite

3.2.1 De-NOx performance of Cu/SSZ-13

Figure 3.1 shows the de-NOx performance of the parent SSZ-13 and Cu/SSZ-13 for HC/NOx ratios between 1 to 8. All catalysts exhibited identical tendencies to increase NOx conversions, as did increasing the HC/NOx ratio. A higher HC/NOx could be achieved by increasing the HC/NOx ratio, because the NOx reduction was enhanced when more of the reducing agent was available. When HC/NOx = 8, the highest NOx conversion of 58.2% was observed for 1Cu/SSZ-13 at 420℃ (Figure 3.1(b)), whereas the parent SSZ-13 without copper loading showed the lowest NOx conversion of less than 32% at 510℃ (Figure 3.1(a)). The maximum NOx conversion ranged from 32% to 58%, in the following order: 1Cu/SSZ-13 (58.2% at T = 420℃) > 5Cu/SSZ-13 (51.7% at T = 420℃) > parent SSZ-13 (31.9% at T = 510℃). It is worth noting that the loading of Cu into the SSZ-13 zeolite highly improved the de-NOx performance, which implies that the Cu species impregnated to the SSZ-13 zeolite provide the active sites for reducing NOx.

3.2.2 De-NOx performance of Cu/ZSM-5

The effects of Cu loading and HC/NOx ratio on the temperature dependence of the de-NOx performance compared to that of the respective Cu/ZSM-5 catalysts are depicted in Figure 3.2. The NOx conversion of all the catalysts was highly dependent on the HC/NOx ratios. Among the Cu/ZSM-5 catalysts, 2Cu/ZSM-5 (Figure 3.2(c)) demonstrated the highest de-NOx performance at HC/NOx = 8, exhibiting 68.5% NOx conversion at 360℃, whereas the parent ZSM-5 without copper loading exhibited the lowest NOx conversion of less than 30% at 540℃ even at the highest HC/NOx ratio (Figure 3.2(a)). The loading of copper into

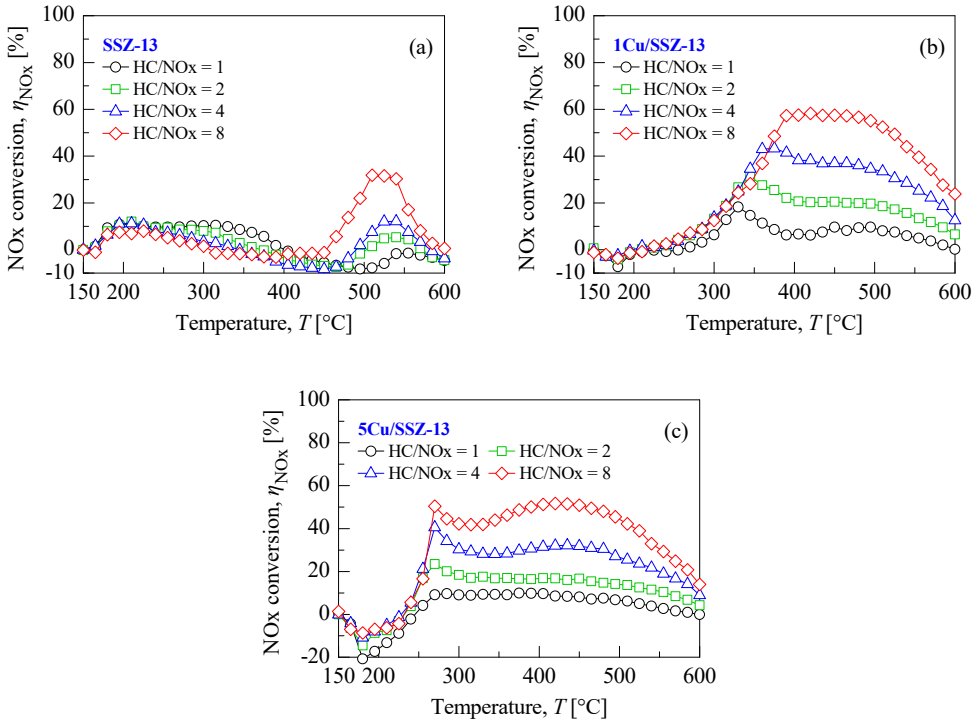

Figure 3.2 NOx conversion of Cu/SSZ-13 as a function of reaction temperature at HC/NOx ratios from 1 to 8: (a) parent SSZ-13, (b) 1Cu/SSZ-13, and (c) 5Cu/SSZ-13.

the ZSM-5 zeolite is beneficial for improving the catalytic activity for NOx reduction as well as shifting the temperature windows of maximum NOx conversion toward lower temperatures. The copper loading also considerably affected the de-NOx performance. The maximum NOx conversion ranged from 38% to 68%, in the following order: 2Cu/ZSM-5 (68.5% at T = 360°C) > 10Cu/ZSM-5 (61.9% at T = 345°C) > 5Cu/ZSM-5 (47% at T = 405°C) > 1Cu/ZSM-5 (38.2% at T = 465°C) > parent ZSM-5 (29.9% T = 540°C).

3.2.3 De-NOx performance of Cu/BETA

The de-NOx performance of Cu/BETA catalysts with different Cu loadings is

represented in Figure 3.3 for various HC/NOx ratios. It is seen that high NOx conversion was obtained for the catalyst with the highest Cu loading, which is the 10Cu/BETA catalyst, exhibiting 56.1% NOx conversion at 375℃ at HC/NOx = 8 (Figure 3.3(e)). The maximum NOx conversion gradually increased with an increase in the Cu loading in the following order: 10Cu/BETA (56.1% at T = 375℃) > 5Cu/BETA (48.2% at T = 420℃) > 2Cu/BETA (28% at T = 480℃) > 1Cu/BETA (15.2% at T = 495℃) > parent BETA (7.7% at T = 525℃). However, the parent BETA zeolite showed the lowest de-NOx performance of less than 8% (Figure 3.3(a)), which exhibited a similar trend to the parent SSZ-13 and ZSM-5 zeolite. The increase in Cu loading also shifted the temperature window of the de-NOx activity toward the low temperature region. When HC/NOx = 8, 10Cu/BETA showed a maximum de-NOx performance at 375℃, whereas the parent BETA showed a maximum de-NOx performance at 525℃. Therefore, the loading of Cu into BETA zeolites clearly improved the de-NOx performance at low temperatures because the Cu species acted as active sites for reduction of NOx over the Cu/BETA catalysts.

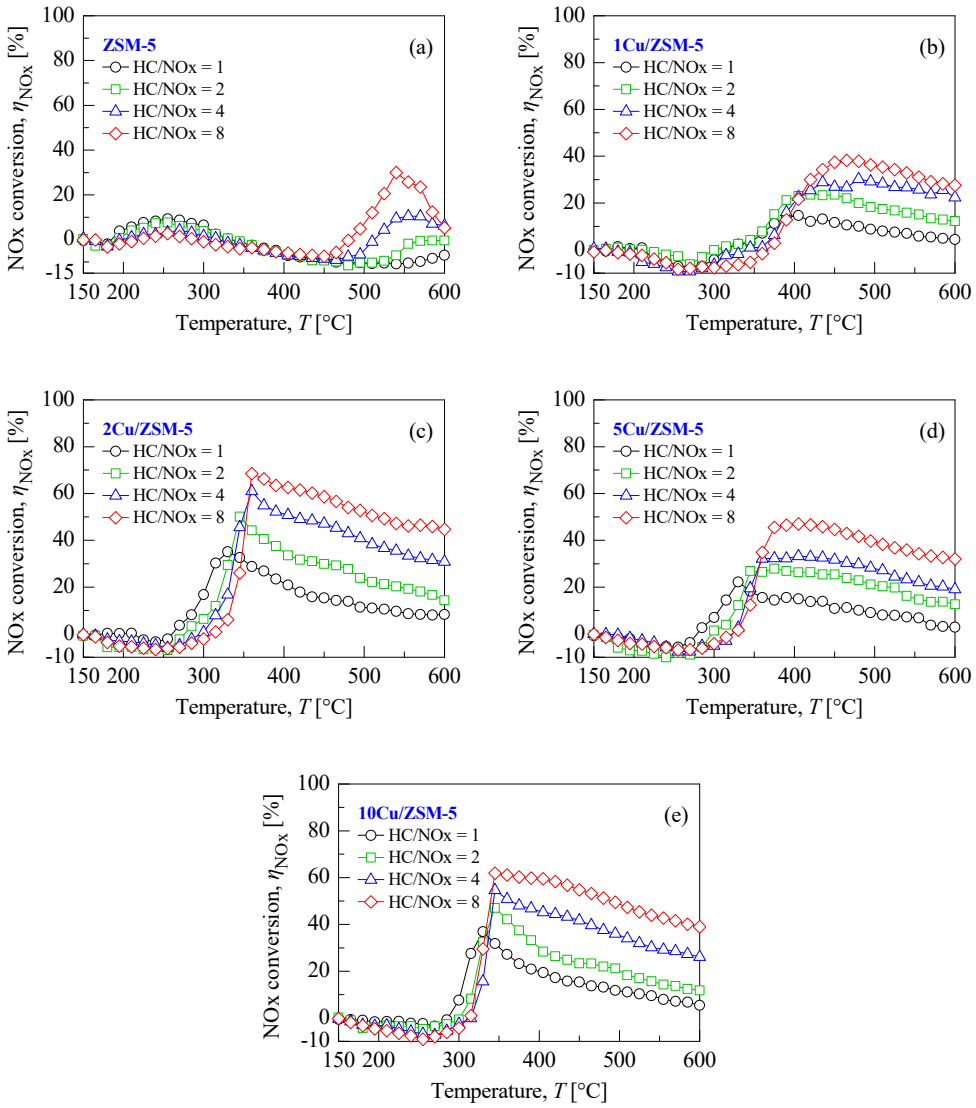

Figure 3.3 NOx conversion of Cu/ZSM-5 as a function of reaction temperature at HC/NOx ratios from 1 to 8: (a) parent ZSM-5, (b) 1Cu/ZSM-5, (c) 2Cu/ZSM-5, (d) 5Cu/ZSM-5, and (e) 10Cu/ZSM-5.

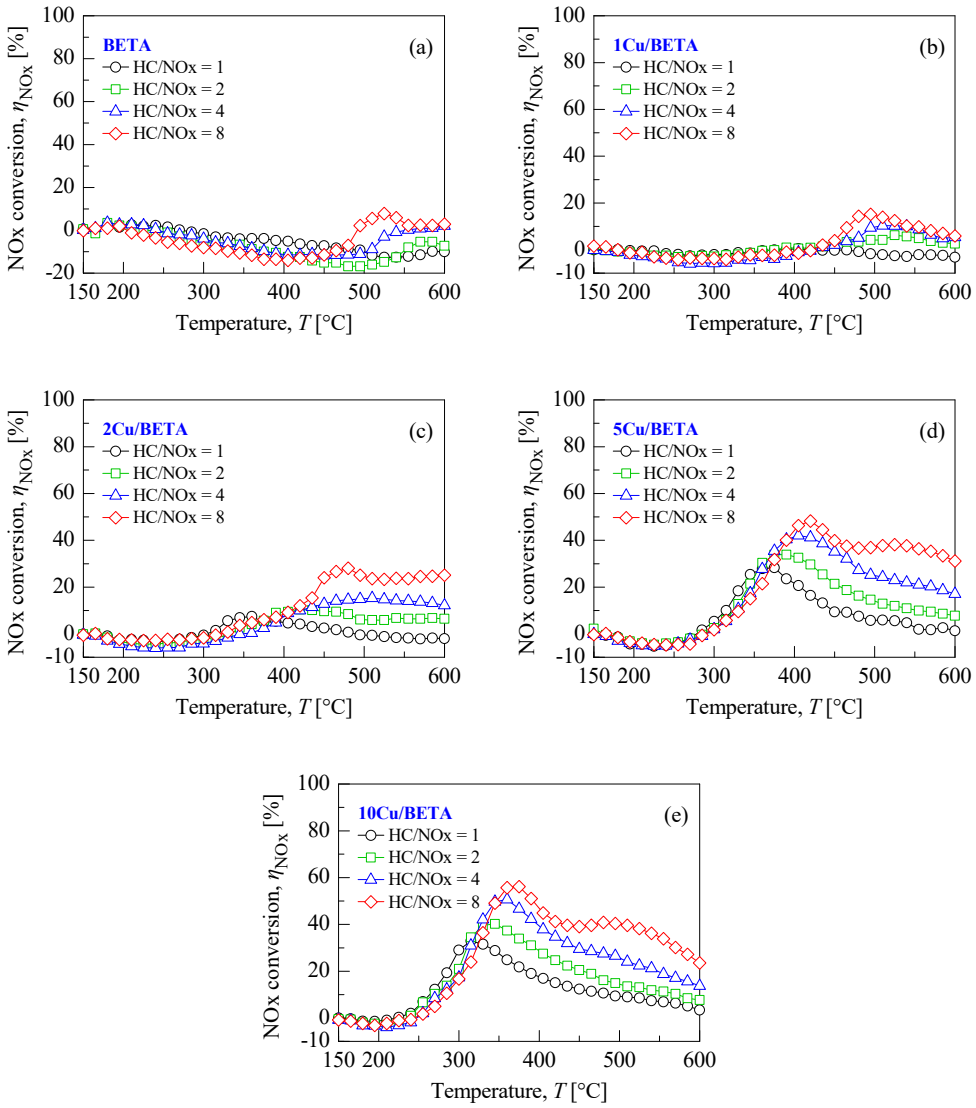

Figure 3.4 NOx conversion of Cu/BETA as a function of reaction temperature at HC/NOx ratios from 1 to 8: (a) parent BETA, (b) 1Cu/BETA, (c) 2Cu/BETA, (d) 5Cu/BETA, and (e) 10Cu/BETA.

3.3 C_3H_6 conversion of Cu/zeolite

The catalytic performance of the C_3H_6-SCR for de-NOx over all the Cu/zeolite catalysts was significantly dependent of the HC/NOx ratios, with a proportional relationship, because more of the reducing agent would be available for NOx reduction. Figure 3.5 shows the C_3H_6 conversion over the pure zeolites and Cu/zeolite catalysts during the SCR reaction with NOx at HC/NOx = 8. It is clear that increasing the Cu loading, where Cu is the active material for the C_3H_6-SCR, substantially enhanced the rate of C_3H_6 oxidation over all the tested Cu/zeolite catalysts. In addition, the higher Cu loading, the lower the light-off temperature (LOT_{50}) of C_3H_6 is. This was evident in the case of Cu/BETA, in which the LOT_{50} of C_3H_6 declined with an increase in the Cu loading in the following order (Figure 3.5(c)): 281℃ (10Cu/BETA) < 308℃ (5Cu/BETA) < 319℃ (2Cu/BETA) < 343℃ (1Cu/BETA) < 462℃ (parent BETA). In the case of the 5Cu/zeolite catalysts at HC/NOx = 8, the LOT_{50} values for C_3H_6 conversion over the 5Cu/SSZ-13 and 5Cu/BETA catalysts were 260℃ and 308℃, which are lower than that of 5Cu/ZSM-5 (LOT_{50} at 329℃). The LOT_{50} for C_3H_6 conversion by the Cu/SSZ-13 catalysts followed a trend similar to that of Cu/BETA and Cu/ZSM-5 at other HC/NOx ratios, as represented in Figures 3.6–3.8.

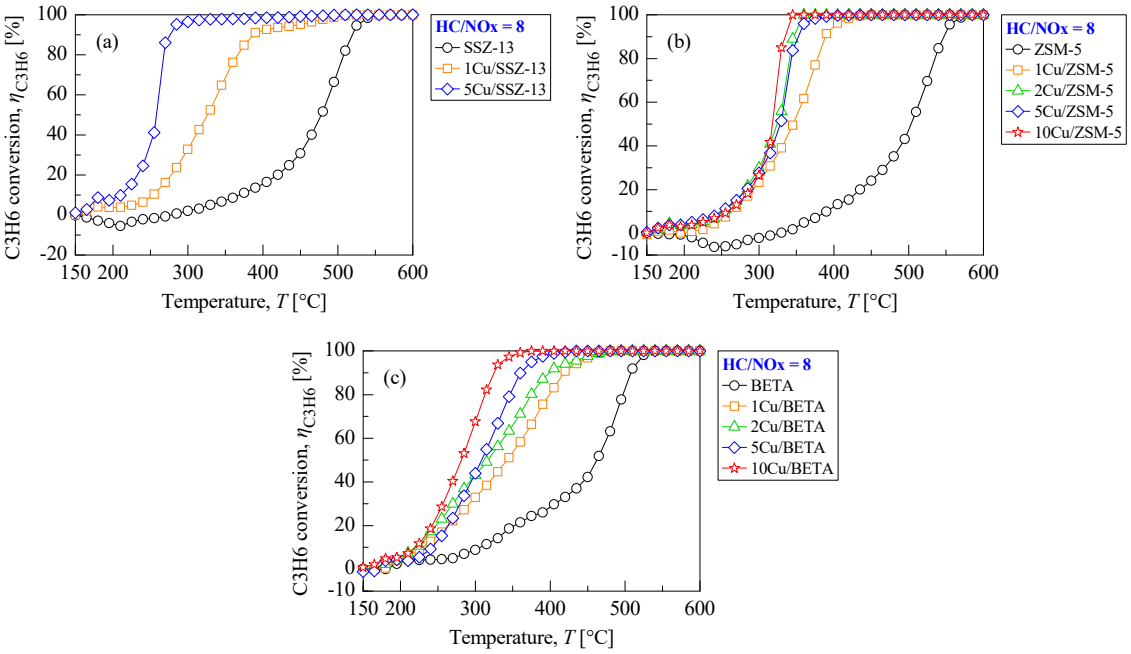

Figure 3.5 C_3H_6 conversion of parent zeolites and Cu/zeolite catalysts as a function of reaction temperature at HC/NOx = 8: (a) Cu/SSZ-13, (b) Cu/ZSM-5, and (c) Cu/BETA.

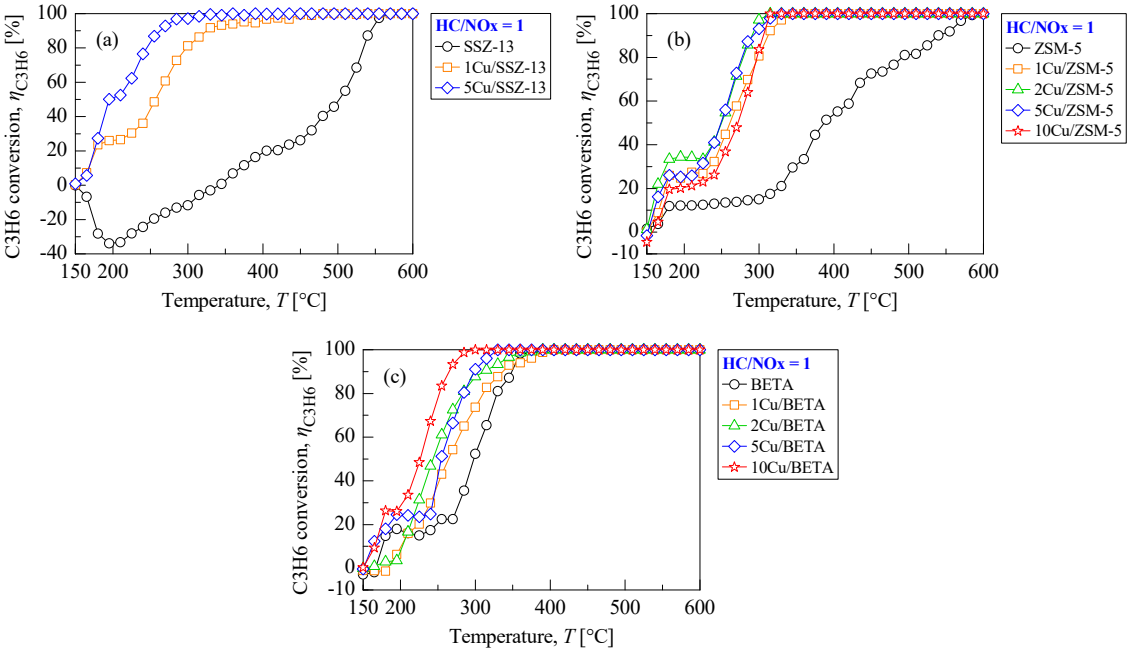

Figure 3.6 C_3H_6 conversion of parent zeolites and Cu/zeolite catalysts as a function of reaction temperature at HC/NOx = 1: (a) Cu/SSZ-13, (b) Cu/ZSM-5, and (c) Cu/BETA.

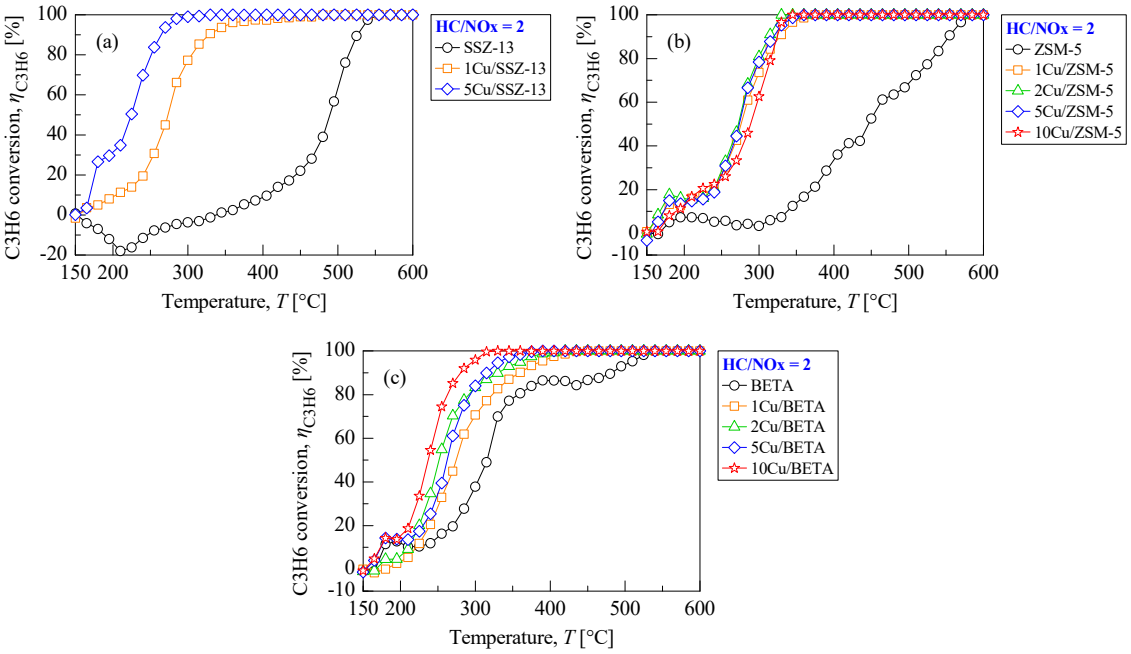

Figure 3.7 C_3H_6 conversion of parent zeolites and Cu/zeolite catalysts as a function of reaction temperature at HC/NOx = 2: (a) Cu/SSZ-13, (b) Cu/ZSM-5, and (c) Cu/BETA.

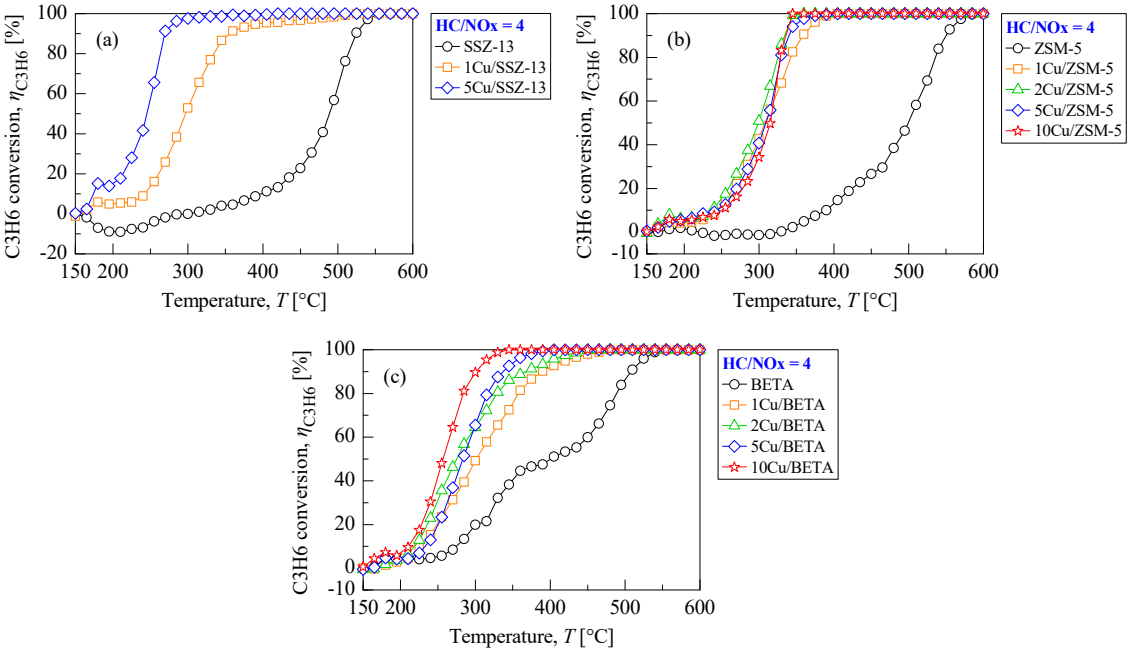

Figure 3.8 C_3H_6 conversion of parent zeolites and Cu/zeolite catalysts as a function of reaction temperature at HC/NOx = 4: (a) Cu/SSZ-13, (b) Cu/ZSM-5, and (c) Cu/BETA.

3.4 CO conversion of Cu/zeolite

During the C_3H_6-SCR process, 500 ppm of CO was simultaneously introduced in the feed gas. CO conversion was also investigated over all the parent zeolites and Cu/zeolite catalysts. As illustrated in Figure 3.9(a), it is found that the ZSM-5 zeolite could not oxidize CO into CO_2 because negative CO conversion was obtained with the evaluated temperature window, and more CO was produced with an increase in HC/NOx ratios. CO conversion gradually decreased with an increase in reaction temperature up to 570°C, when it began to increase. The CO conversion substantially decreased over the ZSM-5 zeolite from −134.3% at HC/NOx = 1 to −890.3% at HC/NOx = 8. CO conversion over the parent SSZ-13 and BETA zeolites also followed a trend similar to that of the ZSM-5 zeolite (Figures 3.10–3.12), indicating that the zeolite without Cu loading could not oxidize CO. Considering the possible reaction for CO formation, this is attributed to the partial oxidation reaction of C_3H_6 by O_2, as expressed in reaction (3.7)

$$NO + C_3H_6 + O_2 \rightarrow N_2 + CO + H_2O \quad (3.7)$$

Comparison of the CO conversion of the parent zeolites and Cu/zeolites at HC/NOx = 8 (Figure 3.9(b)–(d)) shows that increasing the Cu loading shifted the initial temperature of CO conversion to lower temperatures because the impregnated Cu species provided active sites for oxidation of CO to CO_2 over the Cu/zeolites: for example, 510°C (1Cu/BETA) > 495°C (2Cu/BETA) > 420°C (5Cu/BETA) > 360°C (10Cu/BETA). Furthermore, complete oxidation of CO was obtained at even lower temperatures with the highest Cu loadings in the following order: 5Cu/SSZ-13 (345°C) < 10Cu/ZSM-5 (405°C) < 10Cu/BETA (590°C). Among the three types of Cu/zeolite catalysts with the same Cu loading, 5Cu/SSZ-13 exhibited the best activity for CO oxidation compared to 5Cu/ZSM-5 and 5Cu/BETA. As illustrated in Figure 3.9, the

LOT_{50} of CO over the 5Cu/SSZ-13 was 274℃, which is far lower than that of 5Cu/ZSM-5 (513℃) and 5Cu/BETA (348℃). The sizes of the intra-crystalline channels of the zeolites and guest molecules affect the zeolite diffusivity, namely geometry-limited diffusion [215]. The pore-openings of SSZ-13 with extremely small pores are about 2.9–3.8 Å [213], and those of ZSM-5 with medium pores and BETA with large pores are about 5.1–5.6 Å [213] and 5.6–6.7 Å [213, 214], respectively. The kinetic diameter of the CO molecule is about 3.69 Å [216, 217]. Thus, the molecular size of CO is small enough to pass through the internal channels of the three zeolites. However, considering the accessibility of molecular CO to active sites in the zeolite, CO molecules have a relatively favorable proximity to the active sites in the SSZ-13 zeolite, and this zeolite exhibited higher CO conversion than that of the ZSM-5 and BETA zeolites.

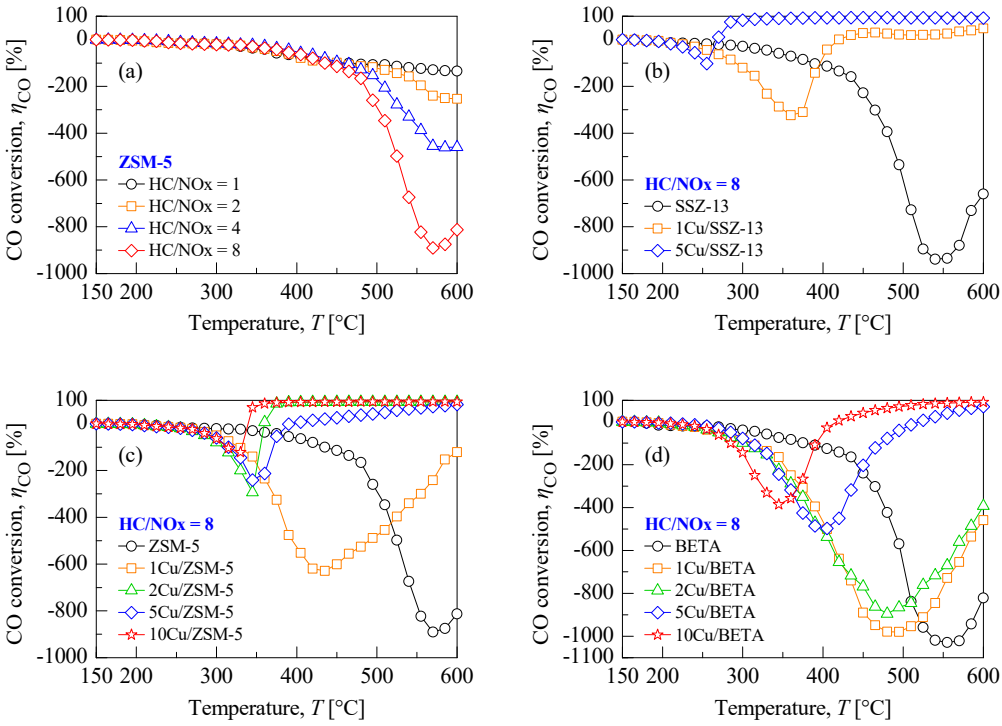

Figure 3.9 CO conversion of (a) parent ZSM-5 zeolite according to HC/NOx ratios from 1 to 8 and (b) Cu/SSZ-13, (c) Cu/ZSM-5, and (d) Cu/BETA at HC/NOx = 8 as a function of reaction temperature.

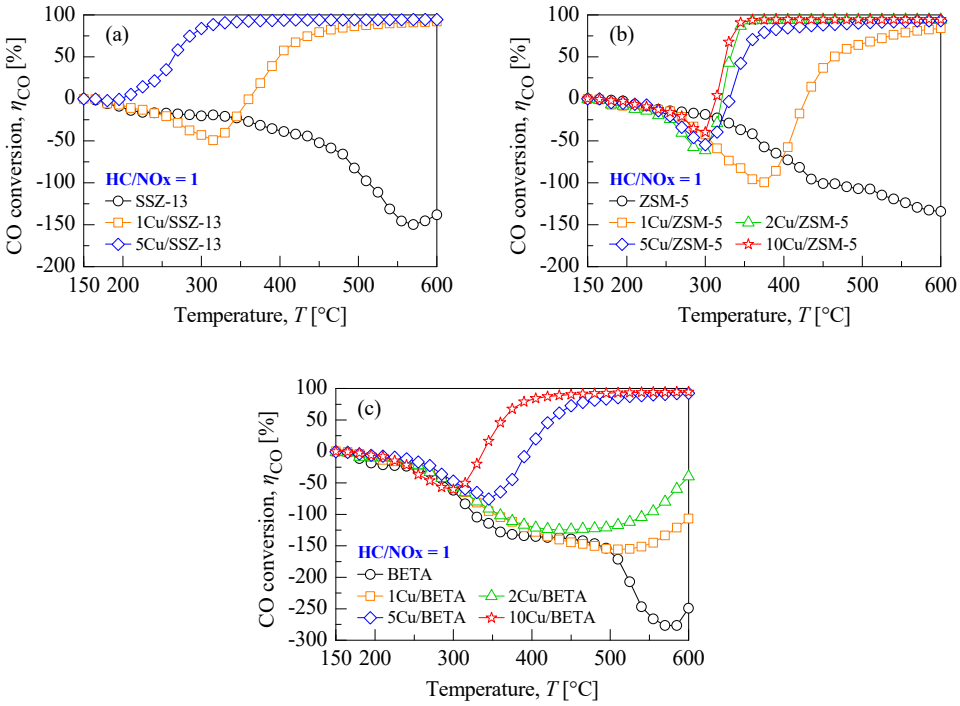

Figure 3.10 CO conversion of parent zeolites and Cu/zeolite catalysts as a function of reaction temperature at HC/NOx = 1: (a) Cu/SSZ-13, (b) Cu/ZSM-5, and (c) Cu/BETA.

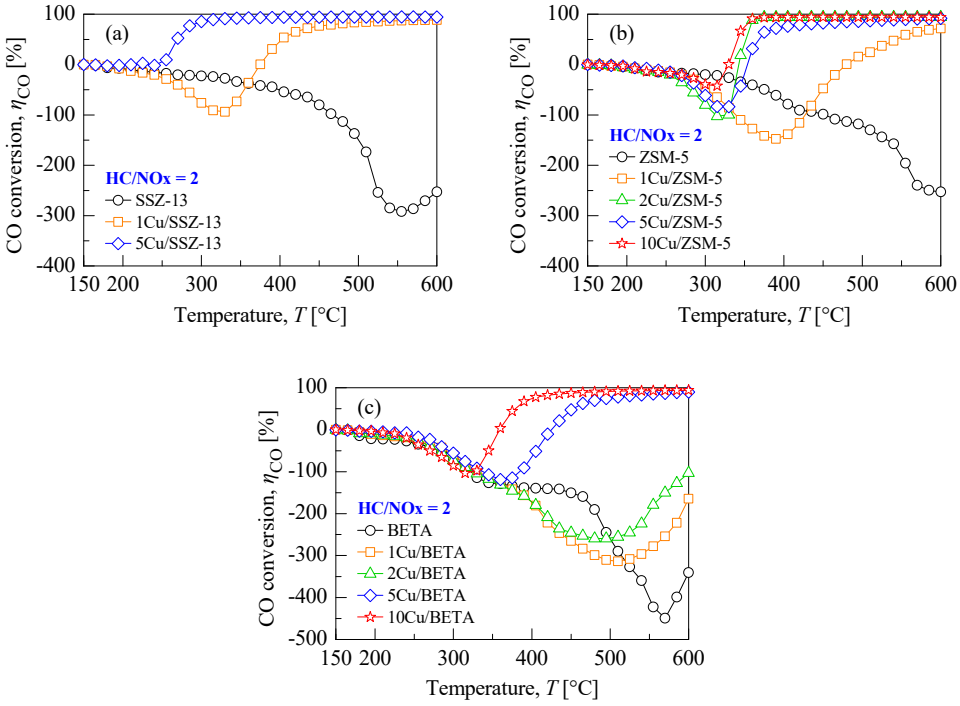

Figure 3.11 CO conversion of parent zeolites and Cu/zeolite catalysts as a function of reaction temperature at HC/NOx = 2: (a) Cu/SSZ-13, (b) Cu/ZSM-5, and (c) Cu/BETA.

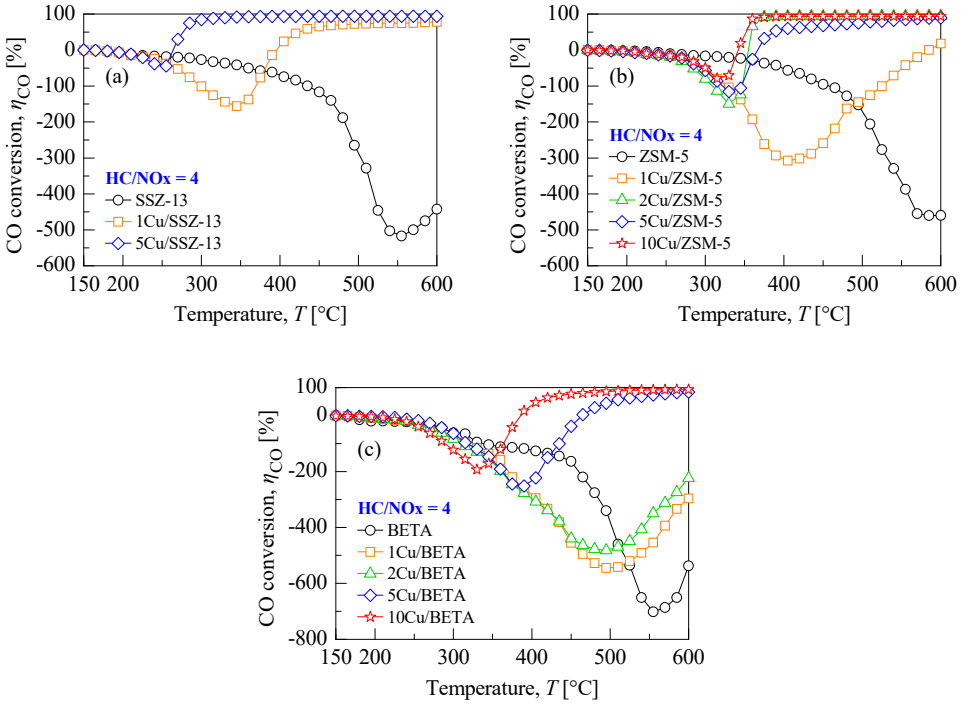

Figure 3.12 CO conversion of parent zeolites and Cu/zeolite catalysts as a function of reaction temperature at HC/NOx = 4: (a) Cu/SSZ-13, (b) Cu/ZSM-5, and (c) Cu/BETA.

3.5 Temperature programmed oxidation of C_3H_6

The formation of CO during the C_3H_6-SCR reaction was observed, and the parent zeolites could not oxidize CO simultaneously supplied in the feed stream. Considering the C_3H_6-SCR reaction, the hydrocarbon reductant participates in NOx reduction as well as in the partial oxidation with coexistent O_2. The temperature programmed oxidation (TPO) of C_3H_6 by O_2 was carried out to evaluate the catalytic oxidation ability of parent zeolites and Cu/zeolites. CO formation was attributed to the incomplete oxidation of C_3H_6 by O_2 to generate CO rather than CO_2, as illustrated in Figure 3.13. Comparison of the CO formation over the parent zeolites and Cu/zeolites shows that CO formation was the predominant reaction over the parent zeolites. The findings of TPO experiments indicate that the hydrocarbon reductant was oxidized by O_2 to CO and CO_2, as expressed below in the reactions (3.8) and (3.9). The parent zeolites followed the reaction (3.8), whereas the Cu/zeolite catalysts followed the reaction (3.9) because C_3H_6 was oxidize to more CO_2 than CO over the Cu/zeolites. The loading of Cu also enhanced the rate of partial oxidation of C_3H_6 during the C_3H_6-TPO: for example, 2Cu/ZSM-5 completely oxidized C_3H_6 at 465°C (Figure 3.13(d)), however, the ZSM-5 zeolite without Cu loading could not completely oxidize C_3H_6 even at high temperature region (Figure 3.13(c)). From the C_3H_6-TPO experiments, the CO over COx ratios are compared, as illustrated in Figure 3.14. It is clear that all the Cu/zeolites could oxidize C_3H_6 to less CO compared to the parent zeolites.

$$C_3H_6 + 3O_2 \rightarrow 3CO + 3H_2O \quad (3.8)$$

$$C_3H_6 + 4.5O_2 \rightarrow 3CO_2 + 3H_2O \quad (3.9)$$

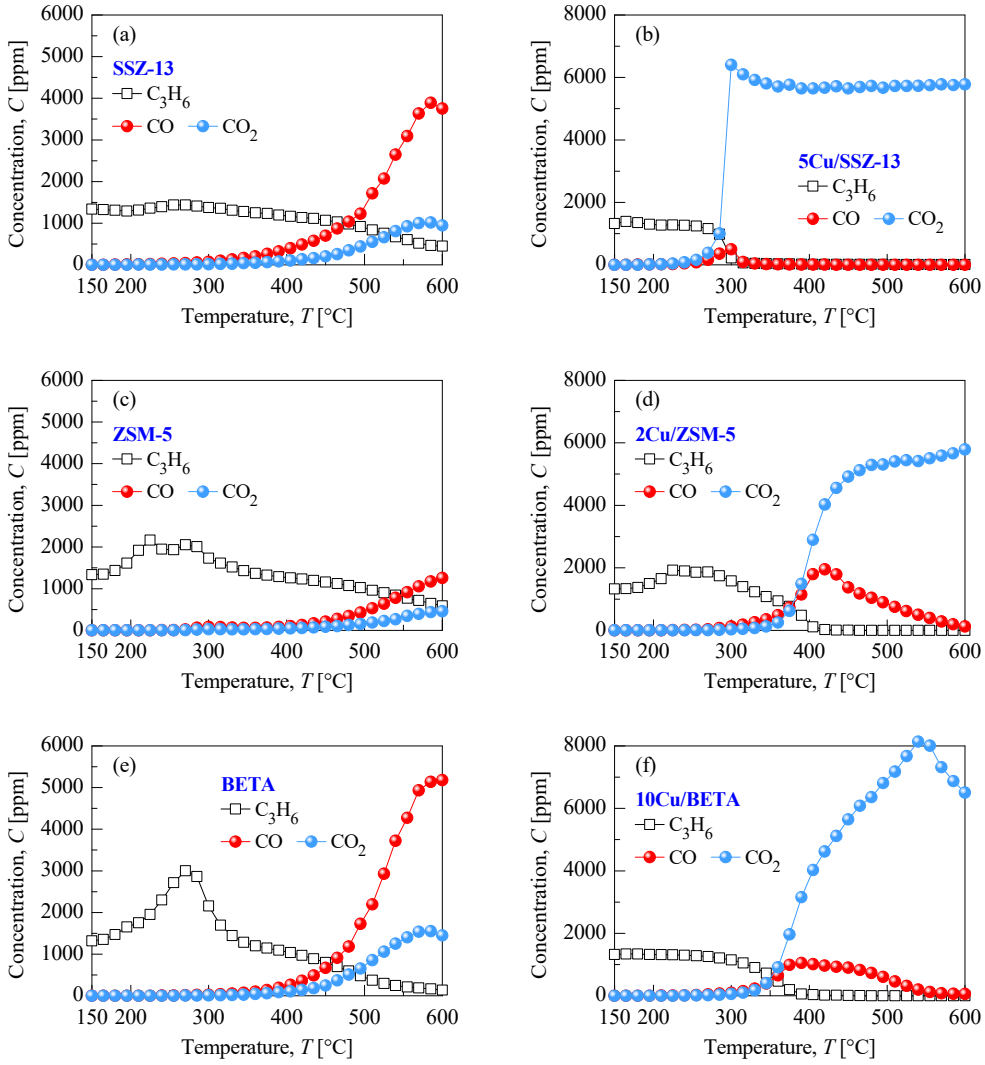

Figure 3.13 Temperature programmed oxidation (TPO) of C_3H_6 by O_2 over the parent zeolites and Cu/zeolite catalysts (TPO experiment: 4,000 ppm C_1 C_3H_6 + 8 vol.% O_2 + balance N_2 at GHSV = 12,500 h^{-1}).

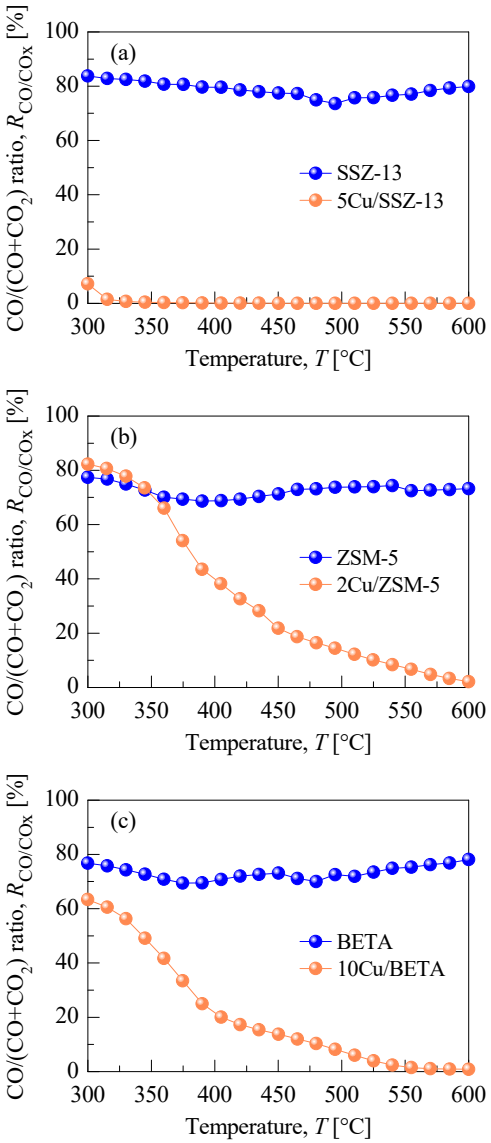

Figure 3.14 CO over COx ratios after oxidation of C_3H_6 by O_2 over the parent zeolites and Cu/zeolite catalysts: (a) SSZ-13 zeolite, (b) ZSM-5 zeolite, and (c) BETA zeolite.

3.6 N_2 yield of Cu/zeolite

One of the major drawbacks of some of the HC-SCR catalysts is the formation of undesired by-products, such as ammonia (NH_3), acetonitrile (CH_3CN), hydrogen cyanide (HCN), and nitrous oxide (N_2O) [124, 169]. Thus, it is important to investigate the feasibility for HC-SCR, particularly from a viewpoint of the range of products that are produced during the HC-SCR process.

During the C_3H_6-SCR reaction over the Cu/zeolite catalysts, N_2 yields was examined by monitoring the possible by-products including nitrogen-containing species that are nitrous oxide (N_2O), isocyanic acid (HNCO), and ammonia (NH_3). Figure 3.15 shows the comparison of N_2 yield and NOx conversion over all the tested Cu/zeolite catalysts at HC/NOx = 8. The N_2 yield was consistent with the NOx conversion, implying that NOx was reduced to N_2 by C_3H_6 without any accompanying side-reactions. Therefore, all the prepared Cu/zeolite catalysts could reduce NOx to N_2 via the ideal HC-SCR reaction, as expressed in reaction (3.10).

$$2NO + 3.5O_2 + C_3H_6 \rightarrow N_2 + 3CO_2 + 3H_2O \qquad (3.10)$$

The NOx conversion and N_2 yield showed similar trends at other HC/NOx ratios, as illustrated in Figures 3.16–3.18. Although N_2 yield decreased at HC/NOx ratios of less than 8 due to a decrease in C_3H_6 available for NOx reduction, N_2 yield followed the NOx conversion without producing any undesired by-products at all tested reaction temperatures. Thus, it can be concluded that the Cu/zeolite catalysts can reduce NOx to N_2 via the ideal C_3H_6-SCR reaction without accompanying any side-reactions.

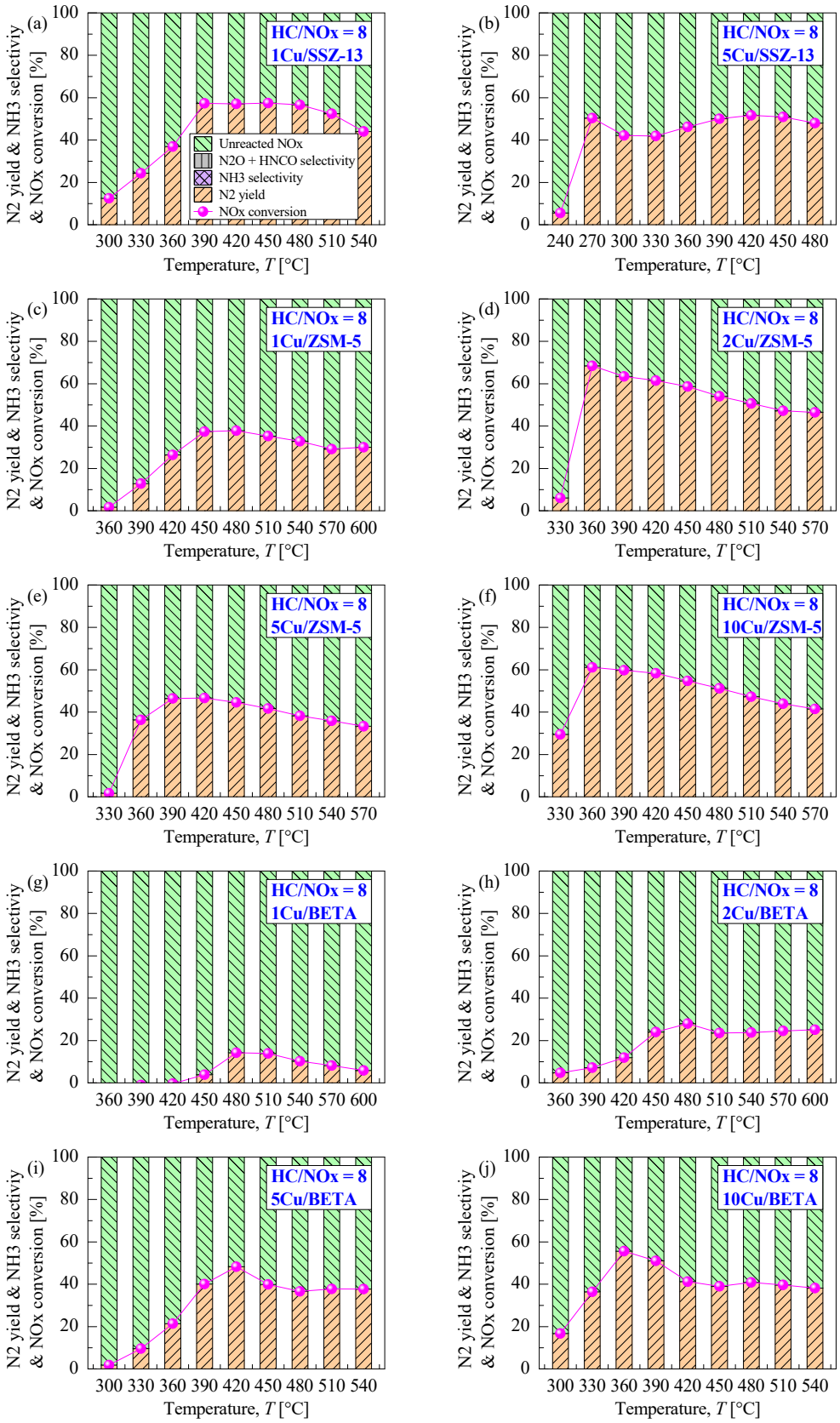

Figure 3.15 Comparison of reaction products after C_3H_6-SCR reaction at HC/NOx = 8.

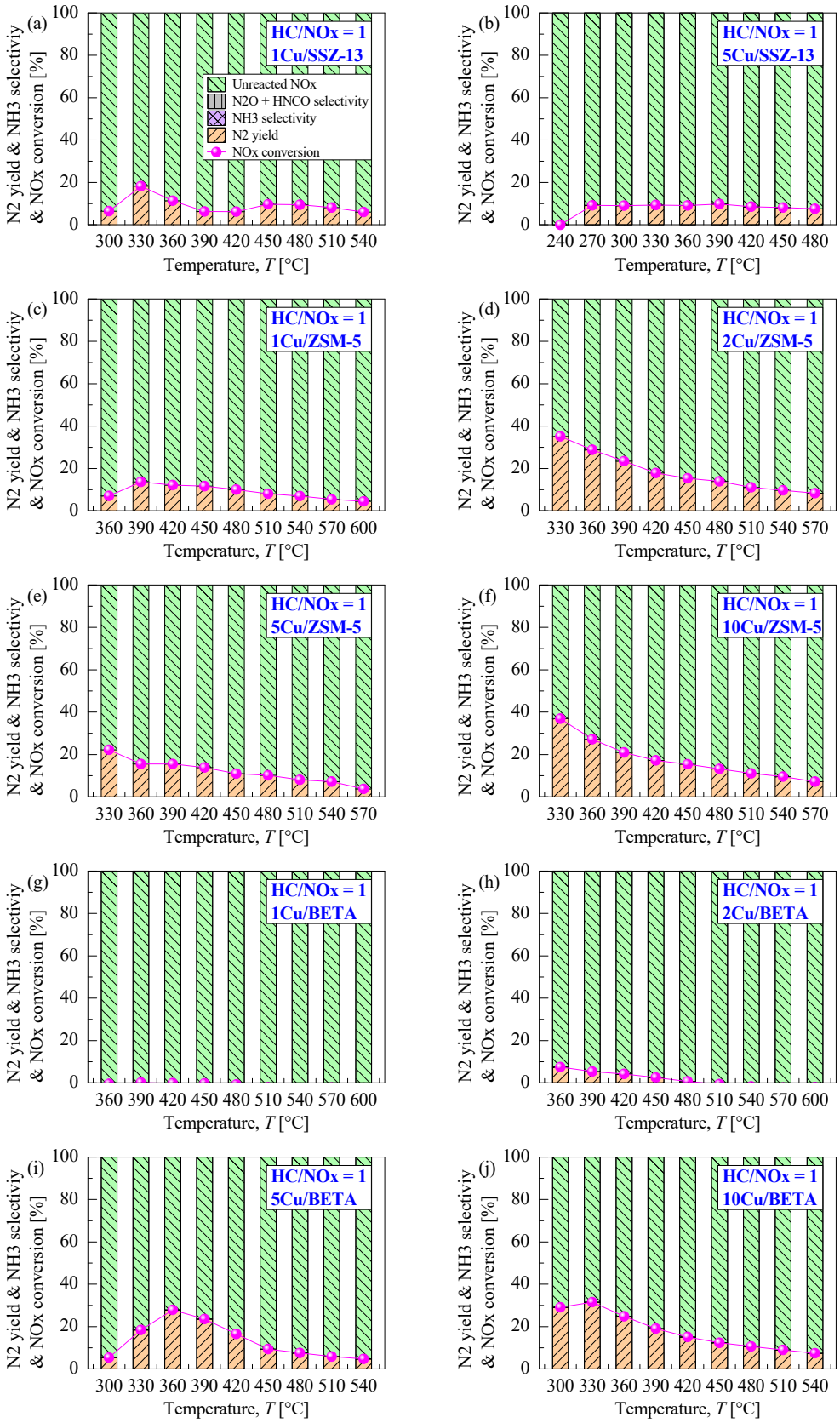

Figure 3.16 Comparison of reaction products after C_3H_6-SCR reaction at HC/NOx = 1.

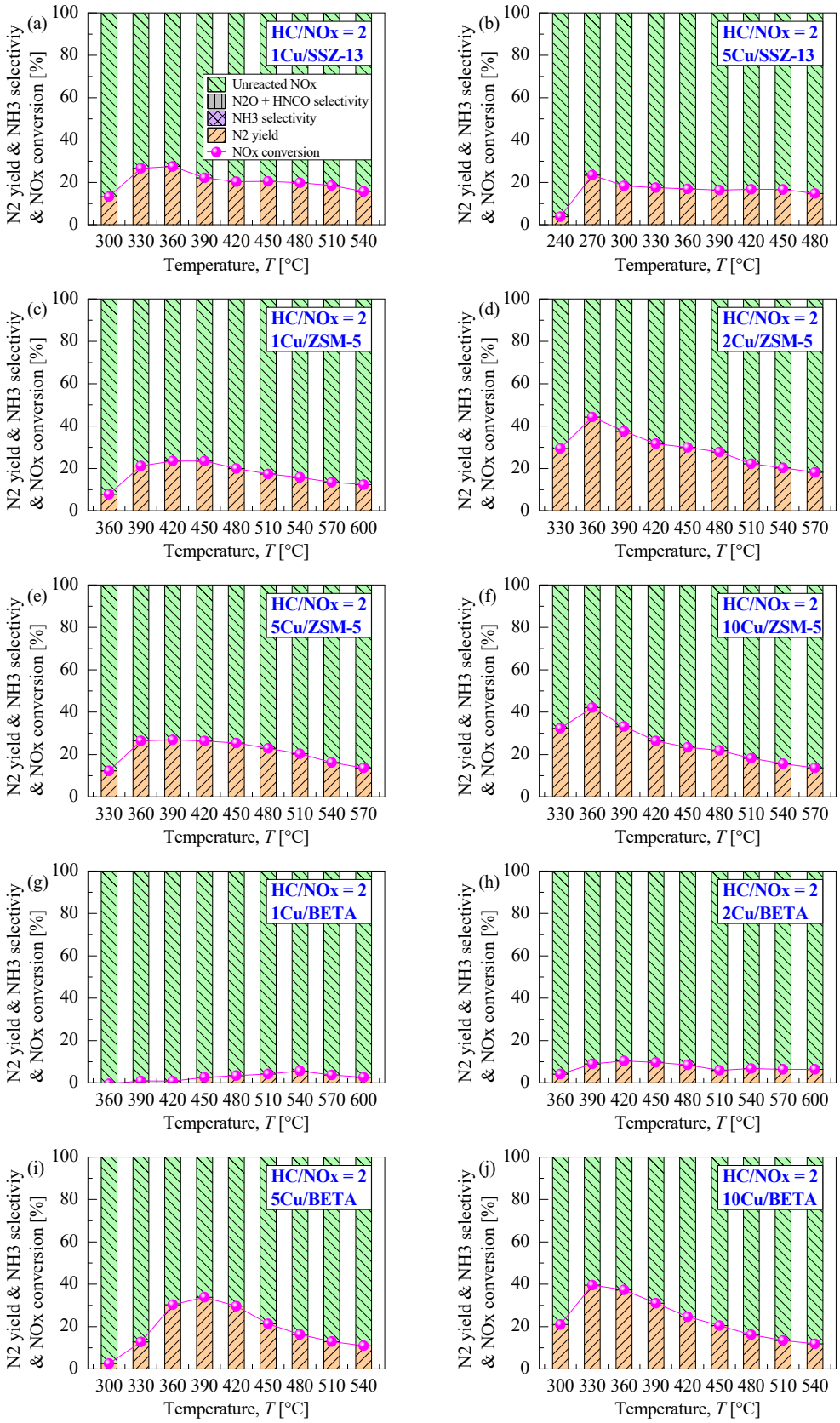

Figure 3.17 Comparison of reaction products after C_3H_6-SCR reaction at HC/NOx = 2.

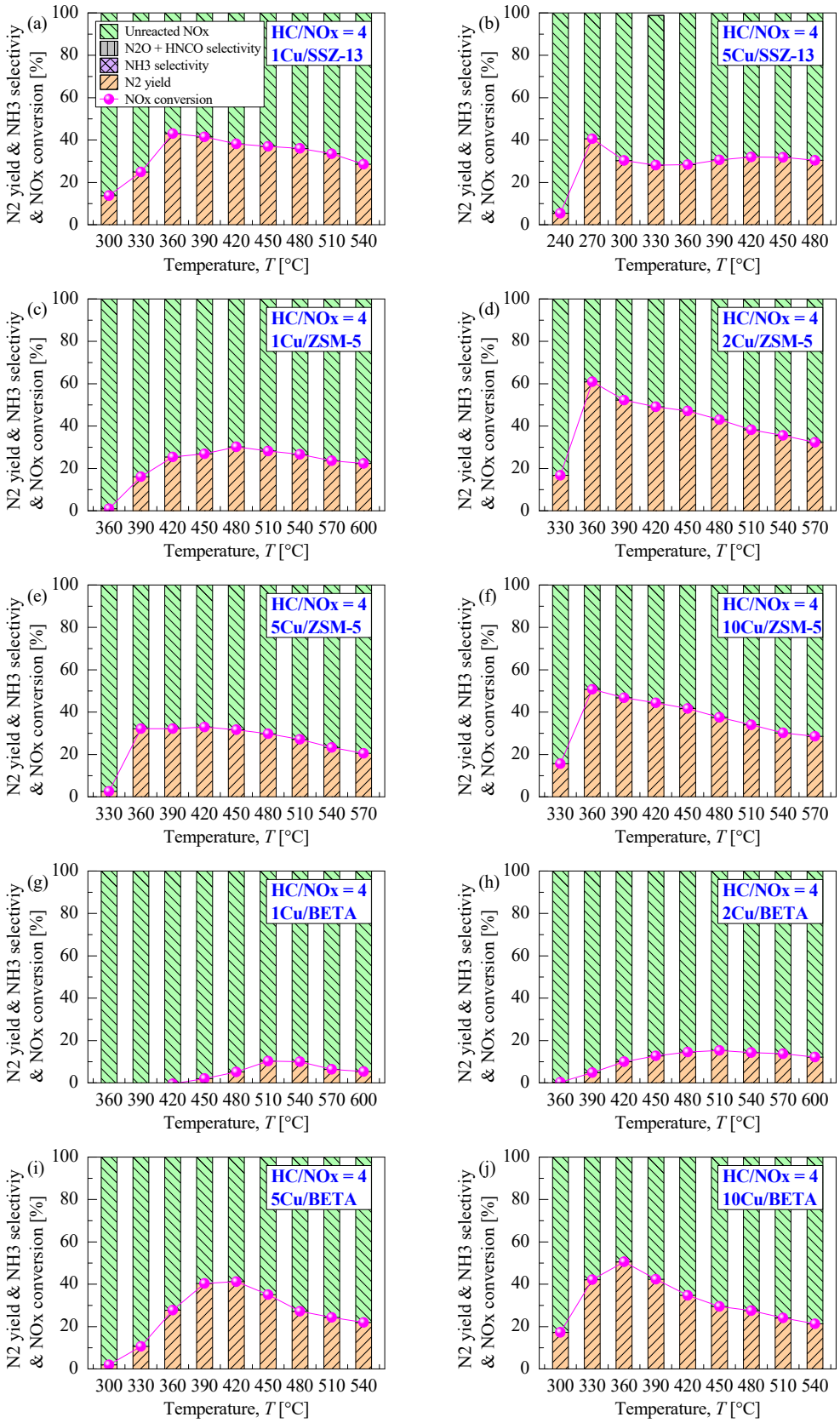

Figure 3.18 Comparison of reaction products after C_3H_6-SCR reaction at HC/NOx = 4.

3.7 Summary

In the work presented in Chapter 3, a series of Cu/zeolite catalysts has been investigated for the C_3H_6-SCR in the presence of O_2, CO, CO_2, and H_2O. The de-NOx performances of Cu/zeolites were substantially affected by the zeolite framework as well as the Cu loading. The introduction of Cu into the parent zeolites improved the NOx conversion and shifted the temperature window to lower temperatures compared to those for the parent zeolites. To achieve a high NOx conversion, a high HC/NOx ratio was needed. Increasing the HC/NOx ratio was favorable for the catalytic activity because more reducing agent could participate in HC-SCR reaction with NOx during the partial oxidation of C_3H_6. Among the prepared Cu/zeolite catalysts, 2Cu/ZSM-5 demonstrated the highest conversion of NOx to N_2 (68.5% at T = 360°C) at the highest HC/NOx ratio, followed by 1Cu/SSZ-13 (58.2% at T = 420°C) and 10Cu/BETA (56.1% at T = 375°C). Thus, the ZSM-5 zeolite, with a medium pore framework, was better suited for the C_3H_6-SCR process than SSZ-13, with a small pore framework, and BETA, with a large pore framework. The catalytic performance of the C_3H_6-SCR for de-NOx over all the Cu/zeolite catalysts was significantly dependent of the HC/NOx ratios, with a proportional relationship, because more of the reducing agent would be available for NOx reduction. Increasing the Cu loading highly enhanced the rate of C_3H_6 oxidation over all the tested Cu/zeolite catalysts. In addition, the higher Cu loading, the lower the light-off temperature (LOT_{50}) of C_3H_6 was. The parent zeolites without Cu loading could not oxidize CO into CO_2 because negative CO conversion was obtained with the evaluated temperature window, and more CO was produced with an increase in HC/NOx ratios. Increasing the Cu loading shifted the initial temperature of CO oxidation to lower temperatures because the impregnated Cu species provided active sites for oxidation of CO to CO_2 over the Cu/zeolites.

Chapter 4. Catalytic Performance of C_4H_{10}-SCR

4.1 Experimental conditions for evaluation of C_4H_{10}-SCR

In this chapter, the selective catalytic reduction of NOx by *n*-butane (*n*-C_4H_{10}) over the copper-impregnated zeolites with different zeolite frameworks is evaluated to identify the optimal Cu/zeolite catalysts. The reducing agent, *n*-C_4H_{10}, has rarely been studied in the field of HC-SCR; thus, evaluating the catalytic performance of Cu/zeolite for C_4H_{10}-SCR is of great importance for furthering the commercial application of Cu-based zeolite catalysts for HC-SCR. The Cu-loaded catalysts supported on (1) small-pore 8-ring SSZ-13 (chabazite framework, Cu/SSZ-13), (2) medium-pore 10-ring ZSM-5 (MFI framework, Cu/ZSM-5), and (3) large-pore 12-ring BETA (BEA framework, Cu/BETA) are prepared with varying Cu loadings from 1 to 10 wt%, as described in Chapter 2. The effect of the C_4H_{10}/NOx ratios on the de-NOx performance is investigated. Table 4.1 summarizes the experimental conditions for evaluation of the C_4H_{10}-SCR, which is tested using a vertically fixed flow reactor at atmospheric pressure, as shown in Figure 3.1. The NOx conversion (η_{NOx}), C_4H_{10} conversion (η_{C4H10}), CO conversion (η_{CO}), and N_2 yield (S_{N2}) were respectively calculated by applying the equations (Eq. (3.1), (3.3), (3.4), and (3.5)), as illustrated in Chapter 3.

The temperature programmed oxidation of C_4H_{10} (C_4H_{10}-TPO) was carried out to investigate the rate of C_4H_{10} oxidation and reaction products at a range of 150–600°C, as summarized in Table 4.2. The adsorption capacity of NO and NO_2 was calculated by the equation (4.1): F_{gas} is a total flow rate of supplied gas (L/min), $V_{ideal\ gas}$ is the molar volume of ideal gas at 150°C (L/mol), and t_{sat} is the exposure time (min). The NOx adsorption capacity was tested with 500 ppm NO + 8 vol.% O_2 + N_2 in a total flow rate of 1.5 L/min for 60 min.

$$\text{Adsorption capacity } (AC_{NOx}) = \frac{F_{gas} \times \left(\frac{\int_{t_0}^{t_{sat}} \left(C_{NO}^{in} - C_{NO}^{out} \right)}{V_{ideal\ gas} } \right) \times t_{sat}}{V_{Monolith}} \text{ [mmol/L]} \quad (4.1)$$

Table 4.1 Experimental conditions for evaluation of C_4H_{10}-SCR.

Parameters	C_3H_6–SCR reaction
Reductant	*n*-Butane (*n*-C_4H_{10})
Nitrogen monoxide (NO)	300 ppm
Oxygen (O_2)	8 vol.%
Carbon monoxide (CO)	500 ppm
Carbon dioxide (CO_2)	10 vol.%
Water vapor (H_2O)	5 vol.%
Balance gas	N_2
n-Butane (*n*-C_4H_{10})	300, 600, 1,200, and 1,800 ppm C_1
HC/NOx ratio	1, 2, 4, and 6
Total flow rate	1.67 L/min
Temperature	150 – 600℃ (5 ℃/min ramp-up)
Gas hourly space velocity (GHSV)	12,500 h^{-1}

Table 4.2 Experimental conditions for temperature programmed oxidation of C_4H_{10}.

Parameters	C_4H_{10}–TPO
n-Butane (*n*-C_4H_{10})	1,800 ppm C_1
Oxygen (O_2)	8 vol.%
Balance gas	N_2
Total flow rate	1.67 L/min
Temperature	150 – 600℃ (5 ℃/min ramp-up)
Gas hourly space velocity (GHSV)	12,500 h^{-1}

4.2 De-NOx performance of Cu/zeolite

4.2.1 De-NOx performance of Cu/SSZ-13

The effects of the Cu loading and HC/NOx ratio on the reaction temperature-dependence of NOx conversion over the parent SSZ-13 without Cu, 1Cu/SSZ-13, and 5Cu/SSZ-13 are compared in Figure 4.1. The parent SSZ-13 zeolite could hardly reduce NOx at ratios less than HC/NOx = 2, and the maximum NOx conversion improved slightly from 9% at 600℃ to 35% at 435℃ with an increase in the HC/NOx ratio from 1 to 6. Notably, the addition of Cu to SSZ-13 zeolite resulted in lower NOx conversion than that of parent SSZ-13. The NOx conversion of Cu/SSZ-13 was negative at reaction temperatures below 400℃, despite an increase in the HC/NOx ratio, where the NOx conversion was 0.9% (parent SSZ-13), −15.2% (1Cu/SSZ-13), and −56% (5Cu/SSZ-13) at 255℃ and HC/NOx = 6. These findings indicate that a higher Cu loading over the parent SSZ-13 could not reduce NOx at temperature below 400℃. It is reasonable to assume that the negative NOx conversion may be attributed to desorbed NOx over the Cu/SSZ-13 catalysts, where the incorporation of Cu enhances the adsorption of NO; thus, more NOx could be desorbed. The temperature programmed desorption of NOx (NOx-TPD) was carried out to make logical sense whether Cu loading improves the adsorption capacity of NOx, and NOx-TPD will be further discussed in the next section.

4.2.2 De-NOx performance of Cu/ZSM-5

Figure 4.2 shows the de-NOx performance of the parent ZSM-5 zeolite and Cu/ZSM-5 catalysts with various Cu loadings for C_4H_{10}-SCR at HC/NOx ratios between 1 and 6. All catalysts exhibited similar ability to enhance the NOx conversion, as did increasing the

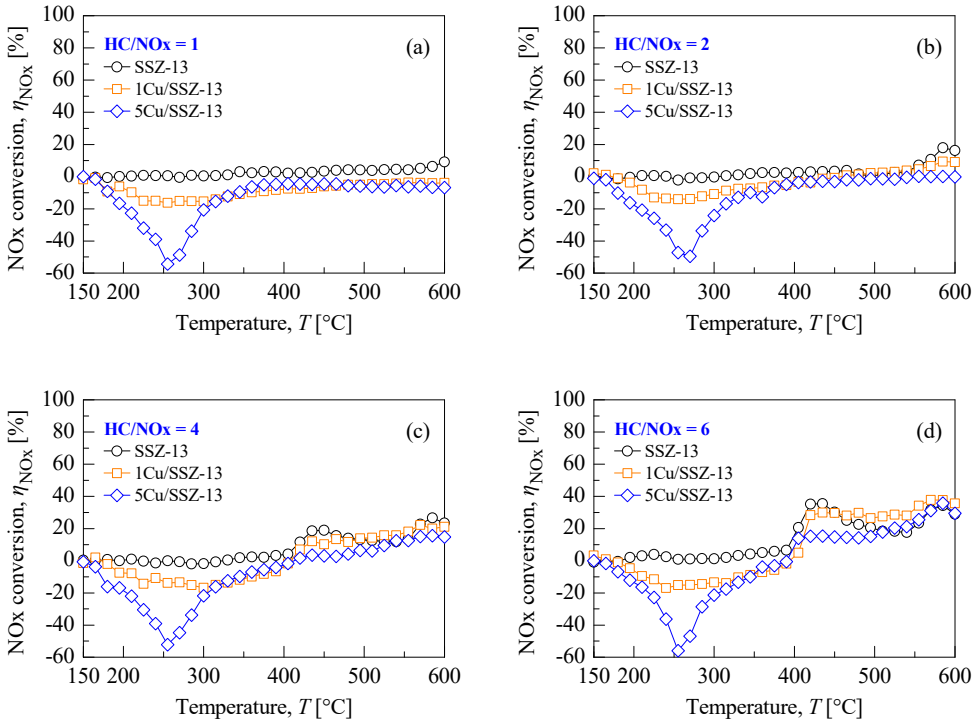

Figure 4.1 NOx conversion of parent SSZ-13 zeolite and Cu/SSZ-13 in SCR with C_4H_{10} as a function of reaction temperature at (a) HC/NOx = 1, (b) HC/NOx = 2, (c) HC/NOx = 4, and (d) HC/NOx = 6.

HC/NOx ratio. The parent ZSM-5 zeolite without Cu loading was inactive for NOx reduction at HC/NOx ratios less than 2, similar to SSZ-13; whereas, the NOx conversion increased from −5.5% (HC/NOx = 1) to 25.3% (HC/NOx = 6) at 465°C. The impregnation of Cu into ZSM-5 and increasing the HC/NOx ratio were substantially beneficial for NOx reduction, resulting in an increase in the NOx conversion compared to that achieved with pure ZSM-5. All Cu/ZSM-5 catalysts exhibited negative NOx conversion, similar to that of Cu/SSZ-13: for example, the NOx conversion was −14.2% (1Cu/ZSM-5), −21% (2Cu/ZSM-5), −16.4% (5Cu/ZSM-5), and −26% (10Cu/ZSM-5) for HC/NOx = 6 in the range of 285–300°C because the adsorbed NOx was desorbed from the catalysts rather than reduced. Among the Cu/ZSM-5 catalysts, 2Cu/ZSM-5 showed the highest catalytic activity for NOx reduction, exhibiting

73.6% of the maximum NOx conversion at 450–465℃ and HC/NOx = 6, whereas 1Cu/ZSM-5 showed the lowest NOx conversion of less than 43.5% at 465℃, followed by 5Cu/ZSM-5 (63.4%) and 10Cu/ZSM-5 (68.8%). In comparison with the parent ZSM-5 zeolite, loading Cu into ZSM-5 obviously improved the NOx conversion, indicating that the impregnated Cu species acted as primary active sites for reduction of NOx over the Cu/ZSM-5 catalysts.

4.2.3 De-NOx performance of Cu/BETA

The effects of the Cu loading and HC/NOx ratio on the de-NOx performance over the parent BETA zeolite without Cu loading and Cu/BETA catalysts as a function of the reaction temperature are shown in Figure 4.3. It is clear that the Cu/BETA catalyst with the highest Cu loading (10Cu/BETA) exhibited the best de-NOx performance, showing 58.4% of NOx conversion at 465℃ and HC/NOx = 6. The highest de-NOx performance of the parent BETA and Cu/BETA catalysts was achieved in the following order: 58.4% (10Cu/BETA) > 49.2% (5Cu/BETA) > 33.5% (parent BETA) > 29.3% (2Cu/BETA) > 25% (1Cu/BETA). The 5Cu/BETA and 10Cu/BETA catalysts showed the maximum de-NOx performance within the temperature window of 450–465℃, whereas the 1Cu/BETA and 2Cu/BETA catalysts showed optimal performance at higher temperature regions ranging from 585 to 600℃. Moreover, the Cu/BETA catalysts with Cu loadings of less than 2 wt% exhibited even lower NOx conversion than that of the parent BETA zeolite at all the experimental conditions, except at reaction temperatures above 525℃ when HC/NOx = 6. Therefore, the loading of Cu into BETA zeolite was beneficial for NOx reduction under specific conditions, i.e., Cu loadings exceeding 5 wt% and higher HC/NOx ratios.

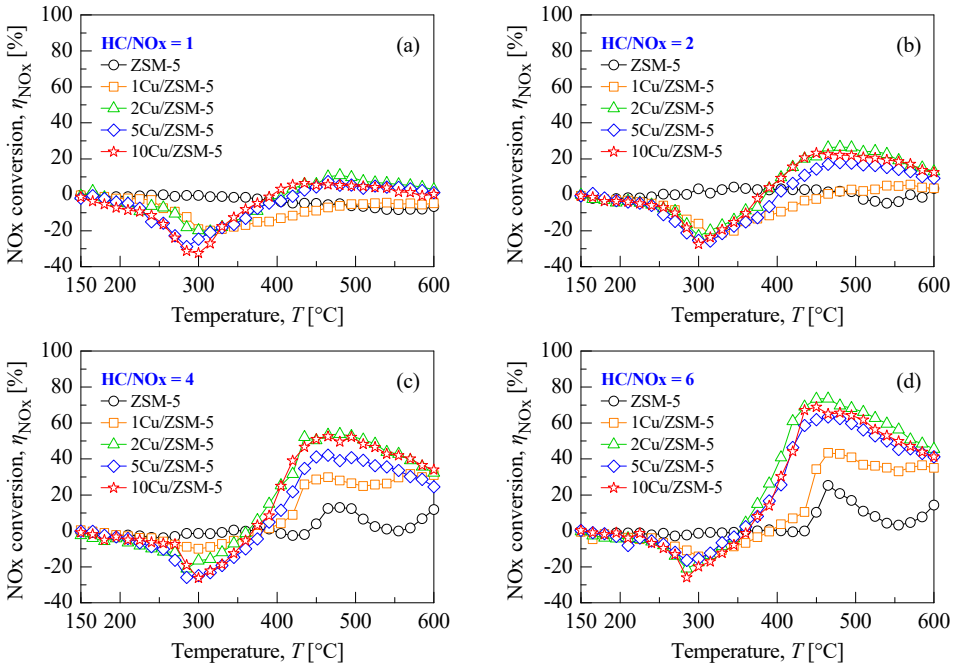

Figure 4.2 NOx conversion of parent ZSM-5 zeolite and Cu/ZSM-5 in SCR with C_4H_{10} as a function of reaction temperature at (a) HC/NOx = 1, (b) HC/NOx = 2, (c) HC/NOx = 4, and (d) HC/NOx = 6.

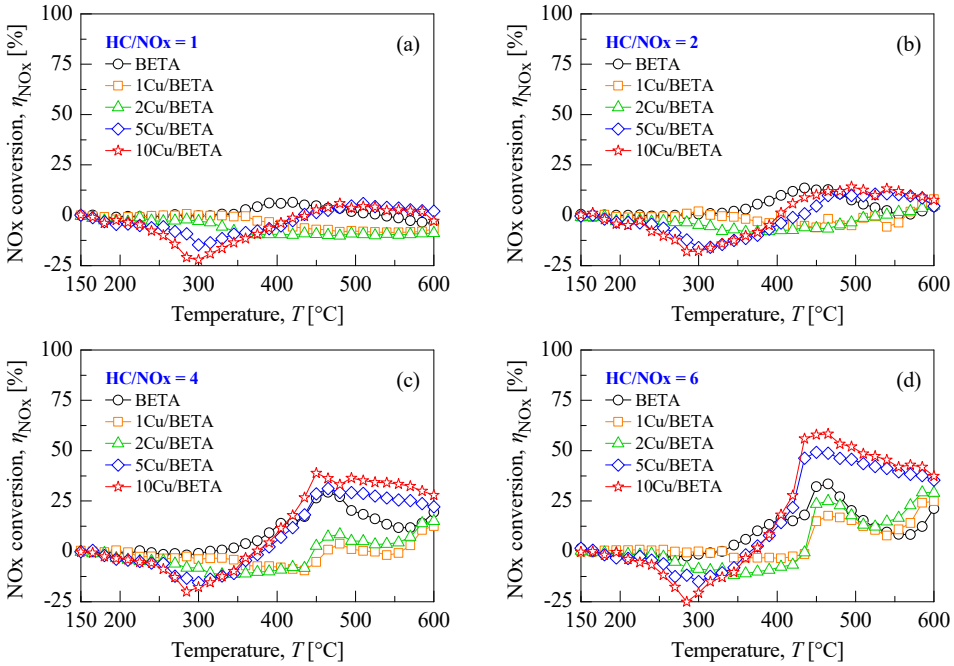

Figure 4.3 NOx conversion of parent BETA zeolite and Cu/BETA in SCR with C_4H_{10} as a function of reaction temperature at (a) HC/NOx = 1, (b) HC/NOx = 2, (c) HC/NOx = 4, and (d) HC/NOx = 6.

4.3 C_4H_{10} conversion of Cu/zeolite

The catalytic performance of the C_4H_{10}-SCR for NOx reduction over the all the Cu/zeolite catalysts was significantly dependent on the HC/NOx ratios, with a proportional relationship, because more of the active reducing agent would be available for NOx reduction. Figures 4.4 and 4.5 show the C_4H_{10} conversion over the parent zeolites and Cu/zeolite catalysts during the SCR reaction with NOx. It is clear that increasing the Cu loading substantially enhanced the rate of C_4H_{10} oxidation. This was evident in the case of Cu/SSZ-13, in which the light-off temperature (LOT_{50}) of C_4H_{10} declined with an increase in the Cu loading in the following order (Figure 4.4(b)): 453℃ (5Cu/SSZ-13) < 518℃ (1Cu/SSZ-13) < 553℃ (parent SSZ-13). In the case of the 5Cu/zeolite catalysts at HC/NOx = 6, the LOT_{50} performance for C_4H_{10} conversion over the 5Cu/ZSM-5 and 5Cu/BETA catalysts were 422℃ and 435℃, which are lower than that of 5Cu/SSZ-13. The LOT_{50} for C_4H_{10} conversion by the Cu/ZSM-5 catalysts followed a trend similar to that of Cu/BETA and Cu/SSZ-13 at other HC/NOx ratios, as shown in Figures 4.4 and 4.5.

From the C_4H_{10} conversion experiments, the Cu species impregnated into the respective zeolite serve as active sites for the partial oxidation of C_4H_{10}. In addition, the de-NOx performance was closely related to the rate of C_4H_{10} oxidation. As illustrated in Figure 4.2, 2Cu/ZSM-5 exhibited the highest de-NOx performance, followed by 10Cu/ZSM-5 and 5Cu/ZSM-5, and the C_4H_{10} conversion for these Cu/ZSM-5 catalysts also followed an identical trend, as shown in Figure 4.4(d). When considering interaction of the reductant with the active sites, the relatively higher NOx conversion of Cu/ZSM-5 and Cu/BETA compared to that of Cu/SSZ-13 can be attributed to geometry-limited diffusion of C_4H_{10} in the respective zeolite channels. As illustrated in Figure 4.6, the kinetic diameter of the *n*-C_4H_{10} molecule is ca. 4.687 Å [216, 217], which is significantly larger than the pore-opening diameter of SSZ-

13, indicating that C_4H_{10} easily access the active sites in the channels of the ZSM-5 and BETA zeolite compared to those of SSZ-13. Therefore, the degree of geometry-limited diffusion affected the partial oxidation of C_4H_{10}, which is related to the de-NOx performance.

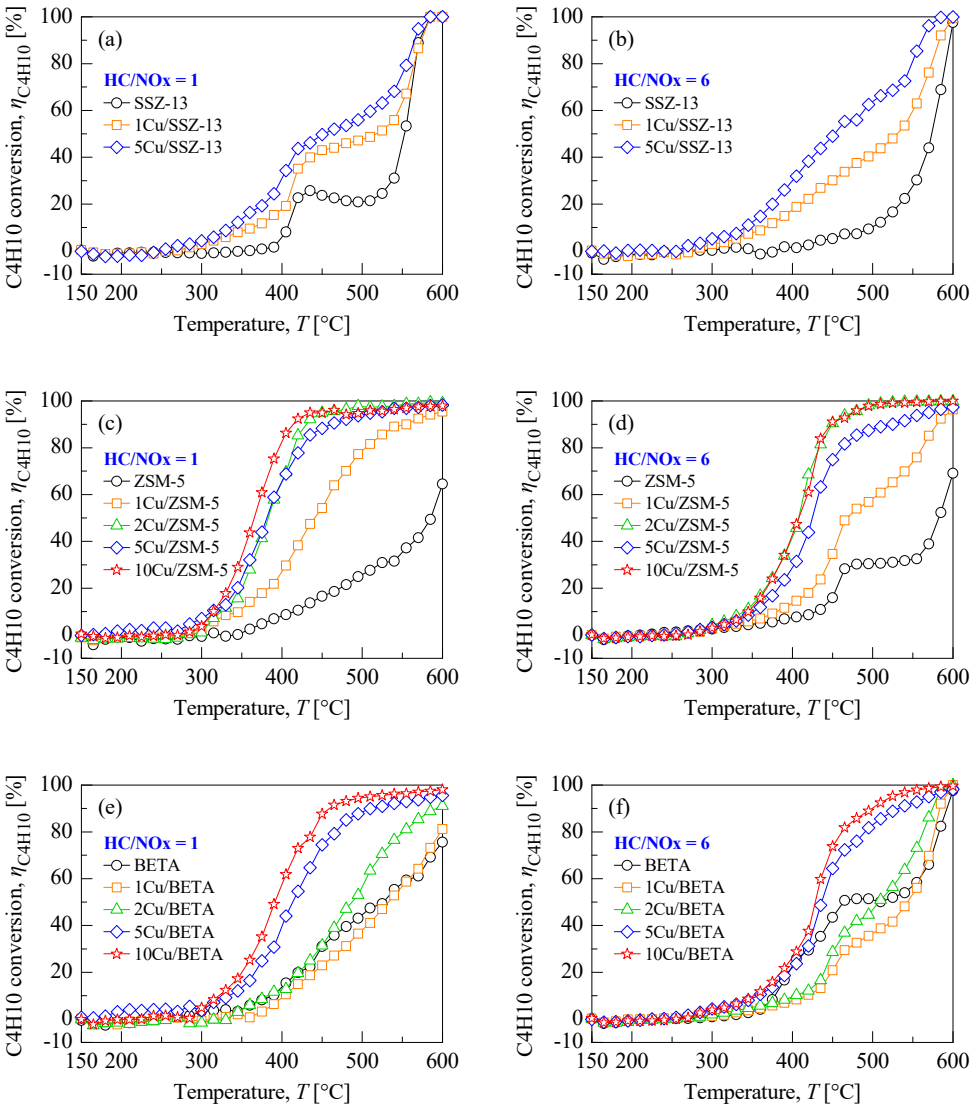

Figure 4.4 Reductant (C_4H_{10}) conversion of pure zeolites and Cu/zeolites as a function of reaction temperature at HC/NOx = 1 and 6: (a), (b) Cu/SSZ-13, (c), (d) Cu/ZSM-5, and (e), (f) Cu/BETA.

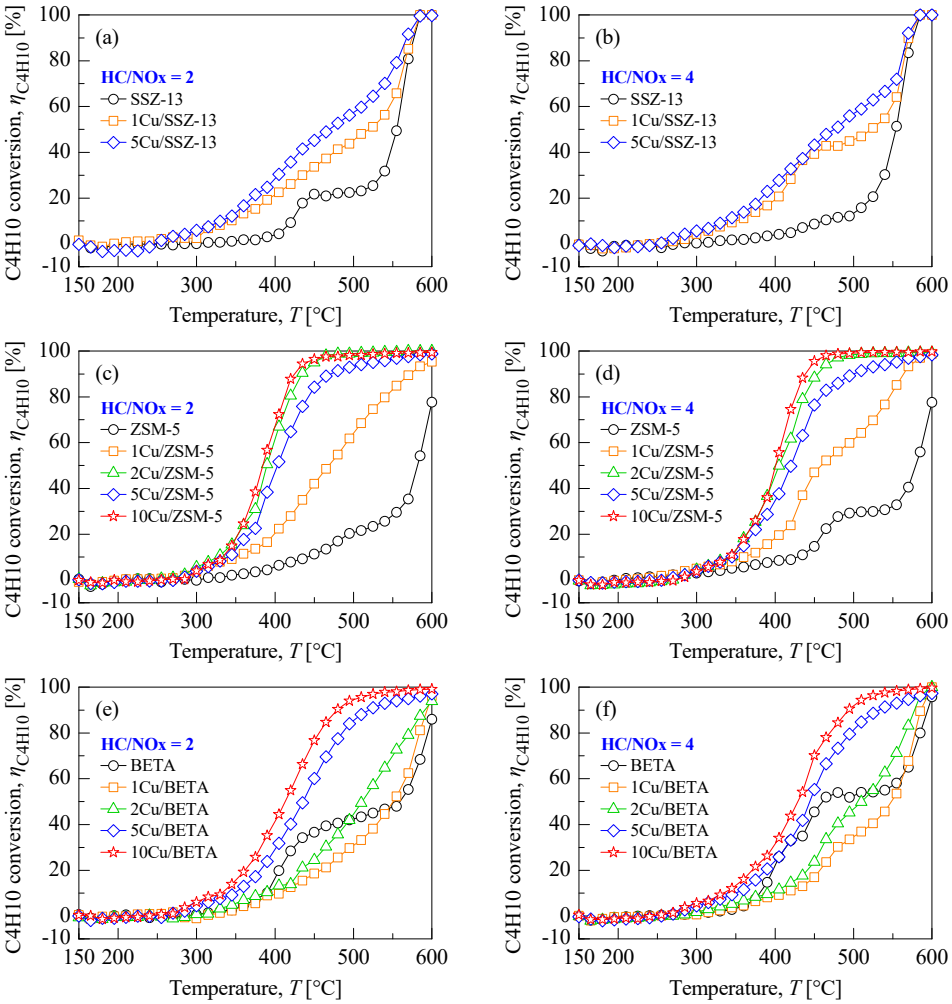

Figure 4.5 Reductant (C_4H_{10}) conversion of pure zeolites and Cu/zeolites as a function of reaction temperature at HC/NOx = 2 and 4: (a), (b) Cu/SSZ-13, (c), (d) Cu/ZSM-5, and (e), (f) Cu/BETA.

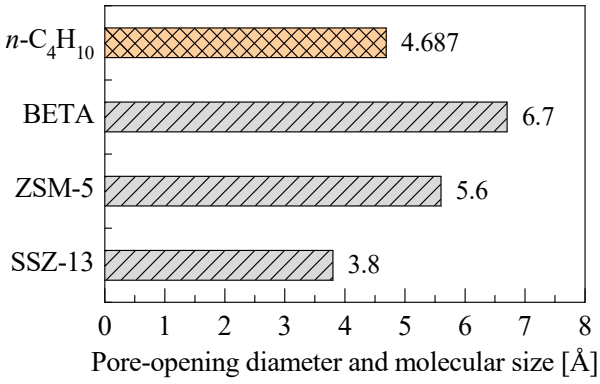

Figure 4.6 Comparison of kinetic diameter of n-C_4H_{10} molecule and pore-opening diameter of zeolites.

4.4 CO conversion of Cu/zeolite

During NOx reduction by C_4H_{10}, 500 ppm of CO was simultaneously supplied in the feed gas. CO conversion was investigated over all the parent zeolites and Cu/zeolite catalysts. As illustrated in Figure 4.7(a), negative CO conversion was observed over the parent ZSM-5 zeolite within the evaluated temperature range. CO conversion over the parent SSZ-13 and BETA zeolites also followed a trend identical to that of the ZSM-5 zeolite, as illustrated in Figures 4.7–4.10, indicating that the zeolite without Cu loading could not oxidize CO in the emitted gas. The CO conversion also decreased substantially over the parent zeolites with an increase in the HC/NOx ratio; for example, in the case of parent SSZ-13 zeolite CO conversion was decreased from −27.4% (Figure 4.8(a), HC/NOx = 1) to −349.1% (Figure 4.7(b), HC/NOx = 6) at 600°C. During the C_4H_{10}-SCR reaction, the reductant participates in NOx reduction as well as in the partial oxidation with oxygen included in the feed gas. Considering the possible reaction for CO formation, this is attributed to the partial oxidation reaction of C_4H_{10} by O_2, as expressed in reaction (4.2)

$$NO + C_4H_{10} + O_2 \rightarrow N_2 + CO + H_2O \quad (4.2)$$

Comparison of the CO conversion of the parent zeolites and Cu/zeolite catalysts at HC/NOx = 6 (Figure 4.7(b)–(d)) shows that increasing the Cu loading highly improved the CO conversion for all Cu/zeolite catalysts because the Cu species provided active sites for oxidation of CO to CO_2 over the Cu/zeolites. The Cu loading also affected the initial temperature for CO oxidation, including a shift toward lower regions (from 285°C for 1Cu/SSZ-13 to 225°C for 5Cu/SSZ-13). From the evaluation of the light-off temperature (LOT_{50}) for CO conversion over the Cu/zeolites with the same Cu loading at HC/NOx = 6,

5Cu/SSZ-13 had the lowest LOT_{50}, followed by 5Cu/ZSM-5 and 5Cu/BETA: 254℃ (5Cu/SSZ-13) < 477℃ (5Cu/ZSM-5) < 584℃ (5Cu/BETA). However, there was a sudden decline in the CO conversion over Cu/SSZ-13 above 550℃, which is attributed to a sharp increase in the rate of partial oxidation of C_4H_{10} from 540℃; thus, the ability to oxidize CO became weak due to the production of more CO. Among the three types of zeolite frameworks, Cu/SSZ-13 exhibited the highest CO conversion, ranging from 225 to 555℃, with even lower Cu loading than Cu/ZSM-5 and Cu/BETA. This may be related to the accessibility of CO molecules to the active sites. The molecular diameter of CO is far smaller than that of the three zeolites; thus, the CO molecules favorably approach the active sites of Cu/SSZ-13.

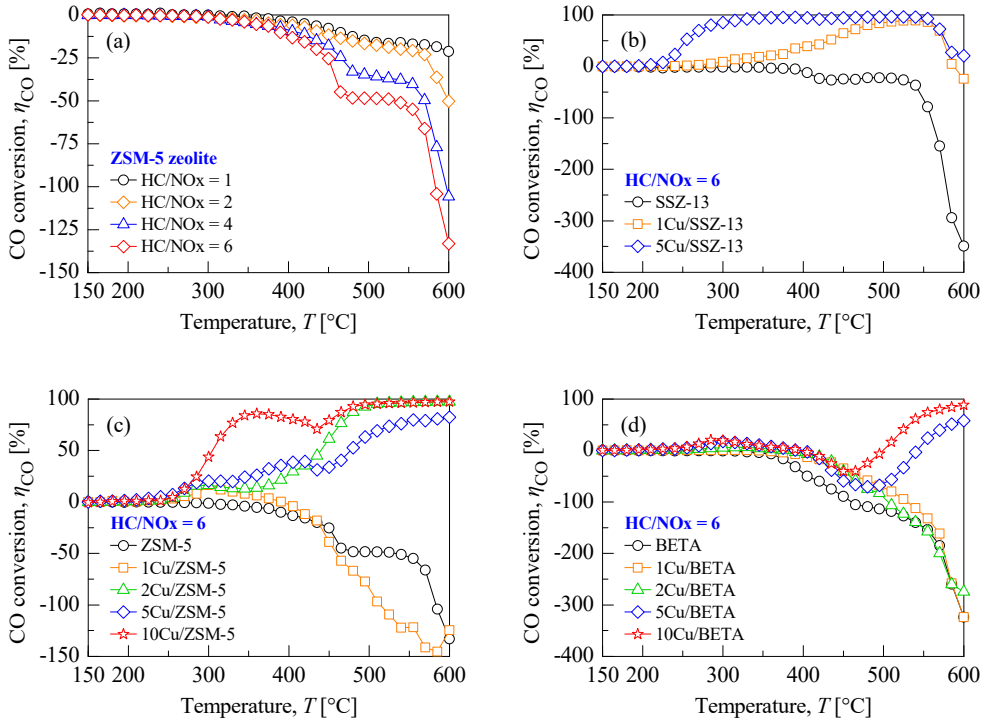

Figure 4.7 CO conversion of (a) parent ZSM-5 zeolite according to HC/NOx ratios from 1 to 6 and (b) Cu/SSZ-13, (c) Cu/ZSM-5, and (d) Cu/BETA at HC/NOx = 6 as a function of reaction temperature.

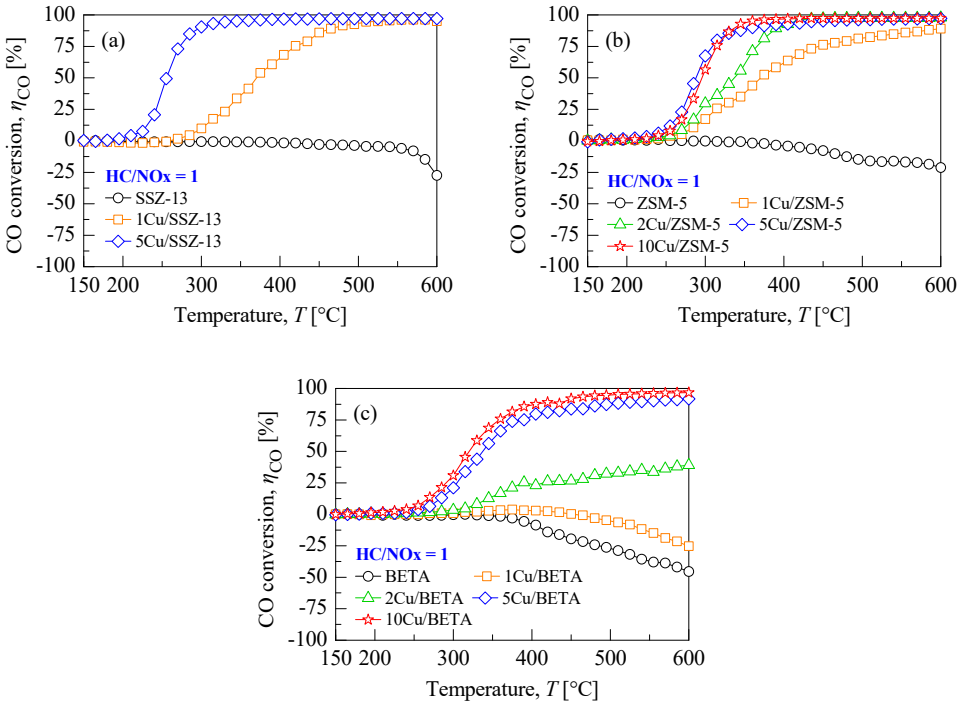

Figure 4.8 CO conversion of parent zeolites and Cu/zeolite catalysts as a function of reaction temperature at HC/NOx = 1: (a) Cu/SSZ-13, (b) Cu/ZSM-5, and (c) Cu/BETA.

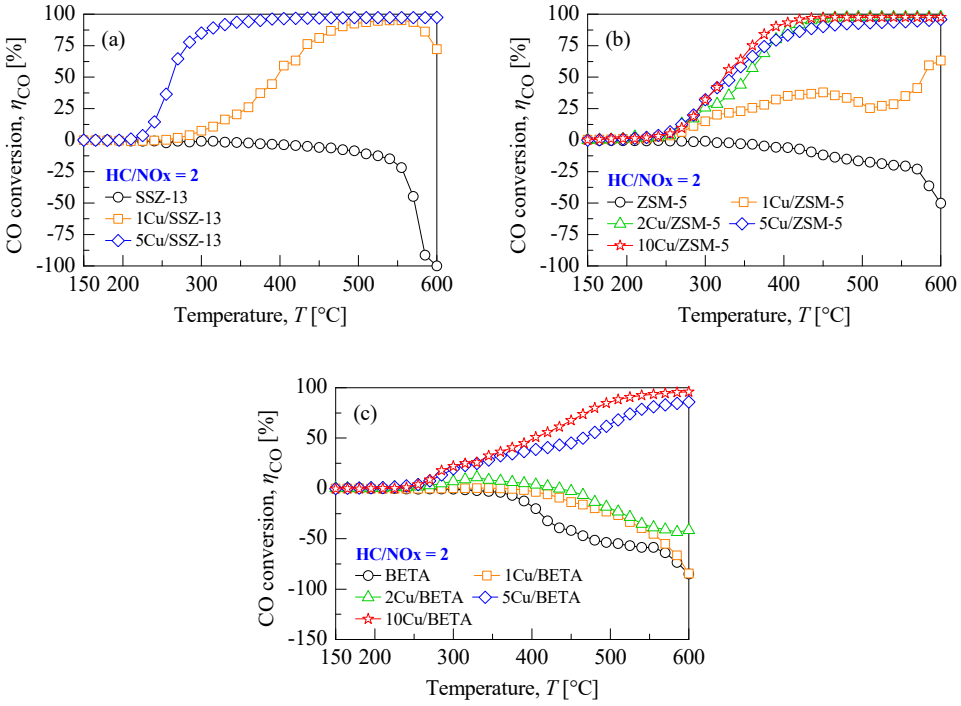

Figure 4.9 CO conversion of parent zeolites and Cu/zeolite catalysts as a function of reaction temperature at HC/NOx = 2: (a) Cu/SSZ-13, (b) Cu/ZSM-5, and (c) Cu/BETA.

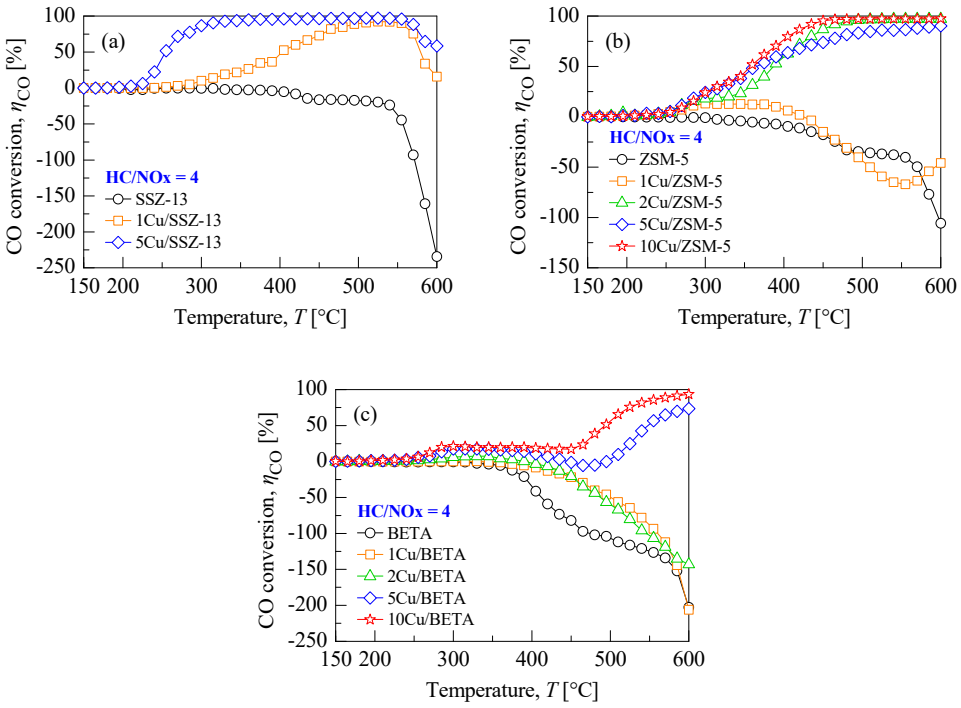

Figure 4.10 CO conversion of parent zeolites and Cu/zeolite catalysts as a function of reaction temperature at HC/NOx = 4: (a) Cu/SSZ-13, (b) Cu/ZSM-5, and (c) Cu/BETA.

4.5 Temperature programmed oxidation of C_4H_{10}

The formation of CO during the C_4H_{10}-SCR reaction was observed, and the parent zeolites could not oxidize CO simultaneously supplied in the feed stream. Considering the C_4H_{10}-SCR reaction, the hydrocarbon reductant participates in NOx reduction and in the partial oxidation with coexistent O_2. The temperature programmed oxidation (TPO) of C_4H_{10} by 8 vol.% O_2 was carried out to evaluate the ability to partially oxidize C_4H_{10} over the parent zeolites and Cu/zeolite catalysts. CO formation was attributed to the incomplete oxidation of C_4H_{10} by O_2 to generate CO rather than CO_2, as illustrated in Figure 4.11. Comparison of the CO formation over the parent zeolites and Cu/zeolites shows that CO formation was the predominant reaction over the parent zeolites. The findings of C_4H_{10}-TPO experiments indicate that the hydrocarbon reductant was oxidized by O_2 to CO and CO_2, as expressed below in the reactions (4.3) and (4.4). The parent zeolites followed the reaction (4.3), whereas the Cu/zeolite catalysts followed the reaction (4.4) because C_4H_{10} was oxidize to more CO_2 than CO over the Cu/zeolites. The loading of Cu also enhanced the rate of partial oxidation of C_4H_{10} during C_4H_{10}-TPO; for instance, 10Cu/BETA completely oxidized C_4H_{10} at 600°C (Figure 4.11(f)), however, the parent BETA zeolite without Cu loading could not completely oxidize C_4H_{10} even at high temperature region (Figure 4.11(e)). From the C_4H_{10}-TPO experiments, the CO over COx ratios are compared, as illustrated in Figure 4.12. Note that all the Cu/zeolites could oxidize C_4H_{10} to less CO compared to the parent zeolites.

$$C_4H_{10} + 4.5O_2 \rightarrow 4CO + 5H_2O \quad (4.3)$$

$$C_4H_{10} + 6.5O_2 \rightarrow 4CO_2 + 5H_2O \quad (4.4)$$

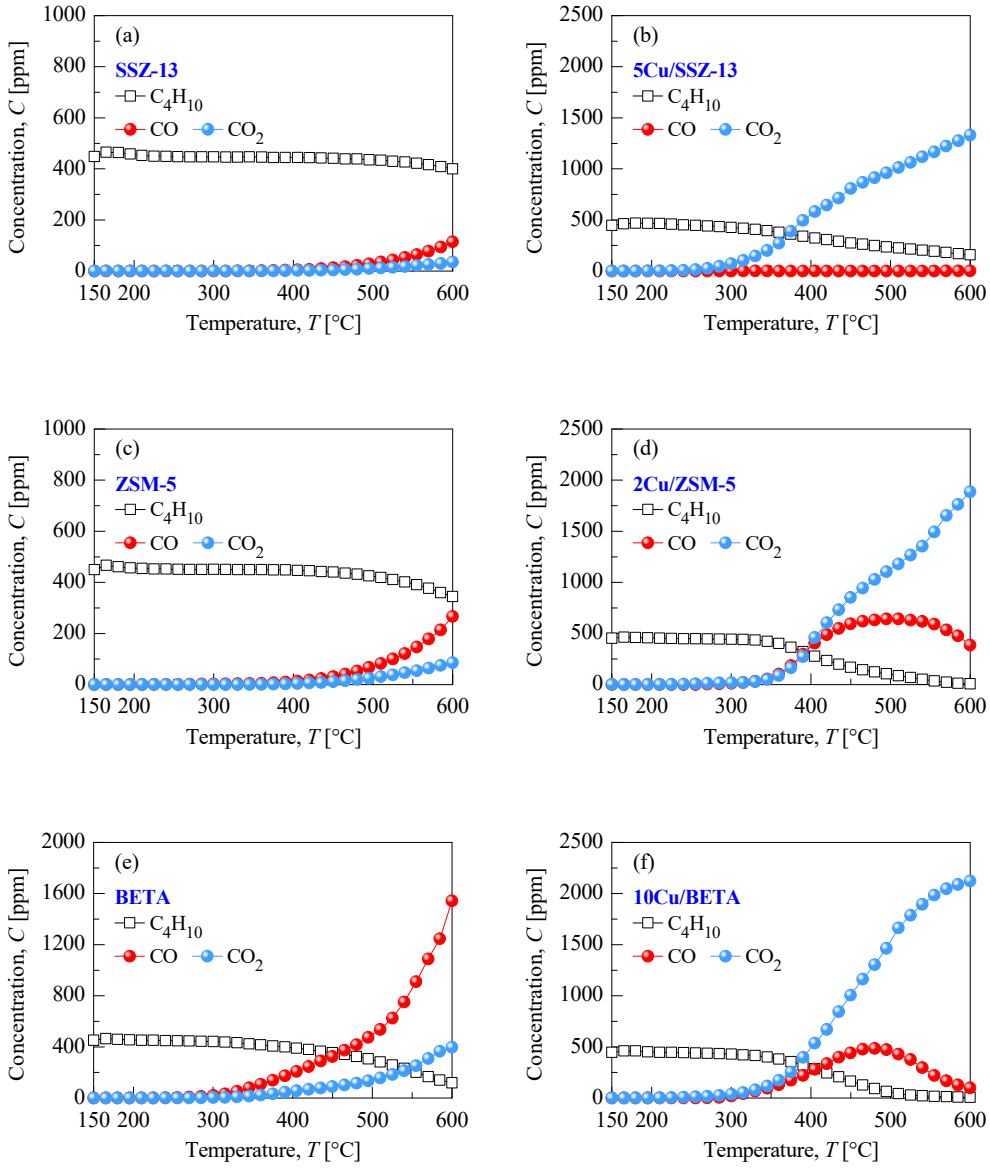

Figure 4.11 Temperature programmed oxidation (TPO) of C_4H_{10} by O_2 over the parent zeolites and Cu/zeolite catalysts (TPO experiment: 1,800 ppm C_1 C_4H_{10} + 8 vol.% O_2 + balance N_2 at GHSV = 12,500 h^{-1}).

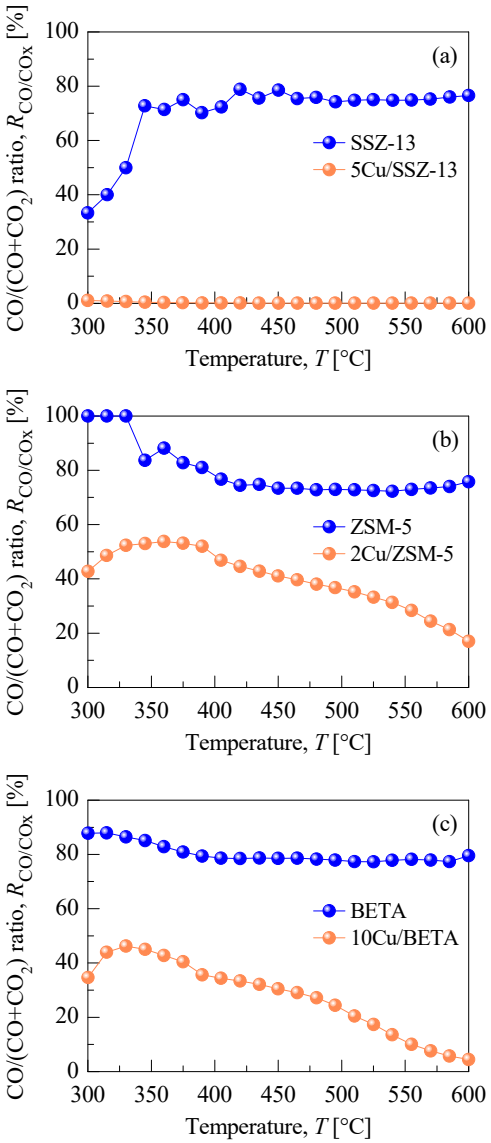

Figure 4.12 CO over COx ratios after oxidation of C_4H_{10} by O_2 over the parent zeolites and Cu/zeolite catalysts: (a) SSZ-13 zeolite, (b) ZSM-5 zeolite, and (c) BETA zeolite.

4.6 Temperature programmed desorption of NOx

Although the NOx adsorption capacity and NOx conversion are not directly proportional in the SCR catalysts, the NOx adsorption mechanism is important as an initial step for the SCR reaction. The NOx adsorption capacities were tested at 150℃ for 60 min over the parent zeolites and Cu/zeolite catalysts, and the adsorption capacity of NOx is shown in Figure 4.13. The adsorption capacity of the parent zeolites without Cu loading ranged from 18 to 22 mmol/L: in detail, 21.28 mmol/L for SSZ-13, 18.09 mmol/L for ZSM-5, and 22.45 mmol/L for BETA. Moreover, the adsorption capacity of NO is much higher than that of NO_2 over the parent zeolites. In the case of Cu/zeolite catalysts, two distinct features were observed. The quantities of NOx adsorbed increased for all the Cu/zeolite catalysts relative to the parent zeolites, and the adsorbed amount of NO_2 was much higher than that of NO. The highest amount of NOx adsorbed was about 35.35 mmol/L for 5Cu/SSZ-13, followed by 10Cu/BETA (24.04 mmol/L) and 2Cu/ZSM-5 (21.57 mmol/L). Accordingly, Cu/zeolite catalysts facilitate the NOx oxidation reaction into NO_2, and this NO_2 can be easily adsorbed on the catalyst surface following the reactions below:

$$O_2\ (g) + \textit{active sites} \rightarrow 2O\ (ad)\text{—}\textit{active sites} \tag{4.5}$$

$$NO\ (g) + 2O\ (ad)\text{—}\textit{active sites} \rightarrow NO_2\ (ad)\text{—}\textit{active sites} \tag{4.6}$$

The Cu/zeolite catalysts exhibited the negative NOx conversion at the temperature windows between 150 to 350℃, especially the highest negative NOx conversion for 5Cu/SSZ-13. The negative NOx conversion is attributed to desorbed NOx on the Cu/zeolite catalysts, where the incorporation of Cu enhanced the adsorption of NOx, and more desorbed NOx was observed during the temperature programmed desorption of NOx (NOx-TPD), as illustrated in Figure 4.14.

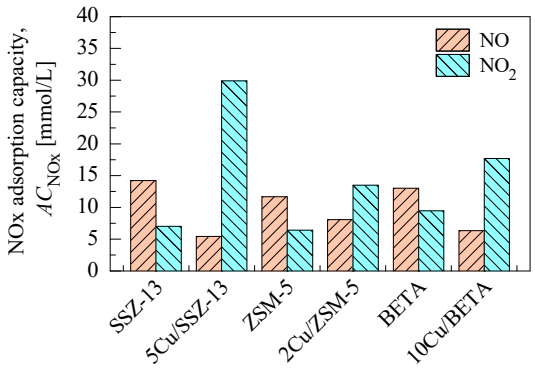

Figure 4.13 NOx adsorption capacity of parent zeolites and Cu/zeolite catalysts at 150°C (NOx adsorption experiment: 500 ppm NO + 8 vol.% O_2 + balance N_2 at GHSV = 12,500 h^{-1} for 60 min).

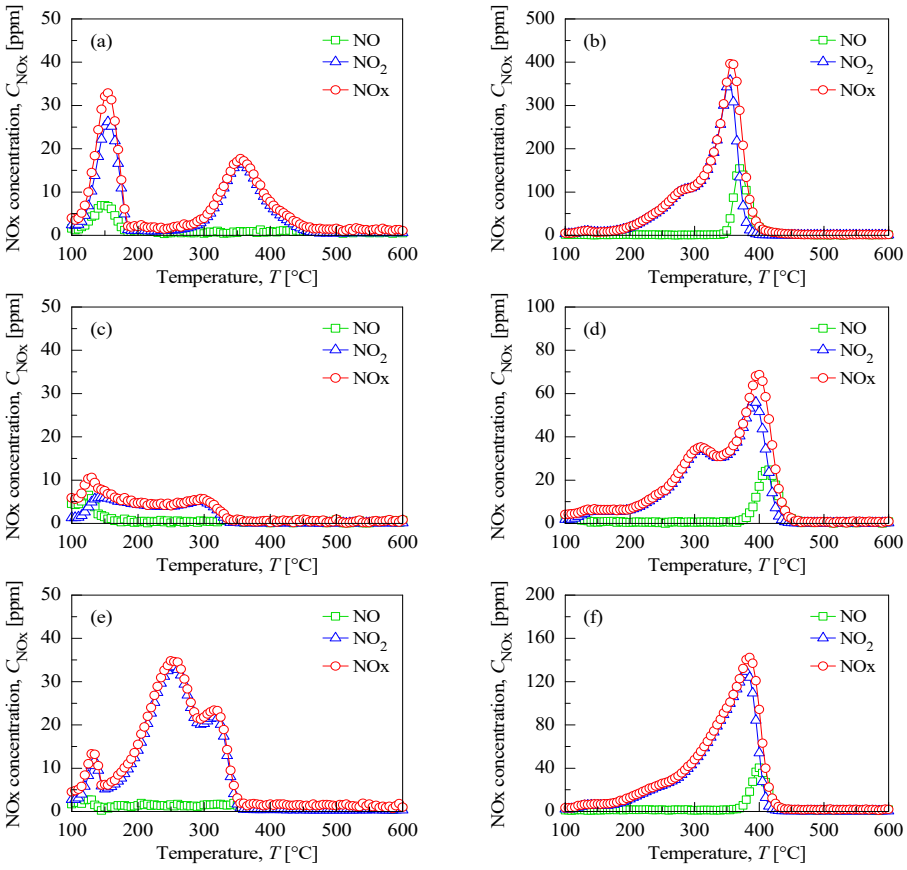

Figure 4.14 NOx profiles of the parent zeolites and Cu/zeolites during the temperature programmed desorption of NOx (NOx-TPD) after adsorption of NOx: (a) SSZ-13 zeolite, (b) 5Cu/SSZ-13, (c) ZSM-5 zeolite, (d) 2Cu/ZSM-5, (e) BETA zeolite, and (f) 10Cu/BETA (NOx adsorption: 500 ppm NO + 8 vol% O_2 at 150°C for 60 min, NOx TPD: balance N_2 at GHSV = 12,500 h^{-1} from 100 to 600°C with a ramp-up rate of 5°C/min).

4.7 N_2 yield of Cu/zeolite

During the C_4H_{10}-SCR reaction over the Cu/zeolite catalysts, N_2 yields was calculated by detecting the possible by-products including nitrogen-containing species that are nitrous oxide (N_2O), isocyanic acid (HNCO), and ammonia (NH_3). Figure 4.15 shows the comparison of N_2 yield and NOx conversion over all the tested Cu/zeolite catalysts at HC/NOx = 6 at reaction temperatures ranging from 360 to 600°C. The N_2 yield was in good agreement with the NOx conversion, indicating that NOx was reduced to N_2 by C_4H_{10} without any accompanying undesired side-reactions, producing N_2O, HNCO and NH_3. Therefore, all the tested Cu/zeolite catalysts could reduce NOx to N_2 via the ideal HC-SCR reaction, as expressed in reaction (4.7):

$$2NO + 5.5O_2 + C_4H_{10} \rightarrow N_2 + 4CO_2 + 5H_2O \quad (4.7)$$

The N_2 yield corresponded well with the NOx conversion over the Cu/zeolite catalysts at other HC/NOx ratios, as illustrated in Figures 4.16–4.18. Although N_2 yield decreased at HC/NOx ratios of less than 6 due to a decrease in C_4H_{10} available for NOx reduction, N_2 yield followed the NOx conversion without producing any undesired by-products at all the tested reaction temperatures. Thus, it can be concluded that the Cu/zeolite catalysts can reduce NOx to N_2 via the ideal C_4H_{10}-SCR reaction without accompanying any side-reactions.

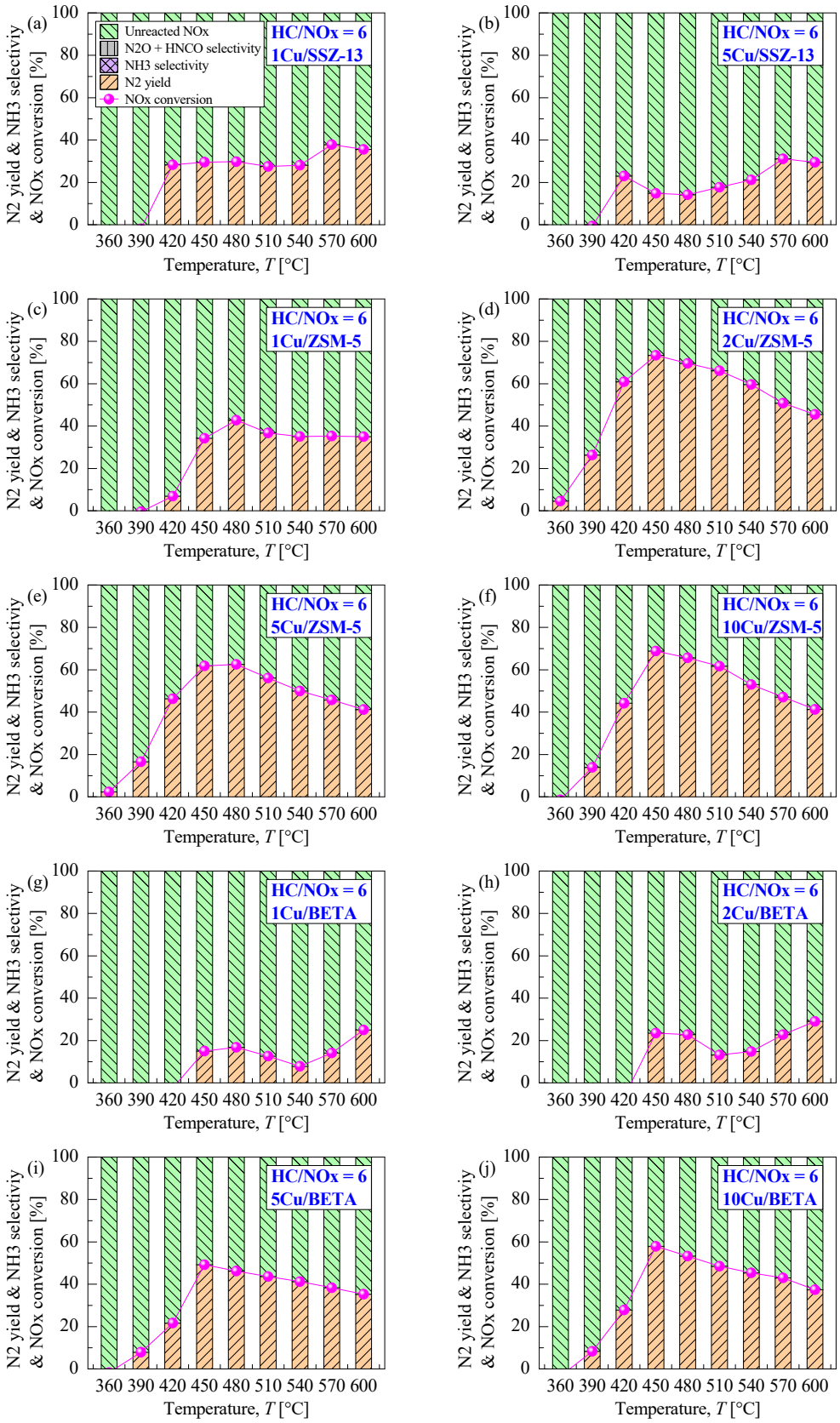

Figure 4.15 Comparison of reaction products after C_4H_{10}-SCR reaction at HC/NOx = 6.

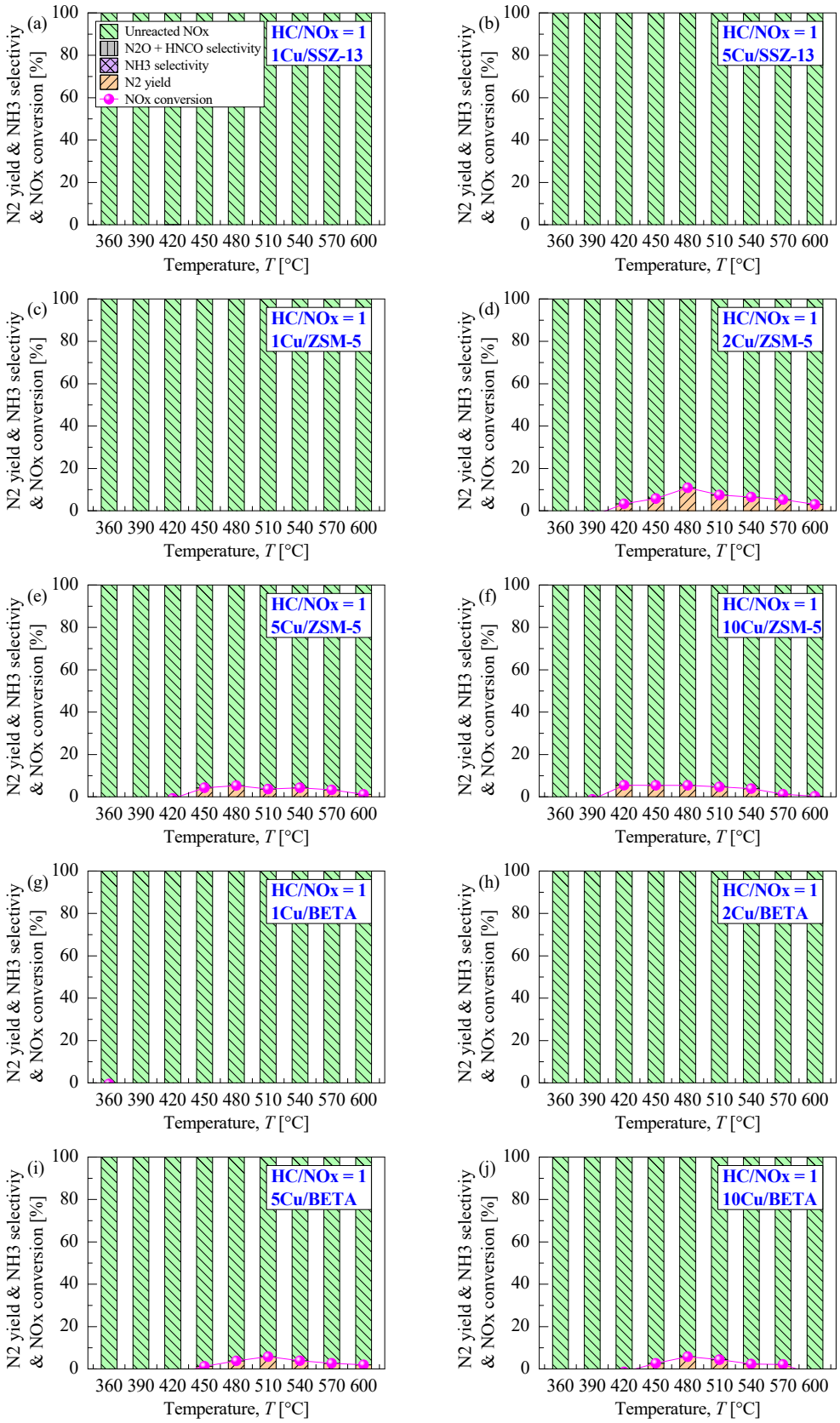

Figure 4.16 Comparison of reaction products after C_4H_{10}-SCR reaction at HC/NOx = 1.

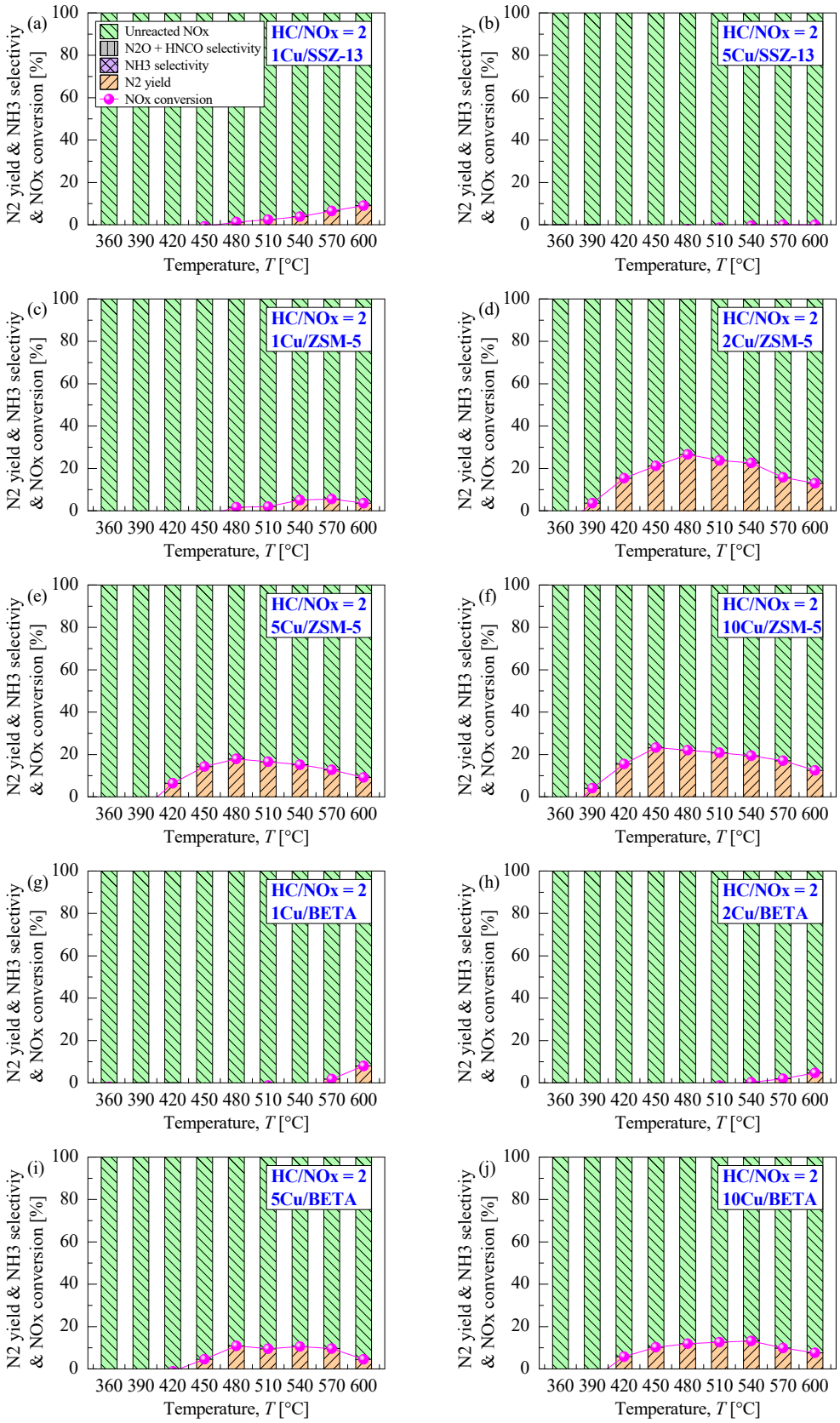

Figure 4.17 Comparison of reaction products after C_4H_{10}-SCR reaction at HC/NOx = 2.

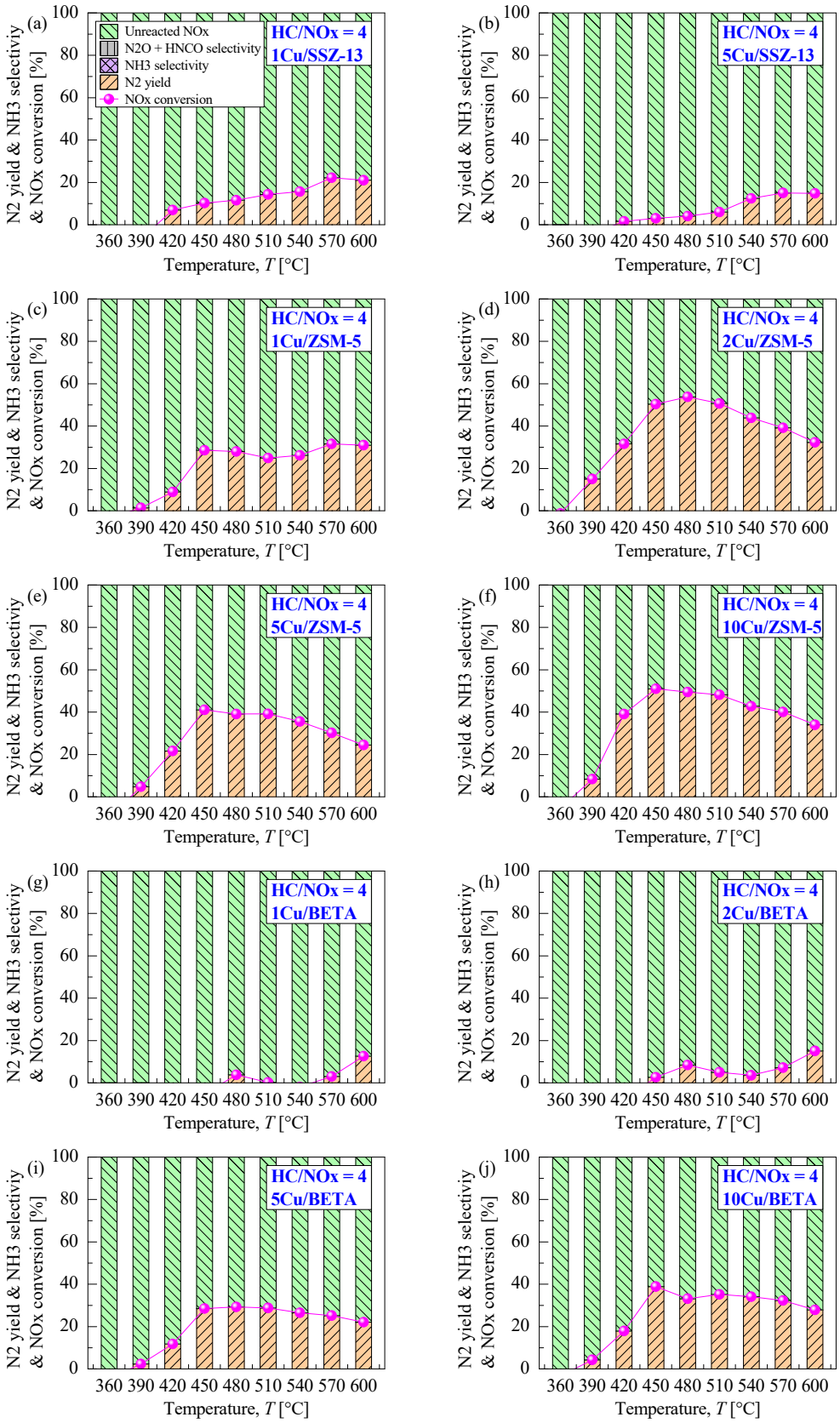

Figure 4.18 Comparison of reaction products after C_4H_{10}-SCR reaction at HC/NOx = 4.

4.8 Summary

The effects of the zeolite framework and Cu loading on the catalytic activity for the C_4H_{10}-SCR in the presence of CO, CO_2, H_2O, and O_2 are presented in Chapter 4. The zeolite framework, Cu loading, and HC/NOx ratio strongly affected the de-NOx reaction over the Cu/zeolite catalysts, accompanied by CO oxidation and partial oxidation of C_4H_{10}. The loading of Cu to the respectively parent zeolites improved the NOx conversion and shifted the temperature window of the peak NOx conversion to lower regions compared to those for the parent zeolites. Among the Cu/zeolite catalysts with different zeolite frameworks prepared by the incipient wetness impregnation method, 2Cu/ZSM-5 exhibited the best de-NOx performance with nearly 74% at 465℃, followed by 10Cu/BETA (58% at T = 465℃) and 1Cu/SSZ-13 (38% at T = 585℃). These results were related to the effect of geometry-limited diffusion of C_4H_{10} in the respective zeolite channel system, in which the reductant had easy access to the active sites in the channels of ZSM-5 and BETA zeolite, but C_4H_{10} was highly restricted in the SSZ-13 channels. The HC/NOx ratio was sensitive to both the NOx and CO conversion. Increasing the HC/NOx ratio enhanced the de-NOx performance because more reducing agent could be available for NOx reduction in the C_4H_{10}-SCR process. The higher Cu loading, the lower the light-off temperature (LOT_{50}) of C_4H_{10} was. The parent zeolites without Cu loading could not oxidize CO into CO_2 because negative CO conversion was obtained with the evaluated temperature window, and more CO was produced with an increase in HC/NOx ratios and reaction temperatures. The N_2 yield was in good agreement with the NOx conversion, suggesting that NOx was reduced to N_2 by C_4H_{10} without any accompanying undesired side-reactions, such as N_2O, HNCO and NH_3. Therefore, all the tested Cu/zeolite catalysts could reduce NOx to N_2 via the ideal C_4H_{10}-SCR reaction.

Chapter 5. Effects of Coexistent Gases and Hydrothermal Aging

5.1 Experimental conditions for evaluation of HC-SCR

The effects of CO_2 concentration and O_2 concentration on the de-NOx performance are investigated in this chapter. 2Cu/ZSM-5 was selected for evaluation of the influence of O_2 and CO_2 because this catalyst exhibited the highest NOx conversion in both the C_3H_6-SCR and C_4H_{10}-SCR process. The supply concentrations of O_2 were determined ranging from 0 to 8 vol.%, and those of CO_2 varied from 0 to 10 vol.%. Table 5.1 summaries the experimental conditions for investigating the effects of coexistent gases in both the C_3H_6-SCR and C_4H_{10}-SCR process.

To study the influence of the hydrothermal tolerance on the de-NOx performance, the monolithic Cu/zeolite catalysts were hydrothermally treated at 700℃ for 12 h with 8 vol.% O_2, 5 vol.% H_2O, and balance N_2 at a gas hourly space velocity of 12,500 h^{-1}; the temperature profiles of hydrothermal treatment are shown in Figure 5.1. The SCR performance was carried out at the highest HC/NOx ratio in both the C_3H_6-SCR and C_4H_{10}-SCR process. Furthermore, to investigate the catalytic stability, the stability test was also carried out to at steady-state 450℃ for 24 h in the C_4H_{10}-SCR process. 5Cu/zeolite catalysts were exposed at 450℃ for 24 h during the C_4H_{10}-SCR at HC/NOx = 6, and the catalytic performance was continuously recorded.

Table 5.1 Experimental conditions for investigating the effects of O_2 and CO_2 concentration in C_3H_6-SCR and C_4H_{10}-SCR.

Parameters	C_3H_6–SCR reaction	C_4H_{10}–SCR reaction
Reductant	Propene (C_3H_6)	*n*-Butane (*n*-C_4H_{10})
Nitrogen monoxide (NO)	500 ppm	300 ppm
Oxygen (O_2)	0, 1, 4, and 8 vol.%	0, 1, 4, and 8 vol.%
Carbon monoxide (CO)	500 ppm	500 ppm
Carbon dioxide (CO_2)	0, 1, 5, and 10 vol.%	0, 1, 5, and 10 vol.%
Water vapor (H_2O)	5 vol.%	5 vol.%
Balance gas	N_2	N_2
Propene (C_3H_6)	4,000 ppm C_1	–
n-Butane (*n*-C_4H_{10})	–	1,800 ppm C_1
HC/NOx ratio	8	6
Total flow rate	1.67 L/min	1.67 L/min
Temperature	150 – 600°C	150 – 600°C
GHSV	12,500 h^{-1}	12,500 h^{-1}

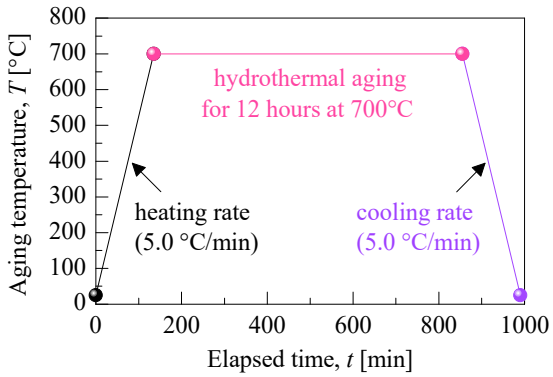

Figure 5.1 Temperature profiles of hydrothermal aging for monolithic Cu/zeolite catalysts (hydrothermal aging condition: 8 vol.% O_2 + 5 vol.% H_2O + balance N_2 at GHSV = 12,500 h^{-1}).

5.2 Effect of CO_2 concentration in C_3H_6-SCR process

Figure 5.2 shows the effect of CO_2 concentration on catalytic performance over the 2Cu/ZSM-5 catalyst at HC/NOx = 6 in the C_3H_6-SCR process. The presence of CO_2 in the feed gas has a negative effect on NOx conversion at reaction temperatures ranging from 300 to 345℃, which considerably decreased from 57.3% (0 vol.% CO_2) to 26.5% (1 vol.% CO_2), 25.3% (5 vol.% CO_2), and 16.5% (10 vol.% CO_2) at 345℃. At reaction temperatures above 375℃, the presence of CO_2 had had a negligible effect on the NOx conversion after the addition of 1 vol.%, 5 vol.%, or even 10 vol.% CO_2. The significant drop in NOx conversion below 345℃ could be induced by the difference in partial oxidation of C_3H_6, as shown in Figure 5.2(b), in which C_3H_6 conversion decreased from 100% (0 vol.% CO_2) to 82.9% (1 vol.% CO_2), 79.8% (5 vol.% CO_2), and 68.8% (10 vol.% CO_2) at 345℃. Increasing the CO_2 concentrations highly inhibited the partial oxidation of C_3H_6 at the reaction temperatures ranging from 300 to 360℃. Furthermore, the presence of CO_2 also negatively affected the CO conversion at the reaction temperatures ranging from 300 to 390℃; the CO conversion of 2Cu/ZSM-5 substantially decreased from 96.9% (0 vol.% CO_2) to −7.8% (1 vol.% CO_2), −98.4% (5 vol.% CO_2), and −280.5% (10 vol.% CO_2) at 360℃. Indeed, recently reported studies described that the CO_2 molecules are readily adsorbed on the surface of the zeolite-based catalysts [218, 219], and the adsorption of NOx is blocked by the pre-adsorbed CO_2. Therefore, it could be concluded that the presence of CO_2 in the feed gas had an inhibitory effect on the C_3H_6-SCR reaction.

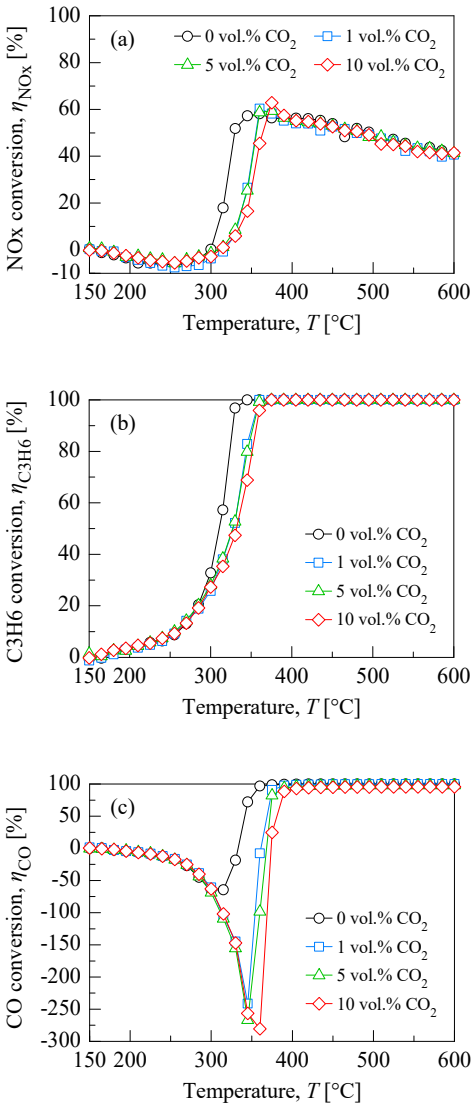

Figure 5.2 Influence of CO_2 concentration (0–10 vol.% CO_2) on catalytic performance of 2Cu/ZSM-5 at HC/NOx = 8 in C_3H_6-SCR process: (a) NOx conversion, (b) C_3H_6 conversion, and (c) CO conversion.

5.3 Effect of O_2 concentration in C_3H_6-SCR process

As a key component of the reaction gases under fuel-lean conditions, excess O_2 had had a decisive effect on the catalytic activity of most of the catalysts in the HC-SCR process [220, 221]. The influence of O_2 concentration, ranging from 0 to 8 vol.% O_2, on the catalytic performance is shown in Figure 5.3 over the 2Cu/ZSM-5 catalyst, which exhibited the highest de-NOx performance. The temperature window of NOx conversion significantly shifted to lower temperatures with an increase in O_2 concentration from 1 vol.% to 8 vol.%. One possible explanation for these findings is that the oxygenated hydrocarbons (CxHyOz), which are produced by partial oxidation of C_3H_6 by O_2 at relatively low temperatures with an increase in O_2 and acted as reaction intermediates to react with adsorbed NOx. Notably, further increase in NOx conversion was observed in the absence of O_2, exhibiting 86.8% maximum NOx conversion at 540℃. Although the removal of O_2 in the feed gas could improve the NOx conversion, this reaction environment was accompanied by undesired side-reactions that produce NH_3 at reaction temperatures above 420℃, as illustrated in Figure 5.4(a). The N_2 selectivity ranged from 1% to 56% at reaction temperatures between 420 to 570℃: 14.4% (420℃), 24.6% (450℃), 40.3% (480℃), 51.5% (510℃), 55.8% (540℃), and 50% (570℃), respectively. The slipped NH_3 after the C_3H_6-SCR reaction was originated by side-reactions from reacting NO with hydrocarbon reductant, and 2Cu/ZSM-5 could reduce NOx to N_2 and NH_3 without producing N_2O and HNCO. It is also clear that the presence of O_2 in the feed gas facilitated the rate of CO and C_3H_6 oxidation reactions, especially at high O_2 concentrations in the feed gas, as illustrated Figure 5.3(b) and (c).

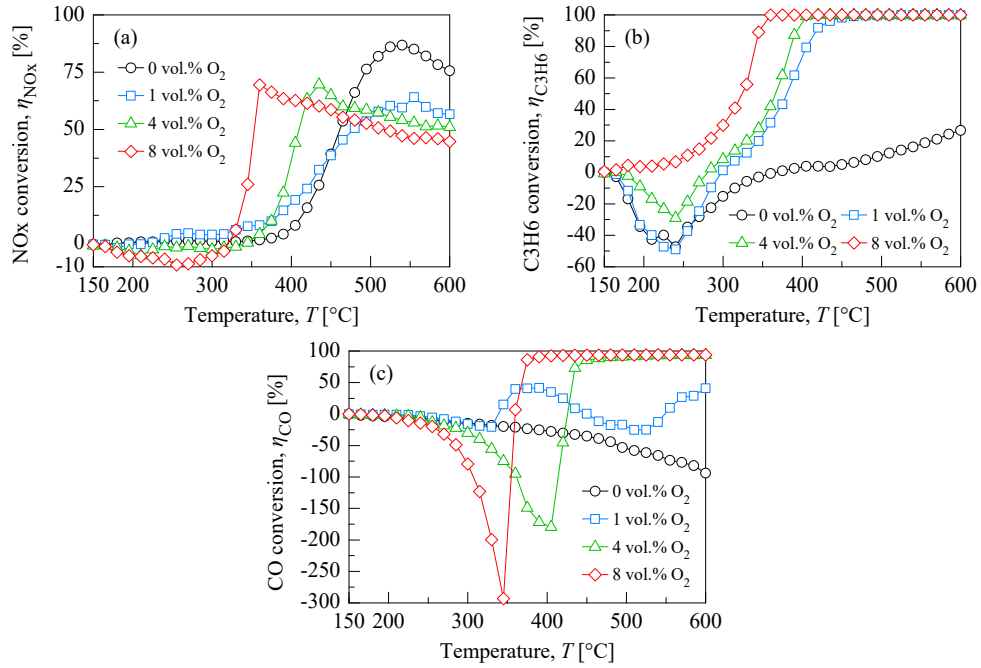

Figure 5.3 Influence of O_2 concentration (0–8 vol.% O_2) on catalytic performance of 2Cu/ZSM-5 at HC/NOx = 8 in C_3H_6-SCR process: (a) NOx conversion, (b) C_3H_6 conversion, and (c) CO conversion.

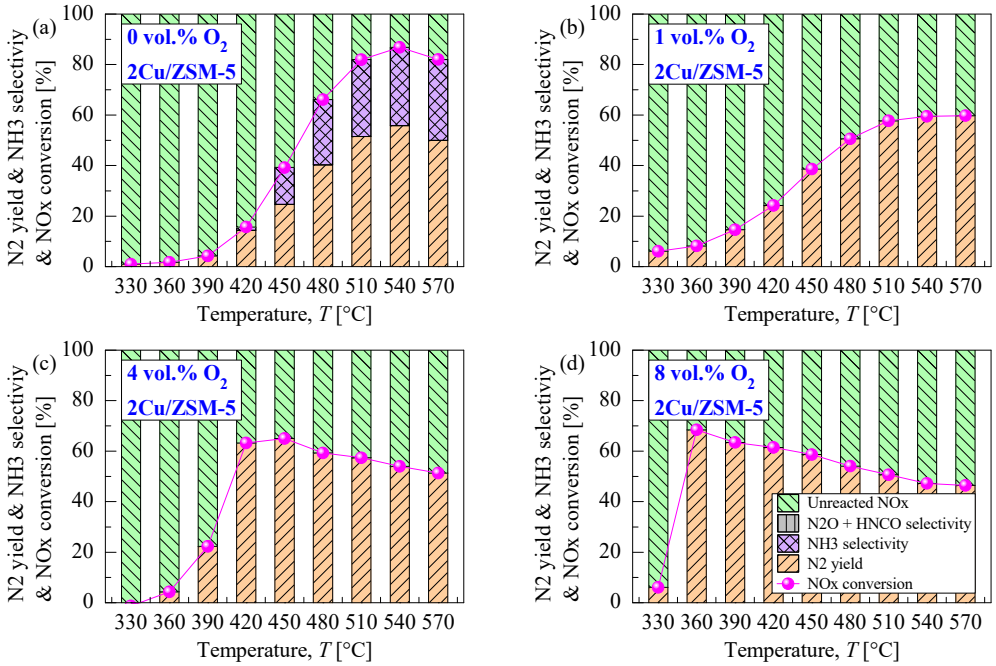

Figure 5.4 Influence of O_2 concentration (0–8 vol.% O_2) on N_2 yield of 2Cu/ZSM-5 at HC/NOx = 8 in C_3H_6-SCR process: (a) 0 vol.% O_2, (b) 1 vol.% O_2, (c) 4 vol.% O_2, and (d) 8 vol.% O_2.

5.4 Effect of CO_2 concentration in C_4H_{10}-SCR process

CO_2 is unavoidable in diesel exhaust emission, and it is also one of the main products in the ideal reduction reaction of NOx with hydrocarbons. The influence of the CO_2 concentration on the catalytic activity is shown in Figure 5.5 for the 2Cu/ZSM-5 catalyst, which exhibited the highest de-NOx performance among the prepared Cu/zeolites. A higher CO_2 concentration in the feed gas was unfavorable for NOx conversion at reaction temperatures ranging from 390℃ to 510℃, where a drop in the NOx conversion from 38.3% (0 vol.% CO_2) to 32.4% (1 vol.% CO_2), 29.0% (5 vol.% CO_2), and 26.5% (10 vol.% CO_2) at 420℃ was observed (Figure 5.5(a)), suggesting that NOx reduction was inhibited by CO_2 in the C_4H_{10}-SCR process. Increasing the CO_2 concentration in the feed gas had no effect on NOx conversion at reaction temperatures above 510℃, even in the presence of 10 vol.% CO_2. The negative effect of CO_2 on the de-NOx performance may be related to partial oxidation of the reductant during the C_4H_{10}-SCR reaction, as shown in Figure 5.5(b). Indeed, increasing the CO_2 concentration induced a decrease in the C_4H_{10} conversion above 390℃ as follows: 18.8% (0 vol.% CO_2) > 18.7% (1 vol.% CO_2) > 16.9% (5 vol.% CO_2) > 16.2% (10 vol.% CO_2) at 420℃. Furthermore, the addition of CO_2 also negatively affected the CO conversion, as shown in Figure 5.5(c), with a significant decrease from 78.1% (0 vol.% CO_2) to 56.0% (1 vol.% CO_2), 35.7% (5 vol.% CO_2), and 7.5% (10 vol.% CO_2) at 525℃. In addition, the light-off temperature (LOT_{50}) of CO shifted toward the higher temperature windows, moving from 508℃ (0 vol.% CO_2) to 522℃ (1 vol.% CO_2), 532℃ (5 vol.% CO_2), and 543℃ (10 vol.% CO_2). Similar results can be found in previous studies, in which CO_2 molecules caused heavy competitive adsorption between CO_2 and NOx on the catalyst surface [222, 223], leading to suppression of the formation of nitrates, which are key reaction intermediates for NOx reduction [219]. Thus, the presence of CO_2 in the feed gas had a strongly inhibitory effect on

the C_4H_{10}-SCR.

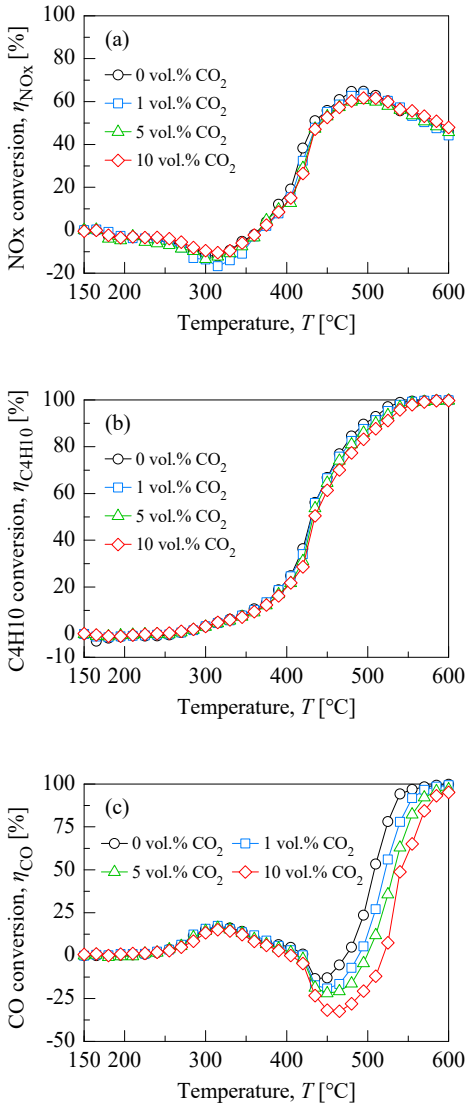

Figure 5.5 Influence of CO_2 concentration (0–10 vol.% CO_2) on catalytic performance of 2Cu/ZSM-5 at HC/NOx = 6 in C_4H_{10}-SCR process: (a) NOx conversion, (b) C_4H_{10} conversion, and (c) CO conversion.

5.5 Effect of O_2 concentration in C_4H_{10}-SCR process

Some reaction schemes have been suggested for the HC-SCR, although the process is still not fully understood. One of the main mechanisms of operation of zeolite-based catalysts suggests that NO is first oxidized to NO_2, followed by reduction by the reductant [134, 224]. The presence of O_2 is essential for the HC-SCR because O_2 can oxidize hydrocarbons, leading to the formation of reaction intermediates, CxHyOz (oxygenated hydrocarbons), that can react with NOx [117, 225]. The influence of the O_2 concentration on the catalytic performance of the 2Cu/ZSM-5 catalyst is shown in Figure 5.6. Although the maximum NOx conversion was not affected by the presence of O_2, the temperature window for the maximum NOx conversion shifted substantially to lower temperatures with an increase in O_2 concentration, i.e., moving from 600℃ (1 vol.% O_2) to 525℃ (4 vol.% O_2), and 465℃ (8 vol.% O_2). These findings are attributed to the enhanced partial oxidation of C_4H_{10} by O_2 at relatively low temperatures with an increase in the O_2 concentration, as shown in Figure 5.6(b): for instance, the light-off temperature (LOT_{50}) of C_4H_{10} was decreased from 508℃ (1 vol.% O_2) to 458℃ (4 vol.% O_2) and 410℃ (8 vol.% O_2). Notably, the NOx conversion gradually increased above 435℃, eventually reaching 97.9% NOx conversion at 600℃ in the absence of O_2. However, these reaction conditions led to an unexpected side-reaction, as shown in Figure 5.7(a), forming NH_3 at reaction temperatures above 510℃. When more than 1 vol.% O_2 was present in the feed gas (Figure 5.7(b)–(d)), the NOx conversion was consistent with the N_2 yield, suggesting that NOx was reduced to N_2 without any accompanying side-reactions. The formation of NH_3 as an intermediate during HC-SCR has been reported [226, 227], and it could be conjectured that the formation of NH_3 was involved in the reaction of NOx with the partially oxidized hydrocarbons. It is also clear that increasing the O_2 concentration highly enhanced the CO oxidation, as illustrated in Figure 5.6(c).

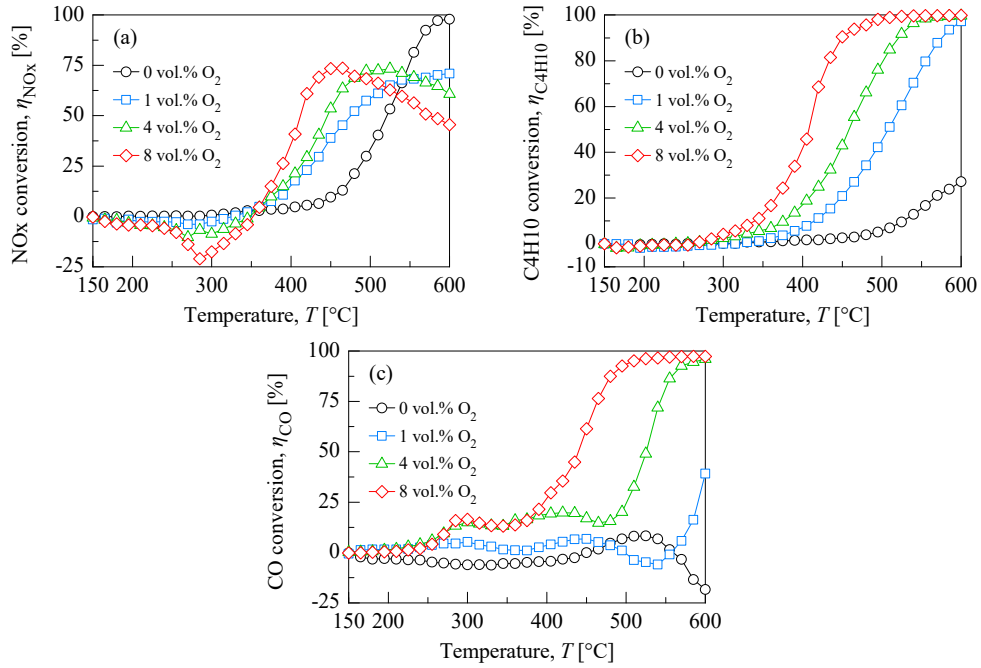

Figure 5.6 Influence of O_2 concentration (0–8 vol.% O_2) on catalytic performance of 2Cu/ZSM-5 at HC/NOx = 6 in C_4H_{10}-SCR process: (a) NOx conversion, (b) C_4H_{10} conversion, and (c) CO conversion.

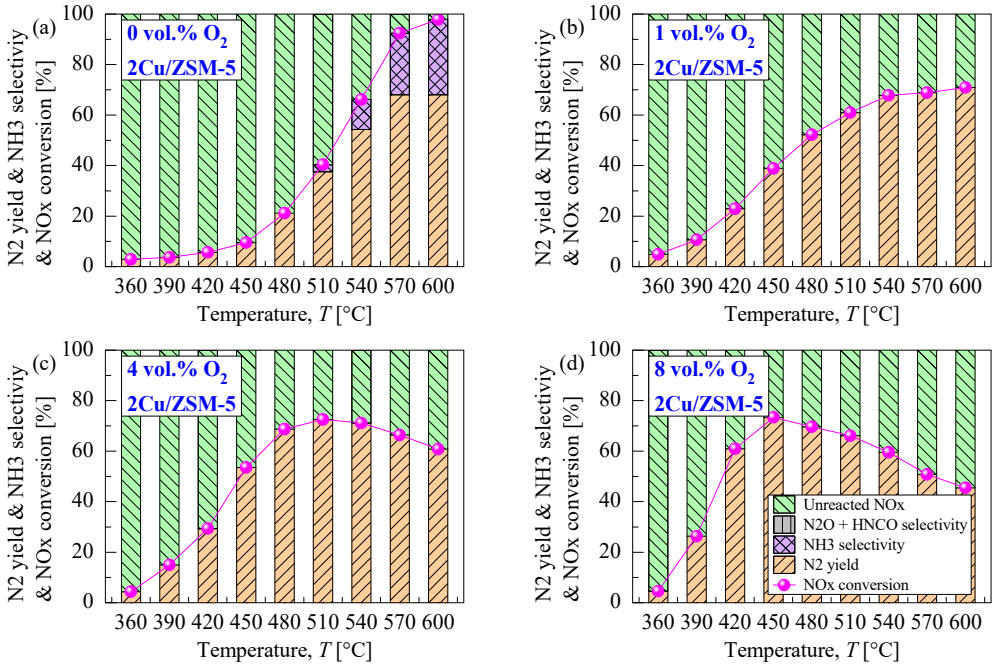

Figure 5.7 Influence of O_2 concentration (0–8 vol.% O_2) on N_2 yield of 2Cu/ZSM-5 at HC/NOx = 6 in C_4H_{10}-SCR process: (a) 0 vol.% O_2, (b) 1 vol.% O_2, (c) 4 vol.% O_2, and (d) 8 vol.% O_2.

5.6 Effect of hydrothermal aging in C_3H_6-SCR process

The catalytic activities of the 1Cu/SSZ-13, 5Cu/BETA, and 5Cu/BETA catalysts before aging and after hydrothermal aging at 700℃ for the C_3H_6-SCR are compared in Figures 5.8–5.10. All the hydrothermally aged catalysts exhibited a similar trend in that the catalytic activity for NOx conversion shifted toward higher temperature regions: for example, the temperature of the maximum de-NOx performance over the 5Cu/ZSM-5 catalyst shifted from 405℃ to 525℃ after hydrothermal aging, as shown in Figure 5.9(a). Compared to the hydrothermally aged 1Cu/SSZ-13, the hydrothermally aged 5Cu/ZSM-5 and 5Cu/BETA catalysts showed significant decrease in the maximum NOx conversion, and particularly, 5Cu/BETA was severely deactivated compared to 1Cu/SSZ-13 and 5Cu/ZSM-5. The rate of C_3H_6 oxidation was also affected by hydrothermal aging. The decreased C_3H_6 conversion could explain the drop in de-NOx performance after hydrothermal aging, because the partial oxidation of C_3H_6 into reaction intermediates (CxHyOz, oxygenated hydrocarbons) was obviously inhibited across entire reaction temperatures. Note that CO oxidation was severely deactivated for the hydrothermally aged Cu/zeolite catalysts because these catalysts could not oxidize the CO, even at higher temperatures.

The catalytic deactivation is usually induced by various phenomena due to the presence of many components that play different roles during the catalytic reaction. In general, the catalytic deactivation of zeolite-based SCR catalysts by hydrothermal aging can occur through three mechanisms, including dealumination of zeolite support, pore elimination, and sintering of metal oxides [228]. To investigate the hydrothermal aging, the characterization of hydrothermally aged catalysts will be further discussed in section 5.9.

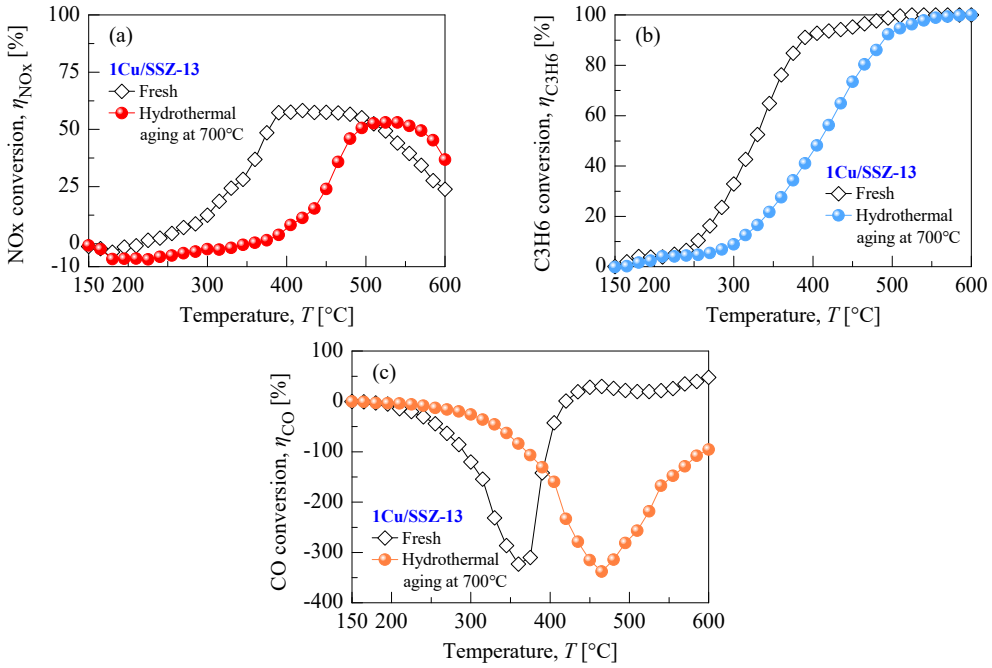

Figure 5.8 Catalytic activities of 1Cu/SSZ-13 before and after hydrothermal aging at 700°C for 12 h in C_3H_6-SCR (hydrothermal aging: 8 vol.% O_2 + 5 vol.% H_2O + balance N_2 at GHSV = 12,500 h^{-1}): (a) NOx conversion, (b) C_3H_6 conversion, and (c) CO conversion.

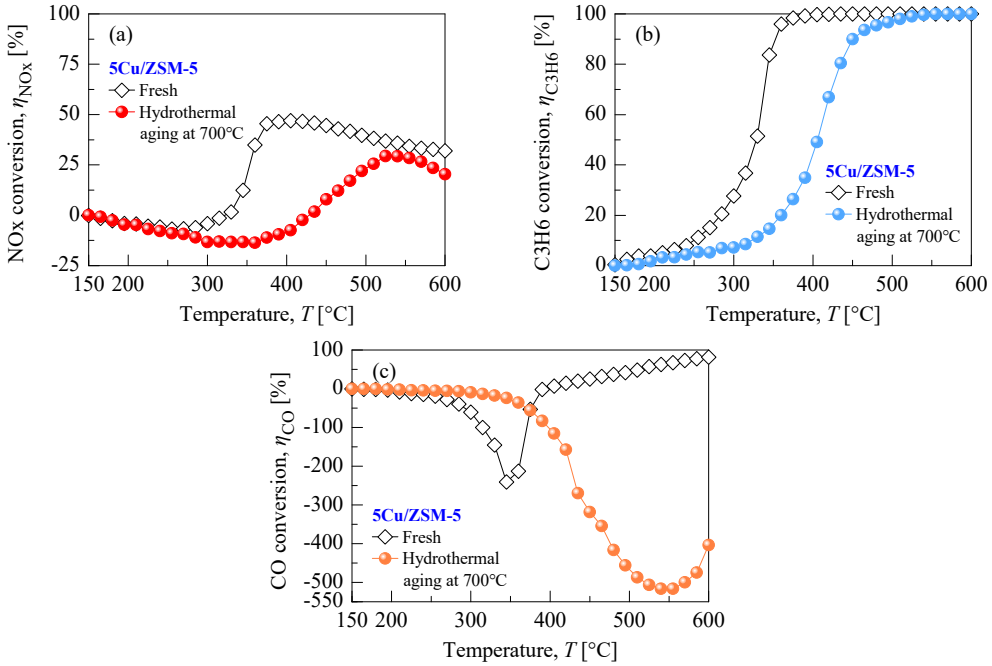

Figure 5.9 Catalytic activities of 5Cu/ZSM-5 before and after hydrothermal aging at 700°C for 12 h in C_3H_6-SCR (hydrothermal aging: 8 vol.% O_2 + 5 vol.% H_2O + balance N_2 at GHSV = 12,500 h^{-1}): (a) NOx conversion, (b) C_3H_6 conversion, and (c) CO conversion.

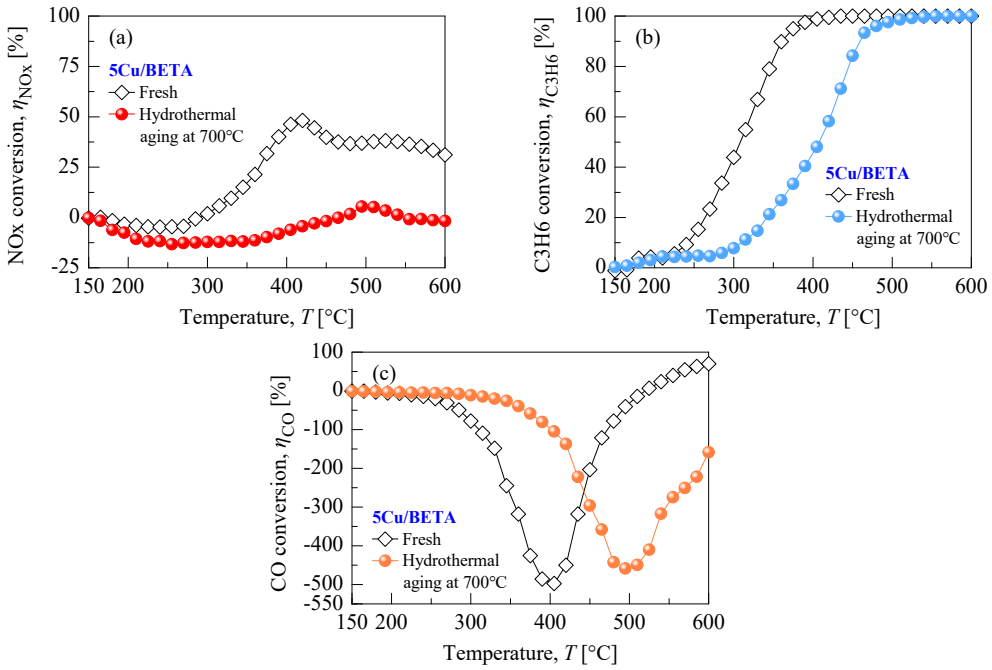

Figure 5.10 Catalytic activities of 5Cu/BETA before and after hydrothermal aging at 700°C for 12 h in C_3H_6-SCR (hydrothermal aging: 8 vol.% O_2 + 5 vol.% H_2O + balance N_2 at GHSV = 12,500 h^{-1}): (a) NOx conversion, (b) C_3H_6 conversion, and (c) CO conversion.

5.7 Effect of hydrothermal aging in C_4H_{10}-SCR process

The catalytic activities of the 5Cu/zeolite catalysts before and after hydrothermal aging at 700℃ for the C_4H_{10}-SCR are compared in Figure 5.11. The hydrothermally aged 5Cu/ZSM-5 and 5Cu/BETA catalysts showed a identical trend whereby the de-NOx performance substantially decreased at reaction temperatures ranging from 350℃ to 555℃ and also temperature windows for the maximum NOx conversion shifted toward higher temperature regions (Figure 5.11(a) and (b)); the temperature of the maximum NOx conversion shifted from 465℃ to 600℃ for 5Cu/ZSM-5 and from 450℃ to 585℃ for 5Cu/BETA. This behavior is attributed to the C_4H_{10} oxidation, which was obviously inhibited over the entire reaction temperature range (Figure 5.11(c) and (d)). The hydrothermally aged Cu/zeolite catalysts showed a shift of the light-off temperature (LOT_{50}) of C_4H_{10} toward higher temperatures, where that of 5Cu/ZSM-5 moved from 422℃ (fresh) to 559℃ (hydrothermal aging) and that of 5Cu/BETA also moved from 435℃ (fresh) to 498℃ (hydrothermal aging). Note that CO oxidation was severely deactivated for the hydrothermally aged catalysts because these catalysts could not oxidize CO, even at high temperatures (Figure 5.11(e) and (f)). Hydrothermally induced deactivation of catalysts can occur through chemically and physically complex phenomenon, i.e., loss of the catalytic surface area and support area and chemical transformation of the active materials [228, 229]. As mentioned in the previous section, the characterization of hydrothermally aged catalysts will be further discussed in section 5.9 to investigate the effect of hydrothermal aging on the physical and chemical properties of 5Cu/zeolite catalysts.

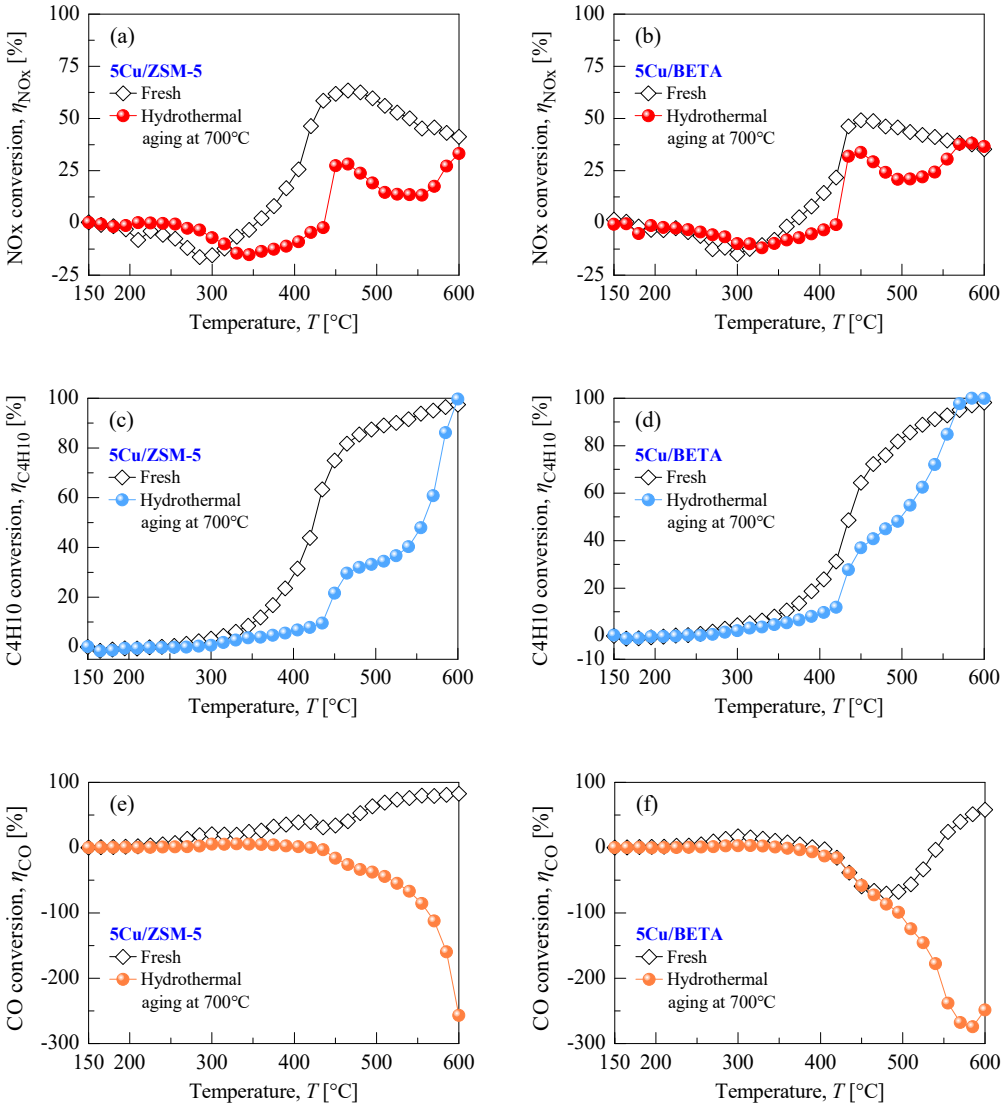

Figure 5.11 Catalytic activities of 5Cu/ZSM-5 and 5Cu/BETA before and after hydrothermal aging at 700°C for 12 h in C_4H_{10}-SCR (hydrothermal aging: 8 vol.% O_2 + 5 vol.% H_2O + balance N_2 at GHSV = 12,500 h^{-1}): (a), (b) NOx conversion, (c), (d) C_4H_{10} conversion, and (e), (f) CO conversion.

5.8 Stability test in C_4H_{10}-SCR process

Some researchers reported catalytic deactivation of the HC-SCR due to coking effect of hydrocarbons on the catalyst surface, which led to a severe deactivation of the de-NOx ability and shortened the lifetime of the catalyst [122, 230, 231]. Figure 5.12 shows the NOx conversion of the 5Cu/zeolites over a long-term test at steady-state 450°C. There was a slight fluctuation of the NOx conversion over the 5Cu/zeolites, and both 5Cu/ZSM-5 and 5Cu/BETA retained the initial de-NOx ability until the end of the stability test; the mean NOx conversion was 63.9 ± 2.3% for 5Cu/ZSM-5 and 57.1 ± 1.8% for 5Cu/BETA. From these findings, there was no catalytic deactivation induced by coke formation by the hydrocarbons within 24 h.

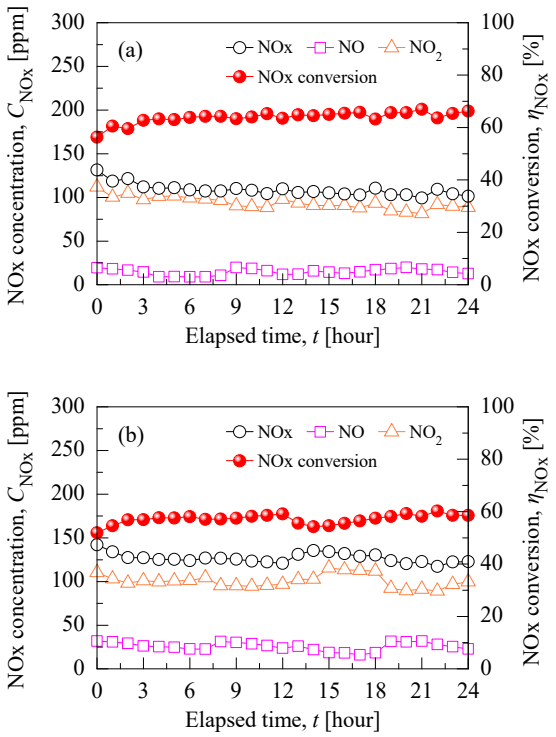

Figure 5.12 Catalytic performance of 5Cu/zeolite catalysts over long-term test for 24 h in C_4H_{10}-SCR at steady-state 450°C, HC/NOx = 6, and GHSV = 12,500 h^{-1}: (a) 5Cu/ZSM-5 and (b) 5Cu/BETA

5.9 Characterization of hydrothermally aged catalysts

The physical properties of the fresh and hydrothermally aged Cu/zeolite catalysts were analyzed by N_2–isotherms, as summarized in Table 5.2. After hydrothermal aging, the BET specific surface area (A_{BET}) decreased from 823.6 m^2/g to 809.5 m^2/g for 1Cu/SSZ-13 and from 390.4 m^2/g to 380.9 m^2/g for 5Cu/ZSM-5. The BET specific surface area of the hydrothermally aged 5Cu/BETA dramatically decreased by 49%, from 495.2 m^2/g to 252.2 m^2/g. The same trend was also observed for the total pore volume (V_P) and average pore diameter (D_P). These observations indicate that hydrothermal aging intensified collapse of the pore structures in the zeolites.

To investigate the damage to the zeolite frameworks, the powder XRD profiles are compared before and after hydrothermal aging in Figure 5.13. The inherent zeolite peaks of the 1Cu/SSZ-13, 5Cu/ZSM-5, and 5Cu/BETA remained intact even after hydrothermal aging, whereas the crystallinity of the zeolites decreased by 7.8% (1Cu/SSZ-13 at $2\theta = 9.64°$), 22.8% (5Cu/ZSM-5 at $2\theta = 23.12°$), and 37.3% (5Cu/BETA at $2\theta = 22.48°$)

The crystallographic positions of Al atoms are analyzed after hydrothermal aging, as

Table 5.2 Physical properties of 5Cu/zeolite catalysts before and after hydrothermal aging at 700℃ for 12 h.

Catalysts	A_{BET} (m^2/g)	V_P (cm^3/g)	V_{Micro} (cm^3/g)	D_P (nm)
1Cu/SSZ-13 (fresh)	823.6	0.3440	0.3023	1.6707
1Cu/SSZ-13 (aged)	809.5	0.4189	0.3047	2.0670
5Cu/ZSM-5 (fresh)	390.4	0.6574	0.1445	6.7357
5Cu/ZSM-5 (aged)	380.9	0.6288	0.1383	6.6033
5Cu/BETA (fresh)	495.2	0.5373	0.1453	4.3401
5Cu/BETA (aged)	252.2	0.4749	0.0681	7.5321

shown in Figure 5.14. The dealumination of the respective Cu/zeolites did not occur, as there was no notable evidence from the ^{27}Al MAS-NMR spectra; chemical shift of ^{27}Al at 0 ppm (δ_{27Al} = 0 ppm) was not observed over the hydrothermally aged Cu/zeolite catalysts.

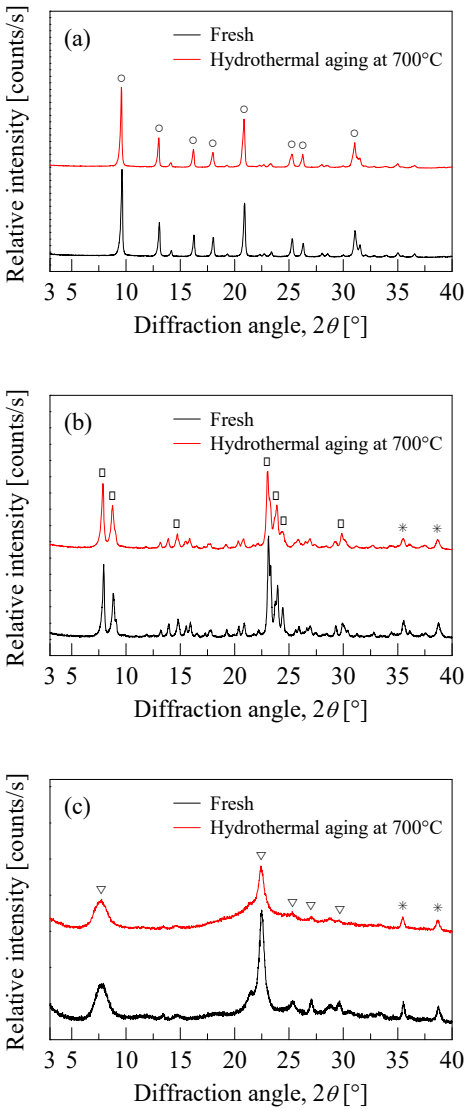

Figure 5.13 Powder X-ray diffraction (XRD) patterns of Cu/zeolite catalysts before and after hydrothermal aging at 700°C for 12 h: (a) 1Cu/SSZ-13, (b) 5Cu/ZSM-5, and (c) 5Cu/BETA.

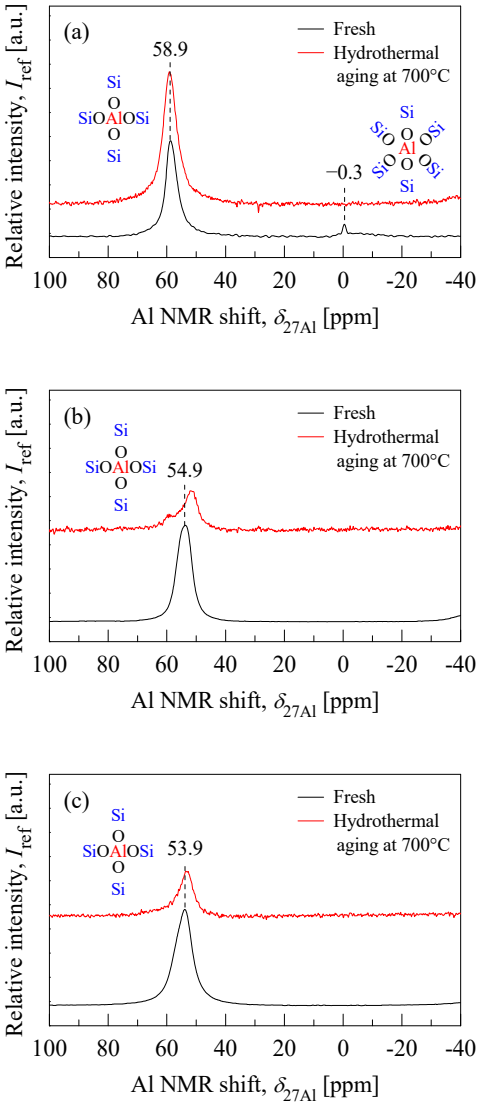

Figure 5.14 Solid-state ^{27}Al MAS–NMR spectra of Cu/zeolite catalysts before and after hydrothermal aging at 700°C for 12 h: (a) 1Cu/SSZ-13, (b) 5Cu/ZSM-5, and (c) 5Cu/BETA.

5.10 Summary

The effect of coexistent gases (CO_2 and O_2) and hydrothermal aging on the catalytic activity were investigated in Chapter 5. In the C_3H_6-SCR process, O_2 is essential gas in the HC-SCR process, whereby improving low-temperuatre de-NOx performance with an increase in O_2 concentration from 0 to 8 vol.%. Furthermore, more O_2 in the feed gas enhanced the partial oxidation of hydrocarbons. However, a negative effect was observed when CO_2 was introduced in the feed gas because NOx adsorption and partial oxidation of hydrocarbons were highly inhibited by coexistent CO_2. The removal of CO_2 in the feed gas improved the NOx conversion between 300 and 345℃. In the case of C_4H_{10}-SCR, O_2 had a positive effect on the de-NOx performance, CO oxidation, and partial oxidation of C_4H_{10}, improving the catalytic activity at relatively low temperatures. When O_2 was not introduced in the feed gas, the NOx conversion gradually increased with the reaction temperature, reaching 98% NOx conversion, but these conditions induced an undesired side-reaction, producing a large amount of NH_3.

The catalytic activities of Cu/zeolite catalysts were sensitive to the hydrothermal aging. In the C_3H_6- and C_4H_{10}-SCR process, a drop in NOx conversion after hydrothermal aging was attributed to an inhibition effect of partial oxidation of hydrocarbons. The hydrothermal aging also induced the collapse of the pore structures of zeolite and a drop in the zeolite crystallinity. However, the Cu/zeolite catalysts could tolerate the catalytic activities at steady state because there was no catalytic deactivation induced by coke formation within 24 h.

Chapter 6. Conclusions

6.1 Concluding remarks

Experimental investigation on the reduction of NOx emissions by HC-SCR process over the Cu-impregnated zeolite-based catalysts has been presented and discussed in this research thesis for the practical application of passive type HC-SCR system. The Cu/zeolite catalysts were prepared by an incipient wetness impregnation method by varying the Cu loading in a range of 1–10 wt%. The zeolite supports have different their frameworks, including SSZ-13 (CHA framework), ZSM-5 (MFI framework), and BETA (BEA framework). A series of Cu/zeolite catalysts were explored in detail for the main purpose of reducing NOx emissions by the 'C_3H_6-SCR' and 'C_4H_{10}-SCR' process. Several techniques, including HC/NOx ratio, hydrocarbon reductant, Cu content, zeolite framework, coexistent gas, and reaction environment (catalytic reactor system), were systematically explored and their effects on the NOx removal efficiency of Cu/zeolite catalysts were assessed. The key conclusions drawn from the experimental results of this thesis are summarized.

In chapter 1, recent de-NOx techniques and relevant reaction mechanisms using automotive catalysts were reviewed including HC-SCR. To investigate the effectiveness of HC-SCR, major preceding research was reviewed for various catalytic components and reducing agents.

In chapter 2, the parent zeolites and Cu/zeolites were characterized by various technique. The loading levels of Cu metal species were close to the theoretical loading amount, suggesting successfully introduction of Cu species. The Cu loading led to a drop of BET specific surface area because Cu species covered both the internal and external surface of zeolite, resulting in blocking the accessible zeolite pores. The XRD patterns demonstrated that the impregnation of Cu did not affect any modification of the respective zeolite structures.

When increasing the Cu loading, chemical shift of ^{27}Al shifted to lower region, indicating the variation of average Al–O–Si angles in the zeolite framework. The valence states of Cu species were mainly presented as isolated Cu^{2+}, d-d transition of Cu^{2+}, and CuO clusters. The Cu/zeolites were more in favorable for the formation of CuO clusters with an increase in the Cu loading. The intra-crystalline diffuse diameter of respective zeolites affected the particle diameter of Cu, which was severely agglomerated over the SSZ-13 zeolite.

In chapter 3, Cu/zeolite catalysts were evaluated for the main purpose of reducing NOx emissions by the C_3H_6-SCR process in the presence of O_2, CO, CO_2, and H_2O. To reach a high NOx conversion, a high HC/NOx ratio was needed. Increasing the HC/NOx ratio was favorable for the catalytic activity because more reducing agent could be available during the C_3H_6-SCR process. Among the prepared Cu/zeolite catalysts, 2Cu/ZSM-5 demonstrated the highest NOx conversion to N_2 (68.5% at T = 360°C) at the highest HC/NOx ratio, followed by 1Cu/SSZ-13 (58.2% at T = 420°C) and 10Cu/BETA (56.1% at T = 375°C). Thus, the ZSM-5 zeolite, with a medium pore framework, was better suited for the C_3H_6-SCR process than SSZ-13, with a small pore framework, and BETA, with a large pore framework. The presence of isolated Cu^{2+} ions provided active sites for NOx reduction.

In chapter 4, the effects of the zeolite framework and Cu loading on the catalytic activity for the C_4H_{10}-SCR were evaluated. The Cu loading improved the NOx conversion and shifted the temperature window of the maximum NOx conversion to lower regions compared to those for the parent zeolites. 2Cu/ZSM-5 exhibited the best de-NOx performance with nearly 74% at 465°C, followed by 10Cu/BETA (58% at T = 465°C) and 1Cu/SSZ-13 (38% at T = 585°C). These results were related to the effect of geometry-limited diffusion of C_4H_{10} in the respective zeolite channel system, in which the reductant had easy access to the active sites in the channels of ZSM-5 and BETA zeolite, but C_4H_{10} was highly restricted in the SSZ-13

channels.

In chapter 5, the effects of coexistent gases and hydrothermal aging on the catalytic activity were investigated in both C_3H_6- and C_4H_{10}-SCR. Increasing the O_2 concentration in the feed gas had a positive effect on the de-NOx performance because the partial oxidation of hydrocarbons was enhanced at relatively low temperature with an increase in O_2 concentration, indicating that O_2 is essential gas in HC-SCR process. However, a negative effect was observed when CO_2 was introduced in the feed gas because NOx adsorption and partial oxidation of hydrocarbons were highly inhibited by coexistent CO_2. When O_2 was not introduced in the feed gas, the NOx conversion increased at a relatively higher reaction temperature, reaching 98% NOx conversion, but this condition induced an undesired side-reaction, producing a large amount of NH_3. The drop in NOx conversion after hydrothermal aging was attributed to the inhibitory effect of the partial oxidation of hydrocarbons. The hydrothermal aging also induced the collapse of micropores, Cu sintering, and a drop in the zeolite crystallinity, thereby deactivating the catalytic activities.

6.2 Future work and recommendations

- The reaction mechanism on the selective catalytic reduction of NOx by hydrocarbon has been debatable despite the extensive reviews. Although some possible reaction mechanisms or reaction pathways have been proposed, general reaction mechanisms are not available due to the different types of catalysts and reaction conditions. In situ Diffuse Reflectance Infrared Fourier Transform (DRIFT) spectroscopy is fundamental to investigate the reaction mechanism because it provides detailed spectroscopic information of how reaction intermediates affect the reactivity of NOx.

- To effectively reduce vehicle emissions, both the engine controls and active after-treatment system should be considered because the HC-SCR catalysts is highly dependent on the reaction temperatures and coexistent gas conponents. Therefore, EGR rate should be minimized, otherwise more higher reaction temperature is required if EGR rate increases. The feasible solution is the close-coupled HC-SCR near the exhaust manifold, thereby reducing the time to light-off.
- The improvement of low-temperature de-NOx activity is essential below 300℃, especially for an on-board application. The feasible approach is the use of optimal promotors or additives that can improve the low-temperature catalytic activity and hydrothermal tolerance. Additionally, to produce hydrogen from the diesel fuel (utilizing the hydrogen effect) reformer catalysts is also a promising way to improve the de-NOx performance by integrating the reformer catalyst and HC-SCR catalyst.
- It is necessary to expand the laboratory-scale test of HC-SCR catalyst toward the real driving environment which is not steady-state condition. For evaluation of the HC-SCR catalysts under the transient condition, catalytic reactor was newly designed and relevant test was carried out that these results were not included in this thesis. Although this new reactor system is more complicated and needs some modifications, the new reactor system will contribute to better understand the catalytic behavior and reaction mechanism under transient environment.

List of References

[1] R. Diesel, Method of igniting and regulating combustion for internal-combustion engines, U.S. patent # US 673,160A (30 April 1901).

[2] L. Yang, V. Franco, A. Campestrini, J. German and P. Mock, NOx control technology for Euro 6 diesel passenger cars, *ICCT White Paper* (2015) pp.1-22

[3] T. Johnson, Vehicular Emissions in Review, *SAE International Journal of Engines* 9 (2) (2016) pp.1258-1275.

[4] E.G. Giakoumis, Driving and Engine Cycles, *Springer International Publishing* (2017) pp.1-408.

[5] M.V. Twigg, Catalytic control of emissions from cars, *Catalysis Today* 163 (2011) pp.33 41.

[6] Emission Standards, EU: cars and Light Trucks (accessed 13 January 2019). https://www.dieselnet.com/standards/eu/ld.php.

[7] R.N. de Carvalho, S.W. Botero and A.C.S. Villela, Fuel Economy and CO_2 Emission–A Comparison between Test Procedures and Driving Cycles, *SAE Technical* Paper 2012-36-0479 (2012).

[8] W. Berg, Legislation for the reduction of exhaust gas emissions. In: Gruden D. (eds.) Traffic and Environment. The Handbook of Environmental Chemistry, Vol 3. *Springer-Verlag Berlin Heidelberg* (2003) pp.175-253.

[9] Final Report of Joint Meeting between the Automobile Evaluation Standards Subcommittee, Energy Efficiency Standards Subcommittee of the Advisory Committee for Natural Resources and Energy and the Automobile Fuel Efficiency Standards Subcommittee, Automobile Transport Section, Land Transport Division of the Council for Transport Policy (Mar 2007) pp.1-51.

[10] World forum for harmonization of vehicles regulations (WP.29). Annex I. Terms of reference and rules of procedure of the world forum for harmonization of vehicle regulations (2012) pp.29-37.

[11] http://www.unece.org/trans/main/wp29/wp29wgs/wp29gen/wp29rep.html (accessed 13 January 2019).

[12] P. Bielaczyc, J. Woodburn and A. Szczotka, Exhaust Emissions of Gaseous and Solid Pollutants Measured over the NEDC, FTP-75 and WLTC Chassis Dynamometer Driving Cycles, *SAE Technical Paper* 2016-01-1008 (2016).

[13] S. Roy, M.S. Hegde and G. Madras, Catalysis for NOx abatement, *Applied Energy* 86 (2009) pp.2283-2297.

[14] E.S.J. Lox and B.H. Engler, Environmental Catalysis – Mobile Sources, in Environmental Catalysis (eds. G. Etrl, H. Knozinger and J. Weitkamp), *Wiley-VHC Verlag GmbH* (1999) pp.1-117.

[15] European Environment Agency (EEA), Emissions of the main air pollutants in Europe (2017) pp.5-23.

[16] Environmental Protection Agency (EPA), Control of Air Pollution From New Motor: Tier 2 Motor Vehicle Emissions Standards and Gasoline Sulfur Control Requirements, *Federal Register* 65 (2000) pp.6698-6870.

[17] Commission regulation (EC) No 692/2008 of 18 July 2008: implementing and amending Regulation (EC) No 715/2007 of the European Parliament and of the Council on type-approval of motor vehicles with respect to emissions from light passenger and commercial vehicles (Euro 5 and Euro 6) and on access to vehicle repair and maintenance information, *Official Journal of the European Union* (2008) pp.1-199.

[18] Central Environment Council, Future Policy for Motor Vehicle Emission Reduction (Eighth Report) (2005) pp.1-39.

[19] T. Helmut, G. Andreas, S. Jurgen, K. Michael, S. Johannes, B. Norbert, E. Kurt and S. Wolfgang, Diesel Engine Exhaust Emissions. In: K. Mollenhauer and H. Tschoeke (eds.) Handbook of Diesel Engines, *Springer-Verlag Berlin Heidelberg* (2010) pp.417-485.

[20] P.G. Gray and J.C. Frost, Impact of Catalysis on Clean Energy in Road Transportation, *Energy & Fuels* 12 (1998) pp.1121-1129.

[21] M.V. Twigg, Progress and future challenges in controlling automotive exhaust gas emissions, *Applied Catalysis B: Environmental* 70 (2007) pp.2-15.

[22] A. Stanislaus, A. Marafi and M.S. Rana, Recent advances in the science and technology of ultra low sulfur diesel (ULSD) production, *Catalysis Today* 153 (2010) pp.1-68.

[23] B. Kegl, M. Kegl and S. Pehan, Guidelines for Improving Diesel Engine Characteristics. In: Green Diesel Engines, Lecture Notes in Energy, Vol 12. *Springer, London* (2013) pp.51-93.

[24] W.B. Kolb, A.A. Papadimitriou, R.L. Cerro, D.D. Leavitt and J.C. Summers, The Ins and Outs of Coating Monolithic Structures, *Journal of Chemical Engineering* Progress 89 (1993) pp.61-67.

[25] A. Cybulski and J.A. Moulijn, Monoliths in Heterogeneous Catalysis, *Catalysis Reviews:*

Science and Engineering 36 (1994) pp.179-270.

[26] J.L. Williams, Monolith structures, materials, properties and uses, *Catalysis Today* 69 (2001) pp.3-9.

[27] P. Avila, M. Montes and E.E. Miro, Monolithic reactors for environmental applications. A review on preparation technologies, *Chemical Engineering Journal* 109 (2005) pp.11-36.

[28] S. Hirose, H. Yamamoto, H. Suenobu, H. Sakamoto, F. Katsube, P. Busch, A. Martin, R. Kai and C.D. Vogt, Development of High Porosity Cordierite Honeycomb Substrate for SCR Application to Realize High NOx Conversion Efficiency and System Compactness, *SAE International Journal of Materials and Manufacturing* 7 (2014) pp.682-687, SAE 2014-01-1528.

[29] S. Govender and H.B. Friedrich, Monoliths: A Review of the Basics, Preparation Methods and Their Relevance to Oxidation, *Catalysts* 7 (2017) pp.1-29.

[30] K.B. Binder, Diesel Engine Combustion. In: K. Mollenhauer and H. Tschoeke (eds.) Handbook of Diesel Engines, *Springer-Verlag Berlin Heidelberg* (2010) pp.61-75.

[31] H. Peng, Y. Chi, L. Shi and K. Deng, Effects of exhaust gas recirculation (EGR) on combustion and emissions during cold start of direct injection (DI) diesel engine, *Energy* 33 (2008) pp.471-479.

[32] A. Maiboom, X. Tauzia and J.-F. Hetet, Experimental study of various effects of exhaust gas recirculation (EGR) on combustion and emissions of an automotive direct injection diesel engine, *Energy* 33 (2008) pp.22-34.

[33] A. Maiboom, X. Tauzia, S.R. Shah and J.-F. Hetet, Experimental Study of an LP EGR System on an Automotive Diesel Engine, compared to HP EGR with respect to PM and NOx Emission and Specific Fuel Consumption, *SAE International Journal of Engines* 2 (2) (2009) pp.597-610.

[34] H.-M. Kim, Y.-J. Kim and K.-H. Lee, A study of the characteristics of Mixture Formation and Combustion in a PCCI Engine Using an Early Multiple Injection Strategy, *Energy & Fuels* 22 (2008) pp.1542-1548.

[35] C.B. Granda, L. Zhu and M.T. Holtzapple, Sustainable liquid biofuels and their environmental impact, *Environmental Progress* 26 (2007) pp.233-250.

[36] H.K. Baek, Hyundai Motor Group's Solution in Powertrain Technologies, *Presentation at JSAE/SAE Powertrains, Fuels & Lubricants*, Kyoto, August 2015.

[37] J.C. Summers and L.L Hegedus, Effects of platinum and palladium impregnation on the

performance and durability of automobile exhaust oxidizing catalysts, *Journal of Catalysis* 51 (1978) pp.185-192.

[38] S. Matsumoto, Recent advances in automobile exhaust catalysts, *Catalysis Today* 90 (2004) pp.183-190.

[39] R.M. Heck and R.J. Farrauto, Automobile exhaust catalysts, *Applied Catalysis A: General* 221 (2001) pp.443-457.

[40] J. Kaspar, P. Fornasiero and N. Hickey, Automotive catalytic converters: current status and some perspectives, *Catalysis Today* 77 (2003) pp.419-449.

[41] J. Wang, H. Chen, Z. Hu, M. Yao and Y. Li, A Review on the Pd-Based Three-Way Catalyst, *Catalysis Reviews* 57 (2015) pp. 79-144.

[42] H. Muraki and G. Zhang, Design of advanced automotive exhaust catalysts, *Catalysis Today* 63 (2000) pp.337-345.

[43] D.D. Beck and C.J. Carr, Effects of High-Temperature Aging on the Dispersion of Rh/ Al_2O_3, *Journal of Catalysis* 144 (1993) pp.296-310.

[44] J. Kaspar, P. Fornasiero and M. Graziani, Use of CeO_2-based oxides in the three-way catalysis, *Catalysis Today* 50 (1999) pp.285-298.

[45] Z. Han, J. Wang, H. Yan, M. Shen, J. Wang, W. Wang and M. Yang, Performance of dynamic oxygen storage capacity, water-gas shift and steam reforming reactions over Pd-only three-way catalysts, *Catalysis Today* 158 (2010) pp.481-489.

[46] J. Wang, M. Shen, J. Wang and W. Wang, Steam effects over Pd/$Ce_{0.67}Zr_{0.33}O_2$ three-way catalyst, *Journal of Rear Earths* 29 (2011) pp.217-224.

[47] N. Takahashi, H. Shinjoh, T. Iijima, T. Suzuki, K. Yamazaki, K. Yokota, H. Suzuki, N. Miyoshi, S.-I. Matsumoto, T. Tanizawa, T. Tanaka, S.-S. Tateishi and K. Kasahara, The new concept 3-way catalyst for automotive lean-burn engine: NOx storage and reduction catalyst, *Catalysis Today* 27 (1996) pp.63-69.

[48] W.S. Epling, L.E. Campbell, A. Yezerets, N.W. Currier and J.E. Parks II, Overview of the Fundamental Reactions and Degradation Mechanisms of NOx Storage/ Reduction catalysts, *Catalysis Reviews: Science and Engineering* 46 (2004) pp.163-245.

[49] F. Basile, G. Fornasara, A. Grimandi, M. Livi and A. Vaccari, Effect of Mg, Ca and Ba on the Pt-catalyst for NOx storage reduction, *Applied Catalysis B: Environmental* 69 (2006) pp.58-64.

[50] G. Liu and P.-X. Gao, A review of NOx storage/reduction catalysts: mechanism, materials and degradation studies, *Catalysis Science & Technology* 1 (2011) pp.552-568.

[51] N. Miyoshi, S. Matsumoto, K. Katoh, T. Tanaka, J. Harada, N. Takahashi, K. Yokota, M. Sigiura and K. Kasahara, Development of New Concept Three-Way Catalyst for Automotive Lean-Burn Engines, *SAE Technical Paper* 950809 (1995).

[52] S. Matsumoto, Y. Ikeda, H. Suzuki, M. Ogai and N. Miyoshi, NOx storage-reduction catalyst for automotive exhaust with improved tolerance against sulfur poisoning, *Applied Catalysis B: Environmental* 25 (2000) pp.115-124.

[53] K. Yamazaki, T. Suzuki, N. Takahashi, K. Yokota and M. Sugiura, Effect of the addition of transition metals of Pt/Ba/Al_2O_3 catalyst on the NOx storage-reduction catalysis under oxidizing conditions in the presence of SO_2, *Applied Catalysis B: Environmental* 30 (2001) pp.459-468.

[54] S. Matsumoto, Catalytic reduction of nitrogen oxides in automotive exhaust containing excess oxygen by NOx storage-reduction catalyst, *CATTECH* 4 (2000) pp.102-109.

[55] L. Castoldi, I. Nova, L. Lietti and P. Forzatti, Study of the effect of Ba loading for catalytic Activity of Pt-Ba/Al_2O_3 model catalysts, *Catalysis Today* 96 (2004) pp.43-52.

[56] H. Abdulhamid, E. Fridell and M. Skoglundh, Influence of the type of reducing agent (H_2, CO, C_3H_6 and C_3H_8) on the reduction of stored NOx in a Pt-Ba/Al_2O_3 model catalyst, *Topics in Catalysis* 30/31 (2004) pp.161-168.

[57] J.H. Kwak, D H. Kim, T. Szailer, C.H.F. Peden and J. Szanyi, NOx uptake mechanism on Pt/BaO/Al_2O_3 catalysts, *Catalysis Letters* 111 (2006) pp.119-126.

[58] C.M.L. Scholz, V.R. Gangwal, M.H.J.M. de Croon and J.C. Schouten, Influence of CO_2 and H_2O on NOx storage and reduction on a Pt-Ba-/γ-Al_2O_3 catalyst, *Applied Catalysis B : Environmental* 71 (2007) pp.143-150.

[59] W.S. Epling, C.H.F. Peden and J. Szanyi, Carbonate Formation and Stability on a Pt/BaO/γ-Al_2O_3 NOx Storage/Reduction Catalyst, *The Journal of Physical Chemistry C* 112 (2008) pp.10952-10959.

[60] X. Wang, Y. Yu and H. He, Effect of Co addition to Pt/Ba/Al_2O_3 system for NOx storage and reduction, *Applied Catalysis B: Environmental* 100 (2010) pp.19-30.

[61] K.S. Lee, A study on a LNT/DPF system for simultaneous removal of NOx and PM of diesel vehicles, Dissertation for the degree of Master, *Chonnam National University* (2013) pp.1-99.

[62] L. Castoldi, L. Righini, R. Matarrese, L. Lietti and P. Forzatti, Mechanistic aspects of the release and the reduction of NOx stored on Pt-Ba/Al_2O_3, *Journal of Catalysis* 328 (2015) pp.270-279.

[63] L. Lietti, P. Forzatti, I. Nova and E. Tronconi, NOx Storage Reduction over Pt–Ba/γ-Al_2O_3, *Journal of Catalysis* 204 (2001) pp.175-191.

[64] P. Forzatti, L. Castoldi, I. Nova, L. Lietti and E. Tronconi, NOx removal catalysis under lean conditions, *Catalysis Today* 117 (2006) pp.316-320.

[65] L. Olsson and E. Fridell, The Influence of Pt Oxide Formation and Pt Dispersion on the Reactions $NO_2 \Leftrightarrow NO + 1/2O_2$ over Pt/Al_2O_3 and $Pt/BaO/Al_2O_3$, *Journal of Catalysis* 210 (2002) pp.340-353.

[66] D. Bhatia, R.W. McCabe, M.P. Harold and V. Balakotaiah, Experimental and kinetic study of NO oxidation on model Pt catalysts, *Journal of Catalysis* 266 (2009) pp.106-119.

[67] R.D. Clayton, M.P. Harold, V. Balakotaiah and C.Z. Wan, Pt dispersion effects during NOx storage and reduction on $Pt/BaO/Al_2O_3$ catalysts, *Applied Catalysis B: Environmental* 90 (2009) pp.662-676.

[68] Babcock & Wilcox Co., Steam: its Generation and Use (35th Edition) pp.1-335.

[69] G. Qi, L. Wang and R.T. Yang, Low-Temperature Selective Catalytic Reduction (SCR) of NOx with NH_3 Over Zeolites and Metal-Based Catalysts and Recent Developments of H_2-SCR. In: I. Nova and E. Tronconi (eds) Urea-SCR Technology for deNOx After Treatment of Diesel Exhausts. Fundamental and Applied Catalysis, *Springer, New York, NY* (2014) pp.149-177.

[70] M. Koebel, M. Elsener and M. Kleemann, Urea-SCR: a promising technique to reduce NOx emissions from automotive diesel engines, *Catalysis Today* 59 (2000) pp.335-345.

[71] A.M. Bernhard, D. Peitz, M. Elsener, A. Wokaun and O. Krocher, Hydrolysis and thermolysis of urea and its decomposition byproducts biuret, cyanuric acid and melamine over anatase TiO_2, *Applied Catalysis B: Environmental* 115-116 (2012) pp.129-137.

[72] M. Koebel, M. Elsener and T. Marti, NOx-Reduction in Diesel Exhaust Gas with Urea and Selective Catalytic Reduction, *Combustion Science and Technology* 121 (1996) pp. 85-102.

[73] P.M. Schaber, J. Colson, S. Higgins, E. Dietz, D. Thielen, B. Anspach and J. Brauer, Study of the urea thermal decomposition (pyrolysis) reaction and importance to cyanuric acid production, *American Laboratory* 31 (1999) pp.13-21.

[74] H. Dong, S. Shuai and J. Wang, Effect of Urea Thermal Decomposition on Diesel NOx-SCR Aftertreatment Systems, *SAE Technical Paper* 2008-01-1544 (2008).

[75] A. Lundstrom, T. Snelling, P. Morsing, P. Gabrielsson, E. Senar and L. Olsson, Urea

decomposition and HNCO hydrolysis studied over titanium dioxide, Fe-Beta and γ-Alumina, *Applied Catalysis B: Environmental* 106 (2011) pp.273-279.

[76] J. Girard, G. Cavataio, R. Snow and C. Lambert, Combined Fe-Cu SCR Systems with Optimized Ammonia to NOx Ratio for Diesel NOx Control, *SAE International Journal of Fuels and Lubricants* 1 (2009) pp.606-610.

[77] S. Brandenberger, O. Krocher, M. Casapu, A. Tissler and R. Althoff, Hydrothermal deactivation of Fe-ZSM-5 catalysts for the selective catalytic reduction of NO with NH_3, *Applied Catalysis B: Environmental* 101 (2011) pp.649-659.

[78] O. Krocher, Aspects of catalyst development for mobile urea-SCR systems – From Vanadia-Titania catalysts to metal-exchanged zeolites, *Studies in Surface Science and Catalysis* 171 (2007) pp.261-289.

[79] P. Forzatti and L. Lietti, The reduction of NOx stored on LNT and combined LNT-SCR systems, *Catalysis Today* 155 (2010) pp.131-139.

[80] R. Snow, G. Cavatatio, D. Dobson, C. Montreuil and R. Hammerle, Calibration of a LNT-SCR Diesel Aftertreatment System, *SAE Technical Paper* 2007-01-1244 (2007).

[81] H.-Y. Chen, E.C. Weigert, J.M. Fedeyko, J.P. Cox and P.J. Andersen, Advanced Catalysts for Combined (NAC+SCR) Emission Control Systems, *SAE Technical Paper* 2010-04-12 (2010).

[82] T. Maunula, NOx Reduction with the Combinations on LNT and SCR in Diesel Applications, *SAE International Journal of Materials and Manufacturing* 7 (2013) pp.195-206.

[83] T. Wittka, B. Holderbaum, T. Maunula and M. Weissner, Development and Demonstration of LNT+SCR System for Passenger Car Diesel Applications, *SAE International Journal of Engines* 7 (2014) pp.1269-1279.

[84] C. Gable and S. Gable, Blue TEC Clean Diesel Technology (Accessed 13 January 2019), https://www.thoughtco.com/bluetec-clean-diesel-technology-85602

[85] B. Pereda-Ayo, D. Duraiswami, J.J. Delgado, R. Lopez-Fonseca, J.J. Calvino, S. Bernal and J.R. Gonzalez-Velasco, Tuning operational conditions for efficient NOx storage and reduction over a Pt–Ba/Al_2O_3 monolith catalyst, *Applied Catalysis B: Environmental* 96 (2010) pp.329-337.

[86] B. Pereda-Ayo, D. Duraiswami, J.A. Gonzalez-Marcos and J.R. Gonzalez-Velasco, Performance of NOx storage–reduction catalyst in the temperature–reductant concentration domain by response surface methodology, *Chemical Engineering Journal*

169 (2011) pp.58-67.

[87] E.C. Corbos, M. Haneda, X. Courtois, P. Marecot, D. Duprez and H. Hamada, NOx abatement for lean-burn engines under lean–rich atmosphere over mixed NSR-SCR catalysts: Influences of the addition of a SCR catalyst and of the operational conditions, *Applied Catalysis A: General*, 365 (2009) pp.187-193.

[88] C.-K. Seo, H. Kim and B. Choi, De-NOx Characteristics of a Combined System of LNT and SCR according to Space Velocity, *SAE Technical Paper* 2011-01-2088 (2011).

[89] C.-K. Seo, H. Kim, B. Choi and M.T. Lim, The optimal volume of a combined system of LNT and SCR catalysts, *Journal of Industrial and Engineering Chemistry* 17 (2011) pp. 382-385.

[90] U.D.L. Torre, B. Pereda-Ayo, J.R. Gonzalez-Velasco, Cu-zeolite NH_3-SCR catalysts for NOx removal in the combined NSR–SCR technology, *Chemical Engineering Journal* 207-208 (2012) pp.10-17.

[91] A. Fritz and V. Pitchon, The current state of research on automotive lean NOx catalysis, *Applied Catalysis B: Environmental* 13 (1997) pp.1-25.

[92] H. Wise and M.F. Frech, Kinetics of Decomposition of Nitric Oxide at Elevated Temperatures. Rate Measurements in a Quartz Vessel, *The Journal of Chemical Physics* 20 (1952) pp.22-24.

[93] F. Garin, Mechanism of NOx decomposition, *Applied Catalysis A: General* 222 (2001) pp.183-219.

[94] M. Iwamoto, H. Yahiro, K. Tanda, N. Mizuno, Y. Mine and S. Kagawa, Removal of Nitrogen Monoxide through a Novel Catalytic Process. 1. Decomposition on Excessively Copper Ion Exchanged ZSM-5 Zeolites, *The Journal of Physical Chemistry* 95 (1991) pp.3727-3730.

[95] M. Iwamoto, H. Yahiro and K. Tanda, Catalytic Decomposition of Nitrogen Monoxide Over Copper Ion-Exchanged Zeolites. Influence of Zeolite Structure and Aluminum Content on the Catalytic Activity, *Studies in Surface Science and Catalysis* 44 (1989) pp.219-226.

[96] M. Iwamoto, H. Yahiro, Y. Yoshihiro, S. Shundo and N. Mizuno, Selective Reduction of NO by Lower Hydrocarbons in the Presence of O_2 and SO_2 over Copper Ion-exchanged Zeolites, *Shokubai (Catalyst)* 32 (1990) pp.430-433, in Japanese.

[97] W. Held, A. Konig, T. Richter and L. Puppe, Catalytic NOx Reduction in Net Oxidizing Exhaust Gas, *SAE Technical Paper* 900496 (1990).

[98] P. Sazama, L. Mokrzycki, B. Wichterlova, A. Vondrova, R. Pilar, J. Dedecek, S. Sklenak and E. Tabor, Unprecedented propane–SCR-NOx activity over template-free synthesized Al-rich Co-BEA* zeolite, *Journal of Catalysis* 332 (2015) pp.201-211.

[99] S. Dzwigaj, J. Janas, J. Gurgul, R.P. Socha, T. Shishido and M. Che, Do Cu(II) ions need Al atoms in their environment to make CuSiBEA active in the SCR of NO by ethanol or or propane? A spectroscopy and catalysis study, *Applied Catalysis B: Environmental* 85 (2009) pp.131-138.

[100] M. Valencia, E. Lopez, S. Andrade, M.L. Iris, V.R. Perez, C.S.M. de Lecea and A.B. Lopez, Proof of concept of the SCR of NOx in a real diesel engine exhaust using commercial diesel fuel and a full size Pt/beta zeolite/honeycomb monolith, *Catalysis Communications* 46 (2014) pp.86-89.

[101] A.W. Aylor, L.J. Lobree, J.A. Reimer and A.T. Bell, NO Adsorption, Desorption, and Reduction by CH_4 over Mn-ZSM-5, *Journal of Catalysis* 170 (1997) pp.390-401.

[102] A. De Lucas, J.L. Valverde, F. Dorado, A. Romero and I. Asencio, Influence of the ion exchanged metal (Cu, Co, Ni and Mn) on the selective catalytic reduction of NOX over mordenite and ZSM-5, *Journal of Molecular Catalysis A: Chemical* 225 (2005) pp.47-58.

[103] T.T. Yang, H.T. Bi and X. Cheng, Effects of O_2, CO_2 and H_2O on NOx adsorption and selective catalytic reduction over Fe/ZSM-5, *Applied Catalysis B: Environmental* 102 (2011) pp.163-171.

[104] S.-K. Park, Y.-K. Park, S.-E. Park and L. Kevan, Comparison of selective catalytic reduction of NO with C_3H_6 and C_3H_8 over Cu(II)-ZSM-5 and Co(II)-ZSM-5, *Physical Chemistry Chemical Physics* 2 (2000) pp.5500-5509.

[105] S.I. Woo, D.K. Kim, Y.K. Park, M.R. Kim and P. Decyk, Wide temperature window in the catalytic activity of novel Pt/ZSM-5 prepared by a sublimation method for selective catalytic Reduction of NO, *Catalysis Letters* 85 (2003) pp.69-72.

[106] J. Shibata, Y. Takada, A. Shichi, S. Satokawa, A. Satsuma and T. Hattori, Influence of zeolite support on activity enhancement by addition of hydrogen for SCR of NO by propane over Ag-zeolites, *Applied Catalysis B: Environmental* 54 (2004) pp.137-144.

[107] H. Berndt, F.-W. Schütze, M. Richter, T. Sowade and W. Grünert, Selective catalytic reduction of NO under lean conditions by methane and propane over indium/cerium-promoted zeolites, *Applied Catalysis B: Environmental* 40 (2003) pp.51-67.

[108] B. Gil, J. Janas, E. Włoch, Z. Olejniczak, J. Datka and B. Sulikowski, The influence of

the initial acidity of HFER on the status of Co species and catalytic performance of CoFER and InCoFER in CH_4-SCR-NO, *Catalysis Today* 137 (2008) pp.174-178.

[109] I. Castellanos and O. Marie, An operando FT-IR study of the NOx SCR over Co-HFER and Fe-HFER using acetylene as a reducing agent, *Catalysis Today* 283 (2017) pp.54-65.

[110] A. Obuchi, A. Ohi, M. Nakanura, A. Ogata, K. Mizuno and H. Ohuchi, Performance of platinum-group metal catalysts for the selective reduction of nitrogen oxides by hydrocarbons, *Applied Catalysis B: Environmental* 2 (1993) pp.71-80.

[111] S.S. Kim, S.H. Choi, S.M. Lee and S.C. Hong, Enhanced catalytic activity of Pt/Al_2O_3 on the CH_4 SCR, *Journal of Industrial and Engineering Chemistry* 18 (2012) pp.272-276.

[112] L.W. Nguyen, C. Salim and H. Hinode, Promotive Effect of MOx (M=Ce, Mn) Mechanically Mixed with Au/TiO_2 on the Catalytic Activity for Nitrogen Monoxide Reduction by Propene, *Topics in Catalysis* 52 (2009) pp.779-783.

[113] B. Azambre, L. Zenboury, P. Da Costa, S. Capela, S. Carpentier and A. Westermann, Palladium catalysts supported on sulfated ceria–zirconia for the selective catalytic reduction of NOx by methane: Catalytic performances and nature of active Pd species, *Catalysis Today* 176 (2011) pp.242-249.

[114] H. He, X. Zhang, Q. Wu, C. Zhang and Y. Yu, Review of Ag/Al_2O_3-Reductant System in the Selective Catalytic Reduction of NOx, *Catalysis Surveys from Asia* 12 (2008) pp. 38-55.

[115] E. Seker, J. Cavataio, E. Gulari, P. Lorpongpaiboon and S. Osuwan, Nitric oxide reduction by propene over silver/alumina and silver–gold/alumina catalysts: effect of preparation methods, *Applied Catalysis A: General* 183 (1999) pp.121-134.

[116] S. Satokawa, Enhancing the $NO/C_3H_8/O_2$ Reaction by Using H_2 over Ag/Al_2O_3 Catalysts under Lean-Exhaust Conditions, *Chemistry Letters* 29 (2000) pp.294-295.

[117] Z. Liu and S.I. Woo, Recent Advances in Catalytic DeNOx Science and Technology, *Catalysis Reviews: Science and Engineering* 48 (2006) pp.43-89.

[118] G. Fierro, G. Moretti, G. Ferraris and G.B. Andreozzi, A Mössbauer and structural investigation of Fe-ZSM-5 catalysts: Influence of Fe oxide nanoparticles size on the catalytic behavior for the NO-SCR by C_3H_8, *Applied Catalysis B: Environmental* 102 (2011) pp.215–223.

[119] S. Erkfeldt, A. Palmqvist and M. Petersson, Influence of the reducing agent for lean NOx reduction over Cu-ZSM-5, *Applied Catalysis B: Environmental* 102 (2011) pp.547-554.

[120] H. Akama and K. Matsushita, Recent lean NOx catalyst technologies for automobile

exhaust control, *Catalysis Surveys from Japan* 3 (1999) pp.139-146.

[121] P.S. Kim, Enhancement of Low-Temperature DeNOx Performance of HC-SCR Technology, Dissertation for the degree of PhD, *Pohang University of Science and Technology* (18 Jun 2013) pp.1-258.

[122] V. Houel, P. Millington, R. Rajaram and A. Tsolakis, Fuel effects on the activity of silver hydrocarbon-SCR catalysts, *Applied Catalysis B: Environmental* 73 (2007) pp.203-207.

[123] A. Frobert, S. Raux, S. Rousseau and G. Blanchard, Analysis of the Coupling of HC–SCR by Ethanol and NH_3–SCR on Real Engine Emissions, *Topics in Catalysis* 56 (2013) pp.125-129.

[124] J.M. Herreros, P. George, M. Umar and A. Tsolakis, Enhancing selective catalytic reduction of NOx with alternative reactants/promoters, *Chemical Engineering Journal* 252 (2014) pp.47-54.

[125] M. Piumetti, S. Bensaid, D. Fino and N. Russo, Catalysis in Diesel engine NOx aftertreatment: a review, *Catalysis, Structure & Reactivity* 1 (2015) pp.155-173.

[126] J.A. Sullivan and J. Cunningham, Selective catalytic reduction of NO with C_2H_4 over Cu/ZSM-5: Influences of oxygen partial pressure and incorporated rhodia, *Applied Catalysis B: Environmental* 12 (1998) pp.275-289.

[127] V.G. Komvokis, E.F. Iliopoulou, I.A. Vasalos, K.S. Triantafyllidis and C.L. Marshall, Development of optimized Cu-ZSM-5 deNOx catalytic materials both for HC-SCR applications and as FCC catalytic additives, *Applied Catalysis A: General* 325 (2007) pp.345-352.

[128] N. Mongkolsiri, P. Praserthdam, P.L. Silveston and R.R. Hudgins, Transient study of the effect of residual cations in Cu/ZSM-5 for SCR of NO by hydrocarbon, *Chemical Engineering Science* 55 (2000) pp.2249-2256.

[129] I.M. Saaid, A.R. Mohamed and S. Bhatia, Comparative study of Cu-ZSM-5 and Fe-ZSM-5 in the SCR of NOx with i-C_4H_{10}, *Reaction Kinetics and Catalysis Letters* 75 (2002) pp. 359-365.

[130] K. Arve, F. Klingstedt, K. Eränen, L.-E. Lindfors and D.Y. Murzin, Engineering HC-SCR : Improved Low Temperature Performance through a Cascade Concept, *Catalysis Letters* 105 (2005) pp.133-138.

[131] L. Čapek, J. Dědeček, B. Wichterlová, L. Cider, E. Jobson and V. Tokarová, Cu-ZSM-5 zeolite highly active in reduction of NO with decane: Effect of zeolite structural parameters on the catalyst performance, *Applied Catalysis B: Environmental* 60 (2005)

pp.147-153.

[132] H.-Y. Chen, T. Voskoboinikov and W.M.H. Sachtler, Reduction of NOx over Fe/ZSM-5 Catalysts: Adsorption Complexes and Their Reactivity toward Hydrocarbons, *Journal of Catalysis* 180 (1998) pp.171-183.

[133] A.V. Kucherov, C.N. Montreuil, T.N. Kucherova and M. Shelef, In situ ESR high-temperature Characterization of FeZSM-5 and FeSAPO-34 catalysts in flowing mixtures of NO, C_3H_6 and O_2, *Catalysis Letters* 56 (1998) pp.173-181.

[134] N.W. Cant and I.O.Y. Liu, The mechanism of the selective reduction of nitrogen oxides by hydrocarbons on zeolite catalysts, *Catalysis Today* 63 (2000) pp.133-146.

[135] F. Heinrich, C. Schmidt, E. Löffler, M. Menzel and W. Grünert, Fe-ZSM-5 Catalysts for the Selective Reduction of NO by Isobutane–The Problem of the Active Sites, *Journal of Catalysis* 212 (2002) pp.157-172.

[136] A. Guzmán-Vargas, G. Delahay, B. Coq, E. Lima, P. Bosch and J.-C. Jumas, Influence of the preparation method on the properties of Fe-ZSM-5 for the selective catalytic reduction of NO by n-decane, *Catalysis Today* 107-108 (2005) pp.94-99.

[137] J. Regalbuto, Catalyst Preparation: Science and Engineering, *CRC Press* (2006) pp.1-463.

[138] Z. Chajar, M. Primet, H. Praliaud, M. Chevrier, C. Gauthier and F. Mathis, Influence of the preparation method on the selective reduction of nitric oxide over Cu-ZSM-5. Nature of the active sites, *Applied Catalysis B: Environmental* 4 (1994) pp.199-211.

[139] C. Yokoyama and M. Misono, Selective reduction of nitrogen monoxide by propene over cerium-doped zeolites, *Catalysis Today* 22 (1994) pp.59-72.

[140] E. Kikuchi, M. Ogura, I. Terasaki and Y. Goto, Selective Reduction of Nitric Oxide with Methane on Gallium and Indium Containing H-ZSM-5 Catalysts: Formation of Active Sites by Solid-State Ion Exchange, *Journal of Catalysis* 161 (1996) pp.465-470.

[141] C. Descorme, P. Gélin, M. Primet and C. Lécuyer, Infrared study of nitrogen monoxide adsorption on palladium ion-exchanged ZSM-5 catalysts, *Catalysis Letters* 41 (1996) pp.133-138.

[142] J.T. Miller, E. Glusker, R. Peddi, T. Zheng and J.R. Regalbuto, The role of acid sites in cobalt Zeolite catalysts for selective catalytic reduction of NOx, *Catalysis Letters* 51 (1998) pp.15-22.

[143] J.-Y. Yan, H.H. Kung, W.M.H. Sachtler and M.C. Kung, Synergistic Effect in Lean NOx Reduction by CH_4 over Co/Al_2O_3 and H-Zeolite Catalysts, *Journal of Catalysis* 175

(1998) pp.294-301.

[144] G.P. Ansell, A.F. Diwell, S.E. Golunski, J.W. Hayes, R.R. Rajaram, T.J. Truex and A.P. Walker, Mechanism of the lean NOx reaction over Cu/ZSM-5, *Applied Catalysis B: Environmental* 2 (1993) pp.81-100.

[145] R.H.H. Smits and Y. Iwasawa, Reaction mechanisms for the reduction of nitric oxide by hydrocarbons on Cu-ZSM-5 and related catalysts, *Applied Catalysis B: Environmental* 6 (1995) pp.L201-L207.

[146] D.B. Lukyanov, E.A. Lombardo, G.A. Sill, J.L. d'Itri and W.K. Hall, Selective Catalytic Reduction (SCR) of NO with Methane over CoZSM-5 and HZSM-5 Zeolites: On the Role of Free Radicals and Competitive Oxidation Reactions, *Journal of Catalysis* 163 (1996) pp.447-456.

[147] T. Sun, M.D. Fokema and J.Y. Ying, Mechanistic study of NO reduction with methane over Co^{2+} modified ZSM-5 catalysts, *Catalysis Today* 33 (1997) pp.251-261.

[148] L.J. Lobree, A.W. Aylor, J.A. Reimer and A.T. Bell, Role of Cyanide Species in the Reduction of NO by CH_4 over Co–ZSM-5, *Journal of Catalysis* 169 (1997) pp.188-193.

[149] R. Burch, P.J. Millington and A.P. Walker, Mechanism of the selective reduction of nitrogen monoxide on platinum-based catalysts in the presence of excess oxygen, *Applied Catalysis B: Environmental* 4 (1994) pp.65-94.

[150] B.K. Cho, J.E. Yie and K.M. Rahmoeller, Autonomous Kinetic Oscillations During NO + C_2H_4 + O_2 Reaction over Pt-ZSM-5 Under Highly Oxidizing Conditions, *Journal of Catalysis* 157 (1995) pp.14-24.

[151] R. Burch and T.C. Watling, Adsorbate-assisted NO decomposition in NO reduction by C_3H_6 over Pt/Al_2O_3 catalysts under lean-burn conditions, *Catalysis Letters* 37 (1996) pp.51-55.

[152] R. Burch and T.C. Watling, The difference between alkanes and alkenes in the reduction of NO by hydrocarbons over Pt catalysts under lean-burn conditions, *Catalysis Letters* 43 (1997) pp.19-23.

[153] L. Li, J. Chen, S. Zhang, F. Zhang, N. Guan, T. Wang and S. Liu, Selective Catalytic Reduction of Nitrogen Oxides from Exhaust of Lean Burn Engine over In-Situ Synthesized Cu-ZSM-5/Cordierite, *Environmental Science & Technology* 39 (2005) pp. pp.2841-2847.

[154] M. Haneda, Y. Kintaichi, M. Inaba and H. Hamada, Infrared study of catalytic reduction of nitrogen monoxide by propene over Ag/TiO_2– ZrO_2, *Catalysis Today* 42 (1998) pp.

127-135.

[155] F.C. Meunier, V. Zuzaniuk, J.P. Breen, M. Olsson and J.R.H. Ross, Mechanistic differences in the selective reduction of NO by propene over cobalt- and silver-promoted alumina catalysts: kinetic and in situ DRIFTS study, *Catalysis Today* 59 (2000) pp.287-304.

[156] S. Sumiya, H. He, A. Abe, N. Takezawa and K. Yoshida, Formation and reactivity of isocyanate (NCO) species on Ag/Al_2O_3, *Journal of the Chemical Society, Faraday Transactions* 94 (1998) pp.2217-2219.

[157] S. Kameoka, T. Chafik, Y. Ukisu and T. Miyadera, Reactivity of surface isocyanate species with NO, O_2 and NO + O_2 in selective reduction of NOx over Ag/Al_2O_3 and Al_2O_3 catalysts, *Catalysis Letters* 55 (1998) pp.211-215.

[158] S.-K. Park, V. Kurshev, Z. Luan, C.W. Lee and L. Kevan, Reaction of NO with copper ions in Cu(II)-exchanged ZSM-5 zeolite: electron spin resonance, electron spin echo modulation and Fourier transform infrared spectroscopy, *Microporous and Mesoporous Materials* 38 (2000) pp.255-266.

[159] R. Burch, J.P. Breen and F.C. Menuier, A review of the selective reduction of NOx with hydrocarbons under lean-burn conditions with non-zeolitic oxide and platinum group metal catalysts, *Applied Catalysis B: Environmental* 39 (2002) pp.283-303.

[160] O. Gorce, F. Baudin, C. Thomas, P.D. Costa and G. Djéga-Mariadassou, On the role of organic nitrogen-containing species as intermediates in the hydrocarbon-assisted SCR of NOx, *Applied Catalysis B: Environmental* 54 (2004) pp.69-84.

[161] V.A. Bell, J.S. Feeley, M. Deeba and R.J. Farrauto, In situ high temperature FTIR studies of NOx reduction with propylene over Cu/ZSM-5 catalysts, *Catalysis Letters* 29 (1994) pp.15-26.

[162] G. Centi, A. Galli and S. Perathoner, Reaction pathways of propane and propene conversion in the presence of NO and O_2 on Cu/MFI, *Journal of the Chemical Society*, *Faraday Transactions* 92 (1996) pp.5129-5140.

[163] E.V. Rebrov, A.V. Simakov, N.N. Sazonova, V.A. Rogov and G.B. Barannik, Propane and oxygen action on NOx adspecies on low-exchanged Cu-ZSM-5, *Catalysis Letters* 51 (1998) pp.27-40.

[164] N.W. Cant, A.D. Cowan, I.O.Y. Liu and A. Satsuma, The reactions of possible intermediates in the selective catalytic reduction of nitrogen oxides by hydrocarbons, *Catalysis Today* 54 (1999) pp.473-482.

[165] H. Hamada, Y. Kintaichi, M. Sasaki and T. Ito, Transition metal-promoted silica and alumina catalysts for the selective reduction of nitrogen monoxide with propane, *Applied Catalysis* 75 (1991) pp.L1-L8.

[166] B.H. Engler, J. Leyrer, E.S. Lox and K. Ostgathe, Catalytic reduction of nitrogen oxides in diesel exhaust gas, *Studies in Surface Science and Catalysis* 96 (1995) pp.529-547.

[167] V. Pitchon and A. Fritz, The Relation between Surface State and Reactivity in the DeNOx Mechanism on Platinum-Based Catalysts, *Journal of Catalysis* 186 (1999) pp. 64-74.

[168] M. Iwamoto and H. Takeda, Pulse study on reactivity of ethene adsorbed on Cu-MFI with nitrogen oxides and oxygen, *Catalysis Today* 27 (1996) pp.71-78.

[169] K.-I. Shimizu, H. Kawabata, A. Satsuma and T. Hattori, Role of Acetate and Nitrates in the Selective Catalytic Reduction of NO by Propene over Alumina Catalyst as Investigated by FTIR, *The Journal of Physical Chemistry B* 103 (1999) pp.5240-5245.

[170] J.-H. Lee, A. Yezerets, M.C. Kung and H.H. Kung, Hydrocarbon reaction pathway in selective NO reduction over a bifunctional SnO_2/Al_2O_3 catalyst, *Chemical Communications* 15 (2001) pp.1404-1405.

[171] K. Sato, T. Yoshinari, Y. Kintaichi, M. Haneda and H. Hamada, Remarkable promoting effect of rhodium on the catalytic performance of Ag/Al_2O_3 for the selective reduction of NO with decane, *Applied Catalysis B: Environmental* 44 (2003) pp.67-78.

[172] G.R. Bamwenda, A. Ogata, A. Obuchi, J. Oi, K. Mizuno and J. Skrzypek, Selective reduction of nitric oxide with propene over platinum-group based catalysts: Studies of surface species and catalytic activity, *Applied Catalysis B: Environmental* 6 (1995) pp. 311-323.

[173] S.I. Zones, Zeolite SSZ-13 and its method of preparation, United States Patent 4 544 538 (1985).

[174] H. Imai, N. Hayashida, T. Yokoi and T. Tatsumi, Direct crystallization of CHA-type Zeolite from amorphous aluminosilicate gel by seed-assisted method in the absence of organic-structure-directing agents, *Microporous and Mesoporous Materials* 196 (2014) pp.341-348.

[175] T.A. Nijhuis, A.E.W. Beers, T. Vergunst, I. Hoek, F. Kapteijn and J.A. Moulijn, Preparation of monolithic catalysts, *Catalysis Reviews: Science and Engineering* 43 (2001) pp.345-380.

[176] R.M. Heck, S. Gulati and R.J. Farrauto, The application of monoliths for gas phase

catalytic reactions, *Chemical Engineering Journal* 82 (2001) pp.149-156.

[177] K.S.W. Sing, D.H. Everett, R.A.W. Haul, L. Moscou, R.A. Pierotti, J. Rouquerol and T. Siemieniewska, Reporting physisorption data for gas/solid systems with special reference to the determination of surface area and porosity, *Pure and Applied Chemistry* 57 (1985) pp.603-619.

[178] M. Thommes, K. Kaneko, A.V. Neimark, J.P. Olivier, F. Rodriguez-Reinoso, J. Rouquerol and K.S.W. Sing, Physisorption of gases, with special reference to the evaluation of surface area and pore size distribution (IUPAC Technical Report), *Pure and Applied Chemistry* 87 (2015) pp.1051-1069.

[179] P.G. Blakeman, E.M. Burkholder, H.-Y. Chen, J.E. Collier, J.M. Fedeyko, H. Jobson and R.R. Rajaram, The role of pore size on the thermal stability of zeolite supported Cu SCR catalysts, *Catalysis Today* 231 (2014) pp.56-63.

[180] H. van Koningsveld, J.C. Jansen and H. van Bekkum, The noloclinic framework structure of zeolite H-ZSM-5. Comparison with the orthorhombic framework of as-synthesized ZSM-5, *Zeolites* 10 (1990) pp.235-242.

[181] W. Fu, T. Liu, Z. Fang, Y. Ma, X. Zheng, W. Wang, X. Ni, M. Hu and T. Tang, High activity and stability in the cross-coupling of aryl halides with disulfides over Cu-doped hierarchically porous zeolite ZSM-5, *Chemical Communications* 51 (2015) pp.5890-5893.

[182] X. Cheng, D. Su, Z. Wang, C. Ma and M. Wang, Catalytic reduction of nitrogen oxide by carbon monoxide, methane and hydrogen over transition metals supported on BEA zeolites, *International journal of Hydrogen Energy* 43 (2018) pp.21969-21981.

[183] W. Fu, T. Liu, Z. Fang, Y. Ma, X. Zheng, W. Wang, X. Ni, M. Hu and T. Tang, High activity and stability in the cross-coupling of aryl halides with disulfides over Cu-doped hierarchically porous zeolite ZSM-5, *Chemical Communications* 51 (2015) pp.5890-5893.

[184] G. Qi and R.T. Yang, Selective catalytic oxidation (SCO) of ammonia to nitrogen over Fe/ZSM-5 catalysts, *Applied Catalysis A: General* 287 (2005) pp.25-33.

[185] S.M. Auerbach, K.A. Carrado and P.K. Dutta, Handbook of Zeolite Science and Technology, *CRC Press* (2003) pp.1-1204.

[186] J. Dědeček, S. Sklenak, C. Li, B. Wichterlova, V. Gábová, J. Brus, M. Sierka and J. Sauer, Effect of Al−Si−Al and Al−Si−Si−Al Pairs in the ZSM-5 Zeolite Framework on the ^{27}Al NMR Spectra. A Combined High-Resolution ^{27}Al NMR and DFT/MM Study, *The Journal*

of Physical Chemistry C 113 (2009) pp.1447-1458.

[187] M. Haouas, F. Taulelle and C. Martineau, Recent advances in application of ^{27}Al NMR spectroscopy to materials science, *Progress in Nuclear Magnetic Resonance Spectroscopy* 94-95 (2016) pp.11-36.

[188] Z. Zhao, R. Yu, R. Zhao, C. Shi, H. Gies, F.-S. Xiao, D.D. Vos, T. Yokoi, X. Bao, U. Kolb, M. Feyen, R. McGuire, S. Maurer, A. Moini, U. Müller and W. Zhang, Cu-exchanged Al-rich SSZ-13 zeolite from organotemplate-free synthesis as NH_3-SCR catalyst: Effects of Na^+ ions on the activity and hydrothermal stability, *Applied Catalysis B: Environmental* 217 (2017) pp.421-428.

[189] Y. Gao, B. Zheng, G. Wu, F. Ma and C. Liu, Effect of the Si/Al ratio on the performance of hierarchical ZSM-5 zeolites for methanol aromatization, *Royal Society of Chemistry Advances* 6 (2016) pp.83581-83588.

[190] L.W. Beck and J.F. Haw, Multinuclear NMR Studies Reveal a Complex Acid Function for Zeolite Beta, *The Journal of Physical Chemistry* 99 (1995) pp.1076-1079.

[191] A. Abraham, S.-H. Lee, C.-H. Shin, S.B. Hong, R. Prins and J.A. van Bokhoven, Influence of framework silicon to aluminium ratio on aluminium coordination and distribution in zeolite Beta investigated by ^{27}Al MAS and ^{27}Al MQ MAS NMR, *Physical Chemistry Chemical Physics* 6 (2004) pp.3031-3036.

[192] X. Zhou, H. Chen, X. Cui, Z. Hau, Y. Chen, Y. Zhu, Y. Song Y. Gong and J. Shi, A facile one-pot synthesis of hierarchically porous Cu(I)-ZSM-5 for radicals-involved oxidation of cyclohexane, *Applied Catalysis A: General* 451 (2013) pp.112-119.

[193] F. Bin, C. Song, G. Lv, J. Song, S. Wu and X. Li, Selective catalytic reduction of nitric oxide with ammonia over zirconium-doped copper/ZSM-5 catalysts, *Applied Catalysis B: Environmental* 150-151 (2014) pp.532-543.

[194] R. Zhang, Y. Li and T. Zhen, Ammonia selective catalytic reduction of NO over Fe/Cu-SSZ-13, *Royal Society of Chemistry Advances* 4 (2014) pp.52130-52139.

[195] S.T. Korhonen, D.W. Fickel, R.F. Lobo, B.M. Weckhuysen and A.M. Beale, Isolated Cu^{2+} ions: active sites for selective catalytic reduction of NO, *Chemical Communications* 11 (2011) pp.800-802.

[196] G. Spoto, A. Zecchma, S. Bordiga, G. Ricchiardi and G. Martra, Cu(I)-ZSM-5 zeolites prepared by reaction of H-ZSM-5 with gaseous CuCl: Spectroscopic characterization and reactivity towards carbon monoxide and nitric oxide, *Applied Catalysis B: Environmental* 3 (1994) pp.151-172.

[197] M.C.N.A. de Carbalho, F.B. Passos and M. Schmal, The behavior of Cu/ZSM-5 in the oxide and reduced form in the presence of NO and methanol, *Applied Catalysis A: General* 193 (2000) pp.265-276.

[198] C. Liang, X. Li, Z. Qu, M. Tade and S. Liu, The role of copper species on Cu/γ-Al_2O_3 catalysts for NH_3-SCO reaction, *Applied Surface Science* 258 (2012) pp.3738-3743.

[199] H. Praliaud, S. Mikhailenko, Z. Chajar and M. Primet, Surface and bulk properties of Cu-ZSM-5 and Cu/Al_2O_3 solids during redox treatments. Correlation with the selective reduction of nitric oxide by hydrocarbons, *Applied Catalysis B: Environmental* 16 (1998) pp.359-374.

[200] Q. Lin, J. Liu, S. Liu, S. Xu, C. Lin, X. Feng, Y. Wang, H. Xu and Y. Chen, Barium-promoted hydrothermal stability of monolithic Cu/BEA catalyst for NH_3-SCR, *Dalton Transactions* 47 (2018) pp.15038-15048.

[201] H. Xue, X. Guo, S. Wang, C. Sun, J. Yu and D. Mao, Poisoning effect of CaO on Cu/ZSM-5 for the selective catalytic reduction of NO with NH_3, *Catalysis Communications* 112 (2018) pp.53-57.

[202] O.A. Zelekew and D.-H. Kuo, Facile synthesis of SiO_2@CuxO@TiO_2 heterostructures for catalytic reductions of 4-nitrophenol and 2-nitroaniline organic pollutants, *Applied Surface Science* 393 (2017) pp.110-118.

[203] U. Arellano, J.M. Shen, J.A. Wang, M.T. Timko, L.F. Chen, J.T. Vázquez Rodríguez, M. Asomoza, A. Estrella, O.A. González Vargas and M.E. Llanos, Dibenzothiophene oxidation in a model diesel fuel using CuO/GC catalysts and H_2O_2 in the presence of acetic acid under acidic condition, *Fuel* 149 (2015) pp.15-25.

[204] J. Wang, Z. Peng, Y. Chen, W. Bao, L. Chang and G. Feng, *In-situ* hydrothermal synthesis of Cu-SSZ-13/cordierite for the catalytic removal of NOx from diesel vehicles by NH_3, *Chemical Engineering Journal* 263 (2015) pp.9-19.

[205] X. Chen, D.-H. Kuo, A.D. Saragih, Z.-Y. Wu, H. Abdullah and J. Lin, The effect of the Cu^+/Cu^{2+} ratio on the redox reactions by nanoflower CuNiOS catalysts, *Chemical Engineering Science* 194 (2019) pp.105-115.

[206] C. Chen, X. Yan, B.A. Yoza, T. Zhou, Y. Li, Y. Zhan, Q. Wang and Q.X. Li, Efficiencies and mechanisms of ZSM5 zeolites loaded with cerium, iron, or manganese oxides for catalytic ozonation of nitrobenzene in water, *Science of The Total Environment* 612 (2018) pp.1424-1432.

[207] K. Guesh, C. Márquez-Álvarez, Y. Chebude and I. Díaz, Enhanced photocatalytic activity

of supported TiO_2 by selective surface modification of zeolite Y, *Applied Surface Science* 378 (2016) pp.473-478.

[208] B. Pereda-Ayo, U.D.L. Torre, M.J. Illán-Gómez, A. Bueno-López, J.R. González-Velasco, Role of the different copper species on the activity of Cu/zeolite catalysts for SCR of NOx with NH_3, *Applied Catalysis B: Environmental* 147 (2014) pp.420-428.

[209] Database of Zeolite Structures, Framework type MFI (accessed 14 January 2019), https://asia.iza-structure.org/IZA-SC/framework.php?STC=MFI.

[210] Database of Zeolite Structures, Framework type BEA (accessed 14 January 2019), https://asia.iza-structure.org/IZA-SC/framework.php?STC=BEA.

[211] Database of Zeolite Structures, Framework Type CHA (accessed 14 January 2019), https://asia.iza-structure.org/IZA-SC/framework.php?STC=CHA.

[212] D.H. Olson, G.T. Kokotailo and S.L. Lawton, Crystal structure and structure-related properties of ZSM-5, *The Journal of Physical Chemistry* 85 (1981) pp.2238-2243.

[213] R. Zhang, N. Liu, Z. Lei and B. Chen, Selective Transformation of Various Nitrogen-Containing Exhaust Gases toward N_2 over Zeolite Catalysts, *Chemical Reviews* 116 (2016) pp.3658-3721.

[214] J.B. Higgins, R.B. LaPierre, J.L. Schlenker, A.C. Rohrman, J.D. Wood, G.T. Kerr and W. J. Rohrbaugh, The framework topology of zeolite beta, *Zeolites* 8 (1988) pp.446-452.

[215] A. Satsuma, A. Shichi and T. Hattori, The zeolite micropore as a unique reaction field for the selective catalytic reduction of NO by hydrocarbon, *CATTECH* 7 (2003) pp.42-43.

[216] S. Sircar, Basic Research Needs for Design of adsorptive Gas Separation Process, *Industrial & Engineering Chemistry Research* 45 (2006) pp.5435-5448.

[217] J.-R. Li, R.J. Kuppler and H.-C. Zhou, Selective gas adsorption and separation in metal–organic frameworks, *Chemical Society Reviews* 38 (2009) pp.1477-1504.

[218] M.R. Hudson, W.L. Queen, J.A. Mason, D.W. Fickel, R.F. Lobo and C.M. Brown, Unconventional, Highly Selective CO_2 adsorption in Zeolite SSZ-13, *Journal of The American Chemical Society* 134 (2012) pp.1970-1973.

[219] Y.J. Kim, K.M. Min, J.K. Lee, S.B. Hong, B.K. Cho and I.-S. Nam, Effect of CO_2 on the DeNOx Activity of a Small Pore Zeolite Copper Catalyst for NH_3/SCR, *ChemCatChem* 6 (2014) pp.1186-1189.

[220] C. Shi, M. Cheng, Z. Qu, X. Yang and X. Bao, On the selectively catalytic reduction of NOx with methane over Ag-ZSM-5 catalysts, *Applied Catalysis B: Environmental* 36 (2002) pp.173-182.

[221] T.T. Yang, T. Zhang and H.T. Bi, A novel continuous reactor for catalytic reduction of NOx–fixed bed simulations, *The Canadian Journal of Chemical Engineering* 86 (2008) pp.395-402.

[222] X. Gou, C. Wu, K. Zhang, G. Xu, M. Si, Y. Wang, E. Wang, L. Liu and J. Wu, Low Temperature Performance of Selective Catalytic Reduction of NO with NH_3 under a Concentrated CO_2 Atmosphere, *Energies* 8 (2015) pp.12331-12341.

[223] P. Sun, X. Cheng, Y. Lai, Z. Wang, C. Ma and J. Chang, NOx reduction by CO over ASC catalysts in a simulated rotary reactor: effect of CO_2, H_2O and SO_2, *RSC Advances* 8 (2018) pp.36604-36615.

[224] Y. Traa, B. Burger and J. Weitkamp, Zeolite-based materials for the selective catalytic reduction of NOx with hydrocarbons, *Microporous and Mesoporous Materials* 30 (1999) pp.3-41.

[225] R.M. Serra, S.G. Aspromonte, E.E. Miró and A.V. Boix, Hydrocarbon adsorption and NOx-SCR on (Cs, Co)mordenite, *Applied Catalysis B: Environmental* 166-167 (2015) pp. 592-602.

[226] Y.H. Yeom, B. Wen, W.M.H. Sachtler and E. Weitz, NOx Reduction from Diesel Emissions over a Nontransition Metal Zeolite Catalyst: A Mechanistic Study Using FTIR Spectroscopy, *The Journal of Physical Chemistry B* 108 (2004) pp.5386-5404.

[227] M.-Y. Kim, J-S. Choi and M. Crocker, Roles of C_3H_6 in NH_3 generation and NOx reduction over a Cu-chabazite SCR catalyst under lean/rich cycling conditions, *Catalysis Toady* 231 (2014) pp.90-98.

[228] C.H. Bartholomew, Mechanisms of catalyst deactivation, *Applied Catalysis A: General* 212 (2001) pp.17-60.

[229] E. Ruckenstein and B. Pulvermacher, Kinetics of crystallite sintering during heat treatment of supported metal catalysts, AlChE Journal 19 (1973) pp.356-364.

[230] S. Sitshebo, A. Tsolakis and T. Theinnoi, Promoting hydrocarbon-SCR of NOx in diesel engine exhaust by hydrogen and fuel reforming, *International Journal of Hydrogen Energy* 34 (2009) pp.7842-7850.

[231] F. Schuricht and W. Reschetilowski, Simultaneous selective catalytic reduction (SCR) of NOx and N_2O over Ag/ZSM-5 – Catalytic studies and mechanistic implications, *Microporous and Mesoporous Materials* 164 (2012) pp.135-144.

[232] JIS G4313 Grade SUS304-CSP (JIS G 4308), (accessed 28 January 2019). https://matmatch.com/materials/minfm42854-jis-g4313-grade-sus304-csp.

[233] A. Biabani-Ravandi and M. Rezaei, Low temperature CO oxidation over Fe–Co mixed oxide nanocatalysts, *Chemical Engineering Journal* 184 (2012) pp.141-146.

[234] K. Rida, A.L. Cámara, M.A. Peña, C.L. Bolívar-Díaz, A. Martínez-Arias, Bimetallic Co–Fe and Co–Cr oxide systems supported on CeO_2: Characterization and CO oxidation catalytic behaviour, *International Journal of Hydrogen Energy* 40 (2015) pp.11267-11278.

[235] G. Peng, L.R. Merte, J. Knudsen, R.T. Vang, E. Lægsgaard, F. Besenbacher and M. Mavrikakis, On the Mechanism of Low-Temperature CO Oxidation on Ni(111) and NiO (111) Surfaces, *The Journal of Physical Chemistry C* 114 (2010) pp.21579-21584.

[236] Y. Yi, P. Zhang, Z. Qin, C. Yu, W. Li, Q. Qin, B. Li, M. Fan, X. Liang and L. Dong, Low temperature CO oxidation catalysed by flower-like Ni–Co–O: how physicochemical properties influence catalytic performance, RSC Advances 8 (2018) pp.7110-7122.

Acknowledgements

This thesis would not have been possible without the support and contribution from a plenty of individuals, whom I believe deserve special acknowledgement. It is my pleasure to gratefully acknowledge them.

I wish to express my gratitude to my supervisors, Associate Prof. Susumu Sato and Prof. Hidenori Kosaka, for their support and assistance at every stage of my studies. I also would like to express sincerest gratitude to Prof. Byungchul Choi (Chonnam National University) and Prof. Choongnyeon Park (Chonnam National University) for their helpful advice and assistance throughout this work, and Associate Prof. Toshiyuki Yokoi (Tokyo Institute of Technology) for the preparation of catalysts and relevant chemical analysis.

I am grateful to the members of the doctoral examination committee, Prof. Mamoru Tanahashi, Prof. Katsunori Hanamura and Prof. Tomohiro Nozaki, for the time and efforts, whose sagacious questions and recommendations helped improve this thesis.

I gratefully thank Mr. Daiji Nagaoka, Mr. Takayuki Sakamoto and Mr. Teruo Nakada from Isuzu Motor, for the supply of the monolithic substrate used in this research, and also for their valuable advice, suggestion and technical expertise throughout the experimental work. I am indebted to my many former and current colleagues, Dr. Masato Yoshioka, Mr. Yuya Ogita, Mr. Shinya Sato, Mr. Yuki Fukushima and Mr. Daeseok Kim, whose help and a contribution throughout the experimental stage of my research was priceless.

I also would like to thank my valuable colleagues in Ph.D course, Mr. Jaehoon Jeong, Mr. Jaeok Bae, Mr. Dittapoom Shinabuth, Mr. Athiwat Butmarasri and Mr. Ewphun Pop-Paul. I hope there will always be good luck and good things in their life. “Your possibility is upper than sky and wider than sea!”

I would like to special thank my friends, Mr. Kwonwoo Lee, Mrs. Gowoon Kim, Mr. Uido Jeong, Ms. Hyewon Seo, Ms. Miju Kwak, Mr. Seokeon Kim and Mr. Hoon Ki. Thanks to their encouragement and advice, I could overcome the difficulties of being a foreign student in Japan. I value their friendship and appreciate all the things that they have done for me.

Above all, I would like to express my heartful gratitude to my beloved parents for all the sacrifices. I could never have been complete my study without endless love and dedication of my parents. I also thank my sister and my wonderful brother-in-law for their encourage and unconditional love.

May 2019 **Kyungseok LEE**

Appendices

Appendix A: C_4H_{10}-SCR Process for Quartz and Stainless-steel Reactor

A.1 Experimental conditions for evaluation of C_4H_{10}-SCR

The effect of catalytic reactor system on the de-NOx performance is investigated in this chapter. The selectivity catalytic reduction of NOx by *n*-butane (*n*-C_4H_{10}) over the copper-impregnated zeolites with different zeolite frameworks is evaluated using the quartz and stainless-steel reactors to compare the catalytic performance. The quartz reactor system is illustrated in Figure 3.1 (Chapter 3). The experimental apparatus of laboratory-scale stainless-steel reactor consists of mass flow controller module (MFC, JCST1005MZFC, Fujikin Inc.), NOx/O_2 meter (TNS-111-031AA, NGK Insulators), flow control valve (NEMA 23 stepper motors, National Instruments), micro air cable heater (SD-II-2, Sakaguchi E.H VOC Inc.), and Fourier transform infrared spectroscopy (FTIR, BOB-2000FT, Bestsokki), as illustrated in Figure 6.1. High-purity feed gases were controlled by a MFC module at a total flow rate of 1.67 L/min, which corresponds to a gas hourly space velocity (GHSV) of 12,500 h^{-1}. 5 vol.% of water vapor was supplied with N_2 carrier gas from a saturator (borosilicate glass), which was continuously heated at nearly 90°C. After the catalytic reaction, the reactor outlet gases, NO, NO_2, CO, CO_2, H_2O, C_4H_{10}, N_2O, HCN, NH_3, and HNCO, were monitored by a FTIR analyzer, in which 1.5 m of sampling line for FTIR analyzer was heated at 191°C to avoid the gas condensation. A volume of 8 cm^3 of washcoated monolith was inserted into a stainless-steel reactor. Two K-sheath thermocouples (diameter 1.0 mm) were located both the inlet and outlet of the catalytic reactor to monitor the reaction temperature. Both thermocouple tips were positioned at 10.0 mm and 5.2 mm from the surface of the monolith catalyst. Table A.1 summarizes the gas compositions and reaction conditions for evaluating the C_4H_{10}-SCR reaction in the quartz and stainless-steel reactors.

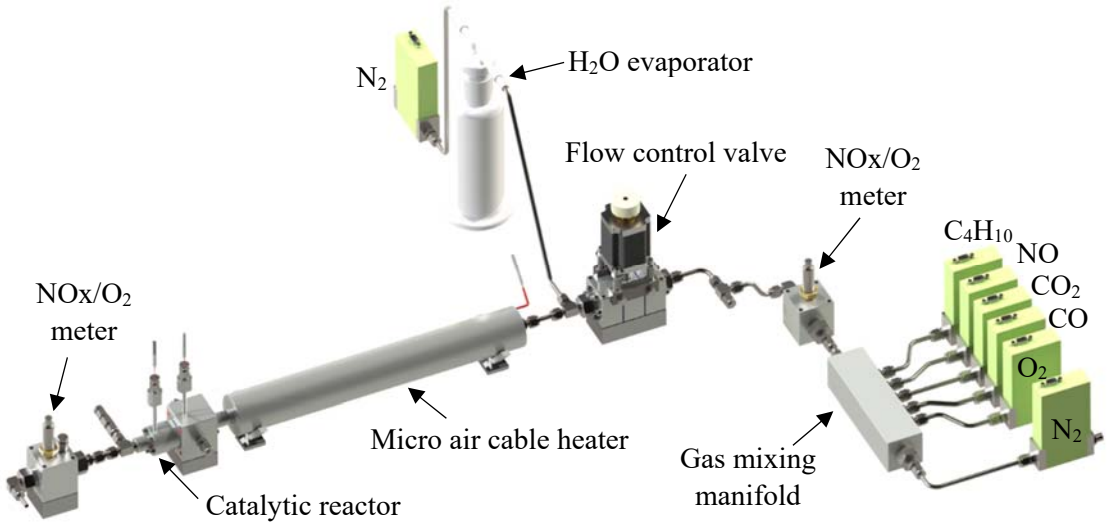

Figure A.1 Experimental apparatus of laboratory-scale stainless-steel reactor for evaluating catalyst reaction of C_4H_{10}-SCR.

Table A.1 Experimental conditions for investigating the effects of quartz and stainless-steel reactors in C_4H_{10}-SCR.

Parameters	Quartz reactor	Stainless-steel reactor
Reductant	*n*-Butane (*n*-C_4H_{10})	*n*-Butane (*n*-C_4H_{10})
Nitrogen monoxide (NO)	300 ppm	500 ppm
Oxygen (O_2)	8 vol.%	8 vol.%
Carbon monoxide (CO)	500 ppm	500 ppm
Carbon dioxide (CO_2)	10 vol.%	10 vol.%
Water vapor (H_2O)	5 vol.%	5 vol.%
Balance gas	N_2	N_2
n-Butane (*n*-C_4H_{10})	300, 600, 1,200, and 1,800 ppm C_1	500, 1,000, 2,000, and 4,000 ppm C_1
HC/NOx ratio	1, 2, 4, and 6	1, 2, 4, and 8
Total flow rate	1.67 L/min	1.67 L/min
Temperature	150 – 600°C	150 – 600°C
GHSV	12,500 h^{-1}	12,500 h^{-1}

A.2 Comparison of de-NOx performance

The effect of reactor system on the reaction temperature-dependence of NOx conversion over the Cu/SSZ-13, Cu/ZSM-5, and Cu/BETA catalysts is compared in Figures A.2–A.4. As illustrated in Figure A.2, the addition of Cu to SSZ-13 zeolite resulted in lower NOx conversion than that of parent SSZ-13 in both the quartz and stainless-steel reactors. The NOx conversion of 5Cu/SSZ-13 exhibited negative conversion at temperatures below 400℃ for the quartz reactor and at temperatures below 315℃ for the stainless-steel reactor, where the NOx conversion of 5Cu/SSZ-13 was −56% (Figure A.2(g), quartz reactor) and −26.8% (Figure 6.2(h), stainless-steel reactor) at 255℃ in the highest HC/NOx ratio. The negative conversion of 5Cu/SSZ-13 showed a similar trend at other HC/NOx ratios, indicating that increasing the Cu loading increased the adsorption capacity of NOx and the desorbed NOx was not reduced over the 5Cu/SSZ-13. The increase in HC/NOx ratio improved the NOx conversion over the Cu/SSZ-13, particularly 1Cu/SSZ-13 showed the highest NOx conversion. At the highest HC/NOx ratio, the maximum NOx conversion of 1Cu/SSZ-13 was 37.8% at 570℃ for the quartz reactor and 30.3% for the stainless-steel reactor. Notably, the NOx conversion of Cu/SSZ-13 slightly decreased at 600℃ for the quartz reactor, whereas that of the stainless-steel reactor significantly decreased to 4.7% (1Cu/SSZ-13) and 3.1% (5Cu/SSZ-13) at 600℃ (Figure A.2(h)).

As illustrated in Figure A.3, all Cu/ZSM-5 catalysts exhibited similar ability to improve de-NOx performance, as did increasing the HC/NOx ratio. The maximum NOx conversion could be achieved at the highest HC/NOx ratio, and especially 2Cu/ZSM-5 exhibited the highest NOx conversion in both the reactor systems. The maximum NOx conversion of 2Cu/ZSM-5 was 73.4% for the quartz reactor (Figure A.3(g)) and 64.4% for the stainless-steel reactor (Figure A.3(h)) at 450℃. It is worth note that the stainless-steel reactor exhibited

lower NOx conversion compared to that of the quartz reactor, even at the higher HC/NOx ratio (HC/NOx = 8). Furthermore, the NOx conversion of Cu/ZSM-5 substantially decreased at reaction temperatures above 570°C in the stainless-steel reactor, reaching 3.9–4.6% NOx conversion at 600°C. However, the quartz reactor exhibited more higher de-NOx performance compared to that of the stainless-steel reactor, exhibiting 35–45.5% NOx conversion at 600°C.

The comparison of NOx conversion over the Cu/BETA catalysts in the quartz and stainless-steel reactors is shown in Figure A.4. It is clear that the Cu/BETA catalyst with the highest Cu loading (10Cu/BETA) exhibited the best de-NOx performance in both reactor systems, exhibiting 58.4% NOx conversion at 465°C for the quartz reactor and 54% NOx conversion at 465°C for the stainless-steel reactor at the highest HC/NOx ratio. Notably, in the stainless-steel reactor, increasing the Cu loading shifted the temperature window of maximum de-NOx performance to lower temperature regions in the following order (Figure A.4(h)): 10Cu/BETA (η_{NOx} = 54% at T = 465°C) < 5Cu/BETA (η_{NOx} = 48.1% at T = 480°C) < 2Cu/BETA (η_{NOx} = 27.2% at T = 570°C) ≈ 1Cu/BETA (η_{NOx} = 14.7% at T = 570°C). Similar to that of the stainless-steel reactor, the temperature window of maximum NOx conversion shifted to lower temperature regions with an increase in the Cu loading in the quartz reactor (Figure A.4(g)): 10Cu/BETA (η_{NOx} = 58.4% at T = 465°C) ≈ 5Cu/BETA (η_{NOx} = 49.2% at T = 450°C) < 2Cu/BETA (η_{NOx} = 29.3% at T = 585°C) ≈ 1Cu/BETA (η_{NOx} = 25% at T = 600°C). As did significant drop in the NOx conversion over the Cu/SSZ-13 and Cu/ZSM-5 catalysts, the NOx conversion of Cu/BETA catalysts considerably decreased at reaction temperatures above 570°C, exhibiting 0.4–5.3% NOx conversion at 600°C. However, the quartz reactor exhibited more higher de-NOx performance compared to that of the stainless-steel reactor, exhibiting 25–37.4% NOx conversion at 600°C.

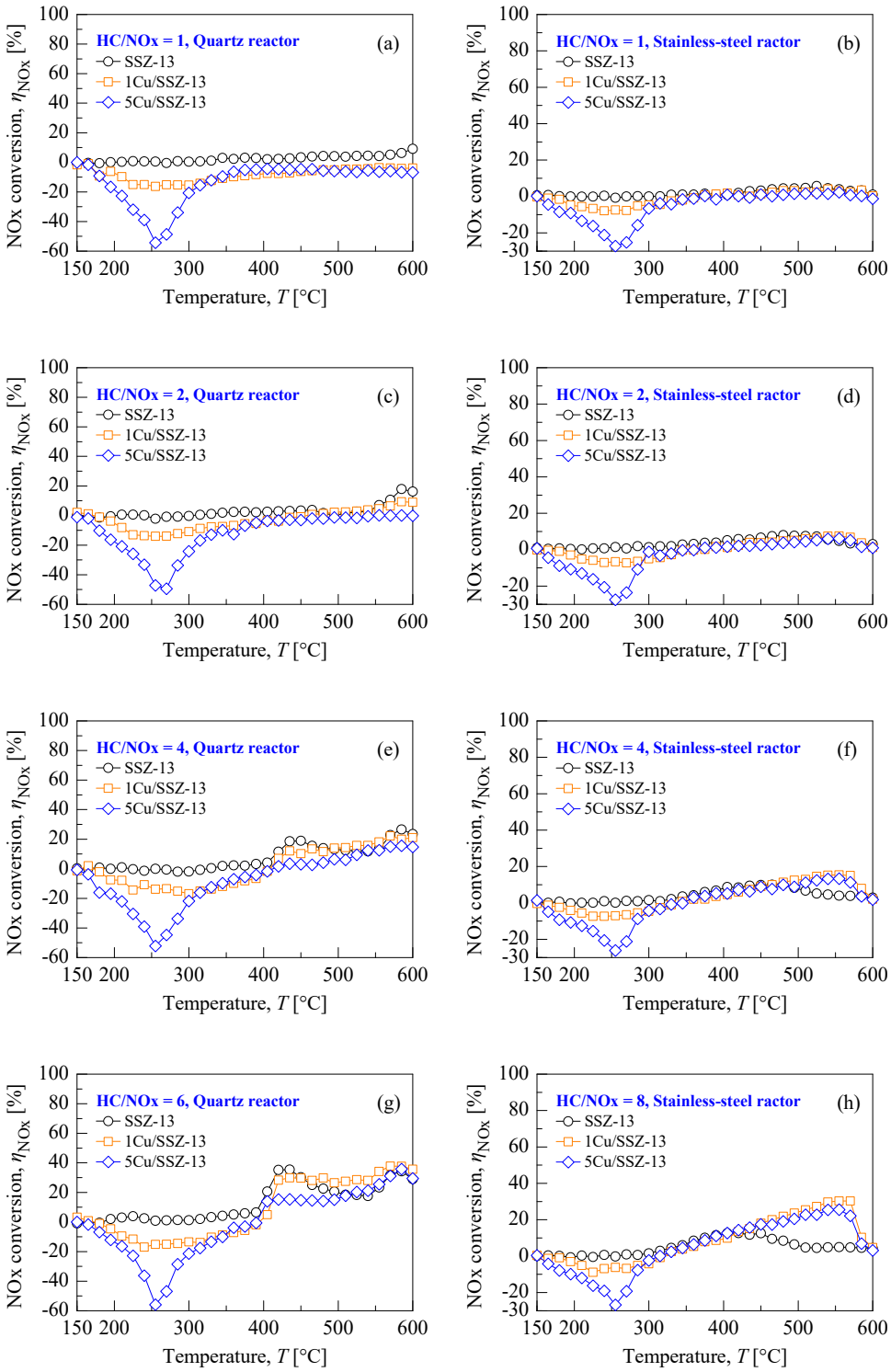

Figure A.2 Comparison of de-NOx performance over the parent SSZ-13 and Cu/SSZ-13 for C_4H_{10}-SCR as a function of reaction temperature in quartz and stainless-steel reactor.

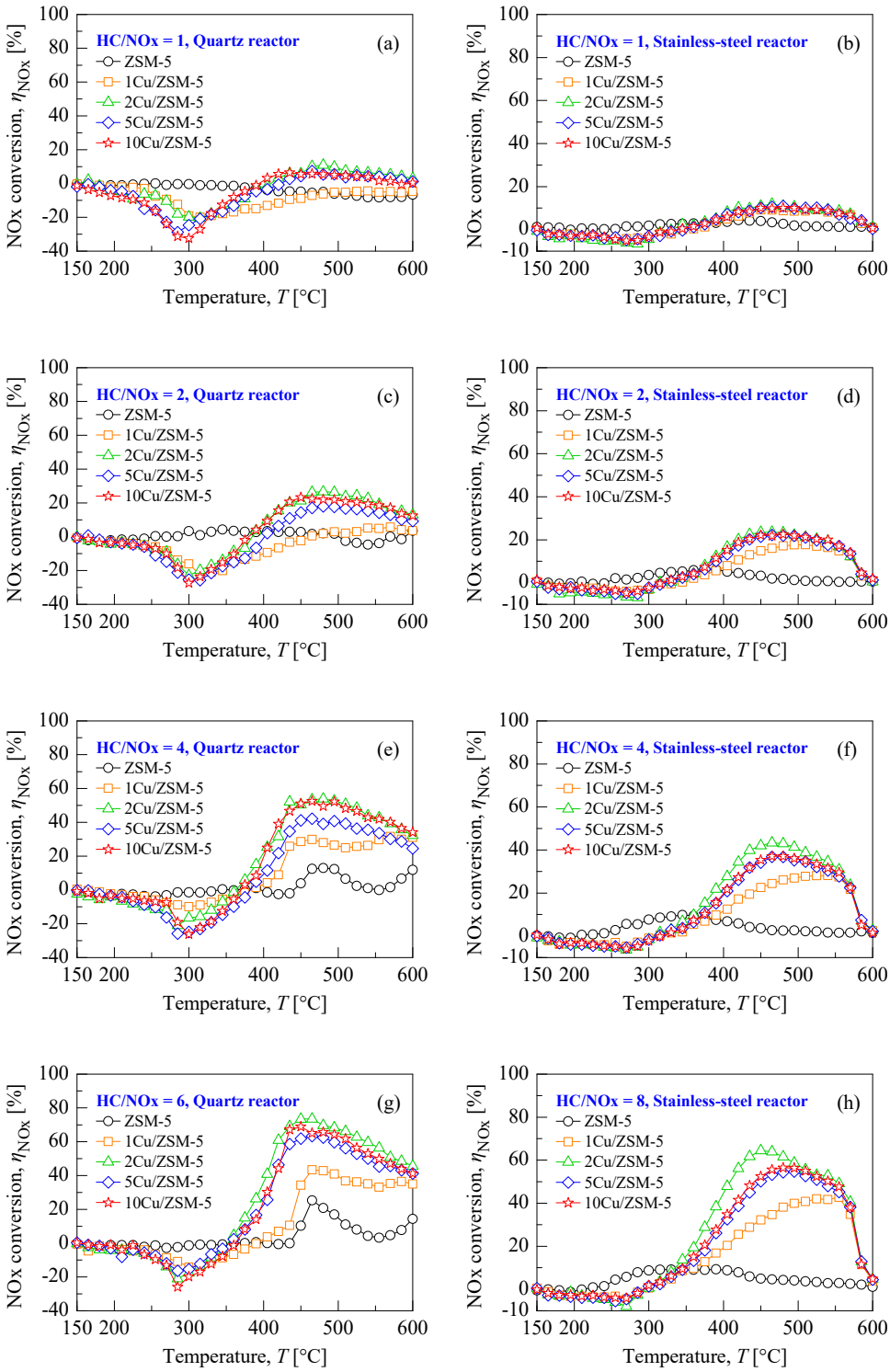

Figure A.3 Comparison of de-NOx performance over the parent ZSM-5 and Cu/ZSM-5 for C_4H_{10}-SCR as a function of reaction temperature in quartz and stainless-steel reactor.

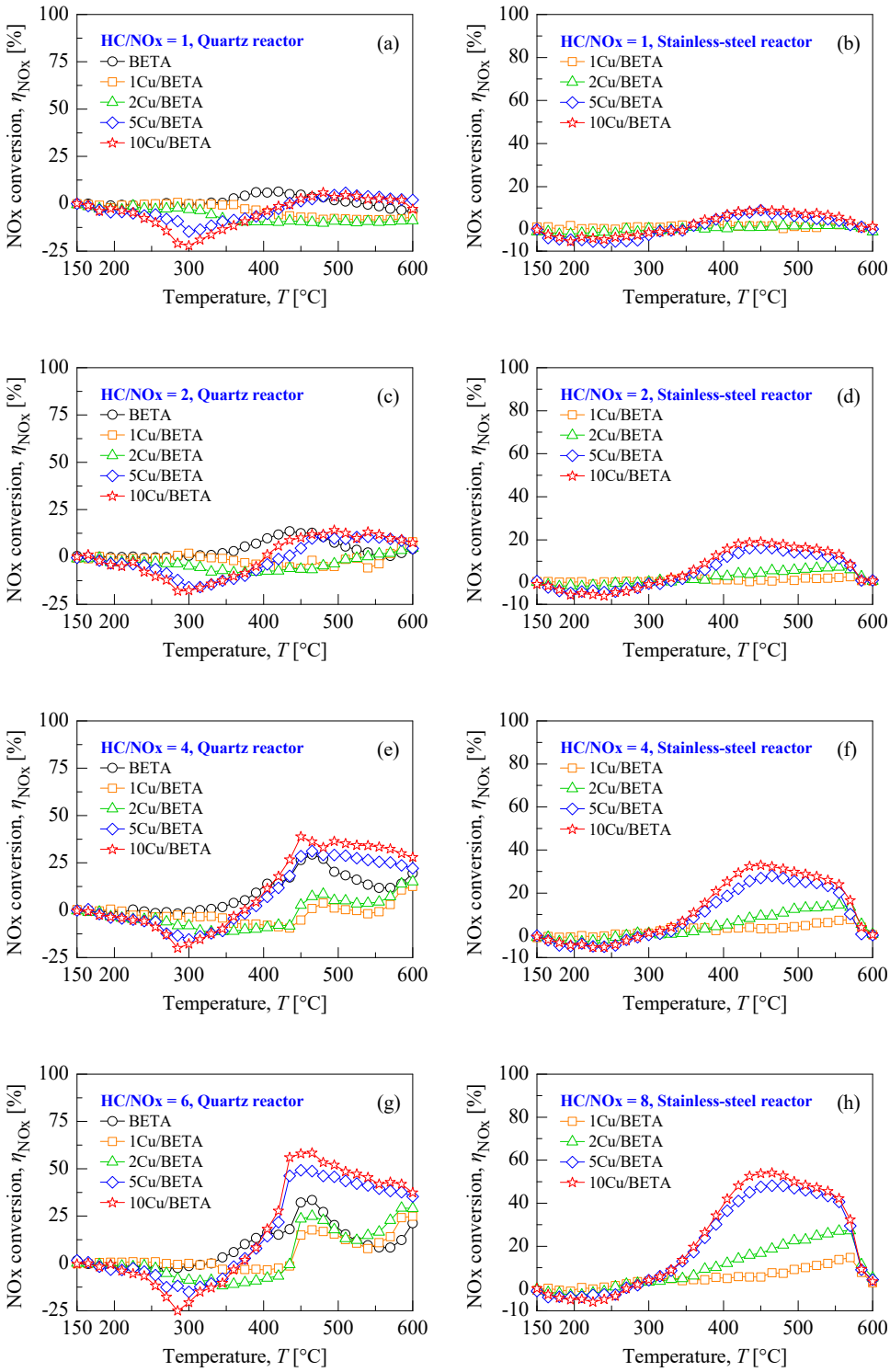

Figure A.4 Comparison of de-NOx performance over the parent BETA and Cu/BETA for C_4H_{10}-SCR as a function of reaction temperature in quartz and stainless-steel reactor.

A.3 Comparison of C_4H_{10} conversion

The effect of reactor system on the reaction temperature-dependence of C_4H_{10} conversion over the Cu/SSZ-13, Cu/ZSM-5, and Cu/BETA is compared in Figures A.5–A.7. The Cu/zeolite catalysts enhanced the rate of C_4H_{10} oxidation with an increase in the Cu loading in both the reactor systems. This was evident in the case of Cu/SSZ-13 and Cu/BETA catalysts. As illustrated in Figure A.7(e), the light-off temperature (LOT_{50}) of Cu/BETA for the quartz reactor decreased in the following order: 429℃ (10Cu/BETA) < 445℃ (5Cu/BETA) < 510℃ (2Cu/BETA) < 551℃ (1Cu/BETA). As similar to that of the quartz reactor, LOT_{50} of Cu/BETA for the stainless-steel reactor also decreased in the following order (Figure A.7(f)): 400℃ (10Cu/BETA) < 415℃ (5Cu/BETA) < 484℃ (2Cu/BETA) < 524℃ (1Cu/BETA). Interestingly, the stainless-steel reactor showed lower LOT_{50} of C_4H_{10} than that of the quartz reactor over the same Cu loading.

From the C_4H_{10} conversion data, the loading of Cu into the respective zeolites improved the C_4H_{10} conversion, and the impregnated Cu species play a key role for the partial oxidation of C_4H_{10}. In addition, the de-NOx performance of Cu/zeolite catalysts was highly related to the rate of C_4H_{10} oxidation. In both the catalytic reactor systems, 2Cu/ZSM-5 exhibited the best de-NOx performance, exhibiting η_{NOx} = 73.6% for the quartz reactor and η_{NOx} = 64.6% at the highest HC/NOx ratio. The LOT_{50} of Cu/ZSM-5 for the quartz reactor at the highest HC/NOx ratio decreased in the following order (Figure A.6(g)): 408℃ (2Cu/ZSM-5) < 410℃ (10Cu/ZSM-5) < 422℃ (5Cu/ZSM-5) < 468℃ (1Cu/ZSM-5). In the case of stainless-steel reactor, the LOT_{50} of Cu/ZSM-5 was in the following order: 420℃ (2Cu/ZSM-5) < 437℃ (10Cu/ZSM-5) < 440℃ (5Cu/ZSM-5) < 474℃ (1Cu/ZSM-5). Therefore, the order of C_4H_{10} conversion exhibited an identical trend between the quartz reactor and stainless-steel reactor.

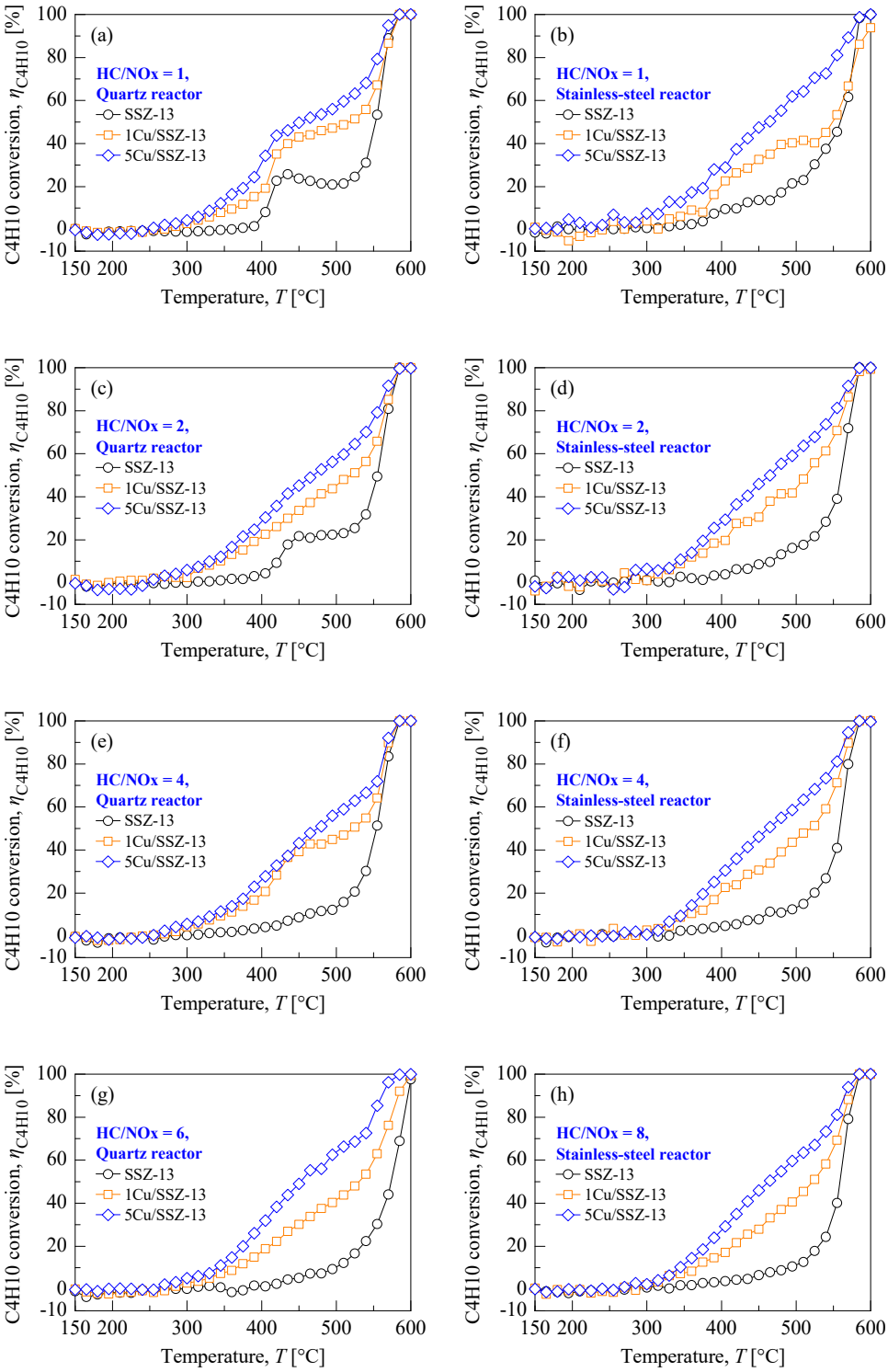

Figure A.5 Comparison of C_4H_{10} conversion over the parent SSZ-13 and Cu/SSZ-13 for C_4H_{10}-SCR as a function of reaction temperature in quartz and stainless-steel reactor.

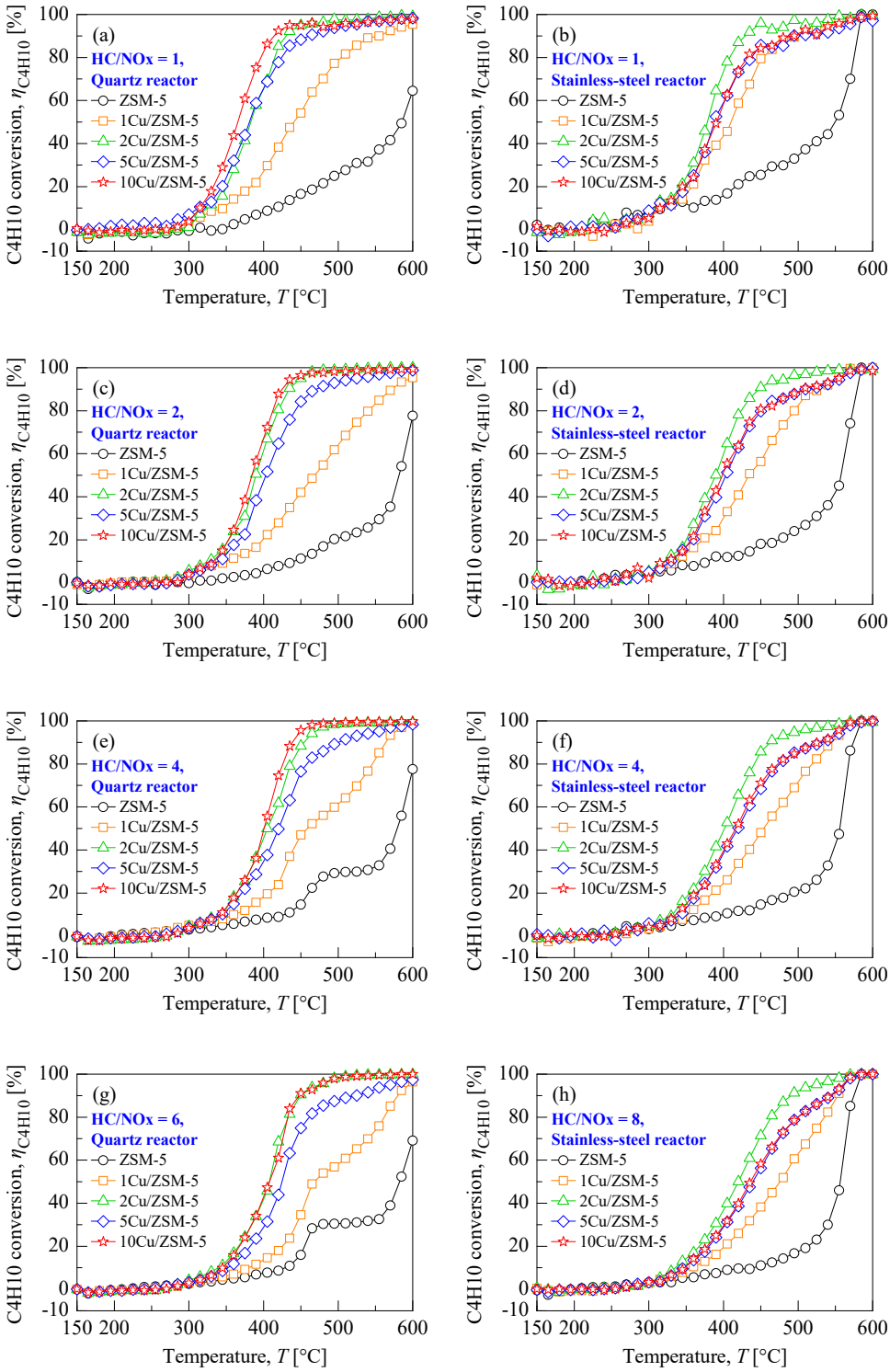

Figure A.6 Comparison of C_4H_{10} conversion over the parent ZSM-5 and Cu/ZSM-5 for C_4H_{10}-SCR as a function of reaction temperature in quartz and stainless-steel reactor.

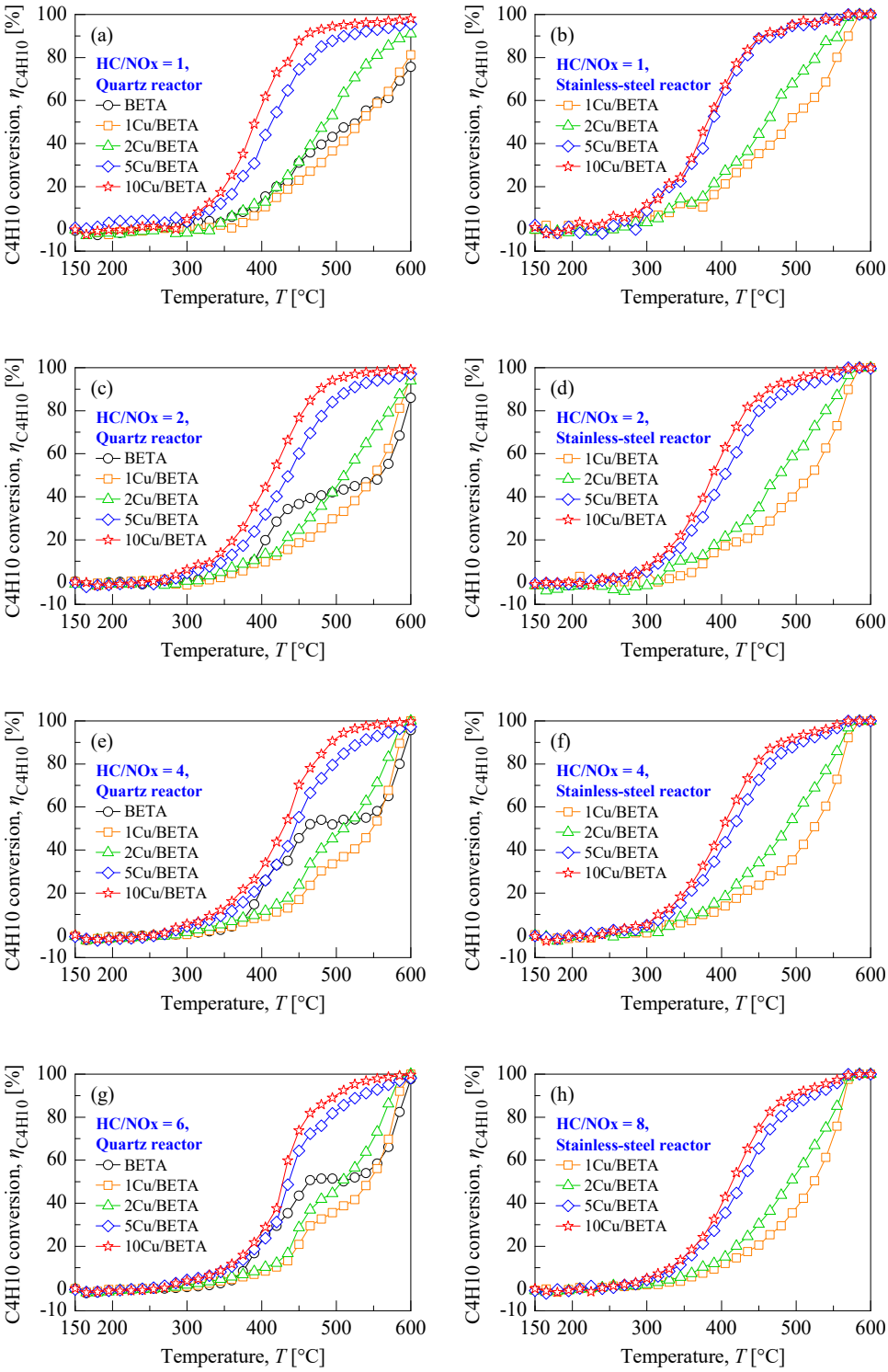

Figure A.7 Comparison of C_4H_{10} conversion over the Cu/BETA for C_4H_{10}-SCR as a function of reaction temperature in quartz and stainless-steel reactor.

A.4 Comparison of CO conversion

The effect of reactor system on the reaction temperature-dependence of CO conversion over the Cu/SSZ-13, Cu/ZSM-5, and Cu/BETA catalysts is compared in Figures A.8–A.10. The negative CO conversion was observed over the parent ZSM-5 zeolite in both reactor systems, and it also considerably decreased with an increased in the HC/NOx ratio, as illustrated in Figure A.8. However, the introduction of Cu into the SSZ-13 zeolite improved the CO conversion over the entire reaction temperatures. In the case of quartz reactor (Figure A.8(a)), the light-off temperature (LOT_{50}) of CO for 5Cu/SSZ-13 was 254°C, which is even lower than that of 1Cu/SSZ-13 (LOT_{50} = 458°C). As similar to the quartz reactor, the LOT_{50} of CO of 5Cu/SSZ-13 and 1Cu/SSZ-13 for the stainless-steel reactor was 257°C and 434°C, respectively (Figure A.8(h)). When HC/NOx ratios of more than 4, the CO conversion of Cu/SSZ-13 began to drop at reaction temperatures above 555°C in the quartz reactor, whereas the stainless-steel reactor retained higher CO conversion even at higher temperature regions. This result may be attributed to the different composition of material for the respective reactors. The quartz reactor is composed of Si and O atoms in a regular framework of SiO_4 silicon-oxygen tetrahedra, with respective oxygen being shared between two tetrahedral units. Whereas, the stainless-steel reactor is composed of stainless-steel 304 (SUS-grade 304), which consists of 66–74 wt% Fe, 18–20 wt% Cr, 8–10.5 wt% Ni, <0.03 wt% S, <1 wt% Si, <0.04 wt% P, <2 wt% Mn, and <0.08 wt% C [232]. Therefore, Fe, Cr and Ni species of the SUS 304 could assist the CO oxidation at higher temperatures in the stainless-steel reactor. Indeed, these materials exhibited the high activity for CO oxidation, especially in the case of Fe [233], Cr [234], and Ni [235, 236].

Comparison of the CO conversion for the quartz reactor and stainless-steel reactor over the parent ZSM-5 zeolite and Cu/zeolite catalysts (Figure A.9) shows that increasing the Cu

loading affected the rate of CO oxidation in both the reactor systems. The distinct feature was observed over the 1Cu/ZSM-5 catalyst. In the case of HC/NOx ratios of more than 4, CO conversion began to decrease from the reaction temperatures of 315–390℃ in the quartz reactor, and the CO conversion ranged negative conversion with increase in the reaction temperatures. However, the CO conversion began to increase at 510℃ (Figure A.9(f)) and 555℃ (Figure A.9(h)), reaching 86−56% CO conversion at 600℃. As described in the previous section, this is attributed to the promotional effect of stainless-steel reactor for CO oxidation at higher temperature regions due to the material component including Fe, Cr and Ni.

In the case of Cu/BETA catalysts as illustrated in Figure A.10, the Cu/BETA catalysts with Cu loadings of less than 5 wt% could not oxide CO at HC/NOx ratios of more than 2 in the both reactor system. In addition, increasing the Cu loading was beneficial for the rate of CO oxidation and LOT_{50} of CO oxidation. For instance, the LOT_{50} of CO for the quartz reactor was 546℃ (5Cu/BETA) and 494℃ (10Cu/BETA) at HC/NOx =4, which is higher than those of the stainless-steel reactor; LOT_{50} of these catalysts for the stainless-steel reactor was 505℃ (5Cu/BETA) and 459℃ (10Cu/BETA) at HC/NOx = 4. The similar trend could be observed at other HC/NOx ratios. Therefore, the stainless-steel reactor had a positive effect on the rate of CO oxidation at relative higher reaction temperatures and LOT_{50} of CO due to the promotional effect of stainless steel for CO oxidation.

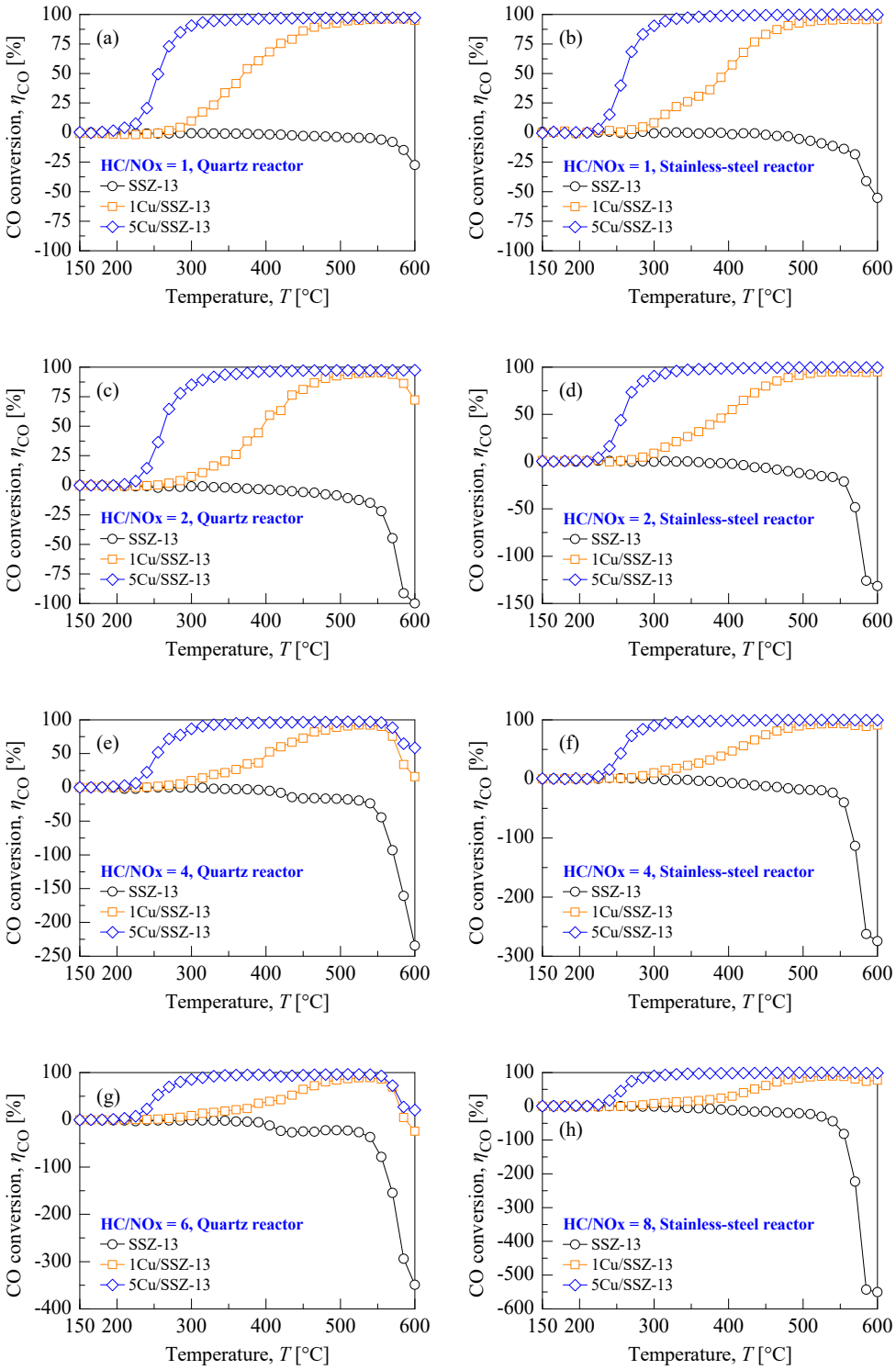

Figure A.8 Comparison of CO conversion over the parent SSZ-13 and Cu/SSZ-13 for C_4H_{10}-SCR as a function of reaction temperature in quartz and stainless-steel reactor.

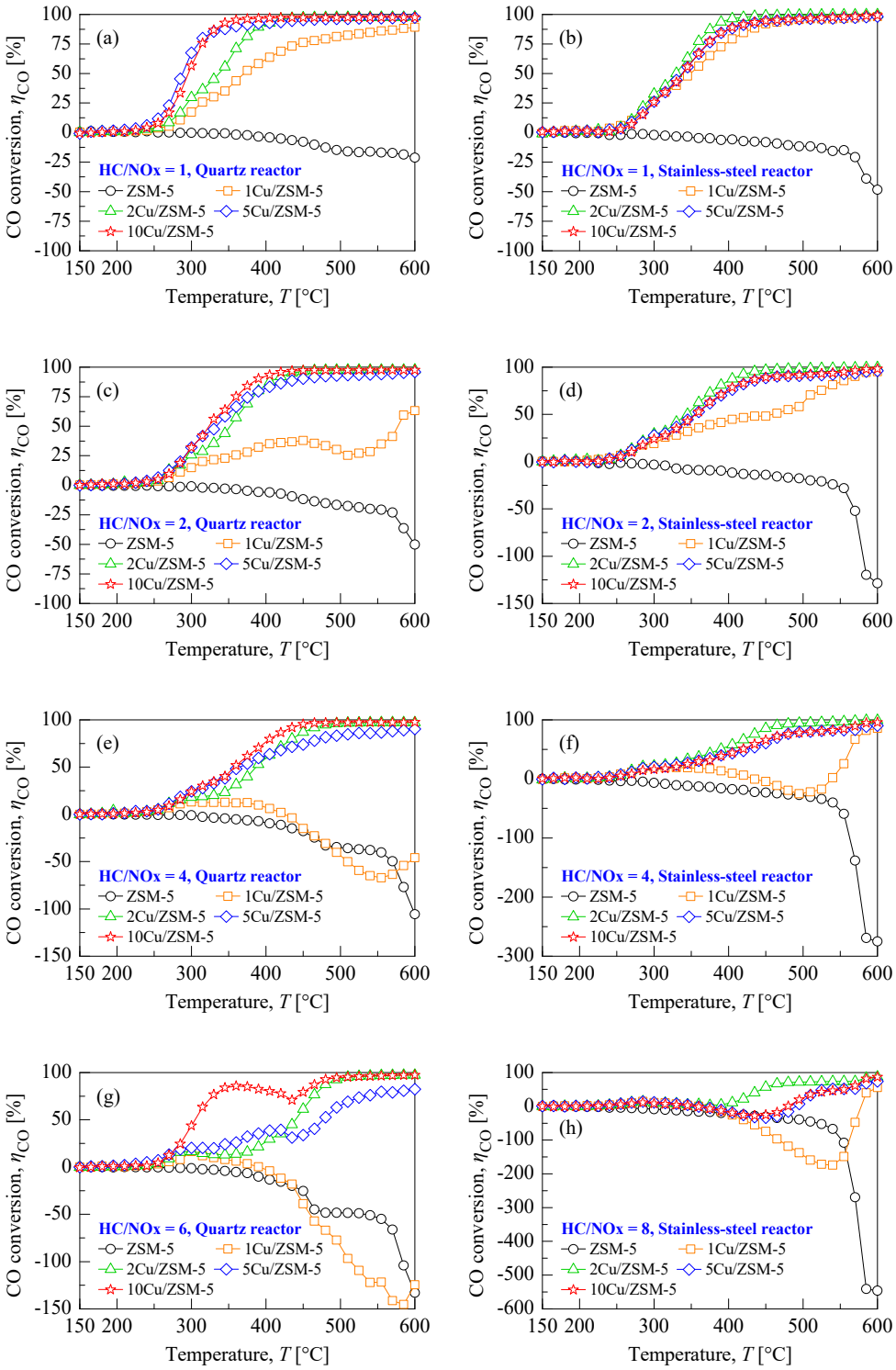

Figure A.9 Comparison of CO conversion over the parent ZSM-5 and Cu/ZSM-5 for C_4H_{10}-SCR as a function of reaction temperature in quartz and stainless-steel reactor.

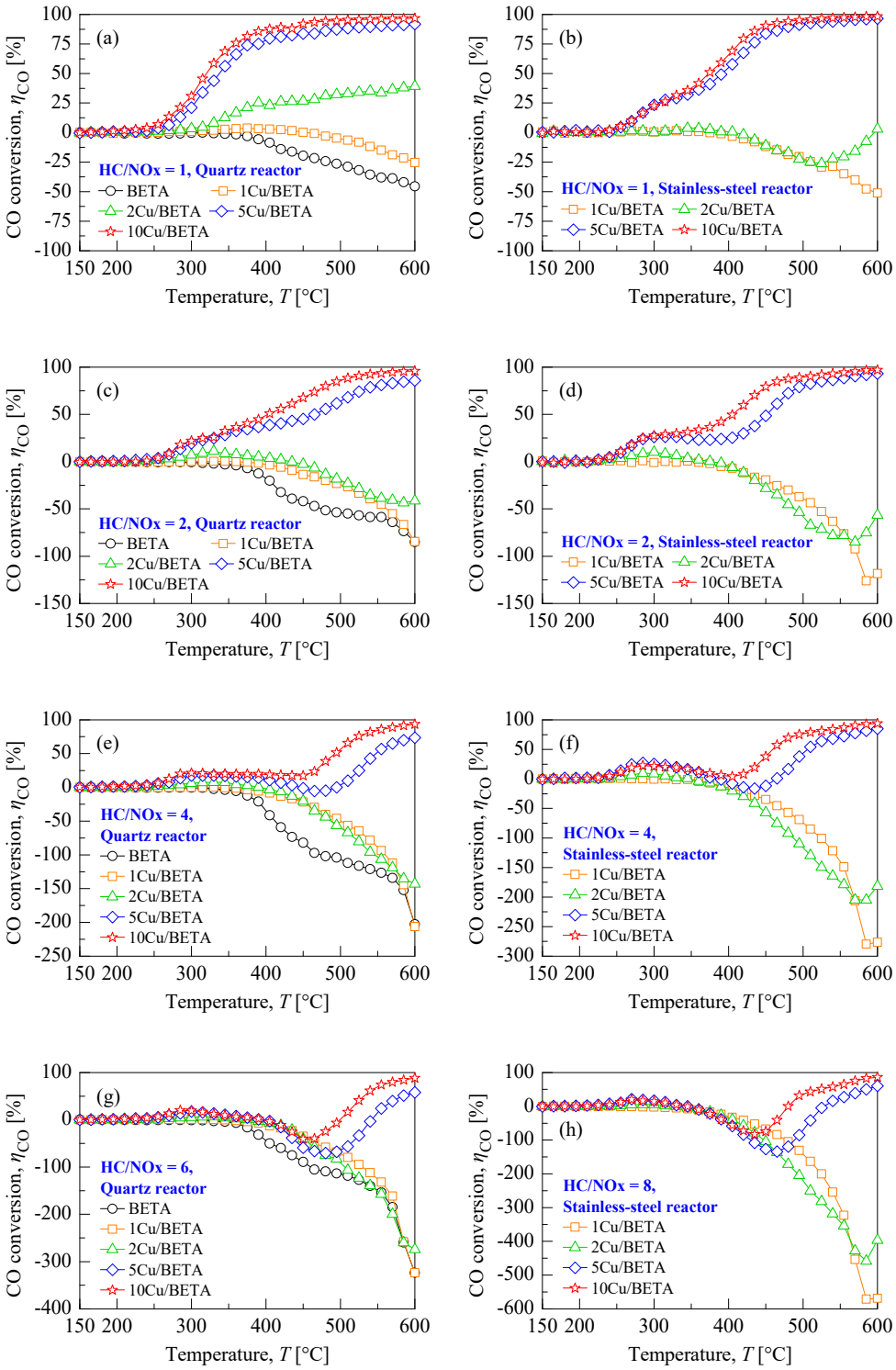

Figure A.10 Comparison of CO conversion over the Cu/BETA for C_4H_{10}-SCR as a function of reaction temperature in quartz and stainless-steel reactor.

A.5 Effect of reactor system on N_2 yield

The effect of catalytic reactor system on N_2 yield over the Cu/zeolite catalysts, that exhibited best de-NOx performance among the respective Cu/zeolites at HC/NOx = 4, is compared at reaction temperature ranging from 360 to 600℃ in Figure 6.11. Notably, there was no appreciable difference between the NOx conversion and N_2 yield, suggesting that both catalytic reactors could reduce supplied NOx to N_2 by C_4H_{10}. The similar trend was also observed at other HC/NOx ratios over the all Cu/zeolite catalysts (not shown in Figure). Although, nitrous oxide (N_2O) was produced over the 10Cu/BETA catalyst for the stainless-steel reactor, the N_2O selectivity was less than 0.8–3.5% from 390 to 540℃ (Figure A.11(f)).

From the influence of O_2 concentration in the feed gas during the C_4H_{10}-SCR process, the N_2 yield did not coincide with the NOx conversion because NOx was reduced to N_2 with accompanying side-reaction to produce NH_3. To investigate the effect of reactor system on side-reaction, the N_2 yield and NOx conversion over the 2Cu/ZSM-5 catalysts is compared, as shown in Figure A.12. The NOx conversion began to sharply increase in the both reactor systems from 450℃ in the absence of O_2, achieving 97.9% NOx conversion for the quartz reactor and 92.6% NOx conversion for the stainless-steel reactor at 600℃. Moreover, N_2 yield did not coincide with the NOx conversion due to the formation of NH_3 by the side-reaction; especially, more NH_3 was produced in the stainless-steel reactor because the HC/NOx ratio was higher than that of the quartz reactor. In contrast, when more than 1 vol.% O_2 was present in the feed gas, the N_2 yield was in good accord with the NOx conversion in both the reactor systems. These findings indicate that O_2 concentration highly effects the catalytic selectivity, largely producing NH_3 as a side-reaction in the absence of O_2.

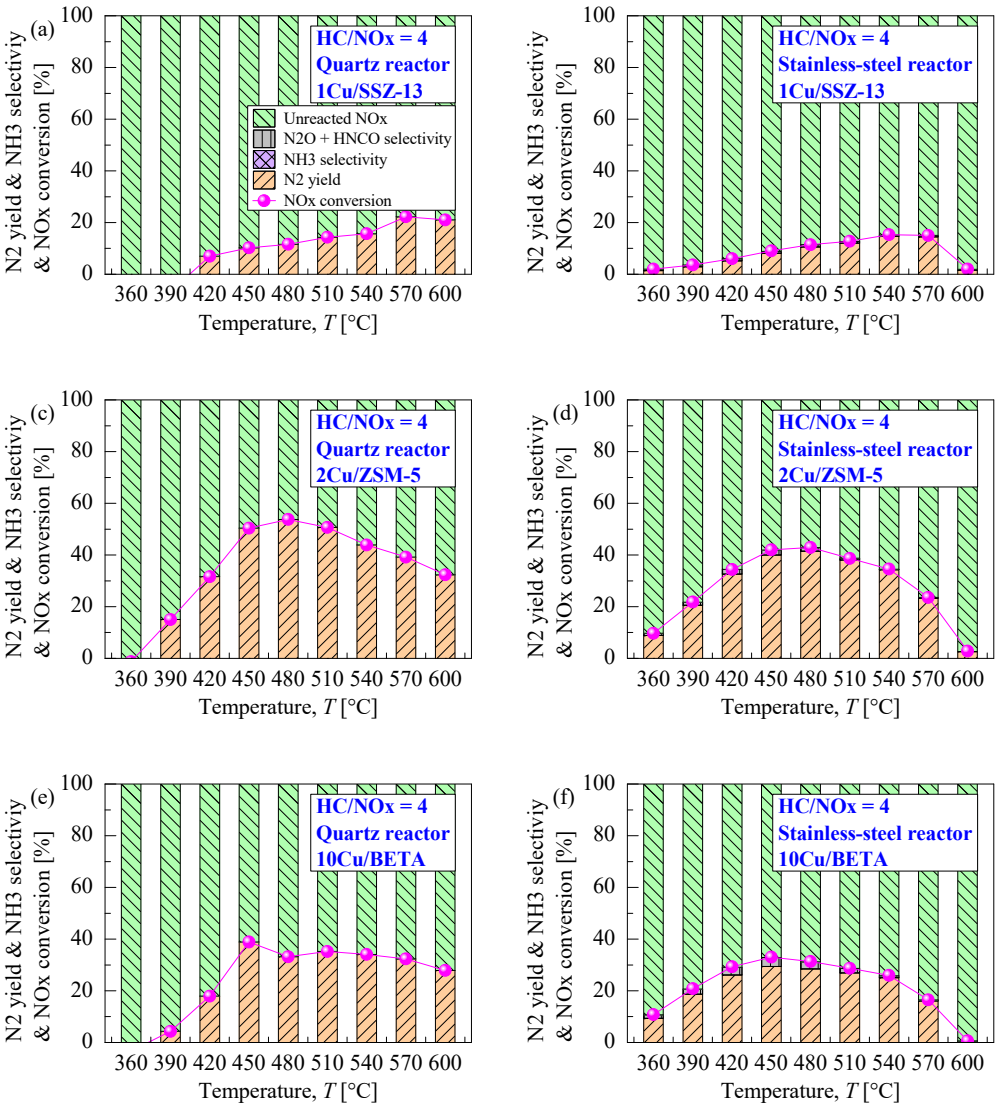

Figure A.11 Effect of catalytic reactor system on N_2 yield over the Cu/zeolite catalysts at HC/NOx = 4 in C_4H_{10}-SCR process.

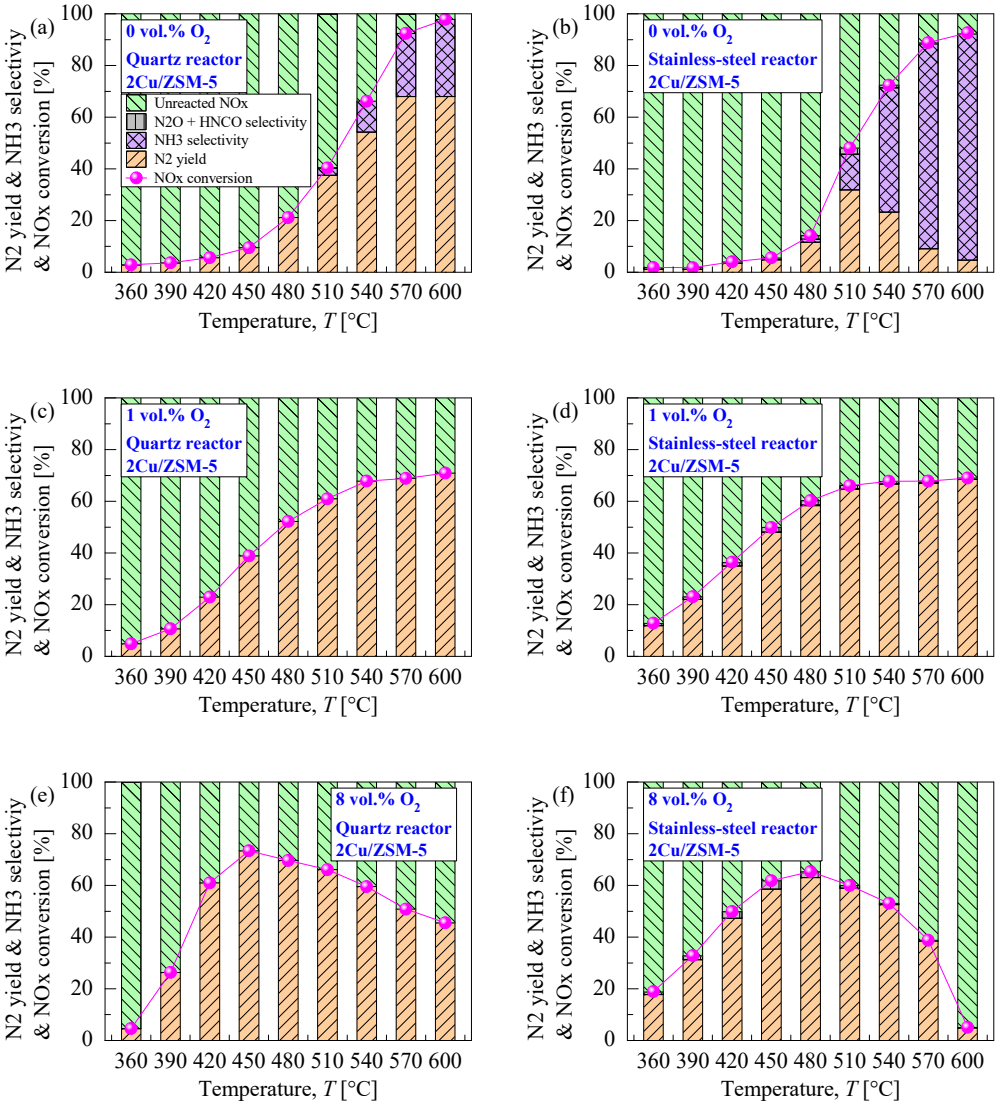

Figure A.12 Effect of O_2 concentration (0–8 vol.% O_2) on N_2 yield over the 2Cu/ZSM-5 catalysts in quartz (HC/NOx = 6) and stainless-steel reactor (HC/NOx = 8) during C_4H_{10}-SCR process.

A.6 Summary

The different reactor systems that are quartz and stainless-steel reactors were compared in the C_4H_{10}-SCR process over the Cu/zeolite catalysts. The catalytic activities, including de-NOx performance, partial oxidation of C_4H_{10}, CO oxidation, N_2 selectivity, and by-products, are discussed in both catalytic reactor systems to identify the effect of catalytic operating environment. The NOx conversion of Cu/zeolites considerably decreased at reaction temperatures above 570℃ in the stainless-steel rector, reaching nearly less than of 5% NOx conversion at 600℃. However, in the case of quartz reactor, the NOx conversion of all the Cu/zeolite catalysts was much higher than that of the stainless-steel reactor, even at higher temperature regions. The quartz reactor was favorable for de-NOx ability. The rate of partial oxidation of C_4H_{10} exhibited an identical trend between the quartz and stainless-steel reactor. When HC/NOx ratios of more than 4, the CO conversion began to drop at reaction temperatures above 555℃ over the specific Cu/zeolite in the quartz reactor, whereas the stainless-steel reactor could retain higher CO conversion even at high temperature regions. This result was attributed to the different composition of material for the respective reactors. Fe, Cr, and Ni, that are included in the stainless-steel reactor as prime element, which had a positive effect on the rate of CO oxidation compared to the quartz reactor at relatively higher reaction temperatures and LOT_{50} of CO. And the temperature distribution of upstream heater and downstream reacor mainly affected the unfavorable effect on the reactor test above 570℃ because the upstream heater was highly heated up to 680℃ (reactor T = 600℃). From the influence of O_2 concentration, the N_2 yield did not coincide with the NOx conversion due to formation of NH_3 as side-reaction in the absence of O_2, whereas, there was no appreciable difference between the NOx conversion and N_2 yield when O_2 was supplied more than 1 vol.%.

Appendix B: Measuring Equipment Technical Data

All the prepared catalysts were characterized by various techniques, such as X-ray diffraction (XRD), ^{27}Al magic angle spinning–nuclear magnetic resonance (^{27}Al MAS–NMR), N_2–isotherms, inductively coupled plasma–atomic emission spectrometry (ICP–AES), high-resolution field emission–scanning electron microscope (FE–SEM), scanning transmission electron microscope (STEM), and Ultraviolet-visible (UV–vis) spectroscopy.

The crystal phases of the powder catalysts were characterized using a 3D high-resolution X-ray diffractometer (Empyrean, Malvern PANalytical) with Cu-Kα radiation (λ = 1.5425 Å) by employing an X-ray generator operating at 40 kV and 30 mA. The X-ray diffraction (XRD) spectra were recorded in the 2θ range of 5–80° at a scanning angle of 0.02°. Table B.1 summarizes the specifications of the powder XRD analyzer.

The structural coordination of the Al species located in the zeolite framework was identified by solid-state ^{27}Al magic angle spinning–nuclear magnetic resonance (^{27}Al MAS–NMR) using a JNM ECA-600 spectrometer (JOEL) operating at a resonance frequency of 156.4 MHz. Aluminium ammonium sulfate dodecahydrate ($(NH_4)Al(SO_4)_2 \cdot 12H_2O$) was used as a reference for the chemical shift of the ^{27}Al species in the powder catalysts at −0.54 ppm. Table B.2 shows the specifications of the JEOL JNM ECA-600 NMR spectrometer.

The liquid N_2 adsorption and desorption were carried out to characterize the surface area and the pore size of the prepared catalysts. The specific surface area and total pore volume were identified by N_2 adsorption-desorption at 77 K using a Belsorp–Mini II (MicrotracBEL). Table B.3 summarizes the specifications of the N_2 isotherms analyzer used in the present study. Prior to the N_2 isotherms measurement, all samples were evacuated at 350℃ for 3 h to remove contaminants and moisture. The Brunauer–Emmett–Teller (BET) specific surface area and average pore diameter were calculated from the N_2 adsorption profiles at a relative

pressure ranging from 0.05 to 0.1, and the pore volume was calculated at a relative pressure of 0.99. The pore size distribution and micropore volume were also calculated from the N_2–isotherms using Barrett–Joyner–Halenda (BJH) and t-plot methods, respectively. The BET surface area (A_{BET}) was calculated by the following equations:

$$A_{BET} = \nu_m \times \frac{N_A}{V_{Ideal}} \times a_m \ [m^2/g] \tag{B.1}$$

$$\nu_m = \frac{1}{Y_i \times C_{BET}} \ [cm^3/g] \tag{B.2}$$

$$C_{BET} = \frac{1 \times S_{BET}}{Y_i} \tag{B.3}$$

The copper content of the prepared catalyst was analyzed by inductively coupled plasma–atomic emission spectroscopy (ICP–AES). Prior to the ICP–AES measurement, the prepared catalyst powder was mixed with sodium hydroxide (NaOH) solution to dissolve the metal species. The mixture of 50 mg of the catalyst sample and NaOH was prepared, and these solutions were supplied to the ICP-AES analyzer. Table B.4 summarizes the specifications of the ICP–AES analyzer used in the present study. From the ICP–AES results, the copper content was calculated by applying the equation (B.4):

$$W_{Cu} = \left(C_{Cu} \times \frac{50}{1000 \times m_{cat}} \right) \times 100 \ [wt\%] \tag{B.4}$$

The cell configurations and physical properties of monolithic cordierite (Table 2.2) were calculated by applying the following equations:

$$L = \sqrt{\frac{1}{N}} \times 25.4 \ [mm] \tag{B.5}$$

$$d_k = L - t_w \ [mm] \tag{B.6}$$

$$OFA = \frac{(L - t_w)^2}{L^2} \tag{B.7}$$

$$GSA = 4\frac{(L - t_w)}{L^2} \ [cm^2/cm^3] \tag{B.8}$$

$$d_{\mathrm{h}} = 4\frac{OFA}{GSA}\ [\mathrm{mm}] \tag{B.9}$$

The microstructure and crystalline morphology of the prepared catalysts were characterized by field emission–scanning electron microscopy (FE–SEM) using an ultra-high-resolution microscope with a cold filed emission gun (CFE) operating at 1.0 kV. Table B.5 summarizes the specifications of FE-SEM analyzer used in the present study.

Transmission electron microscopy (TEM) was analyzed by Hitachi H-8000 to observe the distribution of copper particles. From the obtained TEM micrographs, nearly 100 copper particles were identified, and then an average particle diameter and particle size distribution of copper species were calculated by an ImageJ software.

The valence state of Cu species of the Cu/zeolite catalysts was examined by ultraviolet–visible (UV–vis) spectra in the diffuse reflectance mode using a Jasco V-650 UV–vis spectrophotometer. Table B.6 shows the specifications of the UV–vis analyzer. To identify the Cu species impregnated in the powder Cu/zeolite samples, UV–vis adsorption spectra were recorded in the range of wavelength between 200 nm and 600 nm. The collected reflection spectra were treated by the so-called Schuster–Munk function. The atomic states of the surface elements and their valence states were identified by X-ray photoelectron spectroscopy (XPS) (K-Alpha+, Thermo Fisher Scientific, spot size: 400 μm) using an Al-Kα micro-focused monochromator. The binding energy data from the XPS spectra were acquired in the range of −10 to 1,350 eV at a step size of 1.0 eV. Table B.7 summarizes the specifications of the XPS analyzer.

The specifications of Fourier transform infrared spectroscopy (FTIR) analyzer are summarized in Table B.8 and B.9, respectively.

Table B.1 Specifications of powder XRD analyzer.

Model: Empyrean (Malvern Panalytical, Netherlands)	
X-ray Generator	
Maximum rated output	4 kW
Rated tube voltage	60 kV
Rated tube current	2 – 60 mA
Target material	Copper
Focus size	width 0.4 × length 12 mm
Wavelength	$K\alpha_1$ 1.540598 Å, $K\alpha_2$ 1.544426 Å
$K\alpha_2$/ $K\alpha_1$ ratio intensity	0.50
Divergence slit	Fixed slit 1/2°
Goniometer	
Goniometer radius	240 mm
2θ measuring range	$-111° < 2\theta < 168°$
Minimum step size	0.0001°
Detector	PIXcel3D-Medipix3 1×1

Table B.2 Specifications of MAS–NMR analyzer.

Model: JNM–ECA 600 (JEOL Ltd., Japan)		
Spectrometer		Osicillator, receiver, power amplifier
Magnet	SCM field strength	14.1 T
	Bore diameter	54 mm
Probe		5 mm FG/TH tunable

Table B.3 Specifications of N_2 adsorption-desorption analyzer.

Model: BELSOPR-mini II (MicrotracBEL Corp., Japan)	
Measurement principle	Volumetric gas adsorption method + AFSM
Adsorptive	N_2, Ar, H_2, CO_2, and other non-corrosive gases
Analysis port	High accuracy mode: 3 ports Standard mode: 2 ports
Specific surface area	0.01 m^2/g (N_2 at 77 K)
Pore size distribution	0.35 – 200 nm in pore diameter
Pressure transducer	133 kPa (1,000 Torr) ± 0.5% of full scale
Dewar vessel	Volume: 2 L Holding time: 30 hours
Sample cell	1.8 cm^3

Table B.4 Specifications of inductively coupled plasma–atomic emission spectroscopy (ICP–AES).

Model: ICPE-9000 Plasma Atomic Emission Spectrometer (Shimadzu Corp., Japan)	
Plasma Light Source	
Torch unit	Axial observation
Sample misting chamber	Cyclone chamber
Nebulizer	Coaxial type
Radio Frequency Generator	
Oscillator sample	Crystal oscillator
Max. frequency output	1.6 kW
Radio frequency circuit element	Transistor element
Ignition method	Fully automatic
Spectrometer Unit	
Optical system	Echelle spectrometer
Wavelength range	167 – 800 nm
Resolution	≤ 0.005 nm at 200 nm
Vacuum ultraviolet range compatibility	Vacuum spectrometer
Spectrometer temperature	With thermal control

Table B.5 Specifications of field emission–scanning electron microscopy (FE–SEM).

Model: Ultra-high-resolution SEM SU9000 (Hitachi High-Tech Corp., Japan)	
Resolution	
SE image	0.4 nm (30 kV, sample height = 1.0 mm) 1.2 nm (1 kV, sample height = 2.0 mm)
STEM image	0.34 nm (30 kV, sample height = 0.0 mm, lattice image)
Magnification	
LM mode	× 80 – 10,000 (Mag on photo)
HM mode	× 800 – 3,000,000 (Mag on photo)
Electron optics	
Electron gun	Cold cathode field emission source
Acc. Voltage	0.5 – 30 kV (0.1 kV step)
Beam blanking	Electrostatic type (synchronized with scanning signal)
Detector	
Detector	Secondary electron detector

Table B.6 Specifications of ultraviolet–visible spectroscopy (UV–vis).

Model: V-650 (Jasco Corp., Japan)	
Optical system	Single monochromator Fully symmetrical double beam Czerny-Turner mount
Light source	Deuterium lamp: 190 – 350 nm Halogen lamp: 330 – 900 nm
Detector	Photomultiplier tube
Wavelength range	190 – 900 nm
Wavelength repeatability	± 0.05 nm
Wavelength accuracy	± 0.2 nm (at 656.1 nm)
Scanning speed	10 – 4,000 nm/min
RMS noise	0.00003 Abs
Baseline flatness	± 0.0003 Abs

Table B.7 Specifications of X-ray photoelectron spectroscopy (XPS).

Model: K-Alpha$^+$ (Thermo Fisher Scientific, United States of America)	
Range of motion	100 – 4,000 eV
X-ray monochromator	Al Kα Micro-focused
Ion Gun	EX06 ion source (200 eV to 4 keV)
X-ray spot size	30 – 400 μm in 5 μm steps
Energy resolution	0.5 eV FWHM
Sample tilt	55°
Analysis depth	~10 nm from sample surface
Elementary analysis	from Li (lithium) to U (uranium)

Table B.8 Specifications of Fourier transform infrared spectroscopy (FTIR).

Model: BOB-2000FT (Best Instrument Co. Ltd., Japan)	
Measuring components	Standard 25 + calculated components, max. 40
Wavelength	400 – 7,000 cm^{-1}
Laser source	He-Ne laser
Wavelength resolution	0.5 cm^{-1}
Sampling frequency	0.1 – 10 Hz
Light path length	5.11 m
Cell volume	200 cc
Cell temperature	191℃
Cell window material	ZnSe
Cell inner pressure	Vacuum
Optical mirror	Gold coat
Sampling flowrate	Maximum 12 L/min (variable flowrate)
Response time	1.0 – 1.5 sec (12 L/min sample)
Purge gas	N_2 gas

Table B.9 Specifications of Fourier transform infrared spectroscopy (Midac FTIR).

Model: Midac I-2004 (Midac Corp., United States of America)	
Laser source	He-Ne laser
Wavelength resolution	32 – 0.25 cm^{-1}
Spectral range	With Zn Se optics, MCT: 7, 800 – 650 cm^{-1}
Interferometer	Michelson
Detector	Thermoelectrically cooled MCT
Light path length	4.0 m
Cell volume	300 cc
Cell temperature	150℃
Accuracy	> 0.001 cm^{-1}

Appendix C: List of Research Achievements

S. Sato, Y. Ogita, K. Lee, H. Kosaka, Research on Improvement of NOx Reduction Efficiency in HC-SCR system, *The 25th Internal Combustion Engine Symposium* (2014) pp.1–9.

Y. Ogita, K. Lee, S. Sato, H. Kosaka, ゼオライト系触媒を用いた SCR 排気後処理システムの過渡制御に関する研究, 2014 自動車技術会関東支部学術研究講演会.

K. Lee, Y. Ogita, S. Sato, H. Kosaka, A Study on NOx Reduction Performance of the HC-SCR System over Cu/zeolite Catalysts, *JSAE 2015 Annual Congress Proceedings* (2015), JSAE 20155409, pp.2148–2153.

K. Lee, Y. Ogita, S. Sato, H. Kosaka, NOx Reduction with the HC-SCR System over Cu/Zeolite Based Catalysts, *JSAE/SAE 2015 International Powertrains, Fuels & Lubricants Meeting*, SAE Technical Paper 2015-01-2012, pp.1–8.

K. Lee, Y. Ogita, S. Sato, H. Kosaka, NOx reduction with the HC-SCR system over Zeolite Based Catalysts in Diesel Applications, 9th Japan (Tokyo Institute of Technology) - Korea (Korea Advanced Institute of Science and Technology) - China (Zhejiang University) Student Symposium (2015).

S. Sato, K. Lee, H. Kosaka, T. Yokoi, Cu/ゼオライト触媒を用いた HC-SCR システムによる NOx 浄化技術, ディーゼルエンジン排気浄化における触媒材料およびシステムの開発・要素技術, サイエンス&テクノロジー (2017) pp.266–279.

K. Lee, S. Sato, H. Kosaka, T. Yokoi, B. Choi, Effective Zeolite Topology of Cu/zeolite C_4H_{10}-SCR on deNOx Performance, *KSAE 2018 Annual Spring Conference* (2018) pp.241–242.

K. Lee, S. Sato, H. Kosaka, T. Yokoi, B. Choi, Effect of Zeolite Frameworks on NOx Conversion of Cu Containing-zeolite Catalyst by C_4H_{10}-SCR, *2018 International Conference on Advanced Automotive Technology (ICAT)*.

K. Lee, H. Kosaka, S. Sato, T. Yokoi, B. Choi, D. Kim, Effects of Cu loading and zeolite topology on the selective catalytic reduction with C_3H_6 over Cu/zeolite catalysts, *Journal of Industrial and Engineering Chemistry* 72 (2019) pp.73–86.

K. Lee, H. Kosaka, S. Sato, T. Yokoi, B. Choi, Effect of Cu content and zeolite framework of *n*-C_4H_{10}-SCR catalysts on de-NOx performances, *Chemical Engineering Science* 203 (2019) pp.28–42.